Jordan Journal of
PHYSICS
An International Peer-Reviewed Research Journal

Volume 18, No. 2, June 2025, Moharrm 1447 H

Jordan Journal of Physics (*JJP*): An International Peer-Reviewed Research Journal funded by the Scientific Research and Innovation Support Fund, Jordan, and published quarterly by the Deanship of Research and Graduate Studies, Yarmouk University, Irbid, Jordan.

Manuscripts should be submitted to:

Prof. Muhammad S. Bawa'aneh
Editor-in-Chief, Jordan Journal of Physics
Deanship of Research and Graduate Studies
Yarmouk University-Irbid-Jordan
Tel. 00 962 2 7211111 Ext. 2075
E-mail: *jjp@yu.edu.jo*
Website: *https://jjp.yu.edu.jo*

Jordan Journal of
PHYSICS
An International Peer-Reviewed Research Journal

Volume 18, No. 2, June 2025, Moharrm 1447 H

The Hashemite Kingdom of Jordan

Yarmouk University

Jordan Journal of PHYSICS

An International Peer-Reviewed Research Journal

Funded by the Scientific Research and Innovation Support Fund

Volume 18, No. 2, June 2025, Moharrm 1447 H

Instructions to Authors

Instructions to authors concerning manuscript organization and format apply to hardcopy submission by mail, and also to electronic online submission via the Journal homepage website (http://jjp.yu.edu.jo).

Manuscript Submission

Manuscripts are submitted electronically through the journal's website:

https://jjp.yu.edu.jo/

Original *Research Articles*, *Communications* and *Technical Notes* are subject to critical review by minimum of two competent referees. Authors are encouraged to suggest names of competent reviewers. *Feature Articles* in active Physics research fields, in which the author's own contribution and its relationship to other work in the field constitute the main body of the article, appear as a result of an invitation from the Editorial Board, and will be so designated. The author of a *Feature Article* will be asked to provide a clear, concise and critical status report of the field as an introduction to the article. *Review Articles* on active and rapidly changing Physics research fields will also be published. Authors of *Review Articles* are encouraged to submit two-page proposals to the Editor-in-Chief for approval. Manuscripts submitted in *Arabic* should be accompanied by an Abstract and Keywords in English.

Organization of the Manuscript

Manuscripts should be typed double spaced on one side of A4 sheets (21.6 x 27.9 cm) with 3.71 cm margins, using Microsoft Word 2000 or a later version thereof. The author should adhere to the following order of presentation: Article Title, Author(s), Full Address and E-mail, Abstract, PACS and Keywords, Main Text, Acknowledgment. Only the first letters of words in the Title, Headings and Subheadings are capitalized. Headings should be in **bold** while subheadings in *italic* fonts.

Title Page: Includes the title of the article, authors' first names, middle initials and surnames and affiliations. The affiliation should comprise the department, institution (university or company), city, zip code and state and should be typed as a footnote to the author's name. The name and complete mailing address, telephone and fax numbers, and e-mail address of the author responsible for correspondence (designated with an asterisk) should also be included for official use. The title should be carefully, concisely and clearly constructed to highlight the emphasis and content of the manuscript, which is very important for information retrieval.

Abstract: A one paragraph abstract not exceeding 200 words is required, which should be arranged to highlight the purpose, methods used, results and major findings**.**

Keywords: A list of 4-6 keywords, which expresses the precise content of the manuscript for indexing purposes, should follow the abstract.

PACS: Authors should supply one or more relevant PACS-2006 classification codes, (available at http://www.aip.org/pacs/pacs06/pacs06-toc.html)

Introduction: Should present the purpose of the submitted work and its relationship to earlier work in the field, but it should not be an extensive review of the literature (e.g., should not exceed 1 ½ typed pages).

Experimental Methods: Should be sufficiently informative to allow competent reproduction of the experimental procedures presented; yet concise enough not to be repetitive of earlier published procedures.

Results: should present the results clearly and concisely.

Discussion: Should be concise and focus on the interpretation of the results.

Conclusion: Should be a brief account of the major findings of the study not exceeding one typed page.

Acknowledgments: Including those for grant and financial support if any, should be typed in one paragraph directly preceding the References.

References: References should be typed double spaced and numbered sequentially in the order in which they are cited in the text. References should be cited in the text by the appropriate Arabic numerals, enclosed in square brackets. Titles of journals are abbreviated according to list of scientific periodicals. The style and punctuation should conform to the following examples:

1. Journal Article:

a) Heisenberg, W., Z. Phys. 49 (1928) 619.
b) Bednorz, J. G. and Müller, K. A., Z. Phys. B64 (1986) 189
c) Bardeen, J., Cooper, L.N. and Schrieffer, J. R., Phys. Rev. 106 (1957) 162.
d) Asad, J. H., Hijjawi, R. S., Sakaji, A. and Khalifeh, J. M., Int. J. Theor. Phys. 44(4) (2005), 3977.

2. Books with Authors, but no Editors:

a) Kittel, C., "Introduction to Solid State Physics", 8th Ed. (John Wiley and Sons, New York, 2005), chapter 16.
b) Chikazumi, S., C. D. Graham, JR, "Physics of Ferromagnetism", 2nd Ed. (Oxford University Press, Oxford, 1997).

3. Books with Authors and Editors:

a) Allen, P. B. "Dynamical Properties of Solids", Ed. (1), G. K. Horton and A. A. Maradudin (North-Holland, Amsterdam, 1980), p137.
b) Chantrell, R. W. and O'Grady, K., "Magnetic Properities of Fine Particles" Eds. J. L. Dormann and D. Fiorani (North-Holland, Amsterdam, 1992), p103.

4. Technical Report:

Purcell, J. "The Superconducting Magnet System for the 12-Foot Bubble Chamber", report ANL/HEP6813, Argonne Natt. Lab., Argonne, III, (1968).

5. Patent:

Bigham, C. B., Schneider, H. R., US patent 3 925 676 (1975).

6. Thesis:

Mahmood, S. H., Ph.D. Thesis, Michigan State University, (1986), USA (Unpublished).

7. Conference or Symposium Proceedings:

Blandin, A. and Lederer, P. Proc. Intern. Conf. on Magnetism, Nottingham (1964), P.71.

8. Internet Source:

Should include authors' names (if any), title, internet website, URL, and date of access.

9. Prepublication online articles (already accepted for publication):

Should include authors' names (if any), title of digital database, database website, URL, and date of access.

For other types of referenced works, provide sufficient information to enable readers to access them.

Tables: Tables should be numbered with Arabic numerals and referred to by number in the Text (e.g., Table 1). Each table should be typed on a separate page with the legend above the table, while explanatory footnotes, which are indicated by superscript lowercase letters, should be typed below the table.

Illustrations: Figures, drawings, diagrams, charts and photographs are to be numbered in a consecutive series of Arabic numerals in the order in which they are cited in the text. Computer-generated illustrations and good-quality digital photographic prints are accepted. They should be black and white originals (not photocopies) provided on separate pages and identified with their corresponding numbers. Actual size graphics should be provided, which need no further manipulation, with lettering (Arial or Helvetica) not smaller than 8 points, lines no thinner than 0.5 point, and each of uniform density. All colors should be removed from graphics except for those graphics to be considered for publication in color. If graphics are to be submitted digitally, they should conform to the following minimum resolution requirements: 1200 dpi for black and white line art, 600 dpi for grayscale art, and 300 dpi for color art. All graphic files must be saved as TIFF images, and all illustrations must be submitted in the actual size at which they should appear in the journal. Note that good quality hardcopy original illustrations are required for both online and mail submissions of manuscripts.

Text Footnotes: The use of text footnotes is to be avoided. When their use is absolutely necessary, they should be typed at the bottom of the page to which they refer, and should be cited in the text by a superscript asterisk or multiples thereof. Place a line above the footnote, so that it is set off from the text.

Supplementary Material: Authors are encouraged to provide all supplementary materials that may facilitate the review process, including any detailed mathematical derivations that may not appear in whole in the manuscript.

Revised Manuscript and Computer Disks

Following the acceptance of a manuscript for publication and the incorporation of all required revisions, authors should submit an original and one more copy of the final disk containing the complete manuscript typed double spaced in Microsoft Word for Windows 2000 or a later version thereof. All graphic files must be saved as PDF, JPG, or TIFF images.

Allen, P.B., "…….", in: Horton, G.K., and Muradudin, A. A., (eds.), "Dynamical…….", (North……..), pp….

Reprints

Twenty (20) reprints free of charge are provided to the corresponding author. For orders of more reprints, a reprint order form and prices will be sent with the article proofs, which should be returned directly to the Editor for processing.

Copyright

Disclaimer

Indexing

JJP is currently indexing in:

<table>
<tr><td> 
</td><td>Emerging Sources Citation Index (ESCI)

Journal Impact Factor 2022

0.7</td></tr>
<tr><td colspan="2"> 
</td></tr>
</table>

Jordan Journal of
PHYSICS
An International Peer-Reviewed Research Journal

Volume 18, No. 2, June 2025, Moharrm 1447 H

Table of Contents:

Volume 18, Number 2, 2025. pp. 113-122

Jordan Journal of Physics

ARTICLE

Electronic and Optical Properties of Zr-, Zr-N-doped 2D MoS_2 Using First-Principle Study

A. Ouahdani, R. Takassa, A. E. Mouncharih, F. Elfatouaki, O. Farkad, S. Hassine, O. Choukri, E.A. Ibnouelghazi and **D. Abouelaoualim**

LaMEE, Department of Physics, Faculty of Sciences Semlalia, Cadi Ayyad University, P.O. Box 2390, 40000 Marrakech, Morocco.

Doi: **https://doi.org/10.47011/18.2.1**

Received on: 09/07/2023; *Accepted on: 18/02/2024*

Abstract: A MoS_2 monolayer is an emerging two-dimensional (2D) semiconductor for next-generation flexible and miniaturized electronics. Its doping is of great importance in order not only to adapt its properties, but also to facilitate many potential large-scale applications. In this work, density functional theory (DFT) calculations, including spin-orbit coupling (SOC), were performed to investigate the effects of p-type transition metal Zr doping and Zr–N co-doping on the structural and optoelectronic properties of pristine MoS_2. Results obtained using both the PBE and TB-mBJ approximations show that while pristine and Zr-doped MoS_2 monolayers exhibit semiconductor behavior with direct and indirect band gaps, respectively, Zr-N co-doping leads to a transition to metallic behavior. The Zr and N atoms significantly affect the partial and total density of state profiles, with a main contribution of Zr − d, N − p, and S − p orbitals. The dielectric function and optical refractive index are also determined. The findings show anisotropy in optical characteristics, which is promising for optical applications. The Zr-doping and Zr-N co-doping employed in this study provide an effective tool for changing the electrical and optical properties of MoS_2 monolayers to fulfill the needs of a variety of technological applications while producing an optoelectronic device based on a MoS_2 monolayer.

Keywords: MoS_2 monolayer, Zr doped, Zr-N co-doped, DFT study, Electronic properties, Dielectric function.

1. Introduction

The most significant molybdenum mineral is molybdenum disulfide (MoS_2) [1], which occurs naturally as molybdenite. MoS_2 belongs to the VIB group of the transition metal dichalcogenide (TMDC) monolayers and is one of the most highly debated 2D materials in recent times, second only to graphene [2, 3], due to its easy synthesis, low cost, nontoxicity, and natural abundance [4]. These layered materials have attracted attention due to their weak van der Waals interactions that allow to fabricate them easily using mechanical exfoliation [5, 6]. Researchers reexamined this type of material and succeeded in obtaining atomic-level two-dimensional layered MoS_2 [7-12]. As a typical graphene-like single-layer transition metal compound, single-layer molybdenum disulfide exhibits a substantial band gap ranging from 1.3 to 1.8 eV [13], making it suitable for applications such as transistors [14,15], solar energy harvesting [16], flexible optoelectronic devices [17], and sensors [18]. Lahourpour *et al*. [12] used full potential linear augmented plane waves plus local orbital (FP-LAPW + lo) method based on the DFT technique to study MoS_2 nanolayers. Their findings reveal that the estimated lattice parameters overshoot the actual values, which is a characteristic of the typically

Corresponding Author: D. Abouelaoualim **Email**: dr.abouelaoualim@uca.ac.ma

generalized gradient approximation GGA-PBE functional. Furthermore, they demonstrated that MoS_2 exhibits semiconductor behavior, revealing a direct band gap of 1.72 eV at the K point of the Brillouin zone, consistent with both experimental observations [19] and theoretical predictions [20, 21]. In recent years, numerous studies have been conducted on the structural, electronic, and optical properties of doped MoS_2. The effect of doping with nonmetallic atoms (X = O, C, N, B, Br, Cl, I, and F) using DFT calculations on the structural, electrical, and magnetic properties of single-layered MoS_2 has been investigated. The outcomes indicated that the systems doped with B, C, and N exhibit p-type doping, while the halogen-doped systems demonstrate n-type doping. [21]. The interactions with water molecules (H_2O), carbon dioxide (CO_2), and sulfur dioxide (SO_2) with MoS_2 monolayers doped with Ru and Rh have also been investigated using DFT calculations. The investigation revealed the preferred configuration for the adsorption geometry of SO_2 on the monolayer Ru-MoS_2 [11]. In contrast, Qian *et al.* [16] employed Au as a dopant to modify both the structural and electronic characteristics of MoS_2 fiber materials. Their study utilized DFT theory to investigate the adsorption effectiveness of Au-doped MoS_2 towards gases such as C_2H_6 and C_2H_4. The results indicated that the presence of Au dopant particles enhances the adsorption capability of the MoS2 monolayer by influencing its electronic structure. Furthermore, Xu *et al*. [22] conducted DFT computations to investigate the electronic and optical properties of co-doped monolayers of MoS_2 with C, N, B, and Mn. The co-doped systems containing Mn-N and Mn-B atoms exhibited semiconducting behavior, with energy band gaps of 0.81 and 1.03 eV, respectively. Recently, Raza *et al.* [23] studied the electronic properties of doped monolayers of MoS_2 with transition metals (Ag, Co, Bi, and Zr) using a local combination of atomic orbitals (LCAO) approach within the framework of DFT calculations. They confirmed that doping with transition metals led to a reduction in the band gap to a certain extent.

In the present study, we extend the exploration of electronic and optical properties of MoS_2 monolayers through DFT calculations utilizing the full-potential linearized augmented plane wave (FP-LAPW) method. We introduce p-type transition metal Zr atoms and explore both Zr doping and Zr–N co-doping as strategies to modulate the electronic and optical behavior of MoS_2. This choice is motivated by previous findings showing that such dopants effectively tune the physical properties of other 2D transition metal dichalcogenide (TMD) materials [24–26]. This research introduces a new perspective by examining the effects of Zr doping and Zr-N co-doping on the practical applications of doped MoS_2 monolayers as potential optoelectronic materials.

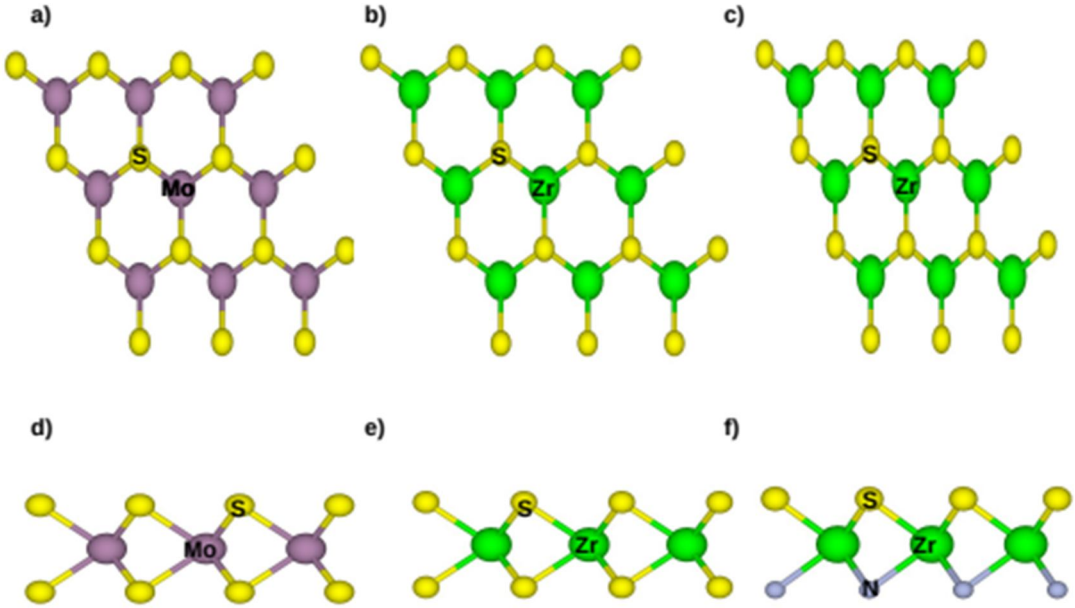

FIG. 1. Optimized geometric structures of the MoS_2 monolayer: (a) top view and (d) side view of the pristine MoS_2 monolayer; (b) top view and (e) side view of the Zr-doped MoS_2 monolayer; (c) top view and (f) side view.

2. Computational Method

This article examines the impact of Zr doping and Zr-N co-doping on the monolayer of MoS_2, as illustrated in Fig.1. To characterize the structural, electronic, and optical properties of both the pristine and doped MoS_2 monolayers, DFT and FP-LAPW method [27-29] are employed using the WIEN2K code [30]. The generalized gradient approximation in the form of the Perdew-Burke-Ernzerhof (GGA-PBE) and Tran-Blaha modified Becke-Johnson (TB-mBJ) [31, 32] is employed to approximate the exchange-correlation (XC) energy functional, accounting for the presence of SOC effects, without including the van der Waals correction due to weak van der Waals interactions [5]. The muffin-tin (MT) radii for Mo, S, Zr, and N are chosen as 2.42, 2.05, 2.40, and 2.00 a.u., respectively. A plane wave cut-off value of $R_{MT} \times K_{max} = 7$ was chosen for the wave function in the interstitial region. Here, R_{MT} represents the smallest radius of the atomic sphere, and K_{max} denotes the largest k-vector in the plane wave expansion. The cut-off energy of -6 Ry was consistently maintained to distinguish the core and valence states. The maximum angular momentum for the atomic orbital basis functions was specified as $l_{max} = 10$. The Fourier expansion's charge density was terminated at $G_{max} = 12$. Throughout the calculations, a 3 × 3 × 1 supercell was employed for both the pristine and doped MoS_2 monolayers in the x-y plane. Periodic boundary conditions were applied, while ensuring a minimum vacuum space of 15 Å along the z-axis to prevent interactions between adjacent layers. The first Brillouin zone (BZ) was sampled using a total of 1000 k-points. The iteration process was concluded when the total energy reached a threshold of 10^{-4} Ry. The random phase approach (RPA) was utilized to compute the optical properties. [33]. The optical spectra's intensity was controlled by dipole selection criteria, which differentiate optically permitted and prohibited transitions [34]. The Kramers-Kronig transformation yielded the real part ε_1 [35] and then the optical refraction index. An additional Drude term was included to account for free-electron intraband input in metallic structures. For accurate evaluation of optical response properties, a denser k-point mesh of 9 × 9 × 58 (equivalent to 5000 k-points in the BZ) was employed [34].

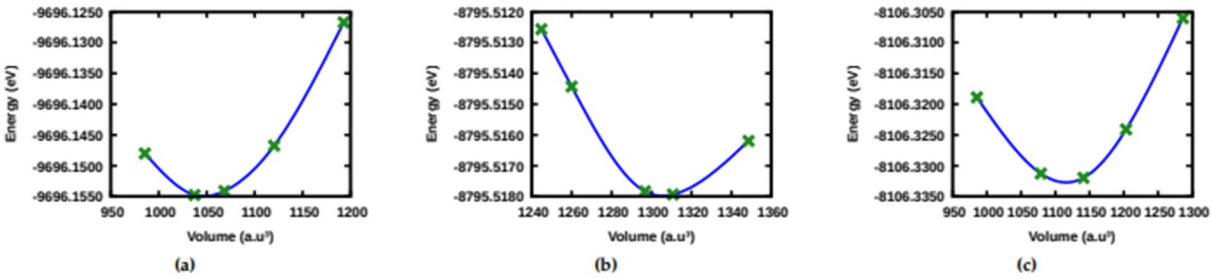

FIG. 2. Optimized energy-volume curves for (a) pristine, (b) Zr-doped, and (c) Zr-N c-doped MoS_2.

3. Numerical Results and Discussion

3.1. Structural Properties and Stability

A 3 × 3 × 1 supercell comprising 27 atoms with hexagonal symmetry was constructed using the supercell approach to model the pristine MoS_2, Zr-doped MoS_2 (ZrS_2), and Zr–N co-doped MoS_2 (ZrSN) structures. The unit cell of a MoS_2 monolayer consists of one Mo atom and two S atoms. In the case of ZrS_2, one Mo atom is substituted with a Zr atom. For the ZrSN structure, one Mo atom is replaced by a Zr atom and one S atom by an N atom, as illustrated in Fig. 1. To determine the stability and ground-state properties of the pristine and doped structures, energy minimization was performed using the generalized gradient approximation (GGA-PBE) in conjunction with the Murnaghan equation of state, expressed as [39]:

$$E(V) = E_0 + \left[\frac{B_0 V}{B_0'}\left(\frac{(V_0/V)^{B_0'}}{B_0'-1}+1\right) - \frac{B_0 V}{B_0'-1}\right]\frac{1}{14703.6} \quad (1)$$

Figure 2 shows the plot of total energy versus volume. Here, E_0, V, V_0, B_0, and B_0' are the minimum energy at T = 0 K, unit cell volume, unit cell volume at P = 0 GPa, bulk modulus, and its pressure derivative, respectively. The crystal structures and the estimated ground-state parameters of all configurations are shown in Table 1. The results show that the pristine MoS_2, Zr-doped, and Zr-N c-doped MoS_2 structures crystallize in hexagonal structures with space

groups P-6m2 (No. 187), P-6m2 (No. 187), and P3m1 (No. 156), respectively. The theoretically optimized lattice parameters for the pristine MoS_2 monolayer unit cell are a = b = 3.19Å, consistent with prior experimental and theoretical values, as shown in Table.1. After Zr doping and Zr-N co-doping, the Zr-S and Zr-N bond lengths become larger than in the case of Mo-S, which can be explained by the difference in the radii of Mo, Zr, S, and N atoms. To validate the thermodynamic stability, the formation energies of all compounds are calculated using the following equation [40], which is deduced experimentally for semiconducting materials in any form:

$$E_f = E_{tot}(X) - E_{tot}(MoS_2) - n_i\mu_i \quad (2)$$

$E_{tot}(X)$ and $E_{tot}(MoS_2)$ serve as representations of the total energy for the doped and pristine MoS_2 monolayers, respectively. The term $n_i > 0$ represents the number of doped atoms, while $n_i < 0$ represents the number of replaced atoms from the MoS_2 monolayer. The chemical potential of a single atom, which is determined as the overall energy per atom of the element's most stable structure, is represented by μ_i. The negative formation energies observed in Table 1 indicate the thermodynamic stability of the doped compounds, suggesting the feasibility of material synthesis. In addition, the Zr-N co-doped MoS_2 structure is more stable than Zr-doped MoS_2 because it presents a smaller formation energy value.

TABLE 1. Space groups, lattice parameters (a, b, c), unit cell volume at P = 0 GPa (V0), bulk modulus (B0), pressure derivative of bulk modulus (B 0 0), formation energy (E_f), and band gap with approximations PBE and TB-mBJ (Eg) for pristine, Zr-doped, and Zr-N co-doped MoS2 monolayers.

	Space group	bond length (Å)	$a = b$ (Å)	c (Å)	V_0 (Å^3)	B_0 (GPa)	B_0'	E_f (eV)	E_g (eV)
MoS_2	P-6m2	$d_{(Mo-S)}$= 2.42	3.19	17.46	1046.001	51.672	4.713	-	1.66_{PBE}
									1.63_{TB-mBJ}
		2.38 [36]	3.16 [36]						1.66 [37]
		2.42 [22]	3.17 [37]						1.80 [38]
									1.79 [36]
Zr / MoS_2	P-6m2	$d_{(Zr-S)}$= 2.59	3.55	17.46	1308.645	46.512	5.000	-1.39	0.99_{PBE}
									1.14_{TB-mBJ}
Zr-N / MoS_2	P3m1	$d_{(Zr-S)}$=2.45	3.36	16.40	1107.009	28.343	0.200	-4,62	0_{PBE}
		$d_{(Zr-N)}$= 2.45							0_{TB-mBJ}

3.2 Electronic Properties

3.2.1 Electronic Band Structure and Band Gap

To fully understand the optoelectronic behavior of semiconductors, it is essential to examine their electronic structure. The electronic band structures were computed using the GGA-PBE approximation while accounting for spin–orbit coupling (SOC) effects. The nature of the band gap, whether direct or indirect, is a critical factor in determining a material's suitability for optoelectronic applications.

The calculated band structures using both PBE and TB-mBJ approximations, along the high-symmetry points in the Brillouin zone (BZ), are presented in Fig. 3. Analysis of the pristine MoS_2 monolayer reveals that both the valence band maximum (VBM) and the conduction band minimum (CBM) occur at the K point, as seen in Figs. 3(a) and 3(d), indicating a direct band gap under both approximations. This confirms that the undoped MoS_2 monolayer is a promising candidate for optoelectronic applications. The estimated band gaps are 1.66 eV (PBE) and 1.63 eV (TB-mBJ), which are in good agreement with experimental values [19].

However, upon Zr doping, a transition from a direct to an indirect band gap is observed, accompanied by a reduction in band gap energy to 0.99 eV (PBE) and 1.14 eV (TB-mBJ), as shown in Figs. 3(b) and 3(e). This suggests that Zr-doped MoS_2 may be less suitable for optoelectronic devices.

In contrast, co-doping with Zr and N atoms eliminates the band gap entirely, reducing it to 0 eV under both approximations. This transition indicates a metallic behavior for the Zr–N co-doped MoS_2, as presented in Figs. 3(c) and 3(f).

3.2.2 TDS and PDOS

Partial (PDOS) and total density of states (TDOS) calculations were carried out to comprehend the role that Zr and N atoms played in the formation of the valence band VB and conduction band (CB) energies for the compound MoS_2, as well as any potential hybridization and interactions between these atoms. Fig. 4 presents the computed TDOS and PDOS of pristine, Zr-doped, and Zr–N co-doped MoS_2 monolayers over the energy range from -5 to 5 eV, using the PBE exchange–correlation (XC) approximation. The VB and CB are divided by the Fermi level, which has a value of 0.0 eV. The results show that the choice of the doping manner and the two Zr and N atoms significantly affect the DOS and PDOS profiles. Indeed, significant effects are observed in the TDOS profile in the energy range of -5 eV to 0 eV. By doping with the Zr atom, the gap value width decreased, as shown in Figs. 4(a) and 4(b), which is due to the d orbital of Zr dominating the conduction band and which was dominated by Mo − d and S − p orbitals [Figs. 4(d) and 4(e)], with a clear annulment of the states in the interval from 2.5 to 3.4 eV, which plays a crucial role in defining the material's electronic behavior. While the valence band is strongly dominated by p-orbitals in both structures, with an annuity of states in -5 to 5 eV in the doped structure. For the third compound, substitution of Mo by Zr and S by N gives a different curve shape. The conduction band retains its structure with a slight diminution in the number of states/eV, and the gap width decreased by 0.25 eV from that of the Zr-doped structure, as presented in Fig. 4(c).

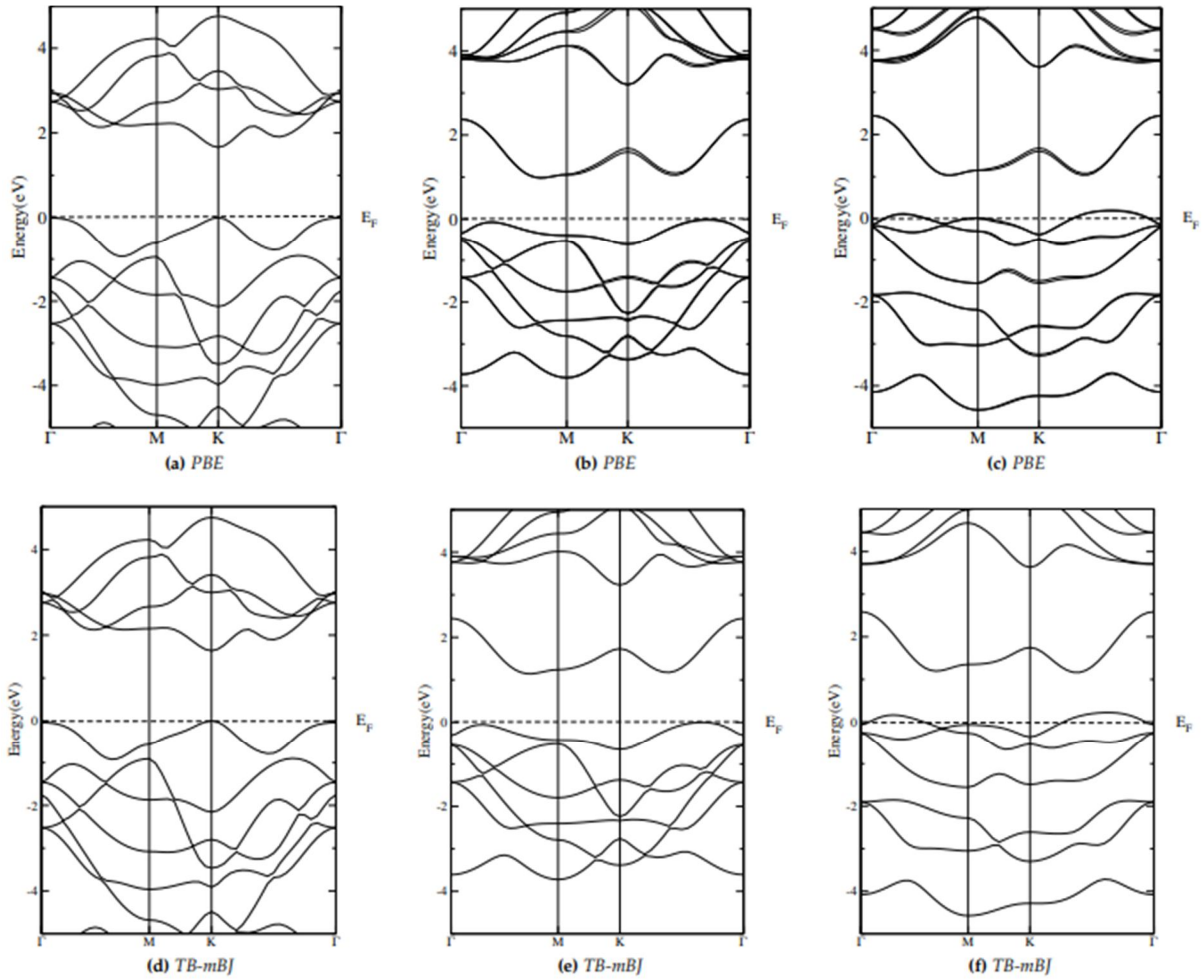

FIG. 3. Calculated band structures using PBE and TB-mBJ approximations for (a), (d) pristine, (b), (e) Zr-doped, and (c), (f) Zr-N co-doped MoS_2.

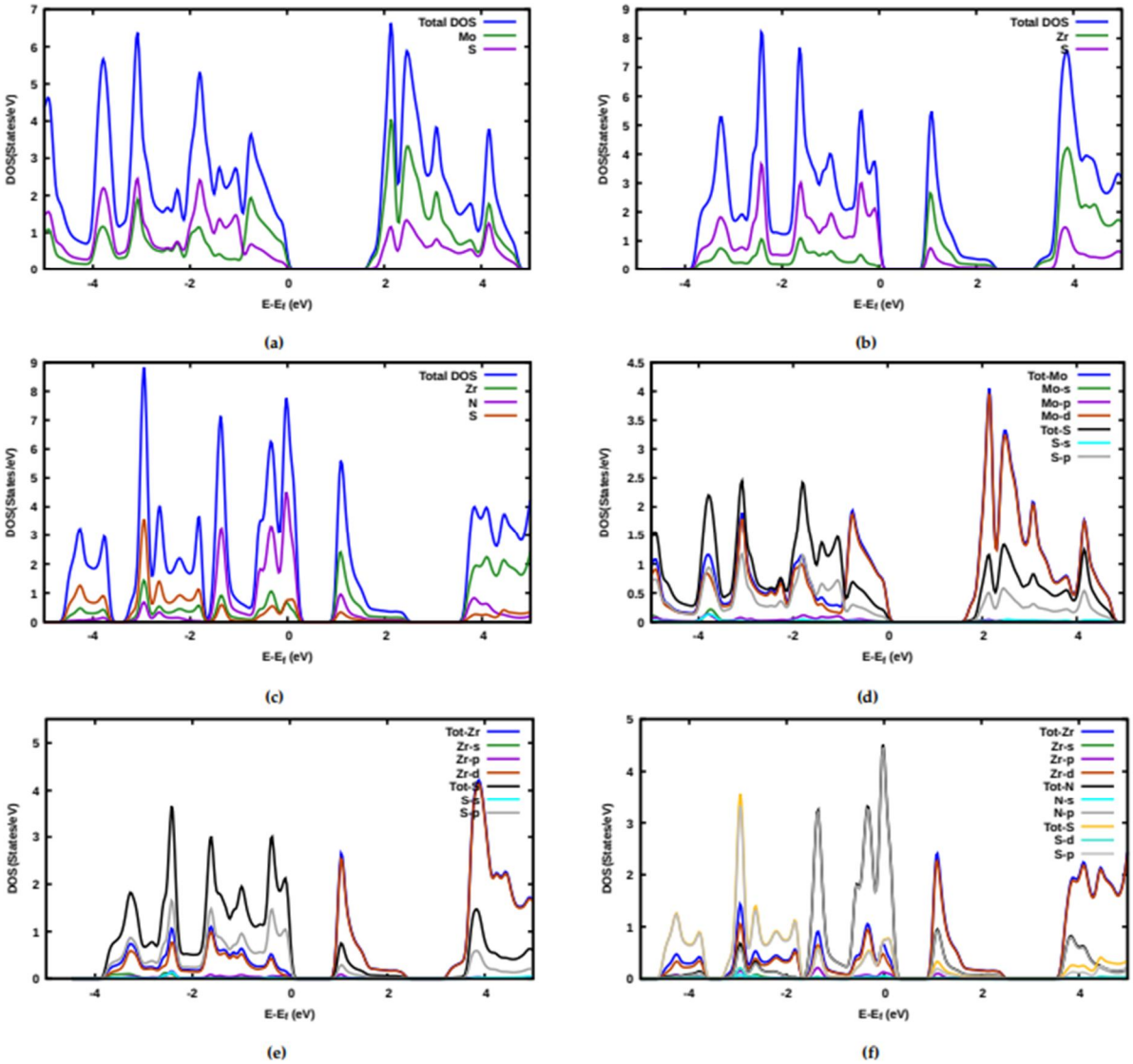

FIG. 4. Calculated total and partial DOS of (a), (d) pristine, (b), (e) Zr-doped, and (c), (f) Zr-N co-doped MoS_2.

This band gap is primarily formed from the d-states of Zr, p-states of N, and p-states of S. Yet, the valence band has undergone a clear change: it has displaced the Fermi level from -2 to 0.25 eV. The N − p orbital is the major contributor, as evidenced by the increased intensity of the observed peaks. In the energy range from -4 to 2 eV, S − p is the dominant orbital, as shown in Fig. 4(f). The contribution from the Zr − d orbitals is smaller, indicating that the hybridization of these atoms occurs mainly between the N − p and S − p orbitals, introducing a strong interaction between them, and they are responsible for the observed TDOS profile. In contrast, the s orbitals of each atom show a weak contribution.

3.3 Optical Properties

3.3.1 Dielectric Function

Investigating the optical properties provides valuable insight into the interaction of materials with electromagnetic radiation [41]. These properties are essential for the design and optimization of photoelectronic devices and semiconductor-based technologies. In this work, the optical characteristics were calculated using the random phase approximation (RPA) within the framework of DFT [42]. This approximation considers only the interband transitions between the valence and conduction bands, neglecting the local field effects [42–44]. The substitutional doping with Zr and co-doping with Zr–N alters the structural parameters and modifies the band structures of MoS_2 (see Fig. 3), which consequently affects the optical transitions. These transitions are captured through the

complex dielectric function ε(ω), which characterizes the linear optical response of the system. The dielectric function consists of a real part, $\varepsilon_1(\omega)$ and an imaginary part, $\varepsilon_2(\omega)$, as shown in the following equation:

$$\varepsilon(\omega) = \varepsilon_1(\omega) + i\varepsilon_2(\omega) \quad (3)$$

Once the ε(ω) is obtained, many other interesting optical properties can be deduced. The $\varepsilon_1(\omega)$ and $\varepsilon_1(\omega)$ for various materials of the pristine, Zr-doped, and Zr-N co-doped MoS_2 monolayers were estimated using the RPA method as implemented in the Wien2k package. Calculations were performed for two polarization directions: parallel (xx) and perpendicular (zz), denoted as $\varepsilon^{\parallel}(\omega)$ and $\varepsilon^{\perp}(\omega)$, respectively. Figs. 5 and 6 demonstrate that ε(ω) exhibits anisotropic behavior for two distinct polarizations of the light. The curves of $\varepsilon_2(\omega)$, shown in Fig. 5, indicate that the threshold energy (optical gap) occurs at 1.8, 0.8 eV, and 2.5, 0.5 eV for pure and Zr-doped MoS_2 monolayer for both polarization xx and zz directions, respectively, while the Zr-N co-doped MoS_2 monolayer exhibits no optical gap. It can be seen that the doped and co-doped MoS_2 monolayer process decreases the optical gap by generating permissible states in the MoS_2 monolayer band gap. As a result, the MoS_2 monolayer exhibits an adjustable band gap. The absorption transitions from the valence bands to the conduction bands are represented by the peaks observed in the $\varepsilon_2(\omega)$. Additionally, the MoS_2 monolayer $\varepsilon_2(\omega)$ shows one main peak at 2.86 eV (visible region) and 5.36 eV (UV region), for the xx and zz polarization directions, respectively. At the same time, the $\varepsilon_2^{\parallel}$ exhibits four prominent peaks at 1.74, 3.65, 3.91, and 4.78 eV and 0.35, 1.22, 4.00, and 6.26 eV, for the Zr-doped and Zr-N co-doped MoS_2 monolayers, respectively. On the other hand, the $\varepsilon_2^{\perp}$shows four main peaks at 1.40, 5.65, 6.26, and 7.30 eV and 2.96, 4.00, 5.65, and 5.91 eV, for the Zr-doped and Zr-N co-doped MoS2 monolayers, respectively. All peaks are formed by π to π ∗, σ to σ ∗, and σ to π ∗ transitions. Fig. 6 presents $\varepsilon_1(\omega)$, showing several peaks across the IR, VL, and UV regions. The $\varepsilon_1(\omega)$ response also varies with doping and co-doping and exhibits noticeable anisotropy in both polarization directions for all investigated models.

3.3.2 Refraction Index

The complex refractive index, denoted as N(ω), characterizes how electromagnetic waves propagate through a material relative to a vacuum. It is calculable using the following relationship [45]:

$$N(\omega) = n(\omega) + ik(\omega) \quad (4)$$

For optical devices, the extinction coefficient is k(ω) while the value of the refractive index is represented by n(ω). Fig. 7 displays the spectra of n(ω) and k(ω), both calculated using the GGA-PBE approximation for MoS_2, Zr-doped MoS_2, and Zr-N co-doped MoS_2. The n(ω) plot indicates the anisotropic behavior, as seen in Fig. 7. The static refractive index, n(0), is one of several key elements in $\varepsilon_1(\omega)$, and it is given by [46]:

$$n(0) = \sqrt{\varepsilon_1(0)} \quad (5)$$

The computed values of n(0) in both parallel and perpendicular orientations are shown in the Table. 2. In the case of the parallel mode, the findings reveal that MoS_2, Zr-doped MoS_2, and Zr-N co-doped MoS_2 exhibit semiconducting and insulating behaviors. In contrast, in the perpendicular direction, all studied structures exhibit typical semiconducting behavior.

Additionally, the results show that after Zr doping and Zr–N co-doping, n(0) increases in the parallel direction but decreases in the perpendicular direction. This is because the refractive index is inversely related to the band gap of the compound.

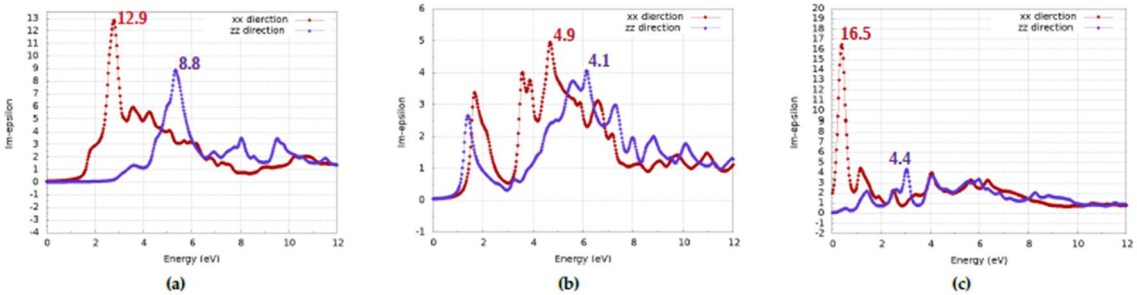

FIG. 5. #2(w) of (a) pristine, (b) Zr-doped, and (c) Zr-N co-doped MoS2 in perpendicular (zz) and parallel (xx) directions.

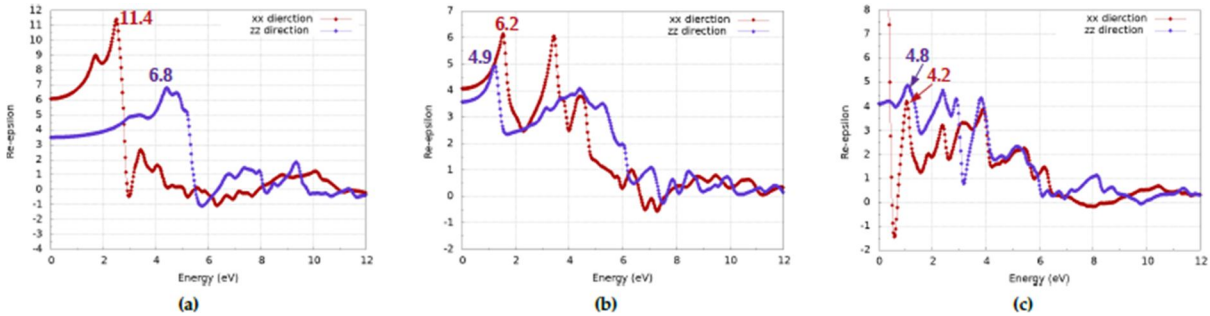

FIG. 6. #1(w) of (a) pristine, (b) Zr-doped, and (c) Zr-N co-doped MoS_2 in perpendicular (zz) and parallel (xx) directions.

TABLE 2. Static refractive index n(0).

Material	$n_{\parallel}(0)$	$n_{\perp}(0)$
MoS_2	2.60	1.85
$Zr\ doped\ MoS_2$	2.30	1.90
$Zr-N\ codoped\ MoS_2$	4.10	2.00

All highest peaks in parallel and perpendicular polarizations are listed in Table 3, corresponding to the pristine, Zr-doped, and Zr-N co-doped MoS_2 monolayer materials. At roughly 6.25 eV, the refractive indices fall below unity in some ranges, which provides the photoluminescence phenomenon, in which the phase velocity of passing light exceeds the speed of light in a vacuum.

4. Conclusion

The structural, electronic, and optical properties of the pristine, Zr-doped, and Zr-N co-doped MoS_2 monolayer were studied by the DFT method with GGA-PBE calculations. The analyses of the formation energy calculations indicate that all doped structures are energetically stable, with the Zr-N co-doped structure being the most stable. More importantly, the band structure results show that the pristine MoS_2 monolayer has a direct band gap of 1.66 eV, which agrees with the experimental results. The band gap decreases after doping with the Zr transition metal and changes its type to an indirect band gap. However, in the case of Zr-N co-doping, the band gap is cancelled, indicating a metallic character for the co-doped structure. The Mo - d, Zr - d, N - p, and S - p orbitals are often responsible for the observed DOS and PDOS profiles. The results also show that the Zr-doping and Zr-N co-doping are practical tools for tuning the pristine MoS_2 monolayer's optical properties. The optical response is completely distinct in the two polarization orientations, suggesting anisotropic optical characteristics, making these materials promising for applications such as linear polarizers. The analyses of the dielectric function show that the $\varepsilon_2(\omega)$ of all studied structures possesses various peaks at different energy regions (IR, VL, and UV regions), indicating the possibility of light absorption in these regions. All investigated structures have refractive indices lower than a unit value in a specified range. The phase velocity of travelling light is greater than the speed of light in a vacuum, resulting in photoluminescence. This study provides valuable insights into the nature of the pristine, Zr-doped, and Zr-N co-doped MoS_2 monolayers and is a powerful tool for experimental research in the future.

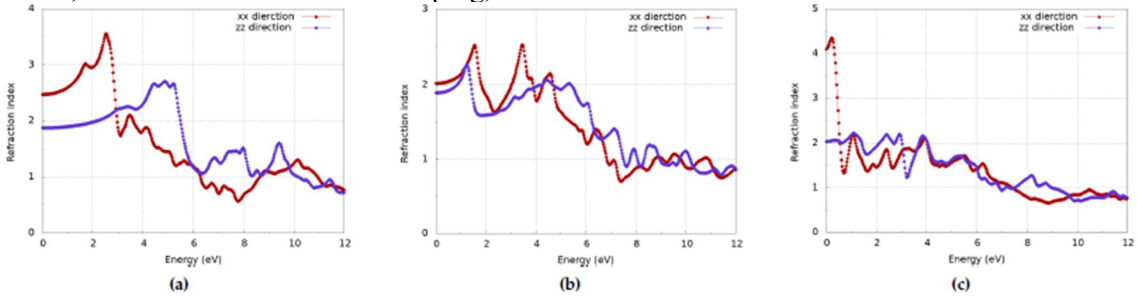

FIG. 7. n(w) of (a) pristine, (b) Zr-doped, and (c) Zr-N co-doped MoS2 in perpendicular (zz) and parallel (xx) directions.

TABLE 3. Energies, polarization states, and spectral region of the refraction index peaks of pristine, Zr-doped, and Zr-N co-doped MoS2 mono-layer materials.

Material	Peaks ∥	Peaks ⊥	Energy [eV]	Spectrum region
MoS_2 monolayer	3.1	-	1.80	VISIBLE
	3.5	-	2.80	VISIBLE
	-	2.60	4.80	UV
	-	2.70	5.00	UV
	-	2.50	5.20	UV
Zr-doped MoS_2	2.60	-	1.50	IR
	2.62	-	3.40	UV
	-	2.22	1.42	IR
	-	2.05	4.25	UV
	-	2.03	5.26	UV
Zr-N codoped MoS_2	4.30	-	0.17	IR
	2.18	-	1.20	IR
	-	2.18	1.20	IR
	-	2.14	2.4	VISIBLE
	-	2.13	2.9	VISIBLE
	-	2.10	3.84	UV

References

[1] Ganta, D., Sinha, S., and Haasch, R.T., Surf. Sci. Spectra, 21 (1) (2014) 19.

[2] Farkad, O., Elfatouaki, F., Takassa, R., Hassine, S., Ijdiyaou, Y., Ibnouelghazi, E., and Abouelaoualim, D., Mater. Today Commun., 33 (2022) 104714.

[3] Farkad, O., Takassa, R., Elfatouaki, F., Hassine, S., Ijdiyaou, Y., Ibnouelghazi, E., and Abouelaoualim, D., Diam. Relat. Mater., 126 (2022) 109082.

[4] Mao, X., Wang, L., Xu, Y., and Li, Y., J. Phys. Chem. C, 124 (19) (2020) 10523.

[5] Ma, H., Shen, Z., and Ben, S., J. Colloid Interface Sci., 517 (2018) 204.

[6] Han, S., Kwon, H., Kim, S.K., Ryu, S., Yun, W.S., Kim, D., Hwang, J., Kang, J.-S., Baik, J., Shin, H., et al., Phys. Rev. B, 84 (4) (2011) 045409.

[7] Wang, A.R., Ruzicka, B.A., Kumar, N., Bellus, M.Z., Chiu, H.-Y., and Zhao, H., Phys. Rev. B, 86 (4) (2012) 045406.

[8] Fang, H., Chuang, S., Chang, T.C., Takei, K., Takahashi, T., and Javey, A., Nano Lett., 12 (7) (2012) 3788.

[9] Yue, Q., Shao, Z., Chang, S., and Li, J., Nanoscale Res. Lett., 8 (1) (2013) 1.

[10] Donarelli, M., Prezioso, S., Perrozzi, F., Bisti, F., Nardone, M., Giancaterini, L., Cantalini, C., and Ottaviano, L., Sens. Actuators B Chem., 207 (2015) 602.

[11] Du, R. and Wu, W., Chem. Phys. Lett., 789 (2022) 139300.

[12] Wu, F., Tian, H., Shen, Y., Hou, Z., Ren, J., Gou, G., Sun, Y., Yang, Y., and Ren, T.-L., Nature, 603 (7900) (2022) 259.

[13] Ullah, M.S., Yousuf, A.H.B., Es-Sakhi, A.D., and Chowdhury, M.H., AIP Conf. Proc., 1957 (2018) 020001.

[14] Omar, O.S., J. Renew. Mater., 10 (7) (2022) 1979.

[15] Kang, M.-A., Kim, S.J., Song, W., Chang, S.-j., Park, C.-Y., Myung, S., Lim, J., Lee, S. S., and An, K.-S., Carbon, 116 (2017) 167.

[16] Qian, G., Peng, Q., Zou, D., Wang, S., Yan, B., and Zhou, Q., Front. Mater., 7 (2020) 22.

[17] Lahourpour, F., Boochani, A., Parhizgar, S., and Elahi, S., J. Theor. Appl. Phys., 13 (3) (2019) 191.

[18] Splendiani, A., Sun, L., Zhang, Y., Li, T., Kim, J., Chim, C.-Y., Galli, G., and Wang, F., Nano Lett. 10 (4) (2010) 1271.

[19] Lebegue, S. and Eriksson, O., Phys. Rev. B, 79 (11) (2009) 115409.

[20] Tenne, R., Angew. Chem. Int. Ed., 42 (42) (2003) 5124.

[21] Hu, A.-M., Wang, L.-l., Xiao, W.-Z., Xiao, G., and Rong, Q.-Y., Comput. Mater. Sci., 107 (2015) 72.

[22] Xu, W.-B., Huang, B.-J., Li, P., Li, F., Zhang, C.-W., and Wang, P.-J., Nanoscale Res. Lett., 9 (1) (2014) 1.

[23] Raza, A., Qumar, U., Haider, A., Naz, S., Haider, J., Ul-Hamid, A., Ikram, M., Ali, S., Goumri-Said, S., and Kanoun, M.B., Dalton Trans., 50 (19) (2021) 6598.

[24] Zhao, X., Xia, C., Wang, T., and Dai, X., J. Alloys Compd., 654 (2016) 574.

[25] Onofrio, N., Guzman, D., and Strachan, A., J. Appl. Phys., 122 (18) (2017) 185102.

[26] Guo, S., Zheng, H., Wang, Y., and Zhang, J., AIP Adv., 9 (7) (2019) 075304.

[27] Takassa, R., Farkad, O., Ibnouelghazi, E., and Abouelaoualim, D., Appl. Surf. Sci., 563 (2021) 150283.

[28] Takassa, R., Farkad, O., Ibnouelghazi, E.A., and Abouelaoualim, D., J. Nano Res., 74 (2022) 1.

[29] Blaha, P., Schwarz, K., Sorantin, P., and Trickey, S.B., Comput. Phys. Commun., 59 (2) (1990) 399.

[30] Blaha, P., Schwarz, K., Madsen, G.K.H., Kvasnicka, D., Luitz, J., Laskowsk, R., Tran, F., Marks, L., and Marks, L., "WIEN2k: An Augmented Plane Wave Plus Local Orbitals Program for Calculating Crystal Properties", (Techn. Universitat, 2019).

[31] Takassa, R., Farkad, O., Ibnouelghazi, E., and Abouelaoualim, D., Diam. Relat. Mater., 123 (2022) 108863.

[32] Elfatouaki, F., Farkad, O., Ibnouelghazi, E., Abouelaoualim, D., and Outzourhit, A., Mater. Sci. Semicond. Process., 143 (2022) 106488.

[33] Hellgren, M. and Baguet, L., Phys. Rev. Res., 3 (2021) 033263.

[34] Blaha, P., Schwarz, K., Tran, F., Laskowski, R., Madsen, G.K.H., and Marks, L.D., J. Chem. Phys., 152 (7) (2020) 074101.

[35] de L. Kronig, R, J. Opt. Soc. Am., 12 (6) (1926) 547.

[36] Kadantsev, E.S. and Hawrylak, P., Solid State Commun., 152 (10) (2012) 909.

[37] Obodo, K.O., Ouma, C.N.M., Obodo, J.T., Braun, M., and Bessarabov, D., Comput. Condens. Matter, 21 (2019) e00419.

[38] Mak, K.F., Lee, C., Hone, J., Shan, J., and Heinz, T.F., Phys. Rev. Lett., 105 (2010) 136805.

[39] Murnaghan, F.D., Proc. Natl. Acad. Sci., 30 (9) (1944) 244.

[40] Ivanovskaya, V.V., Zobelli, A., Gloter, A., Brun, N., Serin, V., and Colliex, C., Phys. Rev. B, 78 (13) (2008) 134104.

[41] Wooten, F., Am. J. Phys., 41 (7) (1973) 939.

[42] Gajdoš, M., Hummer, K., Kresse, G., Furthmüller, J., and Bechstedt, F., Phys. Rev. B, 73 (4) (2006) 045112.

[43] Adler, S.L., Phys. Rev., 126 (2) (1962) 413.

[44] Wiser, N., Phys. Rev., 129 (1) (1963) 62.

[45] Alrashdi, O., Asif, A., Fadhali, M.M., Bakar, A., Afaq, A., and Alqahtani, J., J. Mater. Res. Technol., 20 (2022) 4220.

[46] Takassa, R., Elfatouaki, F., Farkad, O., Hassine, S., Choukri, O., Mouncharih, A., Ijdiyaou, Y., Ibnouelghazi, E., and Abouelaoualim, D., Phys. E Low-Dimens. Syst. Nanostruct., 148 (2023) 115627.

Volume 18, Number 2, 2025. pp. 123-130

Jordan Journal of Physics

ARTICLE

Study of the Nuclear Structure for the ^{19}O Nucleus by Using USDEPN and WCPN Interactions

Hadeel H. Abed[a] and **Ali K. Hasan**[b]

[a] *Department of Physics, College of Education for Girls, University of Kufa, Iraq.*
[b] *College of Health and Medical Technology, University of Alkafeel, Iraq.*

Doi: **https://doi.org/10.47011/18.2.2**
Received on: 18/08/2023; *Accepted on: 14/04/2024*

Abstract: The NuShellX@MSU code, along with the USDEPN and WCPN interactions within the sdpn-shell model space, has been employed to study the energy levels, electromagnetic transition probabilities, and charge density distribution of the ^{19}O nucleus using the nuclear shell model. The model space for this under-researched nucleus contains the configurations ($0d_{5/2}$, 1s1/2, and 0d3/2). In terms of energy levels, a generally acceptable agreement was achieved for several states, while a comparable similarity is anticipated for others. As for electromagnetic transfers, the default values of the effective charge and the g-factors were changed to obtain an acceptable agreement with the experimental magnetic transfer data for the ground state. However, no experimental data for the charge density distribution are currently available for comparison..

Keywords: ^{19}O nucleus**,** Electromagnetic transitions, Charge density, Sdpn-shell.

PACS: 21.60.Cs.

1. Introduction

Several models have been devised to explain the structure of atomic nuclei. One such model is the nuclear shell model (SM), which has been extensively studied. First proposed by Mayer, Haxel, Jensen, and Suess almost half a century ago, this model has been highly effective in explaining the characteristics of different nuclei that have only a small number of valence nucleons. The features encompassed are energy levels, magnetic and electrical moments, electromagnetic transmission possibilities, and the cross-section of different reactions [1]. The shell model is one of the most well-known and useful nuclear models, which can help us understand nuclear structure, which contains the fundamental physical properties of nuclei. The electron shell model of atoms is comparable to this idea. Nucleons, either protons or neutrons, situated beyond closed shells (defined by magic numbers 2, 8, 20, 28, 50, 82, and 126), exert significant influence on shaping nuclear properties, much like the way valence electrons outside a closed shell define atomic traits and behaviors. Nuclei marked by magic numbers are exceptionally stable and display wholly distinctive attributes when contrasted with other nuclei [2].

All shell-model computations commence by deriving an effective interaction, founded on a microscopic theory originating from the free nucleon-nucleon (N-N) interaction. Consequently, these extensive shell-model computations enable us to gauge the extent to which a two-body effective interaction replicates attributes such as excitation spectra and binding energies in scenarios involving numerous valence nucleons. Within a constrained domain known as the model space, a subset of the complete Hilbert space, the challenges of

Corresponding Author: Ali K. Hasan **Email**: alikh.alsinayyid@alkafeel.edu.iq

acquiring such effective operators and interactions are resolved. Various avenues exist to expand effective operators and interactions. As an illustration, the Cohen-Kurath interaction is applied within the p-shell for nuclei with 4 < A < 16, while the USD interaction has its suitability in the SD-shell for nuclei with 16 < A < 40 [3]. Nuclear shell model codes like Oxbash [4], Antoine [5], NuShell [6], NuShellX [7], and others have been widely employed for shell-model calculations in the p-shell, sd-shell, and fp-shell. These codes play a crucial role globally in scrutinizing nuclear structure. Basic inputs for most shell-model configuration mixing codes (TBMEs) involve sets of single-particle matrix elements (SPEs) and two-body matrix elements. These sets are characterized as "model-space Hamiltonians" or "effective interactions" [8]. The present study employed the NuShellX@MSU code to compute energy levels, electromagnetic transitions, and charge density distribution for the ^{19}O nucleus. This was accomplished using the USDEPN and WCPN interactions within the sdpn-shell. Previous theoretical research has been conducted on the studied isotope [9].

2. Theory

NuShellX@MSU encompasses a series of wrapper scripts developed by Alex Brown [7], designed to generate input for NuShellX using model space and Hamiltonian data files. With the aim of computing precise energies, eigenvectors, and spectroscopic overlaps for low-lying states within calculations that involve the shell-model Hamiltonian matrix featuring remarkably expansive basis dimensions, Bill Rae [6] engineered a suite of computer programs recognized as NuShellX.

In the context of the shell model framework, the Hamiltonian of a system comprising A nucleons is decomposed using an auxiliary one-body potential U. This potential is composed of two parts: H_0, representing the independent motion of the nucleons, and H_1, the residual interaction. Thus [10, 11]:

$$H = \sum_{i=1}^{A} \frac{p_i^2}{2m} + \sum_{i<A=1}^{A} V_{ij}^{NN} = T+V = (T+U) + (V-U) = H_0 + H_1 \quad (1)$$

where:

$$H_0 = \sum_{i=1}^{A} \left(\frac{p_i^2}{2m} + U_i\right) \quad (2)$$

$$H_1 = \sum_{i<A=1}^{A} V_{ij}^{NN} - \sum_{i=1}^{A} U_i \quad (3)$$

Once H_0 is introduced, a reduced model space can be delineated by employing a finite subset of HO's eigenvectors [10].

Numerous theories exist to determine the permissible total angular momentum, such as when nucleons (neutrons or protons) are present in a single orbit with n > 2, where n represents the count of particles beyond the closed shell. In this case, the total angular momentum is given by[12]:

$$J_M = n\left[j - \frac{(n-1)}{2}\right] \quad (4)$$

To calculate the physical factor for systems that contain several particles, I followed the method of expressing the total wave function of the group of particles in terms of the wave function of one or two particles, depending on the nature of the physical quantity to be calculated. Using certain mathematical methods, there may be a need to separate the total wave function into the wave function for more than two particles and the wave function for the remaining particles. This is done using specific mathematical methods [13]. To illustrate the computation of a nucleus's spectrum where valence nucleons all occupy a single-particle state, we need to introduce the notion of parentage coefficients. In essence, we introduced the fractional parentage method as a means to calculate the matrix elements of the interaction. Through this technique, we were able to express the condition of having n particles in terms of states involving (n - 1) or (n - 2) particles. In the configuration j^n, the anti-symmetric state with angular momentum (JM) is represented by $\psi_{JM\alpha}$ (1,..., n). The single-particle eigenfunction for the state j is labeled as |jm⟩ or φ_{jm}, and α represents an additional quantum number required for full specification of the state. In instances where the configuration j^{n-1} is composed of entirely anti-symmetric wave functions, they are denoted as $\phi_{J_1 M_1 \beta_1}$, $(1, \ldots\ldots, n-1)$, and we can accordingly formulate these as [14]:

$$\psi_{JM\alpha}(1, \ldots, n) = \sum_{J_1\beta_1} [j^{n-1}\beta_1 J_1) jJ|\}j^n \alpha J][\phi_{J_1\beta_1}(1, \ldots\ldots, n-1) \times \varphi_j(n)]_{JM} \quad (5)$$

The real expansion coefficients, denoted as $[j^{n-1}\beta_1 J_1) jJ|\}j^n \alpha J]$, are referred to as fractional parentage coefficients (c.f.p.). These coefficients

are determined in such a way that the n-particle wave function becomes anti-symmetric when any two particles are interchanged, including both β and α [15, 16].

A second type of parentage coefficient is called a double parentage coefficient, or d.p.c., and it is described as follows: If $\varphi_{KM_2'}$ $(n$ -1, $n)$ denotes all two-particle state $(j^2)_{KM_2'}$, and $\phi_{J_2M_2\beta_2}(1, \dots \dots n-2)$ is the entire set of anti-symmetric states of j^{n-2}, then the anti-symmetric state of the configuration j^n with angular momentum JM can be written in the following form [17]:

$$\psi_{JM\alpha}(1,..,n) = \sum_{J_2\beta_2K}[j^{n-2}\beta_2J_2)j^2(K)J|\}j^n\alpha J][\phi_{J_2\beta_2}(1,\dots,n-2)\times\varphi_K(n-1),n]_{JM} \quad (6)$$

Thus, when there are more than two particles outside the closed shell (n > 2) and these particles occupy the same level, the energy matrix element or the Hamiltonian matrix element is given by [14, 17, 18]:

$$\langle H\rangle = n\varepsilon_j\delta_{\alpha\alpha'} + \left\{\frac{n}{n-2}\right\}\sum_{J_1\beta_1\beta_1'}[j^{n-1}(\beta_1'J),jJ|\}j^n\alpha'J] \times [J^{n-1}(\beta_1J_1),jJ|\}j^n\alpha J] \times \langle jj|V|jj\rangle_{J_1} \quad (7)$$

In an alternative explanation, Eq. (7) articulates how the matrix elements of two-particle operators within the n-particle configuration can be understood as linear constituents within the matrix configuration of (n-1)-particle combinations. Given the time-intensive nature of this procedure, introducing the concept of d.p.c. offers a more streamlined resolution. If these coefficients are available, the subsequent formula is applicable for calculating the energy of the state $(j)^n_J$ [14, 17, 18]

$$\langle H\rangle = n\varepsilon_j\delta_{\alpha\alpha'} + \left\{\frac{n(n-1)}{2}\right\}\sum_{\beta_2J_2K}[j^{n-2}(\beta_2J_2),j^2(K)J|\}j^n\alpha'J] \times [J^{n-2}(\beta_2J_2),j^2(K)J|\}j^n\alpha'J] \times \langle jj|V|jj\rangle_{J_K} \quad (8)$$

When considering gamma-ray emission involving multipolarity L and denoted by the symbol σ, the transition probability λ(σL) is expressed as follows [19]:

$$\lambda(\sigma L,\ J_i \longrightarrow J_f) = \frac{8\pi\,(L+1)}{\hbar L[(\,2L+1)!!]^2}\left(\frac{E_\gamma}{\hbar c}\right)^{2L+1}B(\sigma L,J_i \longrightarrow J_f) \quad (9)$$

where *B(σL)* is the reduced transition probability and Eγ is the γ-ray energy.

The reduced matrix element $\langle\psi\, f\,\|M(\sigma L)\|\psi i\rangle$ can be used to express the reduced transition probability [18]:

$$B(\sigma L, J_i \longrightarrow J_f) = \frac{1}{2J_i+1}\,|\langle\psi\, f\ \|\ M(\sigma L)\ \|\ \psi i\rangle|^2 \quad (10)$$

3. Results and Discussion

The ^{19}O nucleus calculations are executed through the shell model within the NuShellX@MSU code for Windows [7]. This involves employing the sdpn model space coupled with effective interactions, specifically USDEPN and WCPN. Within the sdpn model space, there are three orbitals ($0d_{5/2}$, $1s_{1/2}$, and $0d_{3/2}$) situated above the closed core of ^{16}O, with three neutrons for the given nucleus.

The primary objective of the present study is to carry out computations for energy levels, decrease electromagnetic transition probabilities, and the charge density distribution for the ^{19}O nucleus. These computations are conducted using the harmonic oscillator potential (HO) with parameter b > 0. The corresponding single-particle energies are ($0d_{3/2}$= 1.8896,$1s_{1/2}$ - 3.4150,$0d_{5/2}$ - 4.1692) for the USDEPN interaction, and ($0d_{3/2}$ = 1.64658,$1s_{1/2}$ = -3.16354,$0d_{5/2}$ - 3.9478) for the WCPN interaction.

3.1 Energy Levels

Per the shell model's description, the foundational configuration of the ^{19}O nucleus involves a ^{16}O nucleus in a closed state, encircled by three neutrons positioned outside this closed shell. These neutrons are arranged within the sdpn shell, and their arrangement corresponds to quantum numbers J = 0^+ and T = 1.5. By employing the NuShellX@MSU code within the sdpn shell to implement the interaction USDEPN onto the ^{19}O nucleus, and after comparison with experimental data, we drew the following conclusions:

Upon comparison with the available empirical data, the total angular momentum and parity of the ground state level $5/2\,^+_1$ were found to be in agreement.

A good agreement was obtained for the values of the theoretically calculated MeV energies (0.12,1.602, 2.347, 2.889, 3.209, 6.13) MeV corresponding to the angular momentum ($3/2^+_1$, $1/2^+_1$, $9/2^+_1$, $7/2^+_1$, $5/2^+_2$, $3/2^+_2$), when compared with available experimental data. Additionally, through our calculations, we were able to obtain an agreement that is appropriate for the energy value (3.814, 10.697) MeV calculated theoretically, which corresponds to the angular momentum $3/2^+_2$, $7/2^+_4$ but with a different parity.

The parity of the energy levels at 5.384 and 5.007 MeV, corresponding to the angular momenta $9/2^+_2$ and $5/2^+_3$, was determined to be positive.

Our computations indicate that the total angular momentum and parity corresponding to the experimental energy levels at 7.118, 7.242, 7.508, 8.048, 8.916, 9.430, 9.560, 9.930, 11.250, and 11.580 MeV are projected as $7/2^+_2$, $5/2^+_4$, $1/2^+_2$, $11/2^+_1$, $3/2^+_4$, $7/2^+_3$, $5/2^+_5$, $9/2^+_3$, $1/2^+_3$, and $3/2^+_6$, respectively.

Our calculations revealed 16 levels characterized by specific total angular momentum and parity, yet these levels did not align with any existing empirical data. Additionally, it came to our attention that the theoretically derived maximum energy value stands at 21.805 MeV, while the highest practical energy value observed is 11.580 MeV.

As for our comparison with the theoretical results that we obtained from [9], we observed a good agreement for the ground state angular momentum $5/2^+_1$. Also, the agreement was good for all energy levels.

Figure 1 presents a comparison between the experimental data from Ref. [20] and the theoretical predictions for the ^{19}O nucleus, obtained using the USDEPN interaction, alongside the theoretical results from Ref. [9], which employed the USDBPN interaction.

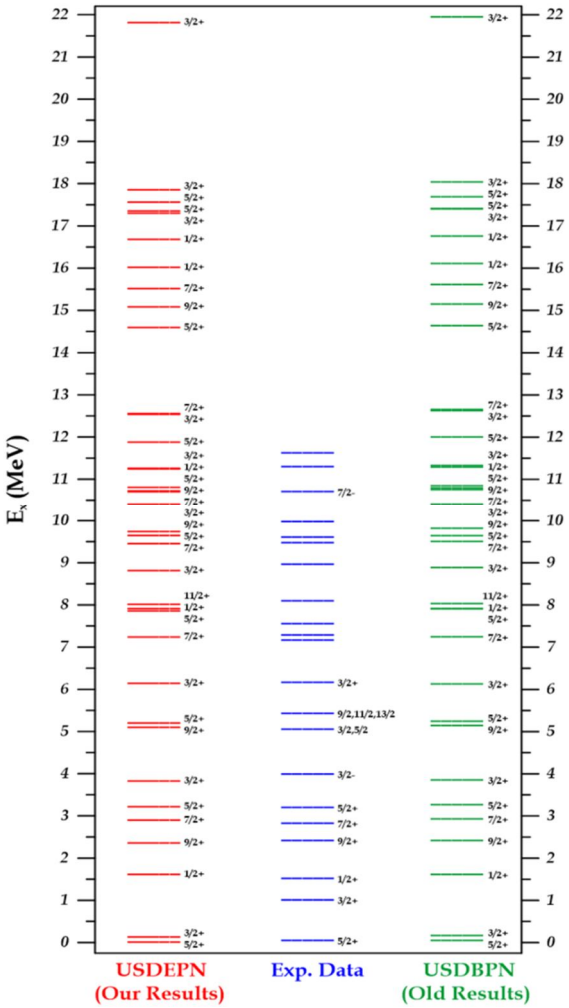

FIG. 1. Comparison of experimental excitation energies from Ref. [20] with our theoretical results using the USDEPN interaction, alongside theoretical results from Ref. [9] employing the USDBPN interaction.

Upon applying the effective interaction WCPN to the ^{19}O nucleus within the sdpn shell, we reached the following conclusions after comparison with experimental data:

Compared with the practical values available, there was a correspondence observed between the total angular momentum and ground state parity of the $5/2^+_1$ level.

Upon comparison with the existing experimental data, a notable concurrence was evident between the theoretically computed energy values (0.294, 1.469, 2.447, 2.96, 3.167, 5.527) MeV and the corresponding angular momenta ($3/2^+_1$, $1/2^+_1$, $9/2^+_1$, $7/2^+_1$, $5/2^+_2$, $3/2^+_3$). Furthermore, our calculations produced acceptable agreement for the energy values 3.747 and 10.253 MeV, corresponding to angular momenta $3/2^+_2$ and $7/2^+_4$, but with a different parity.

The parity for the values of practical energies (5.384, 5.007, 6.466 MeV) corresponding to the angular momenta ($9/2^+_2$, $5/2^+_3$, and $7/2^+_2$) was determined to be positive.

Our computations yielded projections indicating that, owing to the convergence between experimental and theoretical values, the total angular momentum and parity corresponding to the experimental energies 7.118, 7.242, 7.508, 8.247, 8.916, 9.064, 9.324, 9.430, and 11.580 MeV are $1/2^+_2$, $5/2^+_4$, $11/2^+_1$, $3/2^+_4$, $5/2^+_5$, $7/2^+_3$, $9/2^+_3$, $3/2^+_5$, and $5/2^+_7$.

From our calculations, we identified 16 levels characterized by specific total angular momentum and symmetry for which no experimental counterparts can be found. Furthermore, we observed a discrepancy in energy values, with the highest practical energy recorded at 11.580 MeV, whereas the theoretical calculation indicated a peak energy of 20.913 MeV.

Our comparison with theoretical results reported in Ref. [9] shows a match for the ground state value of angular momentum $5/2^+_1$. On the other hand, all other energy levels show good consistency.

As for the highest practical value for our calculations, it was 20.913 MeV. As for the highest practical value for the theoretical calculations that were compared to it, it was 21.902 MeV.

Figure 2 presents a comparison between the experimental findings sourced from Ref. [20] and the theoretical outcomes concerning the ^{19}O nucleus, utilizing the WCPN interaction, along with the theoretical data from Ref. [9] based on the USDBPN interaction.

3.2 Electromagnetic Transition Probabilities

In this study, we undertook the computation of electromagnetic transition probabilities B(E2) and B(M1) using a harmonic oscillator potential (HO, b) with b > 0 for each transition. This was accomplished by applying the USDEPN and WCPN interactions within the sdpn model space for the ^{19}O nucleus. Introducing the primary polarization effect involved the selection of effective charges for protons and neutrons: e_p = 1.410, e_n = 0.410 for the USDEPN interaction, and e_p = 1.400, e_n = 0.400 for the WCPN interaction. Moreover, we adjusted the g factor to achieve conformity with practical values pertaining to the ground state magnetic transitions, to become g_sp = 8.500 and g_s n = 8.500 and g_sp = 9.950 and g_sn = 9.950 for USDEPN and WCPN interactions, respectively.

Regarding the interaction USDEPN, when we compared our results with the experimental results, we observed favorable agreement in electric transitions B(E2) $1/2_1 \rightarrow 5/2_1$, B(E2) $9/2_1 \rightarrow 5/2_1$. Similarly, magnetic transition compatibility was notable for the transitions B(M1) $3/2_1 \rightarrow 5/2_1$, B(M1) $1/2_1 \rightarrow 3/2_1$, aligning well with existing experimental data [20]. Additionally, our calculations unveiled new transitions for which no experimental values have been documented thus far. On the other hand, when we compared our calculations with the theoretical results we obtained from the Ref. [9], we found acceptable agreement for the transitions B(E2) $1/2_1 \rightarrow 5/2_1$, B(E2) $9/2_1 \rightarrow 5/2_1$, B(E2) $7/2_1 \rightarrow 5/2_1$, B(E2) $7/2_1 \rightarrow 9/2_1$, B(E2) $11/2_1 \rightarrow 9/2_1$, B(E2) $11/2_1 \rightarrow 7/2_1$. We also noticed the presence of transfers that were not calculated theoretically. As for magnetic transitions, no comparative theoretical data were available.

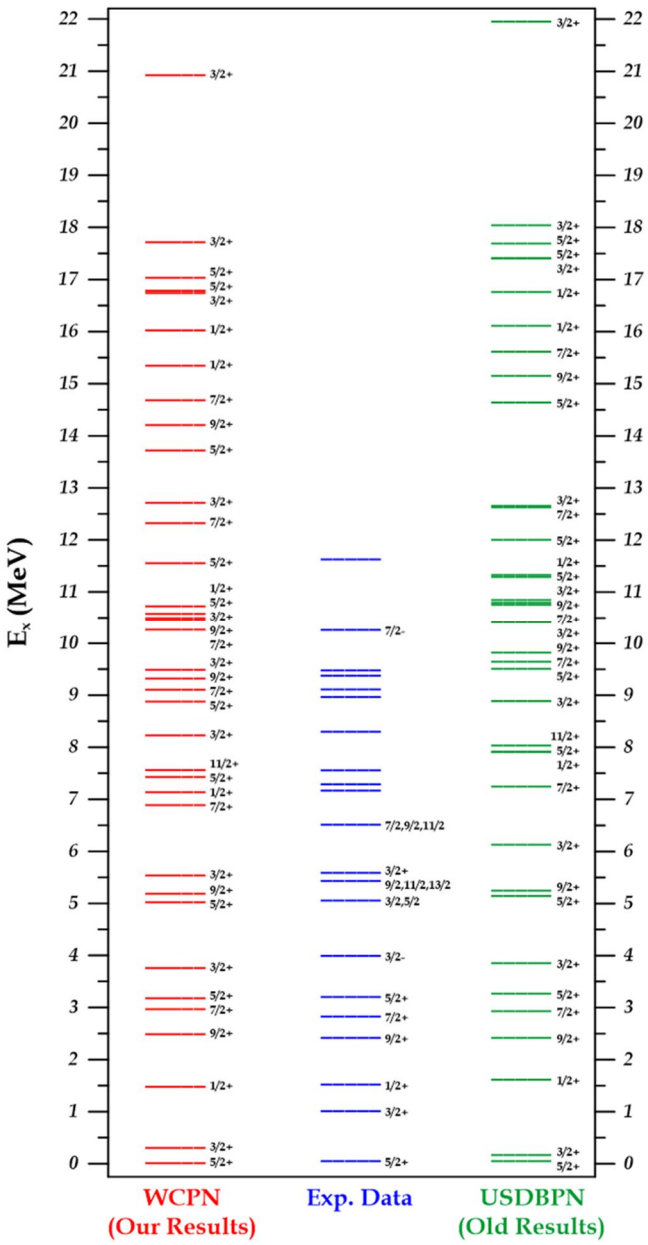

FIG. 2. Comparison of the experimental excitation energies taken from Ref. [20] with our theoretical results using WCPN interaction and theoretical results from Ref. [9] using USDBPN interaction.

Simultaneously, upon applying the WCPN interaction and comparing the results with experimental data, we observed favorable agreement for several transitions, including B(E2) $1/2_1 \rightarrow 5/2_1$, B(E2) $9/2_1 \rightarrow 5/2_1$, B(M1) $3/2_1 \rightarrow 5/2_1$, B(M1) $1/2_1 \rightarrow 3/2_1$ [20]. Additionally, our theoretical calculations predicted new transitions that have not yet been experimentally confirmed. On the other hand, when we compared our calculations with the theoretical results we obtained from the reference [9], we found acceptable agreement for the transitions B(E2) $1/2_1 \rightarrow 5/2_1$, B(E2) $9/2_1 \rightarrow 5/2_1$, B(E2) $7/2_1 \rightarrow 5/2_1$, B(E2) $7/2_1 \rightarrow 9/2_1$, B(E2) $11/2_1 \rightarrow 9/2_1$, B(E2) $11/2_1 \rightarrow 7/2_1$. We also noticed the presence of transfers that were not calculated theoretically. Regarding magnetic transitions, no comparative theoretical data were available in the referenced literature.

Table 1 presents a comparison between some of our theoretical values calculated using effective interaction USDEPN and both the practical values [20] and the theoretical results we obtained from Ref. [9] (using USDBPN interaction) for electric transitions.

Table 2 shows a comparison between some of our theoretical values using effective interaction USDEPN and the practical values [20] for magnetic transitions.

Table 3 compares some of our theoretical values computed using effective interaction WCPN with both the practical values [20] and the theoretical results (USDBPN interaction) we obtained from Ref. [9] for electric transitions. Finally, Table 4 shows a comparison between some of our theoretical values using effective interaction WCPN and the practical values [20] for magnetic transitions.

TABLE 1. Comparison of the B(E2) outcomes (in units of e^2 fm^4) for the ^{19}O isotope, computed using the USDEPN interaction, with the experimental data from Ref. [20] and theoretical results from Ref. [9] based on the USDBPN interaction

Ji→Jf	B(E2), Our results (e^2fm^4) for USDEPN *e_p 1.410= e_n=0.410*	B(E2) Exp. results (e^2fm^4)	B(E2) Theor. results (e^2fm^4) USDBPN
$1/2_1 \rightarrow 5/2_1$	1.748	1.747	10.75
$9/2_1 \rightarrow 5/2_1$	2.022	> 3.012	12.49
$3/2_1 \rightarrow 5/2_1$	7.6150	-----	64.63
$7/2_1 \rightarrow 5/2_1$	2.829	-----	16.579
$7/2_1 \rightarrow 9/2_1$	2.6630	-----	16.23
$5/2_2 \rightarrow 5/2_1$	0.6344	-----	-----
$11/2_1 \rightarrow 9/2_1$	0.8306	-----	5.095
$11/2_1 \rightarrow 7/2_1$	1.2670	-----	7.874
$1/2_1 \rightarrow 3/2_1$	0.4816	-----	-----

TABLE 2. Comparison of the B(M1) outcomes (in units of μ^2) for the ^{19}O nucleus, computed using the USDEPN interaction, with experimental data from Ref. [20].

Ji→Jf	B(M1), Our results USDEPN g_Sp = 8.500, g_Sn = - 8.500	B(M1) Exp. results μ^2
$3/2_1 \rightarrow 5/2_1$	0.1357	0.158
$1/2_1 \rightarrow 3/2_1$	0.1373	0.017
$7/2_1 \rightarrow 5/2_1$	0.1236	-----
$5/2_2 \rightarrow 5/2_1$	0.0099	-----
$5/2_2 \rightarrow 3/2_1$	0.6131	-----
$11/2_1 \rightarrow 9/2_1$	1.1400	-----

TABLE 3. Comparison of the B(E2) outcomes (in units of e^2 fm^4) for the ^{19}O isotope, computed using the WCPN interaction, with the experimental results from Ref. [20] and theoretical results from Ref. [9] using the USDBPN interaction

Ji→Jf	B(E2) Our results(e^2fm^4) for WCPN *e_p 1.400, e_n=0.400*	B(E2) Exp. results (e^2fm^4)	B(E2) Theory. results (e^2fm^4) USDBPN
$1/2_1 \rightarrow 5/2_1$	1.7300	1.747	10.75
$9/2_1 \rightarrow 5/2_1$	1.910	> 3.012	12.49
$3/2_1 \rightarrow 5/2_1$	6.9560	-----	64.63
$7/2_1 \rightarrow 5/2_1$	2.6990	-----	16.579
$7/2_1 \rightarrow 9/2_1$	2.3740	-----	16.23
$5/2_2 \rightarrow 5/2_1$	0.6227	-----	-----
$11/2_1 \rightarrow 9/2_1$	0.7803	-----	5.095
$11/2_1 \rightarrow 7/2_1$	1.5830	-----	7.874
$1/2_1 \rightarrow 3/2_1$	0.4823	-----	-----

TABLE 4. Comparison of the B(M1) outcomes (in units of μ^2) for the ^{19}O nucleus, computed using the WCPN interaction, with experimental data from Ref. [20]

Ji→Jf	B(M1), Ours. results WCPN g_sp=9.950,g_sn=- 9.950	B(M1) Exp. results μ^2
$3/2_1 \rightarrow 5/2_1$	0.1056	0.158
$1/2_1 \rightarrow 3/2_1$	0.3058	0.017
$7/2_1 \rightarrow 5/2_1$	0.2204	
$5/2_2 \rightarrow 5/2_1$	0.0025	
$5/2_2 \rightarrow 3/2_1$	0.8348	
$11/2_1 \rightarrow 9/2_1$	1.4690	

3.3 Charge Density Distribution

Figure 3 illustrates the distribution of charge density within the ^{19}O nucleus. As shown, the value of the charge density at the center of the nucleus is 0.08736 e.fm^{-3}. Then it decreases to r = 4.5 fm, and then its value is fixed at zero.

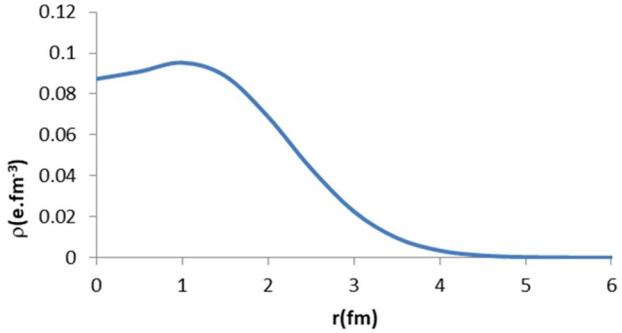

FIG. 3. The charge density distribution of the ^{19}O nucleus.

4. Conclusions:

Utilizing the NuShellX@MSU code within the sdpn shell and employing the effective interactions of USDEPN and WCPN, we conducted calculations concerning energy levels, electromagnetic transition probabilities, and charge density distribution for the ^{19}O nucleus. The present study effectively demonstrates that these interaction files align harmoniously with the available experimental data. Our computations confirmed a multitude of energy levels for both interactions, unveiling novel energy states. The congruence between the B(E2) and B(M1) values and the experimental results was also noteworthy. Furthermore, our calculations led us to conclude that the value of the charge density at the center of the nucleus is 0.08736 e.fm^{-3}, then it gradually diminishes, and eventually stabilizes at zero. Overall, these findings confirm that applying the shell model configuration mixing within the sdpn shell provides reliable and satisfactory results.

References:

[1] Obeed, F.H., Jordan J. Phys., 14 (2021) 25.

[2] Saeed, M., Nemati, G.B., and Shayan, S.N., Nucl. Sci., 2 (2017) 1.

[3] Mohammadi, S. and Kafash, E., Asian J. Eng. Technol. Innov., 2 (2014) 18.

[4] Brown, B.A. et al., MSU-NSCL Rep., 1289 (2004).

[5] Caurier, E. and Nowacki, F., Acta Phys. Pol. B, 30 (1999) 705.

[6] Brown, B. and Rae, W., NuShell@MSU MSU-NSCL Rep., (2007).

[7] Brown, B. and Rae, W., Nucl. Data Sheets, 120 (2014) 115.

[8] Hasan, A. and Abed, H., Nucl. Phys. At. Energy, 24 (2023) 219.

[9] Hasan, A., Ukr. J. Phys., 63 (2018) 189.

[10] Itaco, N., Coraggio, L., Covello, A., and Gargano, A., J. Phys.: Conf. Ser., 336 (2011) 012008.

[11] Coraggio, L. and Itaco, N., Front. Phys., 8 (2020) 345.

[12] Hasan, A.K. and Abed, H.H., AIP Conf. Proc., 2977 (2023) 030017.

[13] Condon, E.U. and Odabasi, H., Atomic Structure: CUP Archive, (1980).

[14] De-Shalit, A. and Talmi, I., "Nuclear Shell Theory", Vol. 14, (Academic Press, 2013).

[15] Elliott, J.P. Proc. R. Soc. Lond. A Math. Phys. Sci., 245 (1958) 128.

[16] Bayman, B.F. and Lande, A., Nucl. Phys., 77 (1966) 1.

[17] Lawson, R., "Theory of the Nuclear Shell Model", (1980).

[18] Brussaard, P.J. and Glaudemans, P.W.M., "Shell-Model Applications in Nuclear Spectroscopy", (North-Holland publishing company, 1977).

[19] Preston, M.A., "Structure of the Nucleus", (CRC Press, 2018).

[20] Tilley, D., Weller, H., Cheves, C., and Chasteler, R., Nucl. Phys. A, 595 (1995) 1.

Volume 18, Number 2, 2025. pp. 131-140

Jordan Journal of Physics

ARTICLE

Shell Model Calculations of Nuclear Properties in (^{91,93}Sr) Strontium Isotopes Using NuShellX@MSU Code

F. H. Obeed[a] and **A. K. Hasan**[b]

[a] *Department of Physics, Faculty of Education for Girls, University of Kufa, Najaf, Iraq.*
[b] *College of Health and Medical Technology, University of Alkafeel, Iraq.*

Doi: **https://doi.org/10.47011/18.2.3**
Received on: 02/09/2023; *Accepted on: 16/04/2024*

Abstract: The nuclear shell model has been applied to calculate various nuclear properties of the ^{91,93}Sr isotopes, including spins and parities, energy spectra, reduced electromagnetic transition possibilities (electric quadrupole and magnetic dipole), magnetic dipole moments, nuclear charge distributions, and mass density as functions of the radial distance from the nucleus center (r). In this study, the NuShellX@MSU code was employed using Gloeckner-Bare G-matrix interaction, within the Gloeckner model space of the orbits ($2p_{1/2}$,$1g_{9/2}$) and ($3s_{1/2}$,$2d_{5/2}$) for protons and neutrons, respectively. The results showed good agreement with the available experimental data (spins and parities of energy spectra) and a confirmation of most levels. Theoretically, new values have been expected for the most nuclear properties, including spin, parities, energy spectra, transition strengths, electric quadrupole, dipole magnetic moments, the nuclear charge, and mass density distributions. Previously, these accounts had not been determined empirically.

Keywords: Energy spectra, Transition strengths, Density distributions.

1. Introduction

The nuclear shell model has been one of the central theoretical keys for interpreting nuclear structure experimental data. Due to the significant growth in Hilbert space dimensions, practical calculations must be carried out in a reduced Hilbert space, known as the model space. Accordingly, effective interactions, such as Gloeckner (Gl) and Gloeckner Pulse bare G-Matrix (Glb), have been designed to fit the space of the chosen model. In these interactions, the shell model has succeeded to describe many properties of the nuclei, including the magic number, spin, valence, binding energy of the nucleus, the cross-section of the neutron captured by the nuclei, and the transmission probabilities of gamma-ray emission from the nuclei, as well as electric quadrupole and dipole magnetic moments [1, 2]. Isotopes around the closed proton and neutron shells (^{88}Sr isotope) play a key role in nuclear physics [3]. Strontium nucleus (^{38}Sr) has four stable, naturally occurring isotopes: ^{84}Sr (0.56%), ^{86}Sr(9.86%), ^{87}Sr(7.0%), and ^{88}Sr (82.58%). Thirty-two unstable isotopes of strontium are known to exist, ranging from ^{73}Sr to ^{108}Sr [4,5]. A large number of studies presented that nuclei in $A \geq 90$ for semi-magic shell closure ($Z = 38$ and $N = 50$) mass region provide suitable objects to investigate the structure level. Many properties of these nuclei have been interpreted in shell-model calculations above the closed core nucleus ^{88}Sr.

Several researchers have contributed to this field. Ahalpara and Bhatt explained the shell-model spectra of ^{92}Tc and ^{93}Ru nuclei [3]. Gloeckner described the nuclear shell model calculations for zirconium and niobium isotopes

Corresponding Author: F. H. Obeed **Email**: fatimahh.alfatlawi@uokufa.edu.iq

with proton filling ($2p_{1/2}$, $1g_{9/2}$) and ($3s_{1/2}$, $2d_{5/2}$) orbits [6]. Several of ^{92,93,94,95}Zr isotopes' properties, including energy spectra, have been well described in shell-model calculations using ($2p_{1/2}$,$1g_{9/2}$) and ($3s_{1/2}$,$2d_{5/2}$) space by many researchers, including Fotiades *et al*. [7]. Wei *et al.* proposed a new high-spin level scheme for the ^{87}Sr nucleus based on coupling a $g_{9/2}$ neutron hole to the yrast states of the ^{88}Sr core, which accounts for its observed energy states [8]. Li *et al*. calculated high-spin states in the semi-magic nucleus ^{89}Y and studied neutron-core excitations in N = 50 isotones [9]. Furthermore, Wu *et al*. performed shell-model calculations of core-excited level structures for the ^{89}Sr nucleus using the NuShellX code [10]. Sihotra *et al.* studied the wave functions for the excited higher-spin states of the ^{96}Tc nucleus utilizing the jj45pn model space of valence protons distributed over the single-particle $2p_{1/2}$ and $1g_{9/2}$ orbitals and neutrons occupying $1g_{7/2}$, $2d_{5/2}$, $2d_{3/2}$, $3s_{1/2}$, and $h_{11/2}$ orbitals [11]. Obeed studied the high-spin states for the ^{90,91,92}Y isotopes by applying nuclear shell model calculations with the OXBASH code [12].

The aim of the present work is to describe some of the nuclear structure properties by increasing the number of valence nucleons (neutrons) outside the closed ^{88}Sr nucleus of ^{91,93}Sr isotopes by using the NuShellX@MSU code with Gloeckner interaction and Bare G-matrix.

2. Theory

Understanding the properties of nuclei, such as energy levels, wave functions, the description of electromagnetic transition rates, electric quadrupole and dipole magnetic moments, and nucleon density distributions, is the key problem in nuclear physics. Therefore, many models have been developed to solve this problem and establish the structure of the nucleus [13, 14]. A successful description of these properties depends critically on the choice of model space and effective interactions. Through these inputs, the reduced one-body matrix elements can specify the shell-model wave functions of initial spin J_i and final spin J_f for a given multipolarity λ. This can be extracted as a linear combination of single-particle matrix elements [12, 15, 16]:

$$\langle \mathrm{NITT_z}\|\mathrm{O}(\lambda)\|\mathrm{NITT_z}\rangle = \sum_{\rho\rho'}\langle\rho|\mathrm{O}(\lambda,\mathrm{M})|\rho'\rangle\, \mathrm{D}^{\mathrm{NITT_z}}(\lambda,\rho,\rho') \quad (1)$$

where $\langle\rho|\mathrm{O}(\lambda,\mathrm{M})|\rho'\rangle$ are the single-particle matrix elements.

When the operator mediates the observable quadrupole electrical elements of a many-body nuclear state $|\mathrm{NITT_z}\rangle$, it can be represented as a sum of one-body operators. The one-body factor O in the nuclear shell model can be represented in the second quantitative formula as:

$$\mathrm{O} = \sum_{K=1}^{A} O_K = \sum_{\rho\rho' \mathrm{mm}'} \langle \rho\mathrm{m}|\mathrm{O}|\rho'\mathrm{m}'\rangle\, a^{+}_{\rho\mathrm{m}} a_{\rho'\mathrm{m}'} \quad (2)$$

Here, the first summation acts on all nucleons, while the second summation acts on all energetic single-particle states $|\rho\mathrm{m}\rangle = |njlmtt_z\rangle$ in the fundamental space of the shell model, and the $a^{+}_{\rho\mathrm{m}}$ and $a_{\rho'\mathrm{m}'}$ A spherical tensor of order λ. In the coordinate space, O = O(λ.,M),

$$\mathrm{D}^{\mathrm{NITT_z}}(\lambda,\rho,\rho') = \frac{\langle \mathrm{NITT_z}\|\left[\mathrm{a}^{\dagger}_{\rho}\times \mathrm{a}_{\rho'}\right]^{\lambda}\|\mathrm{NITT_z}\rangle}{\sqrt{2\lambda+1}} \quad (3)$$

through the appropriate algebraic operations on the model wave functions.

Low-lying levels of even-odd nuclei typically decay via electric quadrupole (E2) and magnetic dipole (M1) transitions to lower yrast levels. The reduced transition probability for a generic multipolar electromagnetic transition is given by [15, 16]:

$$\mathrm{B}(\sigma\lambda;\ \mathrm{J_iT_iT_z} \longrightarrow \mathrm{J_iT_iT_z}) = \frac{1}{2\mathrm{J_i}+1}\left|\langle \mathrm{J_fT_fT_z}\|\mathrm{O}^{\sigma\lambda}\|\mathrm{J_iT_iT_z}\rangle\right|^2 \quad (4)$$

Specifically, the reduced electric and magnetic transition probabilities are expressed as:

$$\mathrm{B}(\mathrm{E1};\ \mathrm{J_iT_iT_z} \longrightarrow \mathrm{J_iT_iT_z}) = \frac{1}{2\mathrm{J_i}+1}\left|\langle \mathrm{J_fT_fT_z}\|\mathrm{O}^{\mathrm{E1}}\|\mathrm{J_iT_iT_z}\rangle\right|^2 \quad (5)$$

and

$$\mathrm{B}(\mathrm{M1};\ \mathrm{J_iT_iT_z} \longrightarrow \mathrm{J_iT_iT_z}) = \frac{1}{2\mathrm{J_i}+1}\left|\langle \mathrm{J_fT_fT_z}\|\mathrm{O}^{\mathrm{M1}}\|\mathrm{J_iT_iT_z}\rangle\right|^2 \quad (6)$$

Here, $\mathrm{O}^{\sigma\lambda}$ refers to a multipolar electromagnetic operator of rank λ, often analogous in form to the matrix of the residual interaction between nucleons.

Among nuclear moments, the quadrupole moment has been particularly challenging to measure accurately, although it provides vital information about the deformation of the nucleus [18]. The spectroscopic quadrupole moment

Q_s of a nuclear state, along with its total angular momentum J, gives insight into the deviation of the charge distribution from spherical symmetry—particularly relevant in nuclei with non-zero projection of angular momentum (K = 0). For a given nucleus, the effective charges of the proton and neutron can be used in shell model calculations to find the quadrupole moments [15, 18, 19]. The spectroscopic electric quadrupole moment can be directly connected to the intrinsic quadrupole moment Q′ by the expression [15, 20]:

$$Q_s(JK) = \frac{3K^2 - J(J+1)}{(2J+3).(J+1)} Q' \quad (7)$$

$Q_s > 0$ indicates a prolate deformation for the isotope. $Q_s < 0$ indicates an oblate deformation for the isotope. $Q_s = 0$ corresponds to an isotope with spherical shape [20]

$$Q' = \sqrt{\frac{16\pi}{5}}.(B(E2))^{1/2} \quad (8)$$

Here, K is the estimation of the total angular momentum of the nucleus along the deformation axis.

The one-body density factor can be transformed into two-body density as the following change [15]:

$$\hat{\rho}(\vec{r}) = \sum_{i=1}^{A} \delta(\vec{r} - \vec{r}_i) \quad (9)$$

The equations of the nuclear charge and mass density can be described as follows:

$$\int \rho_{\circ}(r)\ d\tau = 4\pi \int \rho_{\circ}(r)\ r^2 dr = A \quad (10)$$

where A denotes the nucleus mass number.

The distribution of the nuclear charge density can be explained by the equation:

$$\int \rho_{ch}(r)\ d\tau = 4\pi \int \rho_{ch}(r)\ r^2 dr = z \quad (11)$$

3. Results and Discussion:

The NuShellX@MSU code was implemented by using Gloeckner interaction with Bare G-matrix. The Gloeckner (gl) space model was applied for the deformed orbitals ($2p_{1/2}$, $1g_{9/2}$) and ($3s_{1/2}$, $2d_{5/2}$) of the proton and neutron of the valence particles (three and five neutrons) for ^{91}Sr and ^{93}Sr isotopes, respectively. Valence particles that have determined several nuclear properties are distributed outside $^{88}_{38}Sr$ closed core nucleus. These properties include energy spectra and nuclear states (i.e., total angular momentum and parity). The transition probabilities of the electric quadrupole B(E2) and magnetic dipole B(M1), as well as the nuclear charge distribution $\rho_{ch}(r)$ and mass density $\rho_m(r)$, are functions of the radial distance r from the center of the nucleus and are influenced by the electric and magnetic quadrupole and dipole moments.

The NuShellX@MSU code has been used to compute exact energy levels, eigenvectors, and spectral overlaps of the low-lying states in the Hamiltonian matrix. These large-scale shell model calculations utilize a proton–neutron coupled basis in total angular momentum J, with matrix dimensions reaching up to 100 million [21].

The Skyrme SLy4 interaction was applied to calculate radial wave functions for the single-particle matrix elements. These calculations were performed using the NuShellX@MSU code, incorporating effective nucleon charges and gyromagnetic factors g**,** where g represents the values of orbital parameters and effective spin factors (g) $\{g_s(p), g_s(n), g_l(p), g_l(n)$. The single-particle energy levels for the valence nucleons, as calculated by NuShellX@MSU, are $\{\varepsilon_{2p1/2}(p)$ = -7.124 MeV, $\varepsilon_{1g9/2}(p)$ = -6.248, $\varepsilon_{3s1/2}(n)$ = -5.506 MeV, and $\varepsilon_{2d5/2}(n)$ = -6.338 MeV$\}$. The following section presents and discusses the results obtained for each isotope.

3.1 Energy Levels

1. *^{91}Sr isotope:*

This isotope consists of three valence neutrons occupying the $3s_{1/2}$ and $2d_{5/2}$ orbitals above the $^{88}_{38}Sr$ closed nucleus. The calculated and experimental energy spectra for ^{91}Sr are compared in Fig. 1 [22]. The ground-state energy, spin, and configuration from the present calculations agree well with the available experimental data [22].

In the present results, the experimental energy level at 0.0936^{+4}_{-4} MeV [22] is confirmed to have total angular momentum (3/2), although no spin assignment had been made experimentally. Additionally, the calculated results confirm the spin-parity assignments of two experimental energy levels: $\{1.042^{+25}_{-25}$ and $1.23^{+5}_{-5}\}$. These assignments were not previously determined in experimental data [22].

The experimental level at 2.657^{+6}_{-6} [22], previously known to have positive parity (but no spin), is now confirmed as 9/2. Furthermore, it has been affirmed experimentally [22] with the value of 2.077^{+15}_{-15}. The calculated states $\{5/2^+, 3/2^+ and\ 7/2^+\}$ have been predicted with the values (1.36^{+7}_{-7},1.482^{+10}_{-10} and 1.917^{+12}_{-12}), but are experimentally unknown in states [22].

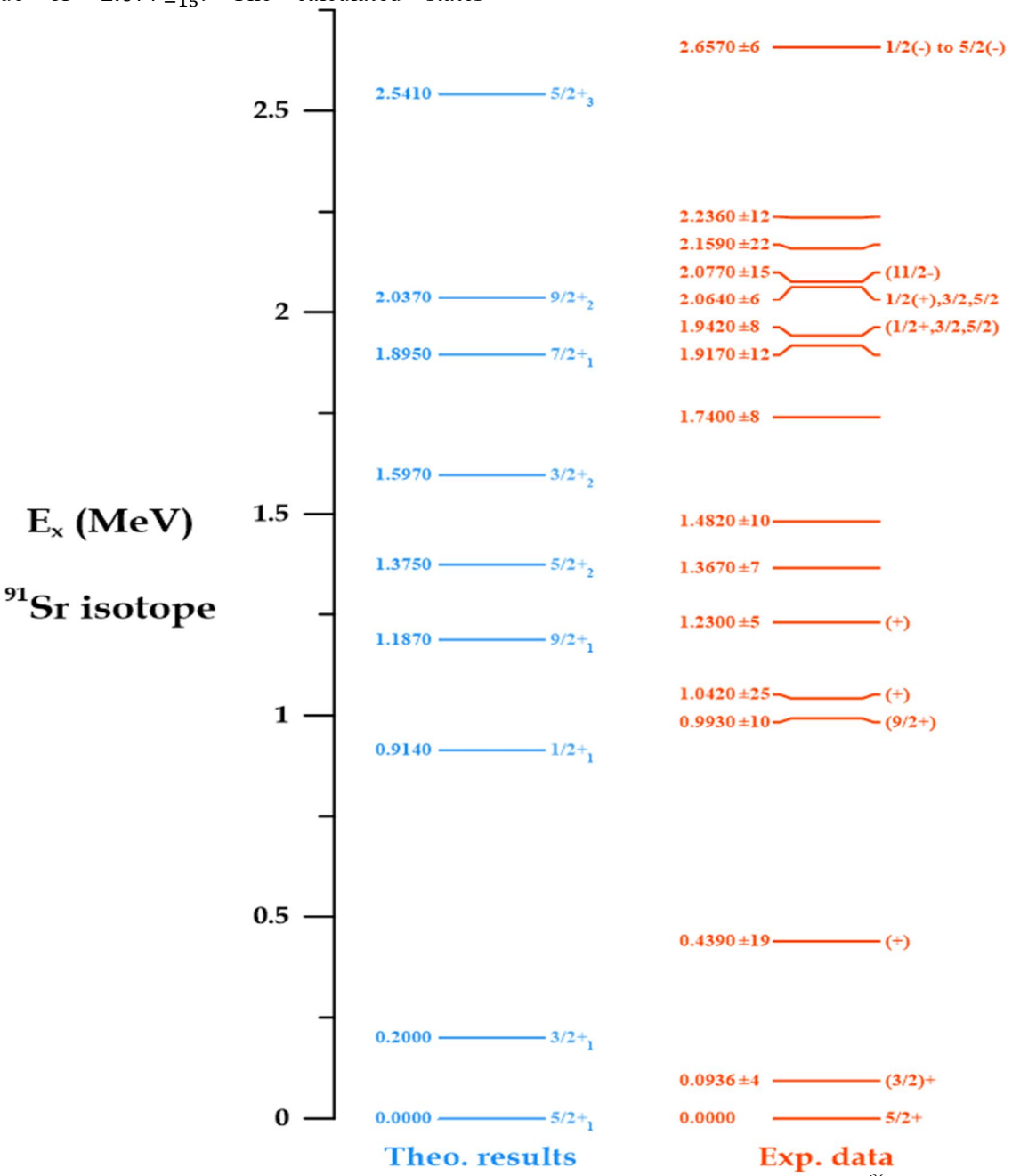

FIG. 1. Comparison of theoretical results with experimental data for the energy values for the ^{91}Sr isotope using glb interaction. The experimental data are adopted from Ref. [22].

2. ^{93}Sr isotope:

This isotope contains five nucleons (neutrons) occupying the ($3s_{1/2}$, $2d_{5/2}$) orbitals above the $^{88}_{38}$Sr closed-core nucleus. The calculated and experimental spectra values [23] for the ^{93}Sr isotope are displayed in Fig. 2 and can be interpreted as follows:

The energy value for the ground state, along with its spin and valence, is well reproduced from the experimental values [23]. The predicted theoretical states $\{3/2^+, 5/2^+, 7/2^+, 9/2^+, 5/2^+$ and $9/2^+\}$ have been confirmed for the experimental energy values $\{1.142^{+4}_{-4}, 1.148^{+6}_{-6}, 1.562^{+9}_{-9}, 1.808^{+6}_{-6}, 2.141^{+11}_{-11},$ and 2.351^{+11}_{-11} MeV.

There is no available experimental energy value to compare with the newly predicted theoretical energy level of 0.739 for the state $1/2^+$. The expected theoretical state $3/2^+$ has been specified for the experimental energy level 1.910^{+9}_{-9} MeV, but not for the experimental data. For the energy levels of ^{91,93}Sr isotopes, the experimental value was higher than the theoretical maximum value for our isotope calculations: 2.541 MeV of the $5/2^+_3$ state and 2.389 MeV of the $9/2^+_2$ state, respectively. Therefore, there are several experimental values that were not compared with our theoretical values.

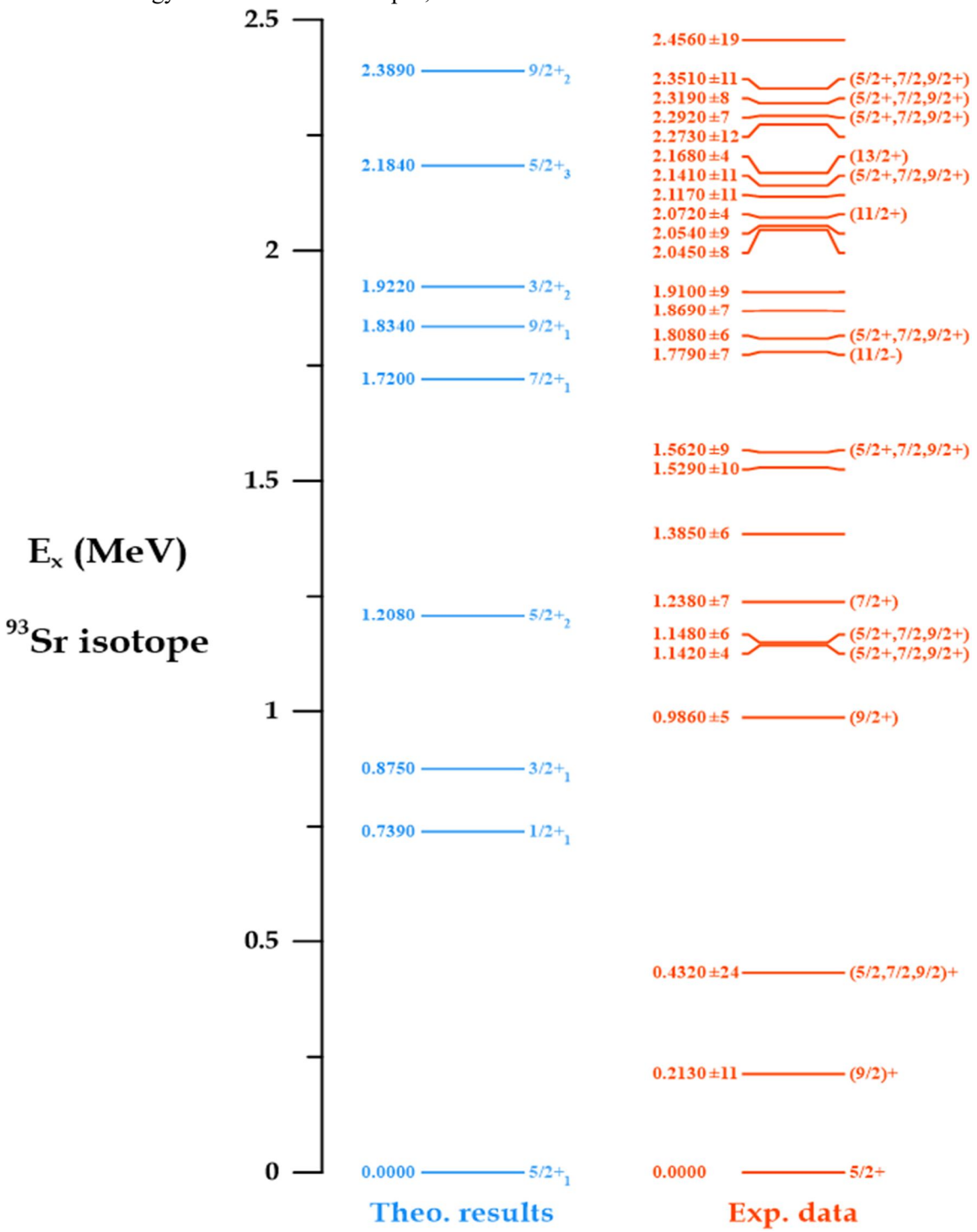

FIG. 2. Comparison of theoretical results with experimental data for the energy values for the ^{93}Sr isotope using glb interaction. The experimental data are adopted from Ref. [23].

3.2 Reduced Electric Quadrupole and Magnetic Dipole Transition Probabilities

In our calculations, the NuShellX@MSU code was also applied to generate the one-body transition density matrix (OBDM) elements using Gloeckner interaction with Bare G-matrix. These interactions took place in the orbits of the Glockner space model, namely, ($2p_{1/2}$, $1g_{9/2}$) and ($3s_{1/2}$, $2d_{5/2}$) for protons and neutrons, respectively. The wave functions of the single-particle matrix elements were estimated for the two isotopes using the Skyrme29 potential, with the following effective nucleon charges for protons and neutrons: {(e_p = 1.622e,e_n = 1.244e); (e_p = 1.5e,e_n = 1.720e)}. The values of the orbital parameters and effective spin factors (g){$g_s(p)$, $g_s(n)$, $g_l(p)$, $g_l(n)$ were equal to (5.027, -3.443, 1.418, 0.418); (5.027, -3.443, 1.474, 0.474) } and were used to conduct the magnetic dipole B (M1) for the ^{91,93}Sr isotopes, respectively.

The theoretical values for the transition probabilities of the electric quadrupole and the magnetic dipole in the Sky29 potential with nucleons of effective charges (protons and neutrons) for ^{91,93}Sr isotopes are shown in Tables 1 and 2, respectively. Table 1 explains E2 and M1 transition strengths for the ^{91}Sr isotope. The computed B(E2) transition probabilities show good agreement with the experimental data [22], particularly for the strong E2 decays from states $3/2_1^+$ to $5/2_1^+$, with a theoretical value of 362.3 (e^2fm^4) and 42.33×10^{-5} (μ_N^2) for the electric quadrupole and magnetic dipole transitions, respectively. These results were compared with the experimental values, which were reported as > 340.8 (e^2fm^4) and < 2.148×10^{-5} (μ_N^2). However, the M1 transition strength remains unconfirmed experimentally.

For the ^{93}Sr isotope, the theoretical E2 and M1 transition strengths are listed in Table 2. These values do not yet have corresponding experimental data for comparison [23]. Several new electromagnetic transitions for B(E2;↓) and B(M1;↓) have been computed applying the NuShellX@MSU code with Glb interaction for ^{91,93}Sr isotopes, illustrated in Tables 1 and 2. These predicted transitions, currently unobserved experimentally, contribute additional theoretical insights into the energy levels and electromagnetic properties of these isotopes.

TABLE 1. Comparison of experimental and theoretical values for electric quadrupole and magnetic dipole transition probabilities for positive-parity spin states in the ^{91}Sr isotope. The experimental data are adopted from Ref. [22].

	Theoretical Results		Experimental Results		
$J_i \rightarrow J_f$	$(BE2\downarrow)(e^2fm^4)$	$(BM1\downarrow)(\mu_N^2))$	Multi-polarity	$(BE2\downarrow)(e^2fm^4)$	$(BM1\downarrow)(\mu_N^2))$
$3/2_1^+ \rightarrow 5/2_1^+$	362.3	42.33×10^{-5}	E2(+M1)	> 340.8	<2.148× 10^{-5}
$1/2_1^+ \rightarrow 5/2_1^+$	96.47	-----	-----	-----	-----
$1/2_1^+ \rightarrow 3/2_1^+$	25.18	-----	-----	-----	-----
$9/2_1^+ \rightarrow 5/2_1^+$	84.68	-----	-----	-----	-----
$7/2_1^+ \rightarrow 5/2_1^+$	215.8	-----	-----	-----	-----
$7/2_1^+ \rightarrow 3/2_1^+$	78.63	-----	-----	-----	-----
$7/2_1^+ \rightarrow 9/2_1^+$	161.9	1.61×10^{-2}	-----	-----	-----

TABLE 2. Comparison of experimental and theoretical values for electric quadrupole and magnetic dipole transition probabilities for positive-parity spin states in the ^{93}Sr isotope. The experimental data are adopted from Ref. [23].

	Theoretical Results		Experimental Results		
$J_i \rightarrow J_f$	$(BE2\downarrow)(e^2fm^4)$	$(BM1\downarrow)(\mu_N^2))$	multi-polarity	$(BE2\downarrow)(e^2fm^4)$	$(BM1\downarrow)(\mu_N^2))$
$1/2_1^+ \rightarrow 5/2_1^+$	25.03	-----	-----	-----	-----
$3/2_1^+ \rightarrow 5/2_1^+$	571	-----	-----	-----	-----
$3/2_1^+ \rightarrow 1/2_1^+$	111	-----	-----	-----	-----
$7/2_1^+ \rightarrow 5/2_1^+$	582.9	-----	-----	-----	-----
$7/2_1^+ \rightarrow 3/2_1^+$	183.5	-----	-----	-----	-----
$7/2_1^+ \rightarrow 5/2_2^+$	0.8489×10^{-2}	-----	-----	-----	-----
$9/2_1^+ \rightarrow 5/2_1^+$	88.45	-----	-----	-----	-----
$9/2_1^+ \rightarrow 5/2_2^+$	40.52	-----	-----	-----	-----
$9/2_1^+ \rightarrow 7/2_1^+$	26.76	-----	-----	-----	-----

3.3 Electric Quadrupole and Magnetic Dipole Moments

The electric quadruple moments (Q_s) and magnetic dipoles (μ) of the ^{91,93}Sr isotopes have been calculated and are presented in Table 3, which compares the theoretical values with the experimental data [22, 23] for the two isotopes used in this study. The calculations show that the quadrupole moments of ^{91}Sr isotope in the states {$5/2_1^+$, $9/2_1^+$, $3/2_2^+$, $7/2_1^+$, $9/2_2^+$, and $5/2_3^+$} have negative signs (oblate shape dominance), while for the ^{93}Sr isotope, the states {$5/2_1^+$, $7/2_1^+$, $9/2_1$, $3/2_2^+$, and $5/2_3^+$ } of the quadrupole moments have appeared with positive signs (prolate shape dominance), whereas the states {$3/2_1^+$, $5/2_2^+$, and $9/2_2^+$} exhibit negative signs, representing the oblate shape dominance.

The calculated magnetic dipole moments (μ) of the ground state $5/2_1^+$ are -0.889 μ_N and -0.792 μ_N for ^{91,93}Sr isotopes. These values agree with the corresponding experimental results {0.885^{+2}_{-2} and -0.7926^{+12}_{-12}}. Additionally, the calculated quadrupole moment of 25.81(efm^2) for ^{93}Sr matches well with the experimental value of {$+25.8^{+11}_{-11}$} efm^2. The remaining quadrupole (Q_s) and magnetic dipole (μ) moments have been predicted theoretically but have not yet been confirmed experimentally.

TABLE 3. Comparison of experimental [22, 23] and theoretical values for the quadrupole with magnetic dipole moments in ^{91,93}Sr isotopes using glb interaction.

Isotopes		Theoretical Results		Experimental Results	
	J^π	$(Q)(efm^2)$	$\mu(\mu_N)$	$(Q)(efm^2)$	$\mu(\mu_N)$
^{91}Sr isotope	$5/2_1^+$	-1.62	-0.889	4.2 ±11	-0.885± 2
	$3/2_1^+$	14.59	-0.397	-----	-----
	$1/2_1^+$	0	-1.722	-----	-----
	$9/2_1^+$	-5.73	-1.614	-----	-----
	$5/2_2^+$	2.35	-2.302	-----	-----
	$3/2_2^+$	-6.69	0.261	-----	-----
	$7/2_1^+$	-14.47	-0.039	-----	-----
	$9/2_2^+$	-10.06	-3.119	-----	-----
	$5/2_3^+$	-9.19	-1.011	-----	-----
^{93}Sr isotope	$5/2_1^+$	25.81	-0.792	+25.8±11	-0.7926±12
	$1/2_1^+$	0	-1.722	-----	-----
	$3/2_1^+$	-32.17	0.167	-----	-----
	$5/2_2^+$	-20.18	-2.164	-----	-----
	$7/2_1^+$	20.06	0.136	-----	-----
	$9/2_1^+$	32.92	-2.912	-----	-----
	$3/2_2^+$	21.23	-0.155	-----	-----
	$5/2_3^+$	6.09	-0.931	-----	-----
	$9/2_2^+$	-11.04	-1.440	-----	-----

3.4 Nuclear Charge and Mass Density Distributions

The nuclear charge and mass density distributions of the ^{91,93}Sr isotopes have been computed by implementing the NuShellX @MSU code and sky29 potential as displayed in Figs. 3 and 4 for the above isotopes, respectively. For the ^{91,93}Sr isotopes, the nuclear charge density at the center of the nucleus was found to be ρ_{ch} = 0.08072 Ze/fm^{-3} and ρ_{ch} = 0.0828Ze/fm^{-3}, respectively. These values remain stable at a distance of r = 0.1 fm, as shown in Figs. 3 and 4. At r = 0.2 fm, the charge density begins to decrease, reaching values of ρ_{ch} = 0.08063Ze/fm^{-3} for ^{91}Sr and ρ_{ch} = 0.08346 Ze/fm^{-3} for ^{93}Sr. Beyond these points, the charge density continues to decline gradually until it reaches zero at r = 6.9 fm in both isotopes. Similarly, the nuclear mass density at the center of the nucleus is calculated as ρ_m = 0.1628 nucleon/fm^{-3} for ^{91}Sr and ρ_m = 0.1656 nucleon/fm^{-3} for ^{93}Sr, with a slight increase at r = 0.1 fm. As r increases to 0.2 fm, the mass density also increases slightly to ρm = 0.1631 nucleon/fm^{-3} for ^{91}Sr and ρ_m = 0.1659 nucleon/fm^{-3} for ^{93}Sr. For the ^{91}Sr isotope, the mass density distribution gradually increases, reaching a maximum value of ρ_m = 0.1701 nuclei/fm^{-3} at distances between r = 1.3 and 1.4

fm. Beyond this point, it gradually decreases until it reaches zero at r = 7.3 fm. The nuclear mass density of the ^{93}Sr isotope continues to increase gradually at distances from 0.2 to 1.4 fm, and also at the distance r = 1.5 fm, after which the mass density distribution of this isotope begins to decrease until it stabilizes at zero (r = 7.2 fm). As for the experimental values of the nuclear charge and mass density distributions for the ^{91,93}Sr isotopes, no ratios have been determined.

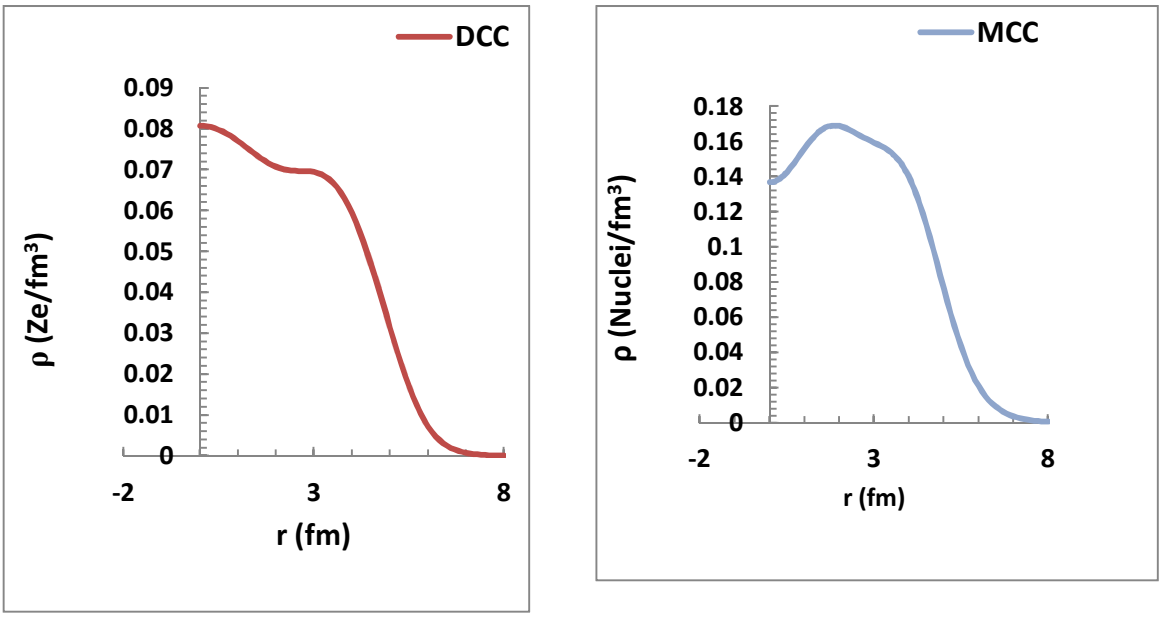

FIG. 3. Nuclear charge and mass density distributions as functions of the radial distance from the center of the nucleus (r) in ^{91}Sr isotope.

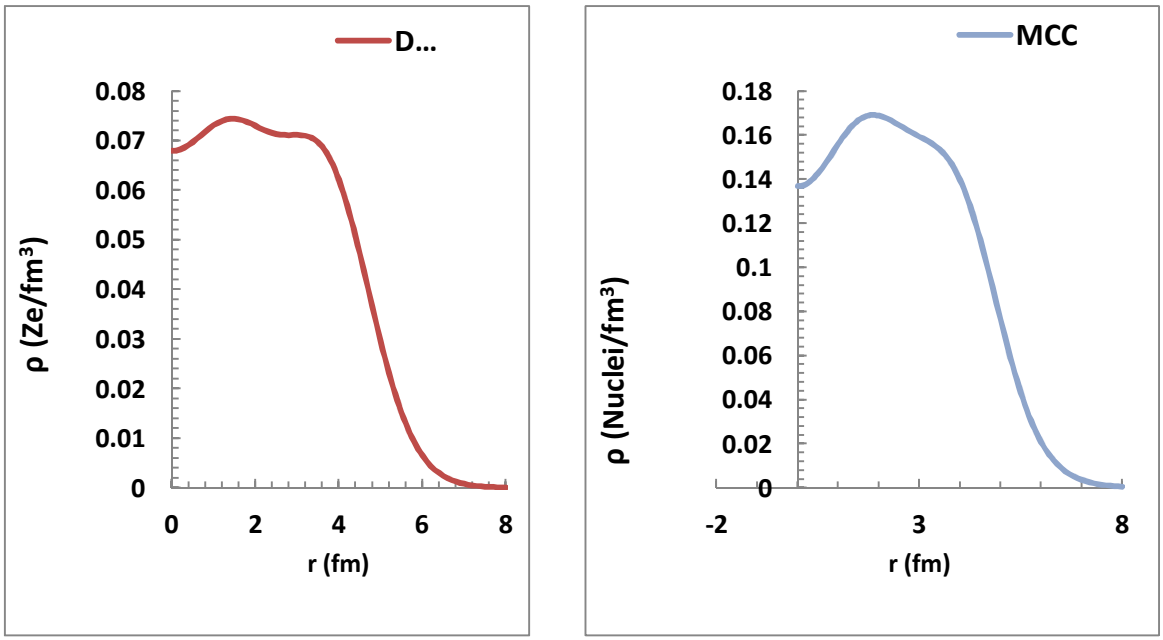

FIG. 4. Nuclear charge and mass density distributions as functions of the radial distance from the center of the nucleus (r) in ^{93}Sr isotope.

4. Conclusions

Through the calculated results of the nuclear properties studied in this manuscript for the ^{91,93}Sr isotopes, and by comparing these characteristics with the experimental data, the following conclusions can be drawn:

- The energy value of the ground state with spin and parity has been well reproduced with the experimental values for both isotopes (^{91}Sr and ^{93}Sr).
- The total angular momentum with parity has been confirmed and determined for some experimental data values of ^{91,93}Sr isotopes.
- Several theoretical energy levels of the ^{91,93}Sr isotopes do not have corresponding values in the experimental data.
- There are experimental energy levels whose values exceed the theoretical maximums calculated in this study: 2.541 MeV for the $5/2_3^+$ state in ^{91}Sr and 2.389 MeV for the $9/2_2^+$ state in ^{93}Sr.
- For the ^{91}Sr isotope, good agreement has been achieved between the calculated magnetic transition probabilities (quadrupole and dipole) and the experimental values, particularly for the strong transition ($3/2_1^+ \rightarrow 5/2_1^+$).
- Some multipolarity types previously listed in experimental data as (E1), (E1 + M2), or (M1 + E2) for transitions in ^{91}Sr have not been definitively confirmed. However, in this study, these transitions are predicted to be of the E2 and M1 types.
- New electromagnetic transition values have been predicted for both ^{91}Sr and ^{93}Sr isotopes using the NuShellX@MSU code with the GLB interaction. These transitions have not yet been observed experimentally.
- The calculated electric quadrupole and magnetic dipole moments of ^{91}Sr and ^{93}Sr indicate that some nuclear states exhibit oblate shapes, while others show prolate shapes. These shape variations reflect structural sensitivities in the nuclear chart and may vary from one nucleus to another.
- Furthermore, it has been found that shape changes with increasing neutron number may also occur with changes in excitation energy or angular momentum within the same nucleus. These changes are attributed to the rearrangement of orbital configurations or to dynamic structural responses.
- The magnetic dipole moments (μ) for the ground state $5/2_1^+$ in both ^{91}Sr and ^{93}Sr isotopes are consistent with available experimental values. For ^{93}Sr, the predicted moment for the $5/2_1^+$ ground state also agrees well with experimental measurements.
- It has been observed that many new values of the electric quadrupole moments (Q_s) and magnetic dipole moments (μ) have been theoretically predicted, but remain experimentally unconfirmed or underestimated.
- The distribution of the nuclear charge density of the ^{91,93}Sr isotopes is stable at the center of the nucleus, at the value at r = 0.1. Beyond this point, the values of the nuclear charge density distribution gradually decrease until they stabilize at zero. On the contrary, the distribution of the nuclear mass density of the ^{91,93}Sr isotopes also begins at a stable value at r = 0.1, so this distance gradually becomes the value of the nuclear mass density distribution, then these values gradually decrease until they settle at zero over a certain distance, and this behavior in the distribution of nuclear charge and mass density explains that the charge density distributions of ^{91,93}Sr isotopes have behaved well, while the charge density distributions of ^{91,93}Sr isotopes have been in an opposite manner due to the presence of a deviation in the center of the nucleus. The nuclear charge distribution and mass density of the ^{91,93}Sr isotopes have not been compared with practical values because they are not currently available.
- The use of the NuShellX@MSU code with glb interaction and gl model space has been suitable for calculating the nuclear properties of ^{91,93}Sr isotopes reported in this study. For ^{91}Sr, the highest value in the experimental energy spectrum is 2.657^{+6}_{-6} MeV for the 1/2 (-) to 5/2 (-) transition, which can be compared to the theoretical prediction of 2.541 MeV for the $5/2_3^+$ state. For ^{93}Sr, the theoretical maximum energy value is 2.389 MeV at the $9/2_2$ state, while the highest observed experimental energy level is 2.456^{+19}_{-19} MeV.

References

[1] Tsunoda, N., Takayanagi, K., Jensen, M.H., and Otsuka, T., Phys. Rev. C, 89 (3) (2014) 02431.

[2] Browne, F., PhD Thesis, University of Brighton, (2016).

[3] Ahalpara, D.P. and Bhatt, K.H., Pramana J. Phys., 6 (1976) 4.

[4] Dickin, A.P., "Radiogenic Isotope Geology", 3rd Ed., (Cambridge University Press, United Kingdom, 2018) p24.

[5] Reddy, E.K., Robinson, R.G., and Mansfield, C.M., J. Natl. Med. Assoc., 78 (1986) 1.

[6] Gloeckner, D.H., Nucl. Phys. A, 253 (1975) 2.

[7] Fotiades, N., Cizewski, J.A., Becker, J.A., Bernstein, L.A., McNabb, D.P., Younes, W.R.X., Clark, W., Fallon, P., Lee, I.Y., Macchiavelli, A.O., Holt, A., and Hjorth, J.M.H., Phys. Rev. C, 65 (2002) 044303.

[8] Wei, L.I.H., Bin, L.U.J., Sheng, L.I.G., Zheng, Y., He, Y.S., Guang, W.X., Ye, H.C., Liang, X.Q., Jian, L.J., Bo, L.C., Peng, H.S., Long, W.J., Heng, W.Y., Wei, L.P., Yan, M.K., Chuan, X., and Jie, S., J. Chin. Phys. C, 38 (7) (2014) 074004.

[9] Li, Z.Q., Wang, S.Y., Niu, C.Y., Qi, B., Wang, S., Sun, D.P., Liu, C., Xu, C.J., Liu, L., Zhang, P., Wu, X.G., Li, G.S., He, C.Y., Zheng, Y., Li, C.B., Yu, B.B., Hu, S.P., Yao, S.H., Cao, X.P., and Wang, J.L., Phys. Rev. C, 94 (2016) 014315.

[10] Wu, Y.H., Yanma, M.K.Y., Cheng, F., and Cai, X.Y, Pramana. J. Phys., 94 (2020) 53.

[11] Sihotra, S., Trivedi, T., Singh, V., Kumar, A., Singh, N., Singh, R.P., Muralithar, S., Kumar, R., Bhowmik, R.K., and Mehta, D., Proc. DAE Symp. Nucl. Phys., 65 (2021).

[12] Obeed, F.H., Jordan J. Phys., 14 (2021) 1.

[13] Brack, M., Damgaard, J., Jensen, A.S., Pauli, H.C., Strutinsky, V.M., and. Wong, C.Y., Rev. Mod. Phys., 44 (1972) 320.

[14] Yoshinaga, N., Yanase, K., Watanabe, C., and Higashiyama, K., Prog. Theor. Exp. Phys., 2021 (2021) 6.

[15] Brussard, P. and Glaudemans, P., "Shell-Model Applications in Nuclear Spectroscopy", (North Holl and Amesterdam, 1977) p452.

[16] Carchidi, M.V., Aldenthal, B.H., and Brown, B.A., Phys. Rev., 34 (1986) 6.

[17] Abood, S.N., Zahra, N.Z.A., and Najam, L.A., J. Rad. Nucl. Appl., 6 (2021) 1.

[18] Gado, K.A., GJMBR-G Interdisciplinary, 14 (2014) 1.

[19] Mantica, P.F., Crawford, H.L., Pinter, J.S., Stoker, J.B., Utsuno, Y., and Weerasiri, R.R., Phys. Lett. B, 662 (2008) 5.

[20] Raman, S., Nestor, C.W., and Tikkanen, Jr.P., At. Data Nucl. Data Tables, 78 (2001) 1.

[21] Brown, B.A. and Rae, W.D.M., Nucl. Data Sheets, 2014 (2014) 1467.

[22] Baglin, C.M., Nucl. Data Sheets, 114 (2013) 1293.

[23] Baglin, C.M., Nucl. Data Sheets, 112 (2011) 1163.

Volume 18, Number 2, 2025. pp. 141-155

Jordan Journal of Physics

ARTICLE

Calculation and Evaluation of the Best Orbit for Satellites Convenience to Transfer to the Geosynchronous Transfer Orbit (GTO)

Marwah Issa Abood Alnidawi and **Abdul-Rahman H. Saleh**

Departments of Astronomy and Space, College of Science, University of Baghdad, Baghdad, Iraq.

Doi: **https://doi.org/10.47011/18.2.4**

Received on: 14/10/2023; *Accepted on: 19/02/2024*

Abstract: This study focuses on optimizing satellite transfers from a low Earth orbit (LEO) to a geosynchronous transfer orbit (GTO) using Ariane 5 rockets. The primary objective is to select the best parking orbit, enhancing the mission stability and cost-effectiveness. Two key goals were identified: improving the initial conditions of parking orbits to reduce fuel consumption and evaluating perturbations affecting satellite trajectories during transfers. The methodology employs a dataset from Ariane 5-launched satellites utilizing MATLAB simulations and the Runge-Kutta method for accurate satellite position and velocity estimations under various perturbations. This research provides a detailed analysis of the propulsion and trajectory dynamics of five satellites, offering insights into orbital mechanics. The key findings include the significant impacts of atmospheric drag, solar radiation pressure, and gravitational effects on satellite trajectories. An inverse relationship was observed between the total velocity change and the fuel mass ratio, suggesting that lower velocity changes result in reduced fuel requirements, thereby improving launch vehicle efficiency and reducing costs. In conclusion, this study affirms the effectiveness of the Hohmann transfer method and underscores the importance of optimal parking orbit selection for successful GTO insertion. This lays the foundation for further research on satellite dynamics and orbital transfers, highlighting the need to manage orbital perturbations for reliable satellite missions.

Keywords: Satellite transfers, Geosynchronous transfer orbit, Hohmann transfer orbits, Ariane 5 rockets, Orbital mechanics, Perturbation analysis, Satellite trajectory.

1. Introduction

The deployment of satellites into the geosynchronous transfer orbit (GTO) is vital for a variety of space missions, encompassing global communications and Earth observation [1, 2]. This study focuses on optimizing satellite transfers from a low Earth orbit (LEO) to a GTO by employing widely used Hohmann transfer orbits [3, 4]. Our aim is to unravel the intricacies of these transfer processes, specifically utilizing the Ariane 5 rockets, renowned for their payload efficiency. This study focuses on the strategic selection of the optimal parking orbit, which is a crucial step that ensures mission stability and extensive coverage. The efficiency of this selection process not only streamlines satellite alignment with target orbits but also enhances the accuracy and cost-effectiveness of the mission [5, 6].

The Ariane 5 launch vehicle, with over 117 successful launches and a remarkable 96 percent success rate, serves as our primary focus [1, 5]. Its consistent performance in deploying satellites to various orbits, including the coveted GTO, has established it as a global benchmark, particularly for communications satellites [7, 8]. This research draws upon a range of studies investigating satellite perturbations, orbital elements, and transitions, thus providing a

Corresponding Author: Marwah Issa Abood Alnidawi **Email**: memaissa6@gmail.com

comprehensive backdrop for our study. Here is a chronological overview of these studies:

In 1993, Mains, conducted research on satellite trajectories, particularly concerning the transfer of satellites from Earth parking orbits. This study is detailed in the thesis titled "Transfer Trajectories from Earth Parking Orbits" [9]. In 2009, Al-Burmani and Aref investigated the impact of atmospheric drag and zonal harmonics on satellite orbits in low Earth orbit (LEO). Their findings emphasized the dominant role of atmospheric drag, resulting in a gradual decrease in orbit altitude over time [52].

In 2011, Wesam calculated satellite orbits while considering various perturbations, highlighting the significant influence of factors such as atmospheric drag and Earth's oblateness on LEO orbits [43]. In 2015, Almohammadi and Mutlag, made substantial contributions by modifying a model for calculating low Earth orbit trajectories [8].

In 2018, Wang and Zhang conducted a study investigating the impact of solar radiation pressure on changes in satellite orbits, providing valuable insights into this phenomenon [18]. Also in 2018, Yosif and Saleh carried out a comprehensive analysis of orbital maneuvers associated with the transition from low Earth orbit to geostationary Earth orbit [21]. Also in 2018, Kim and Lee conducted a thorough investigation into transfers between geosynchronous orbits, with a particular emphasis on the critical role played by atmospheric drag in such maneuvers [10].

In 2019, Chen *et al.* conducted a significant study on geosynchronous orbit transfers. Their research explored various factors affecting satellite paths during orbit transfers, with specific attention to perturbations in the process [16]. In the same year, Ibrahim and Saleh revisited Kepler's equation for elliptical orbits, presenting innovative solution methods and contributing to the advancement of this field [12].

In 2020, Farid, Abdul-Rahman, and Majeed explored methods for orbital transitions between two elliptical Earth orbits, emphasizing the importance of initial conditions and accounting for satellite mechanical anomalies [11]. Also in 2020, Rasha and Abdul-Rahman dedicated their research efforts to improving the accuracy of perturbed orbital elements for LEO satellites. Their work focused on enhancing the application of the fourth-order Runge–Kutta method [13]

This study is focused on the optimization of satellite transfers from low Earth orbit (LEO) to geosynchronous transfer orbit (GTO) through the utilization of Ariane 5 rockets. Particular emphasis is placed on selecting the optimal parking orbit and implementing MATLAB simulations, combined with the Runge-Kutta method, to estimate satellite positions and velocities under various perturbations.

A notable finding is the identification of an inverse relationship between total velocity change and the fuel mass ratio. This relationship suggests that minimizing velocity changes can enhance launch vehicle efficiency and reduce mission costs.

In comparison to prior research, this study distinguishes itself by its concentrated approach to parking orbit selection and its extensive utilization of numerical simulations, shedding light on a deeper understanding of satellite transfer processes. This research serves as a unique contribution to the field of satellite dynamics and orbital transfers.

2. Objective of the Study

This research is structured around two primary objectives. The first is to enhance the initial conditions of parking orbits, thereby reducing fuel consumption during transfer missions by ascertaining the efficacy of Hohmann transfer orbits from LEO to GTO. The second objective involves a thorough evaluation of the various perturbations affecting satellite trajectories during these transfers. This includes an examination of factors such as atmospheric drag, solar radiation pressure, gravitational effects, and magnetic field influences, all of which play pivotal roles in the trajectory of a satellite.

3. Data and Methodology

Our dataset comprises data archives from satellites launched via Ariane 5 rockets to the GTO [5]. These data, sourced from the official Ariane 5 website, form the empirical basis of this study. The methodology centers on the use of the parking orbit, which has been extensively documented in the context of the Hohmann transfer method, particularly in relation to co-axial elliptical orbits [14-16].

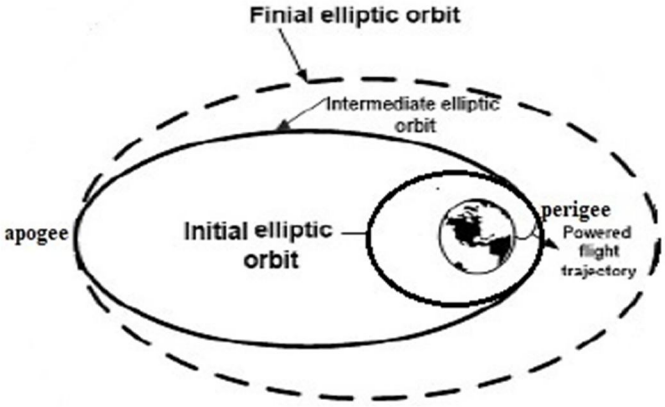

FIG. 1. Trajectory from parking orbit to geosynchronous transfer orbit (GTO) [14, 17].

To illustrate the concept of trajectory transfer from the parking orbit to the geosynchronous transfer orbit (GTO), Fig. 1 presents a visual representation. This figure depicts the path a satellite follows when transitioning from its initial parking orbit to its final GTO, showing the complexity and precision required in such maneuvers [18, 19].

Because celestial dynamics is a labyrinthine field, we implemented a MATLAB algorithm for an in-depth analysis of orbits from a heliocentric inertial reference frame (Appendix A). This code meticulously evaluates satellite movements, simulating the trajectory from the parking orbit to the GTO, as depicted in Fig. 1. Initial calculations focused on orbital elements in the absence of perturbation forces, followed by the inclusion of perturbing factors, such as Earth's oblateness, solar and lunar gravity, and solar radiation pressure. Utilizing the Runge-Kutta method allowed us to integrate motion equations, yielding precise estimations of the satellite positions and velocities at each step. This method is pivotal in determining the perturbed orbital elements, thereby delineating the satellite's ultimate trajectory (Appendix A).

3.1. Hohmann Transfers the Method between Coaxial Elliptical Orbits

The Hohmann transfer method is an efficient technique for transitioning spacecraft between two elliptical orbits, as shown in Fig. 2 [20]. This approach is instrumental in saving fuel and energy, thereby enhancing the cost-effectiveness and time-efficiency of space missions [21].

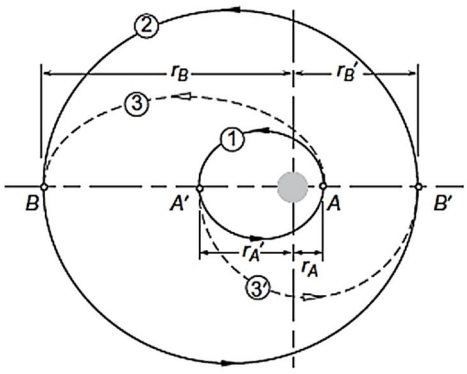

FIG. 2. Illustration of Hohmann Transfers between Coaxial Elliptical Orbits [20].

- Fundamental Equations:

The primary orbital parameter, represented by a, is the semi-major axis of an ellipse or the average satellite distance from the center of an elliptical orbit, calculated as

$$a = (r_p + r_a)/2 \quad (1)$$

where r_p and r_a are the perigee and apogee distances, respectively. This parameter is pivotal in determining the trajectory of a satellite [22].

- Velocity Calculations for Orbital Transitions:

To facilitate successful orbital transitions to GTO, we calculated the necessary velocity changes at different orbit stages [23]:

For initial orbit:

$$V_{p1} = \sqrt{\mu\left(\frac{2}{r_{p1}} - \frac{1}{a}\right)} \quad (2)$$

$$V_{a1} = \sqrt{\mu(\frac{2}{r_{a1}} - \frac{1}{a})} \quad (3)$$

For intermediate orbit:

$$V_{p2} = \sqrt{\mu(\frac{2}{r_{p2}} - \frac{1}{a})} \quad (4)$$

$$V_{a2} = \sqrt{\mu(\frac{2}{r_{a2}} - \frac{1}{a})} \quad (5)$$

For final orbit:

$$V_{p3} = \sqrt{\mu(\frac{2}{r_{p3}} - \frac{1}{a})} \quad (6)$$

$$V_{a3} = \sqrt{\mu(\frac{2}{r_{a3}} - \frac{1}{a})} \quad (7)$$

Here, V_p and V_a denote velocities at the perigee and apogee, respectively, and μ represents the standard gravitational parameter (μ: G Me = 398602.4415 at r in km) [23].

$$\Delta V1 = Vp2 - Vp1$$

$$\Delta V2 = Va3 - Va2 \quad (8)$$

$$\Delta Vtotal = \Delta V1 + \Delta V2$$

The total velocity change for orbital transfer (ΔVtotal) is the sum of the changes at the perigee (ΔV1) and apogee (ΔV2), as outlined in Eqs. (8)-(10). These calculations are critical for precise maneuvering and fuel efficiency [23].

- *Considerations for Launch Location:*

Launching from Kourou in French Guyana near the equator eliminates the need for inclination changes during the transfer. However, launches from other locations require calculating the rotational velocity change (ΔV_{rot}) to account for orbital inclination adjustments [24, 25]:

$$\Delta V_{rot} = \sqrt{{V_{a2}}^2 + {V_{a3}}^2 - 2{V_{a2}}^2{V_{a3}}^2\cos(\Delta i)} \quad (9)$$

where Δi is the orbital inclination change.

So:

$$\Delta V_{total} = \Delta V_1 + \Delta V_2 + \Delta V_{rot} \quad (10)$$

Equations (2)-(10) lay the groundwork for determining the essential velocities and changes required for effective orbital transfers, highlighting the importance of launch location and trajectory planning in space missions [26].

3.2. Satellite Motion Analysis under Perturbations:

Satellite motion in the presence of perturbations can be studied using two primary methods: special and general. This research utilizes Cowell's method, a specific type of special perturbation known for its simplicity and effectiveness. Cowell's method employs two first-order differential equations to analyze the trajectory of a satellite [27-29]:

$$\dot{\mathbf{r}} = v$$

This equation represents the rate of change of the satellite's position vector, r, where v is the velocity vector [30].

$$\dot{\mathbf{v}} = -\frac{\mu}{r^3}\mathbf{r} + \mathbf{a_p} \quad (11)$$

Here, μ is Earth's gravitational constant, and a_p denotes the sum of perturbing accelerations affecting the satellite's orbit [31].

The perturbing accelerations (a_p) encompass several components [30, 31]:

$$\mathbf{a_p} = \mathbf{a_{J2}} + \mathbf{a_{drag}} + \mathbf{a_{SPR}} + \ddot{r}_l \quad (12)$$

where:

a_{J2}: geopotential acceleration due to Earth's oblateness,

a_{drag}: acceleration due to atmospheric drag,

a_{SPR}: solar radiation pressure acceleration, and

$\ddot{r}_l$: third-body gravity acceleration, representing the gravitational influence of celestial bodies other than Earth.

Equation (12) forms the core of our analysis, allowing us to understand the complex dynamics of the satellite motion under various perturbative forces. Detailed discussions and transactions of this method are thoroughly covered in the literature [6, 31].

3.2.1. Atmospheric Drag

The acceleration due to atmospheric drag (a_{drag}) is expressed as [32]:

$$\mathbf{a_{drag}} = -\frac{1}{2}\rho\,\frac{C_D A}{m}v^2\mathbf{i}_v \quad (13)$$

where ρ represents the atmospheric density, CD is the drag coefficient, A is the satellite's cross-sectional area perpendicular to the velocity vector, m is the mass of the satellite, v is the velocity of the satellite relative to the atmosphere, and iv is a unit vector in the direction of the satellite velocity. A negative sign

indicates that the acceleration direction is opposite to the velocity [33].

3.2.2. Non-spherical Gravitational Field of the Earth

The perturbative acceleration due to the Earth's non-spherical gravitational field is determined by factors including the Earth's radius (R_e) and the satellite's position components (x, y, z) [34-37]:

$$\mathbf{a}_{J_2} = \frac{-3\mu R_e^{\,2} J_2}{2r^7}\begin{bmatrix} x\left(x^2+y^2-4z^2\right) \\ y\left(x^2+y^2-4z^2\right) \\ z\left(3x^2+3y^2-2z^2\right) \end{bmatrix} \quad (14)$$

3.2.3. Third-Body Attractions

Third-body attractions refer to the gravitational impact of celestial bodies other than the Earth, such as the Moon. These forces lead to periodic and long-term fluctuations in various orbital elements. For instance, the gravitational influence of the Moon results in additional perturbations to the motion of the satellite [34, 38, 39].

$$\ddot{r} = -\frac{GM}{r^3}\vec{r} + GM_l\left(\frac{\vec{r}_{satl}}{{r_{satl}}^3} - \frac{\vec{r}_l}{{r_l}^3}\right) \quad (15)$$

The first term is due to the acceleration caused by Earth (central term). The additional perturbation acceleration caused by the gravitational attraction of the Moon acting on the satellite is then [40-43]:

$$\ddot{r}_l = GM_l\left(\frac{\vec{r}_l - \vec{r}}{|r_l - r|^3} - \frac{\vec{r}_l}{{r_l}^3}\right) \quad (16)$$

3.2.4. Solar Radiation Pressure Perturbation (SRP)

The acceleration from solar radiation pressure occurs when the Moon passes through a constellation; due to gravitational lensing and radiation from the constellation, more cosmic radiation is bent. This bent radiation impinges deep inside the atmosphere of the Earth, which produces more secondary gamma-radiation particles. For the Earth–to–GTO transfer, a_{SPR} is given by [44-47]:

$$a_{SPR} = \mu P_s C_R \frac{A}{m} \quad (17)$$

where C_R is the reflectivity coefficient, A is the satellite's cross-sectional area, m is the mass of the satellite, μ is a function of shadow (1 in full sunlight, 0 in umbra, and between 0-1 in penumbra), and P_s is the solar radiation pressure. The equation ($\frac{E}{C}$) accounts for the solar radiation constant E (1358 w/m²) and the speed of light in vacuum c [48-52].

4. Results and Discussion

In a comprehensive evaluation of the propulsion and trajectory parameters for five satellites launched by Ariane 5: NILESAT 201, JCSAT-12, ARABSAT 5A, WILDBLUE-1, and W3B (detailed in Tables 1 and 2), we discern the nuances of their journey from low Earth orbit (LEO) to geosynchronous transfer orbit (GTO). This transition, executed via the Hohmann transfer method, is a two-stage propulsion process that entails an initial velocity increase at the perigee (ΔV1) to extend the orbit and a subsequent burn at the apogee (ΔV2) to circularize at the GTO.

Table 1 shows the initial and final orbital elements for each satellite, such as the perigee and apogee altitudes, semi-major axis, eccentricity, and time for half an orbit (t = T/2). These figures indicate the energy requirements for transfer, with the semi-major axis and eccentricity dictating the orbit's size and shape, respectively, and consequently, the satellite's total orbital energy.

Table 2 sheds light on critical velocity parameters, such as perigee and apogee velocities pre- and post-burn, and the total required velocity change (ΔV_{Total}). The ΔV_{Total} is a direct indicator of the mission's propellant budget, with lower values signifying more fuel-efficient transfers, thereby impacting the economic and operational aspects of the mission.

The data suggest that the transfer efficiency of each satellite varies and is influenced by its mass, initial orbit, and specific perturbations encountered, such as gravitational variations, atmospheric drag, and solar radiation pressure. These perturbations require precise velocity adjustments to maintain the desired trajectory.

A key finding is the inverse relationship between the total velocity change (ΔV_{Total}) and fuel mass ratio (Δm/m1). A lower ΔV_{Total} corresponds to a reduced need for fuel, improved launch vehicle performance, and decreased launch costs. Such optimization is essential for mission success and hinges on the strategic planning of orbital transfer, considering the unique characteristics of each satellite and the trade-offs between velocity changes, fuel

consumption, and operational requirements in GTO.

Collectively, the insights from Tables 1 and 2 provide a scientific foundation for determining the preliminary conditions for future satellite launches. This integrated analysis enables the design and execution of fuel-efficient and cost-effective orbital maneuvers, ensuring that satellites are inserted into their intended orbits with adequate fuel reserves for their operational lifespans. Moreover, it sets a precedent for future mission planning and launch strategy refinement.

TABLE 1. The five most efficiently transferred satellites launched by Ariane 5 using the Hohmann transfer method between coaxial elliptical orbits.

	Flights	Perigee Altitude (km)	r Perigee (km)	apogee Altitude (km)	r apogee (km)	Semi-major axis (km)	Eccentricity (e)	Time (Sec)	t = T/2 (Sec)
1	The NILESAT 201	259.2	6637.337	500	6878.1370	6757.7369	0.0178166	5528.5507112	2764.2753556
2	The JCSAT-12	219.7	6597.8369	500	6878.1370	6737.987	0.0207999	5504.3320136	2752.1660068
3	The ARABSAT 5A	210.7	6588.837	500	6878.1370	6733.4869	0.0214821	5498.8187888	2749.4093944
4	The WILDBLUE-1	231.8	6609.937	500	6878.1370	6744.037	0.0198842	5511.7471398	2755.8735699
5	The W3B	213.2	6591.3369	500	6878.1370	6734.7369	0.0212925	5500.3500554	2750.1750277

TABLE 2. Delta-V and change of fuel mass for the five best-transferred satellites.

	Flights	Vp_1 (km/sec)	Vp_2 (km/sec)	ΔV_1 (km/sec)	Va_2 (km/sec)	Vf_2 (km/sec)	ΔV_2 (km/sec)	ΔV_{Total} (km/sec)	$\Delta m/m_1$
1	The NILESAT 201	7.81822802	10.1891178	2.3708898475	1.59889330	1.597935	-0.0009582775	2.369931569	0.4290
2	The JCSAT-12	7.85308024	10.2215245	2.3684442800	1.59946242	1.602633	0.00317064053	2.371614920	0.4293
3	The ARABSAT 5A	7.86106732	10.2294472	2.3683799147	1.59851867	1.602633	0.00411438673	2.372494301	0.4294
4	The WILDBLUE-1	7.84236909	10.2135307	2.3711616074	1.59505200	1.596949	0.00189748043	2.373059087	0.4295
5	The W3B	7.85884696	10.2293215	2.3704745898	1.59430345	1.598146	0.00384292184	2.374317511	0.4296

Our assessment of the orbit of the NILESAT 201 satellite revealed distinct variations between the theoretical model and the actual path with perturbations. The idealized trajectory, illustrated in Fig. 3(a), was established with the initial parameters: a semi-major axis of 6757.74 km, an inclination of 2°, an eccentricity of 0.0178166, a longitude of the ascending node at 0°, and an argument of perigee at 178°. This scenario assumes an undisturbed orbit, providing a controlled baseline for our analysis.

Upon introducing perturbative forces, as shown in Fig. 3(b), the satellite trajectory demonstrated notable deviations. We attribute these variations to several predominant forces: atmospheric drag, solar radiation pressure, gravitational influences from celestial bodies, and geomagnetic field interactions.

Specifically, the atmospheric drag exerted a substantial impact, inducing a quasi-linear decrease in the semi-major axis. This decay reflects progressive orbital degradation due to atmospheric resistance, which is particularly significant at the perigee where the atmospheric density is higher. Concurrently, there was a linear increment in the perigee's argument, suggesting a gradual shift in the orientation of the orbit.

In addition to drag, the orbit inclination underwent alterations that manifested as a combination of linear and secular trends. This pattern suggests an interplay between the direct atmospheric drag effects at lower altitudes and the more gradual, long-term influences of third-body gravitational interactions. The lunar

gravitational pull was evidenced by secular changes in both the longitude of the ascending node and the true anomaly, underscoring the Moon's proximity and its significant perturbative effect compared to the more distant Sun.

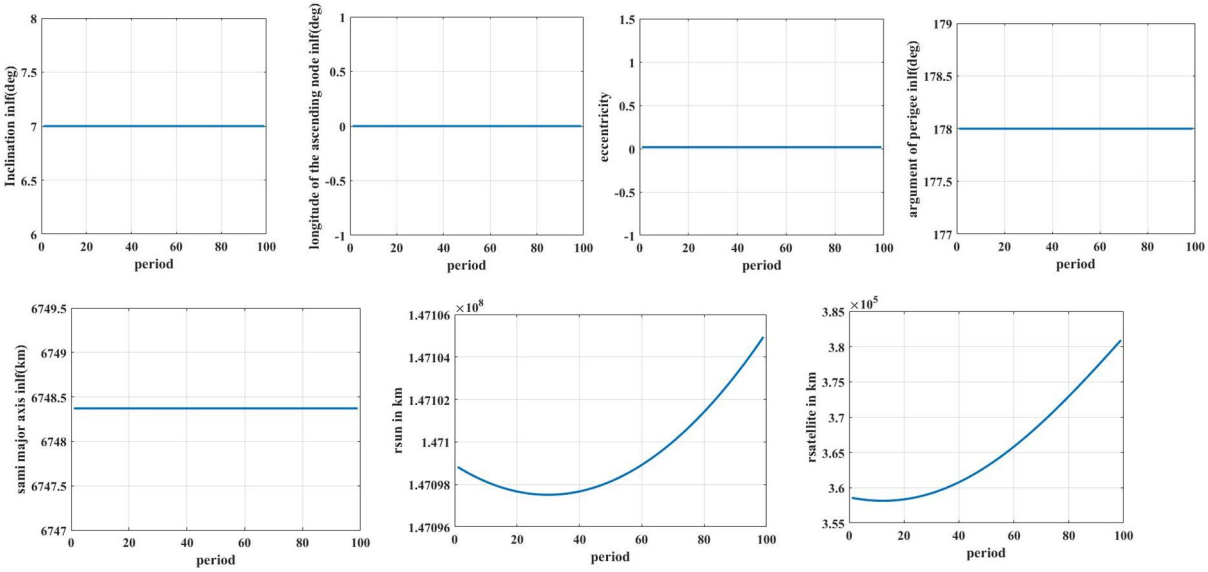

FIG. 3(a). Changes in orbital elements before the perturbation effects for the parking orbit of satellite NILESAT 201.

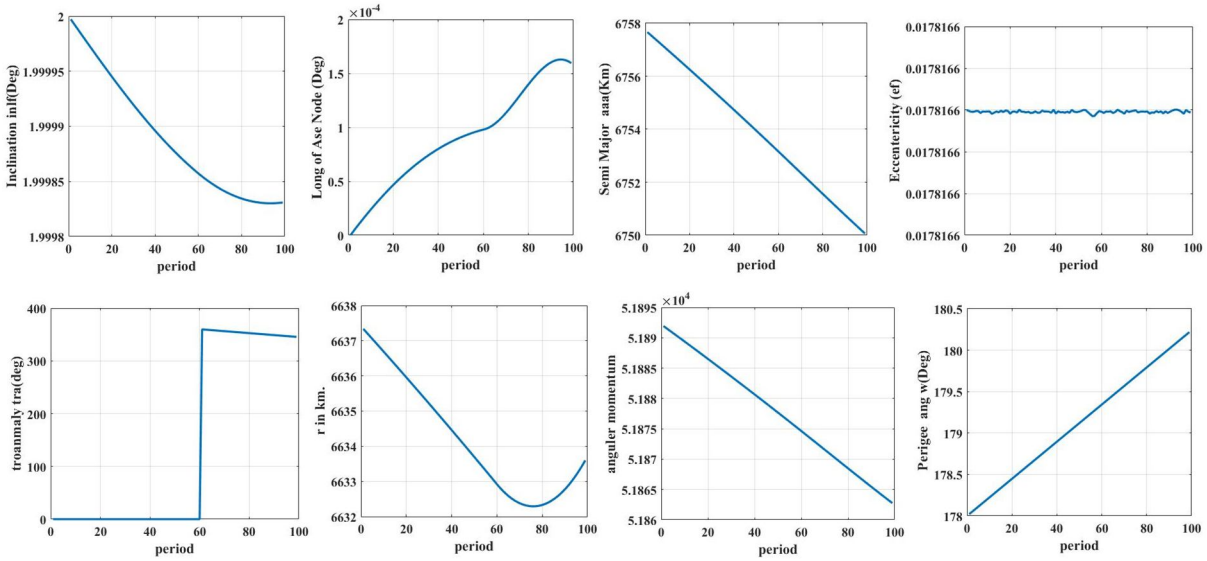

FIG. 3(b). Changes in orbital elements after perturbation effects for the parking orbit of satellite NILESAT 201.

Eccentricity remains largely consistent over time, which points to a minimal impact from orbital perturbations. This stability could be attributed to the satellite being located in a "sweet spot", where the gravitational influences of the Earth, Moon, and Sun largely cancel out, leading to a naturally stable orbit.

In summary, the perturbed orbit of NILESAT 201 presents a complex dynamical system that is influenced by a combination of deterministic and stochastic forces. Understanding these effects is paramount for effective station-keeping strategies, ensuring the longevity and reliability of the satellite's communication services. Future work will focus on quantifying the fuel budget for corrective maneuvers and optimizing the satellite's response to these perturbative forces.

The graphical representation of JCSAT-12's orbital parameters in Figs. 4(a) and 4(b) illustrates the stark contrast between an unperturbed orbit and on affected by various perturbative forces. In the ideal state shown in Fig. 4(a), the semi-major axis, inclination, eccentricity, longitude of the ascending node, and argument of perigee are presented with values of 6737.99 km, 2, 0.0207999, 0°, and 178°, respectively. These figures indicate a geostationary transfer orbit and are expected to

remain constant over time in the absence of external influences.

Under the perturbed conditions shown in Fig. 4(b), the trajectory of JCSAT-12 deviates from the ideal trajectory. The semi-major axis shows a decreasing trend, commonly associated with the atmospheric drag encountered by satellites at lower altitudes. The inclination exhibits both linear and secular behavior, suggesting the combined effects of atmospheric drag, which impacts the orbit immediately, and the more gradual influence of third-body attractions such as the gravitational pull of the Moon or Sun. The argument of the perigee's steady increase is typically linked to atmospheric drag effects, which are most pronounced at the orbit's closest approach to the Earth.

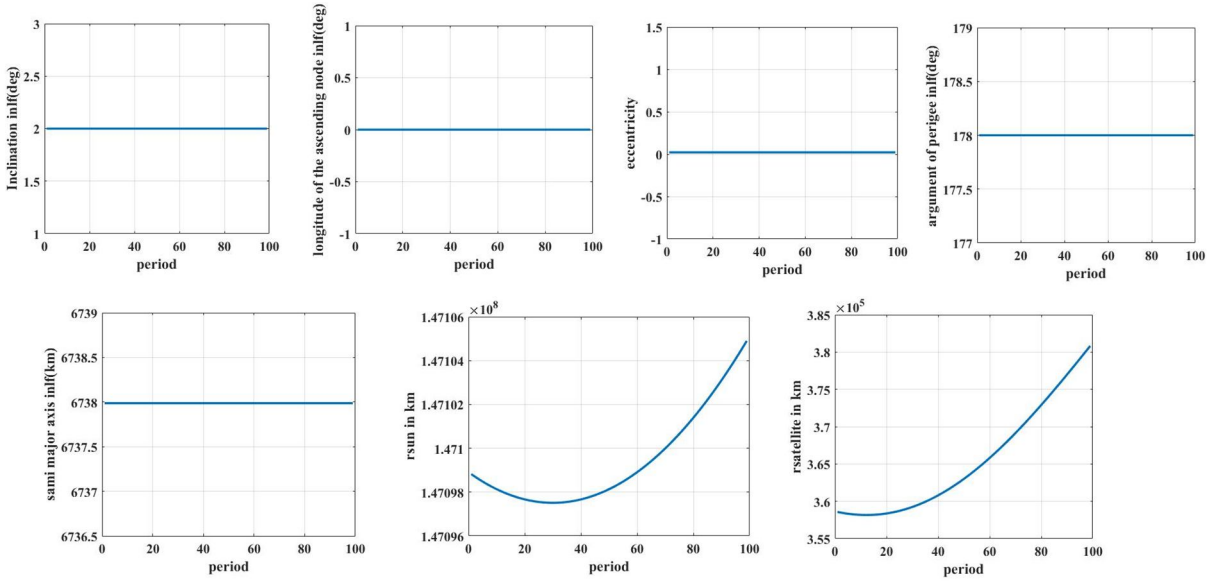

FIG. 4(a). Orbital elements' changes before the perturbations' effects for the parking orbit of satellite JCSAT-12

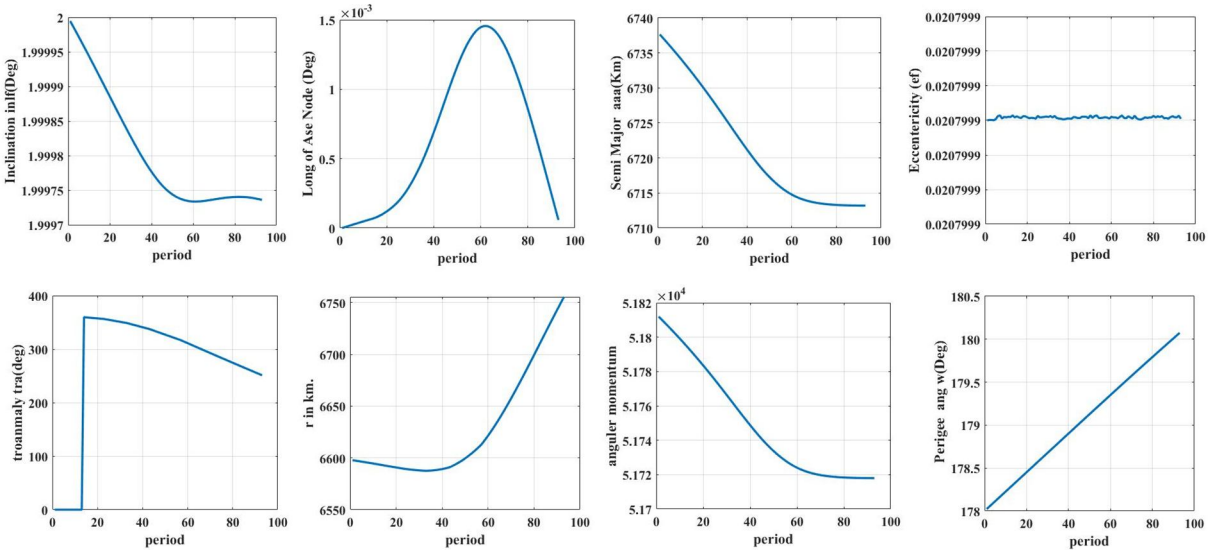

FIG. 4(b). Orbital elements' changes after the perturbations' effects for the parking orbit of satellite JCSAT-12.

Additionally, the longitude of the ascending node displays a mixture of secular drift and periodic variations. The secular drift can be attributed to Earth's oblateness, while the periodic component is likely due to the gravitational effects of the Moon and Sun, which are known to cause regression or progression of the node. Eccentricity exhibits remarkable consistency throughout the observed period, suggesting that the orbital perturbations have a negligible effect. The maintained stability implies a geostationary trajectory where disruptive forces may not significantly alter the orbit.

These variations in orbital parameters are critical for satellite operation because they

require precise station-keeping maneuvers to counteract these natural forces and maintain the satellite's desired geostationary orbit for reliable communication.

When examining the trajectory of the ARABSAT 5A satellite, we observed distinct behaviors under ideal and perturbed conditions. Fig. 5(a) outlines the initial, unperturbed orbit with the semi-major axis at 6733.49 km, inclination at 2 degrees, eccentricity at 0.0214821, right ascension of the ascending node at 0 degrees, and argument of perigee at 178 degrees. These values represent a controlled scenario without external perturbing influences, providing a reference for the designed path of the satellite.

According to Fig. 5(b), the introduction of perturbations significantly alters the trajectory of the satellite. The semi-major axis and inclination demonstrate not only a direct, linear response to atmospheric drag but also a secular trend over time, indicative of the sustained influence of third-body gravitational forces, such as those from the Moon and possibly the Sun. The argument of the perigee's linear increase further corroborates the impact of atmospheric drag, particularly at the point of the satellite's orbit closest to the Earth. The secular change in the true anomaly points to a steady alteration in the satellite's position within its orbit over time, primarily influenced by the gravitational pull of celestial bodies.

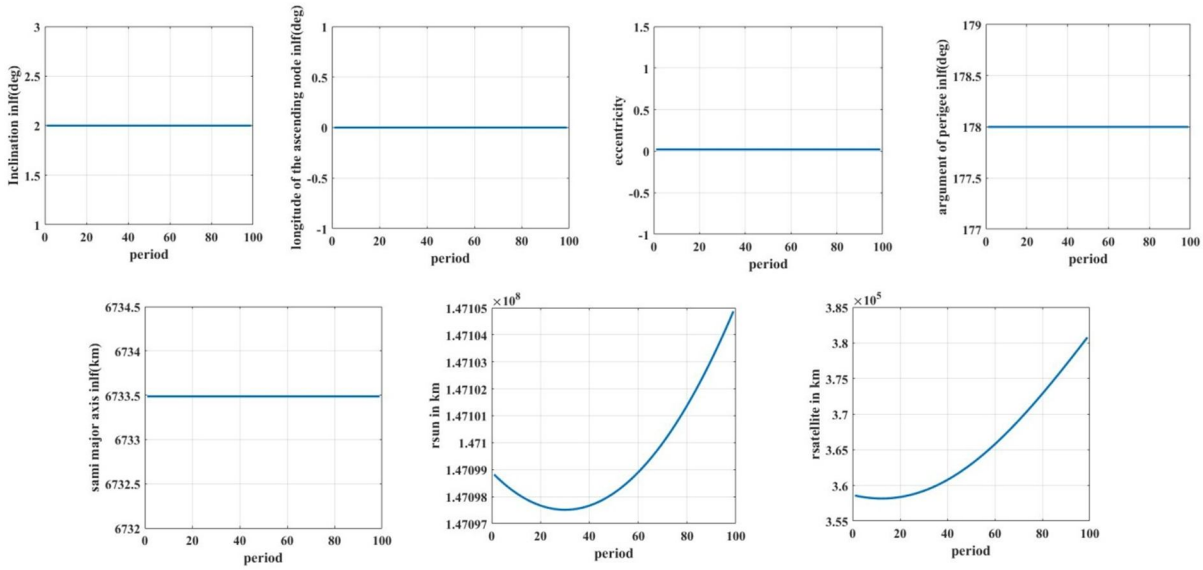

FIG. 5(a). Orbital elements' changes before the perturbations' effects for the parking orbit of satellite ARABSAT 5A.

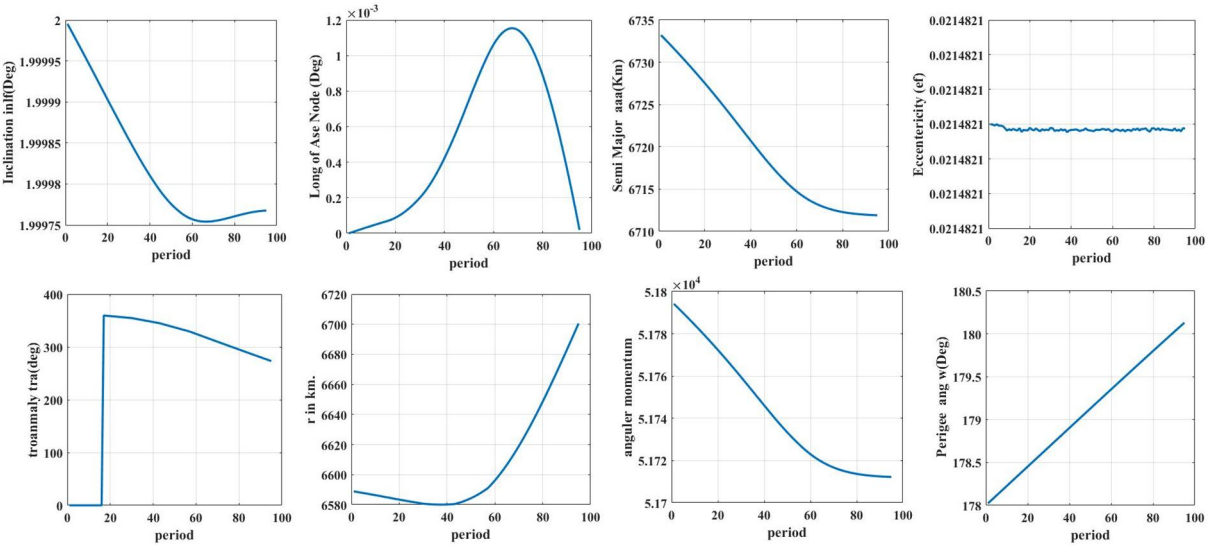

FIG. 5(b). Orbital elements' changes after the perturbations' effects for the parking orbit of satellite ARABSAT 5A.

Moreover, the right ascension of the ascending node's behavior reveals both secular drift and minor periodic fluctuations, a signature of the Earth's oblate shape affecting the orientation of the orbital plane. Finally, eccentricity demonstrates significant stability over time, indicating that the satellite's orbit is minimally affected by external perturbations. This consistent pattern suggests an equilibrium in the orbital path, where perturbative forces, such as atmospheric drag, Earth's non-uniform gravitational field, and third-body effects, do not substantially disrupt the satellite's trajectory.

These findings underscore the complex dynamical environment of orbital mechanics, necessitating continuous monitoring and adjustment to maintain ARABSAT 5A's intended orbit, ensuring its operational longevity and consistent delivery of satellite services.

The trajectory of the WILDBLUE-1 satellite, represented in Fig. 6(a), establishes a baseline for its orbital elements in an unperturbed state with a semi-major axis at 6744.04 km, inclination at 2°, eccentricity at 0.0198842, right ascension of the ascending node at 0°, and the argument of perigee at 178°. These values depict the expected path of the satellite in an idealized scenario, without the influence of external forces.

When we incorporate the dynamics of perturbations, the trajectory is significantly altered, as shown in Fig. 6(b). The forces at play include atmospheric drag, gravitational pull from third bodies such as the Moon and the Sun, and geopotential variations due to the Earth's non-spherical shape. Atmospheric drag is particularly impactful, reducing the velocity of the satellite and causing a decrease in the semi-major axis, which manifests as a secular decrease over time. This drag also influences the inclination, leading to a slow regression over time.

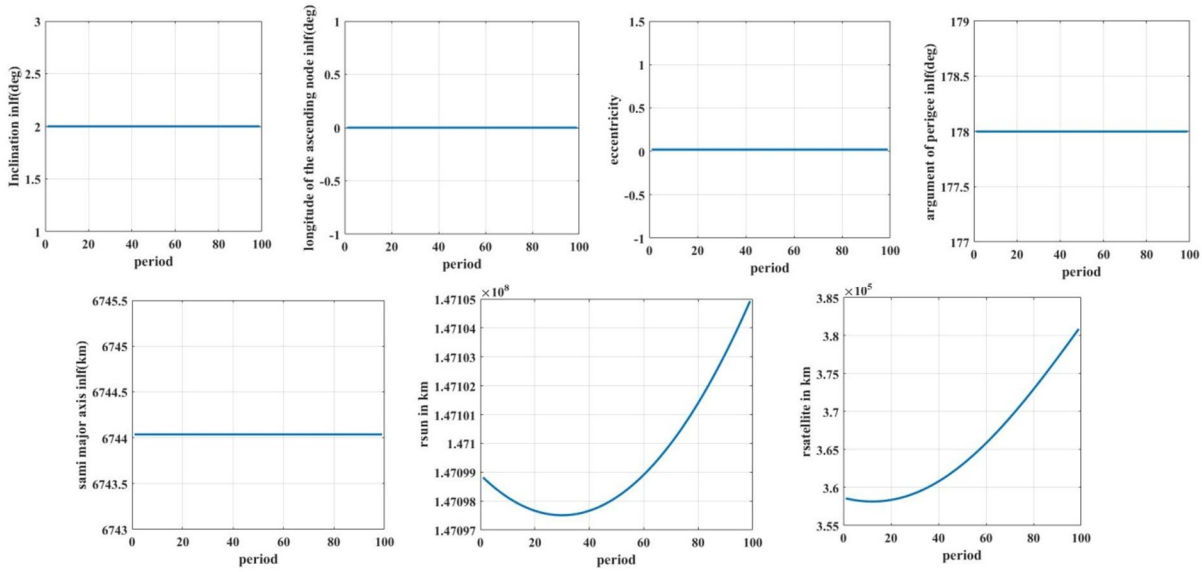

FIG. 6(a). Orbital elements' changes before the perturbations' effects for the parking orbit of satellite WILDBLUE-1.

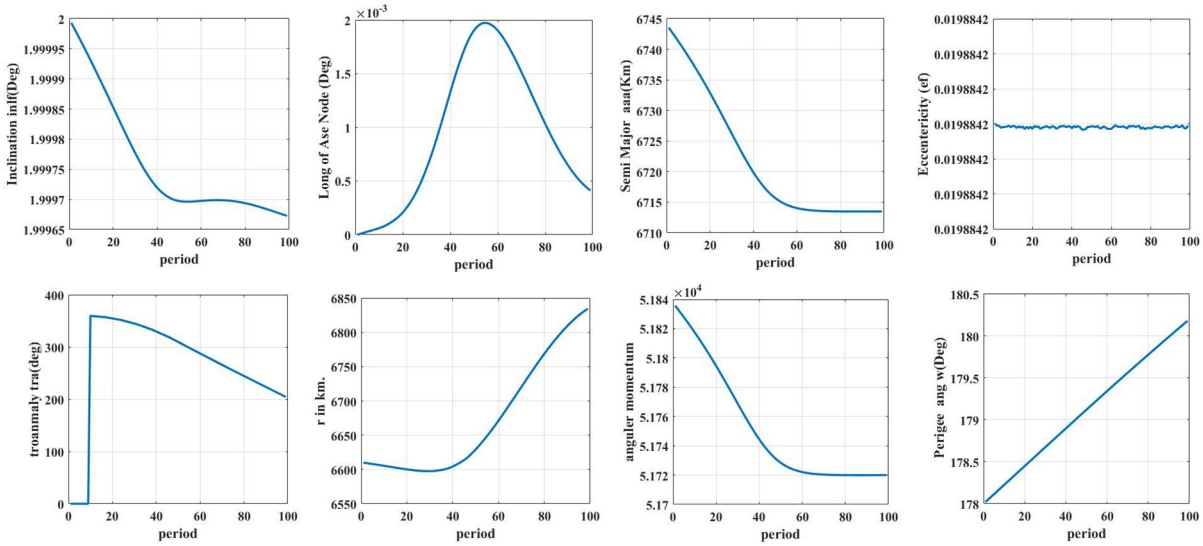

FIG. 6(b). Orbital elements' changes after the perturbations' effects for the parking orbit of satellite WILDBLUE-1.

The argument of perigee rises owing to atmospheric drag, indicating a gradual shift in the orientation of the orbit within its plane. This is a consequence of the differential drag experienced at various points in the orbit, especially at the perigee, where the atmosphere is denser. The periodic variation of the true anomaly, influenced by third-body attractions, shows that the Moon's gravitational pull alters the satellite's position within its orbit.

The longitude of the ascending node's behavior, with its mix of secular and periodic changes, signifies Earth's oblateness effect. This oblateness causes the precession of the orbital plane, which can be observed over an extended period. Eccentricity displays a persistent uniformity over the observed timeframe, implying that the influence of common orbital disturbances is limited. The steadiness of this orbital element suggests a resilient trajectory against perturbative forces.

In operational terms, these perturbations require regular orbital adjustments to maintain WILDBLUE-1's intended path for optimal service provision. The satellite controllers must constantly monitor these parameters and execute station-keeping maneuvers to counteract the perturbative effects, ensuring the longevity of the satellite and the continuity of its communication capabilities.

The figures for the W3B satellite present two distinct scenarios: an ideal trajectory without perturbations and one that includes the complex effects of various perturbative forces.

Figure 7(a) illustrates the initial, ideal state of W3B's orbit with parameters set at a semi-major axis of 6734.74 km, an inclination of 2°, an eccentricity of 0.0212925, a longitude of the ascending node at 0°, and an argument of perigee at 178°. These parameters define the expected orbit in a controlled environment without external influence.

Figure 7(b) depicts how this trajectory evolves under the influence of perturbations. Atmospheric drag, a result of the satellite's interaction with the Earth's atmosphere, impacts the satellite's motion, causing a decrease in both the altitude and semi-major axis over time. This effect is evidenced by the decreasing trend in the semi-major axis and is indicative of orbital decay common to satellites, particularly at lower altitudes where the atmosphere is denser.

The gravitational pull from other celestial bodies, specifically the Moon and Sun, introduces additional forces that alter the satellite's inclination and true anomaly. These changes manifest as secular variations in the orbit tilt and position, demonstrating the far-reaching influence of these third-body attractions.

Owing to its equatorial bulge and mass distribution, the non-spherical nature of the Earth's gravitational field exerts additional complexity on the motion of satellites. This uneven gravitational field leads to the precession of the orbit, as seen in the periodic and secular changes in the longitude of the ascending node and the argument of the perigee.

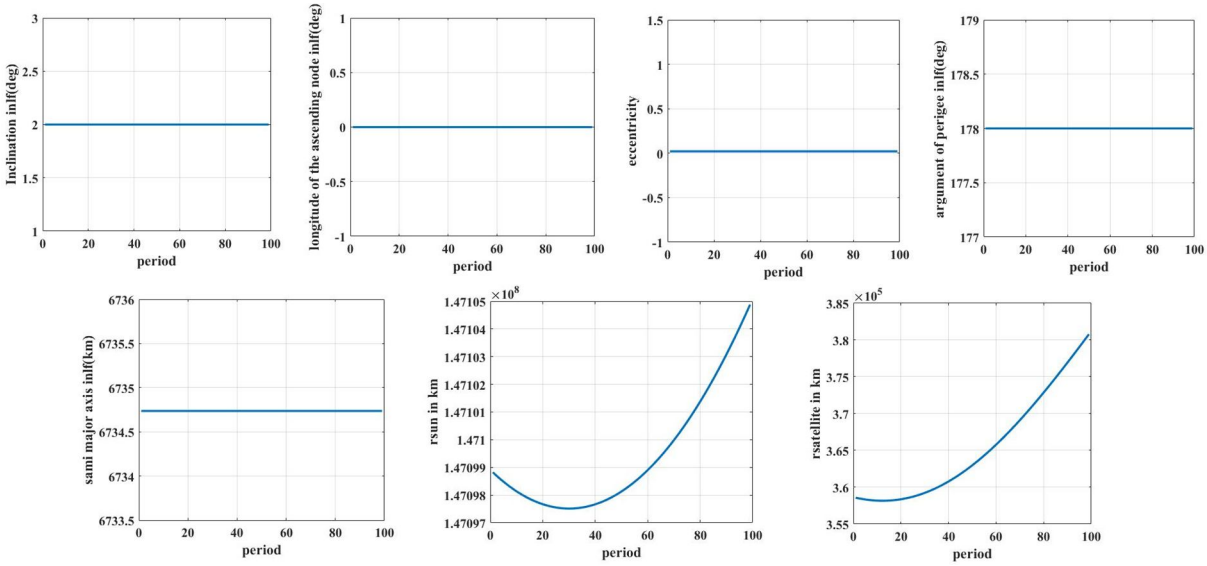

FIG. 7(a). Orbital elements' changes before the perturbations' effects for the parking orbit of satellite W3B.

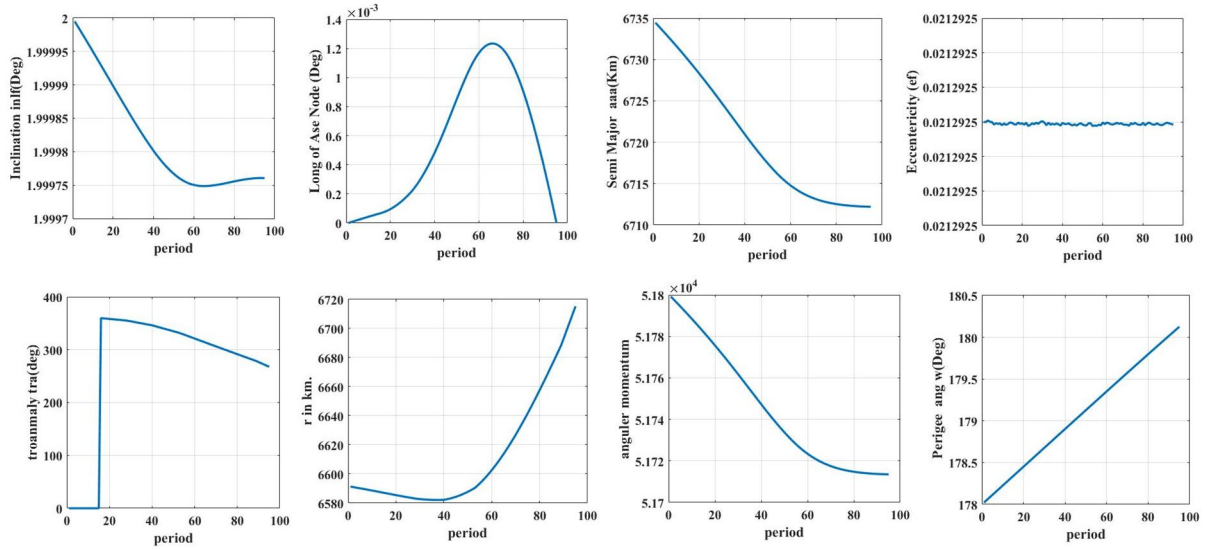

FIG. 7(b). Orbital elements' changes after perturbations' effects for the parking orbit of satellite W3B.

The perturbations did not influence eccentricity; the satellite maintained remarkable stability in this parameter, suggesting an orbit relatively unaffected by typical orbital disturbances.

This analysis underscores the need for continuous adjustment and control of the satellite's orbit. To counteract these perturbations and maintain the intended path of the satellite, regular station-keeping maneuvers are essential. These adjustments are crucial for the operational efficiency and reliability of satellite services.

Our study meticulously analyzed the propulsion and trajectory dynamics of five satellites: NILESAT 201, JCSAT-12, ARABSAT 5A, WILDBLUE-1, and W3B, as they transitioned from a low Earth orbit (LEO) to a geosynchronous transfer orbit (GTO) using the Hohmann transfer method. The efficacy of this technique was exemplified by the satellites' perigee and apogee heights, which were aligned with the desired calculated values, confirming their ability to maintain a stable position in the geosynchronous orbit. The high degree of agreement between our projections and actual outcomes emphasizes the pivotal role of precise transfer methods in conducting cost-effective satellite transport operations.

Perturbations, particularly atmospheric drag, have a significant influence on the trajectories of satellites, leading to a reduction in the semi-major axis and inclination, and signifying the impact on orbital decay. The gravitational pull from the Moon introduces additional complexity, causing periodic and secular changes in the

inclination and true anomalies of the satellites. Moreover, Earth's non-spherical gravitational field contributes to orbital precession, highlighting the intricacies of managing satellite trajectories.

The post-perturbation trajectory of each satellite, while commencing from comparable initial conditions, diverged owing to slight yet impactful differences in mass distribution, structural design, and size. This divergence necessitated a closer look at individual satellite responses, revealing nuanced reactions to varied perturbative forces.

In summary, the consolidated findings from our research deepen the understanding of satellite orbital mechanics, proving invaluable for precise crafting of satellite trajectories. This enhanced understanding is essential for mission planners to accurately steer satellites to their designated orbits, optimize their operational efficacy, and ensure the longevity of the service. Our study's insights equip mission designers with the foresight to anticipate and counteract perturbations, culminating in more dependable and successful satellite missions.

5. Conclusions

1. Efficiency of the Hohmann Transfer method: Our research confirms the Hohmann transfer method, which utilizes coaxial elliptical orbits, as a highly effective technique employed by Ariane 5 for satellite transfers. This method has demonstrated reliability in multiple satellite launches, reinforcing its value in space mission planning.
2. Optimization of parking orbit parameters: Through detailed analysis, we identified the optimal parameters for the parking orbit, which is a critical aspect of transitioning to the geosynchronous transfer orbit (GTO). Our findings suggest that initiating the transfer from an orbit altitude of 259.2 kilometers with a velocity of 7.81822802 kilometers/second, coupled with precise semi-major axis, eccentricity, inclination, argument of perigee, and longitude of ascending node values, is essential for efficient and accurate impulsive maneuvers into GTO.
3. Importance of revolutions in low orbit:

   For a successful impulsive maneuver into the GTO, it is essential that satellites complete a minimum of 50 revolutions in their parking orbit. This precondition is vital for achieving the desired orbital alignment and energy requirement for GTO insertion.
4. Perturbation analysis and management:

   Our comprehensive examination of various perturbations, including atmospheric drag, solar radiation pressure, gravitational effects, and magnetic field influences, sheds light on their impact on satellite trajectories. For satellites such as NILESAT 201, JCSAT-12, ARABSAT 5A, WILDBLUE-1, and W3B, these perturbations were significant but could be quantified and managed effectively. This management ensures the preservation of the trajectory integrity of these satellites.
5. Foundational research for future exploration: This study not only provides immediate insights into satellite dynamics and orbital transfers but also establishes a foundation for future research in this field. Understanding and managing the complex interplay between orbital perturbations is crucial for the advancement of satellite technology and strategic mission planning, particularly in the evolving landscape of space exploration.

Funding Statement

No funding was received for conducting this study. All research activities were performed without any financial support from external sources.

Conflict of Interest Declaration

The authors declare no conflicts of interest. This means they don't have any financial or personal connections that could unduly influence (bias) their work.

Author Contributions

All authors contributed equally to all aspects of the research and manuscript preparation.

Note: The flowchart presented in Appendix A provides a high-level overview of the computational model used in the code. Due to the complexity and detail of the calculations involved, detailed mathematical expressions and algorithmic steps are encapsulated within each block of the diagram. This approach is adopted to depict the overall structure and sequence of operations in the program while avoiding the intricacies of every mathematical expression or algorithmic step, which could be extensive and

complex. It's worth noting that these complex operations may require more than one sheet to explain in detail.

Appendix A. Flowchart of the Program for Orbital Parameter Calculations and Perturbation Analysis

The following flowchart illustrates the computational process used to calculate orbital parameters and analyze perturbations for satellites. The program begins with the initialization of the essential variables and the iterative calculations that account for various forces acting on the object. The process uses the Runge-Kutta integration method to solve the differential equations arising from these calculations. The flowchart delineates the sequence of operations from input parameters to the final output, ensuring a systematic approach to achieving accurate simulation results.

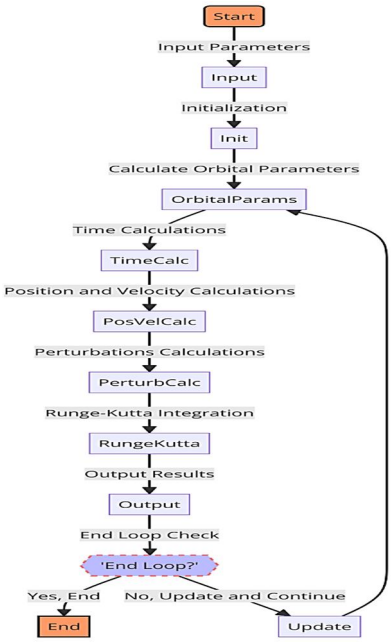

References

[1]"National Aeronautics and Space Administration (NASA)", [Online]. Available: https://www.nasa.gov.

[2] Ibraheem, A. and Salah, A., Iraqi J. Sci., 59 (4B) (2018) 2150.

[3]Vallado, D.A., "Fundamentals of Astrodynamics and Applications", (Springer Science & Business Media, 2001).

[4] Saleh, A. and Ghanem, H., Iraqi J. Sci., 54 (4) (2013) 1193.

[5] "Arianespace Official", [Online]. Available: https://www.arianespace.com.

[6] Hussien A., Jarad, M.M., and Mahdi, F.M., Iraqi J. Sci., 60 (4) (2019) 891.

[7] "International Telecommunication Union (ITU) publications on satellite communications", [Online]. Available: https://www.itu.int.

[8] Almohammadi, Mutlag, Iraqi J. Sci., 56 (2B) (2015) 1521.

[9] D. L. Mains, "Transfer Trajectories from Earth Parking Orbits", (Purdue University, 1993).

[10] Kim, J.L.S., Atmospheric Drag in Transfers between Geosynchronous Orbits, (2018).

[11] Yosif, M.A. and Saleh, A.-R.H., Iraqi J. Sci., 59 (1A) (2018) 199.

[12] Ibrahim, R.H. and Saleh, A.-R.H., Iraqi J. Sci., 60 (10) (2019) 2269.

[13] Mahdi, F.M., Salih, A.-R.H., and Jarad, M.M., Iraqi J. Sci., 61 (1) (2020) 224.

[14] Sharaf, M.A. and Sharaf, S.A.S., Rev. Mex. Astron. Astrofís., 52 (2) (2016) 283.

[15] Fadhil, O.A. and Saleh, A.-R.H., Iraqi J. Sci., 62 (2) (2021) 699.

[16] Yu, J., Yu, Y., Hao, D., Chen, X., and Liu, H., J. Aerosp. Eng., 233 (2) (2019) 686.

[17] Baron, A.S., "Orbital Mechanics and Astrodynamics: Techniques and Tools for Space Missions", Springer (2008).

[18] Wang, C., Guo, J., Zhao, Q., and Liu, J., Remote Sens., 10 (1) (2018) 118.

[19] Salih, M.J.F.A.R.H., Iraqi J. Sci., 57 (1B) (2016) 530.

[20] Al-Mohammadi, A.R.H.S., College of Science, University of Baghdad, Dec (2014).

[21] Yosif, M.A., and Saleh, A.-R.H., Iraqi J. Sci., 59 (1A) (2018) 199.

[22] Hale, F.J., "Introduction to Space Flight", 1st Ed. (1994).

[23] Ibrahim, R.H., "Improvement the Accuracy of State Vectors for the Perturbed Satellite Orbit Using Numerical Methods", University of Baghdad, College of Science, Department of Astronomy and Space, May 26, 2021.

[24] Cakaj, S.K.B. and Cakaj, A.E., Trans. Netw. Commun., (–) (–) 39.

[25] Al-Bermani, M.J.F. and Baron, A.S., J. Kufa Phys., 2 (1) (2010) 17–26.

[26] Saleh, A.-R.H., Iraqi J. Sci., 62 (2) (2021) 81.

[27] Singh, A.K.P.V.V.S.S., Adv. Space Res., 15 (3) (2018) 1170.

[28] Dos Santos, M.C., Department of Geodesy and Geomatics Engineering, University of New Brunswick, Canada, 1995.

[29] Al-Hiti, A.S.T., Master Thesis, Faculty of Science, University of Baghdad, 2002.

[30] Kaplan, E.D. and Kaplan, H.C., "Understanding GPS: Principles and Applications", 2nd Ed., Artech House, November 2005.

[31] Almohammadi, A.H.S. and Qahtan, A.Y., Iraqi J. Sci., 58 (3B) (2017) 1534.

[32] Leick, A., "GPS Satellite Surveying", 3rd Ed., Wiley, 2004.

[33]Mohammed, A., "Calculation of Perturbations Effect and Orbit Transfers for Earth Satellites", Ph.D. Thesis, University of Baghdad, 2019.

[34] Senga, D.P. and Senga, P., "Variation of Secondary Gamma Radiation Flux during Closest Approach of Mars towards Earth", Bhupal Nobles University, 2021.

[35]Yosif, M.A. and Saleh, A.-R.H., Sci.Int.(Lahore), 30 (5) (2018) 785.

[36]Hayder, R., "Computing the Perturbation Effects on Orbital Elements of the Moon", M.Sc. Thesis, University of Baghdad, 2011.

[37]Fortescue, S.J.G. and Fortescue, J., "Spacecraft Systems Engineering", 4th Ed., John Wiley & Sons, 2011.

[38] Saad, F.A. and Saleh, A.S.D.J., Iraqi J. Sci., 63 (12) (2022) 4090.

[39] Seeber, G., "Satellite Geodesy", 2nd Ed., revised, Walter de Gruyter, 2003.

[40] Liu, Y.L.Y.T.Z.D.X.Q.Y. and Liu, L.M., Remote Sens., 11 (24) (2019) 3024.

[41] Saleh, A.-R.H. and Damin, T.A., Iraqi J. Sci., 57 (1C) (2016) 775.

[42] Zainal, A.Q.I., Ph.D. Thesis, College of Science, University of Baghdad (2007).

[43] Wesam, W., Ph.D. Thesis, University of Baghdad (2011).

[44] Izzet, M.H.A.J.A.K.I., Iraqi J. Sci., 61 (2) (2020) 453.

[45] Fadhil, O.A., M.Sc. Thesis, Department of Astronomy and Space, College of Science, University of Baghdad, 2020.

[46] Battin, R.H., "An Introduction to the Mathematics and Methods of Astrodynamics", Rev. Ed., AIAA (1999).

[47] Crash, B., "Satellite Orbits: Models, Methods, and Applications", Springer, 2000.

[48] Montenbruck, O.G.E. and Gill, D.S., "Satellite Orbits: Models, Methods and Applications", 2nd Ed., Springer-Verlag Berlin Heidelberg, 2000..

[49] Markley, F.L. and Crassidis, J.L., "Fundamentals of Spacecraft Attitude Determination and Control", Springer, 1991.

[50] Broucke, R., Celest. Mech. Dyn. Astron., 25, 149–157, 1982.

[51] Izzet, A.K., Tikrit J. Pure Sci., 20(1), 142–149, 2015.

[52] Al-Bermani, M.J.F., Ali, A.H., Al-Hashmi, A.M., and Baron, A.S., J. Kufa Phys., 4(2), 1–6, 2012.

Volume 18, Number 2, 2025. pp. 157-164

Jordan Journal of Physics

ARTICLE

Utilizing Semi-Empirical Miedema's Model for Gibbs Free Energy Calculations in Fe-Al-Cr and Fe-Al-Cu Alloys

Ali Kadhim Alsaedi[a], **Ahmed Rahem Karrawi**[b], **Hussien Abid Ali Bakir Mraity**[a] and **Faeq A. Al-Temimei**[a]

[a] *Department of Physics, Faculty of Science, University of Kufa, Najaf, Iraq.*
[b] *Faculty of dentistry, University of Kufa, Najaf, Iraq.*

Doi: **https://doi.org/10.47011/18.2.5**
Received on: 31/10/2023; *Accepted on: 14/03/2024*

Abstract: The Miedema semi-empirical model represents a promising technique for estimating the Gibbs free energy ***(ΔG)*** in Fe-Al-Cr and Fe-Al-Cu alloys. In this study, the software Materials Analysis Applying Thermodynamics (MAAT) was utilized to calculate ***ΔG***. The results indicated that the ***ΔG*** values for the binary alloys (Fe-Al, Fe-Cr, Al-Cr, and Al-Cu) were negative and lower than the ideal Gibbs free energy ***(ΔG^{ideal})***, except for Fe-Cu, which exhibited a positive ***ΔG***. For the ternary alloys (Fe-Al-Cr and Fe-Al-Cu), the ***ΔG*** values were predominantly negative across a wide range of compositions. This suggests the presence of driving forces promoting the formation of solid solutions from Fe, Al, Cr, and Cu throughout the entire composition range.

Keywords: Miedema's model, Gibbs free energy, FeAlCr, FeAlCu alloys.

1. Introduction

The thermodynamic properties of ternary alloys are crucial for understanding their phase behavior and relative stability. However, conducting experiments to determine these properties is challenging and time-consuming. Theoretical findings obtained through the application of Miedema's model can offer valuable information about the thermodynamic behavior of alloys [1]. Miedema's model is widely used to calculate the thermodynamic properties of binary and ternary alloys [2, 3]. It utilizes parameters such as electronegativity, electron density, and molar volume to calculate ***(ΔG)***.

Iron-aluminum (Fe-Al) alloys hold significant technological importance with promising properties. However, their limited ductility at ambient temperatures and reduced strength at high temperatures have hindered their widespread use in structural applications. Recent studies have focused on improving their mechanical properties through composition control, microstructure manipulation, and the addition of suitable alloying elements [4].

Fe-Al-Cr alloys are renowned for their exceptional resistance to oxidation at elevated temperatures, attributed to the formation of a protective alumina scale. These alloys are commonly used in heating foils, wires, and automotive catalyst supports [4]. Strengthening the dispersion and controlling grain size are effective approaches for enhancing their mechanical properties at high temperatures, and these methods are commonly applied in commercial production via powder metallurgy techniques [5]. Extensive research has been conducted on the structural and microstructural

Corresponding Author: Ali Kadhim Alsaedi **Email**: Alik.alsaaedi@uokufa.edu.iq

changes in mechanically alloyed Fe-Al-Cr powder mixtures.

Aghili *et al*. investigated the formation and structural changes in $Fe_{50}Cr_{25}Al_{25}$ powder particles and observed the generation of a composite lamellar structure of Fe, Cr, and Al with the dissolution of Al and Cr atoms in the Fe lattice [6]. In another study, Liu *et al*. reported the formation of a solid solution of Fe-Cr(Al) through Al diffusion into Fe-20Cr in nanocrystalline powders of Fe-40Al-5Cr [7].

Al-Cu-Fe alloys are notable for their low toxicity, availability, and cost-effectiveness [8]. The Al-Cu-Fe quasicrystalline phase has been widely used as a reinforcement to create composites with excellent mechanical and tribological properties [9-12]. Several publications have focused on the fabrication of Al-Cu-Fe quasicrystalline phases through mechanical alloying (MA) with or without subsequent annealing treatments. For example, direct formation of the quasicrystalline phase was achieved in $Al_{65}Cu_{20}Fe_{15}$ alloy after 15 hours of milling [12,13]. Mitka *et al*. studied the impact of mechanical alloying variables on phase formation in the $Al_{62}Cu_{25.5}Fe_{12.5}$ alloy and observed a mixture of icosahedral quasicrystal and β-Al(Cu, Fe) phases after 20 hours of milling at 300 rpm [13].

Travessa *et al*. found that the quasicrystalline phase could not be directly obtained in the $Al_{65}Cu_{20}Fe_{15}$ alloy [14]. Other studies have investigated the phase reactions during ball milling of $Al_{65}Cu_{23}Fe_{12}$, noting complex solid-state transformations upon annealing of the as-milled sample. These phase transformation results were linked to variations in the thermodynamic driving forces, including the positive heat of mixing for the Cu-Fe system and negative heats of mixing for the Al-Fe and Al-Cu systems [15]. This work aims to calculate the thermodynamic properties of Fe-Al-Cr and Fe-Al-Cu alloys employing the semi-empirical Miedema's model.

Gibbs Free Energy (ΔG)

Elucidating the practical implications of the highest and lowest Gibbs free energy ($\boldsymbol{\Delta G}$) values recorded in binary systems is essential for understanding how these values can impact alloy properties and applications. Also, the $\boldsymbol{\Delta G}$ values can be used to construct phase diagrams, which are essential for predicting the phases present in an alloy at different temperatures and compositions. This is valuable for alloy design and understanding how an alloy's composition affects its properties [16, 17].

The Gibbs free energy can be calculated using the equation:

$$\boldsymbol{\Delta G = \Delta H + T\Delta S} \quad (1)$$

where $\boldsymbol{\Delta H}$ is the mixing enthalpy change, $\boldsymbol{\Delta s}$ is the mixing entropy change, and $\boldsymbol{T}$ is the absolute temperature of the solid solution.

If we consider only entropy, the change in mixing entropy for the solid solution can be calculated using the following formula:

$$\boldsymbol{\Delta S = -R(X_A lnX_A + X_B lnX_B)} \quad (2)$$

$$\boldsymbol{X_A + X_B = 1}$$

where R is the universal gas constant and X_A and X_B are atomic concentrations in the solid solution.

2. Miedema's Model

The estimation of formation enthalpy ($\boldsymbol{\Delta H}$) is a valuable tool provided by the Miedema model. Initially developed for binary alloys, efforts have been made to extend it to ternary systems [18-20]. In this model, Wigner-Seitz cells form the basis of the binary alloy hypothesis. As pure metal atoms combine to form alloys, the boundaries of the Wigner-Seitz cells change. Miedema's model proposes two mechanisms contributing to the formation enthalpy of binary alloy systems. The first mechanism is directly proportional to $(\Delta\boldsymbol{\varphi}^*)^2$, which represents the charge transfer between neighboring cells resulting from attractive forces. The second mechanism is proportional to $(\Delta\boldsymbol{n_{ws}^{2/3}})$, which takes into account the repulsive forces arising from surface tension. The negative impact of $(\boldsymbol{\varphi}^*)$ and the positive effect of $(\Delta\boldsymbol{n_{ws}^{1/3}})$ determine their contributions to the mixing enthalpy [21, 22].

The equation representing $\boldsymbol{\Delta H}$ of a binary system can be formulated using the Miedema model [21-23]:

$$\boldsymbol{\Delta H_{AB}^{total} = \Delta H_{AB}^{chemical} + \Delta H_{AB}^{elastic} + \Delta H_{AB}^{structural}} \quad (3)$$

where $\boldsymbol{\Delta H^{chemical}}$ refers to the chemical contribution, $\boldsymbol{\Delta H^{elastic}}$ represents the elastic enthalpy, and $\boldsymbol{\Delta H^{Stractural}}$ refers to the structural

enthalpy resulting from the crystal structure difference of the binary system. In this regard, structural enthalpy is negligible due to its minimal effect on the total enthalpy [24].

The chemical enthalpy results from a difference in the binding energy of atoms in their initial elemental states compared to their mixed alloy states.

The following equation can determine the chemical enthalpy term for each binary system [23]:

$$\Delta H_{A\ in\ B}^{Chemical} = 2k\, X_A^S X_B^S\, C(x) \frac{(X_A\, V_A^{2/3} + X_B\, V_B^{2/3})}{(n_{ws}^A)^{-1/3} + (n_{ws}^B)^{-1/3}} \times \left[-(\Delta\emptyset^*)^2 + {}^{Q}/_{P}\left(\Delta n_{ws}^{1/3}\right)^2 - {}^{R^*}/_{P}\right] \quad (4)$$

where

$$\boldsymbol{X_A^S} = \frac{X_A\, V_A^{\frac{2}{3}}}{X_A\, V_A^{\frac{2}{3}} + X_B\, V_B^{\frac{2}{3}}} \quad (5)$$

$$\boldsymbol{X_B^S} = \frac{X_B\, V_B^{\frac{2}{3}}}{X_A\, V_A^{\frac{2}{3}} + X_B\, V_B^{\frac{2}{3}}} \quad (6)$$

To overcome the differences between the enthalpy of mixing obtained from Miedema's model and experimental data, Wang *et al.* [25] proposed a correction factor, ***C(x),*** which takes into account the atomic size of solvent and solute atoms.

$$\boldsymbol{C(x)} = \mathbf{1} - \boldsymbol{S}\frac{X_A X_A |V_A - V_B|}{X_A^2 V_A + X_B^2 V_B} \quad (7)$$

where S represents a semi-quantitative empirical variable that explains the influence of atomic size disparities. S equals 1 for a disordered solid solution. The liquid alloy and ordered compound S are considered equivalent to 0.5 and 2.0, respectively [26]. $V_{.A.}$ and $V_{.B.}$ are the molar volumes of ***A*** and ***B,*** respectively, X_A and X_B are the molar fractions of ***A*** and ***B***, respectively, Φ^* is the constituent element work function, and n_{ws} is the density of electrons. ***P***, ***Q***, and ***R**** are known to be constants. ***P*** can be equal to 14.2 or 10.7, depending on whether the metals are transition or non-transition. Additionally, the value of ***P/Q*** was obtained to be 9.4. The ***R**** is an additional parameter for the enthalpy for both transition and non-transition metals.

The $\Delta H^{elastic}$ represents the elastic enthalpy caused by the atom-sized mismatch. It can be written as [27]:

$$\Delta H_{AB}^{elastic} = K_B G_A (X_A \Delta H_{B\ in\ A} + X_B \Delta H_{A\ in\ B}) \quad (8)$$

where ***K*** and ***G*** refer to the bulk and shear modulus, respectively.

The structural enthalpy results from the crystal structure difference of the binary system. The $\Delta H^{Structural}$ refers to the transition metals, which tend to crystallize preferentially in one out of three crystallographic phases, namely, bcc, fcc, and hcp, based principally on the number of valence electrons (***Z***). For binary solutions of transition–transition elements with shared bonds, this approach can be applied. Bakker et al. proposed the following expression for structural enthalpy [28]:

$$\Delta H_{A\ in\ B}^{struct} = (E_B^{struct} - E_A^{struct}) + (Z_A - Z_B)\frac{\partial E^{struct}(B)}{\partial Z} \quad (9)$$

where both Z_A and Z_B represent the valence electrons of ***A*** and ***B*** atoms, respectively, while E_B^{struct} and E_A^{struct} refer to the lattice stability of each crystal structure (bcc, fcc, and hcp).

The thermodynamic parameters needed to compute the formation enthalpies are provided in Table 1.

TABLE 1. The required parameters to compute the Gibbs free energy change.

Metal	$\emptyset^*[V]$	$n_{ws}^{1/3}\,[d.u]^{1/3}$	$V_m^{2/3}\,[cm]^2$	Atomic radius [pm]
Fe	4.93	1.77	3.7	126
Al	4.20	1.39	4.6	143
Cr	4.65	1.73	3.7	125
Cu	4.45	1.47	3.7	128

3. Results and Discussion

3.1 Fe-Al-Cr Alloy

The highest ΔG value typically corresponds to the most thermodynamically stable phase under specific conditions, whereas the lowest ΔG value indicates the least stable phase. This information is critical for phase selection in alloy design. Phases with lower ΔG values are generally less stable and may undergo phase

transformations at relatively lower temperatures. Such transformations can significantly influence the alloy's mechanical and thermal properties..

The outcomes of the thermodynamic computations for the binary alloys at 298K are shown in Fig.1. The graph illustrates the values of the Gibbs free energy change (ΔG) and the ideal Gibbs free energy change (ΔG^{ideal}) for different compositions. It is observed that for all concentrations, the (ΔG) values of Fe-Al, Fe-Cr, and Al-Cr alloys are negative and lower than the ΔG^{ideal} values. This indicates a strong interaction between the Fe, Al, and Cr atoms in these alloys.

Specifically, looking at Table 2, it can be noted that the ΔG of Fe-Cr is -3.13 kJ/mol, indicating a negative Gibbs free energy change for the formation of Fe-Cr alloy. This, combined with the small mismatch between the atomic radii and electronegativity of Fe and Cr, suggests that the formation of Fe-Cr alloy is relatively easy and feasible in the context of mechanical alloying (MA). These findings emphasize the favorable thermodynamic conditions for the formation of Fe-Cr alloy and provide insights into the potential for their synthesis and application in materials processing.

TABLE 2. Gibbs free energy in kJ/mol and atomic size mismatch for Fe-Al, Fe-Cr, and Al-Cr.

Binary alloy	ΔG [kJ/mol]	Atomic size mismatch %
FeAl	-15.48	13.4
FeCr	-3.13	0.8
AlCr	-14.8	12.5

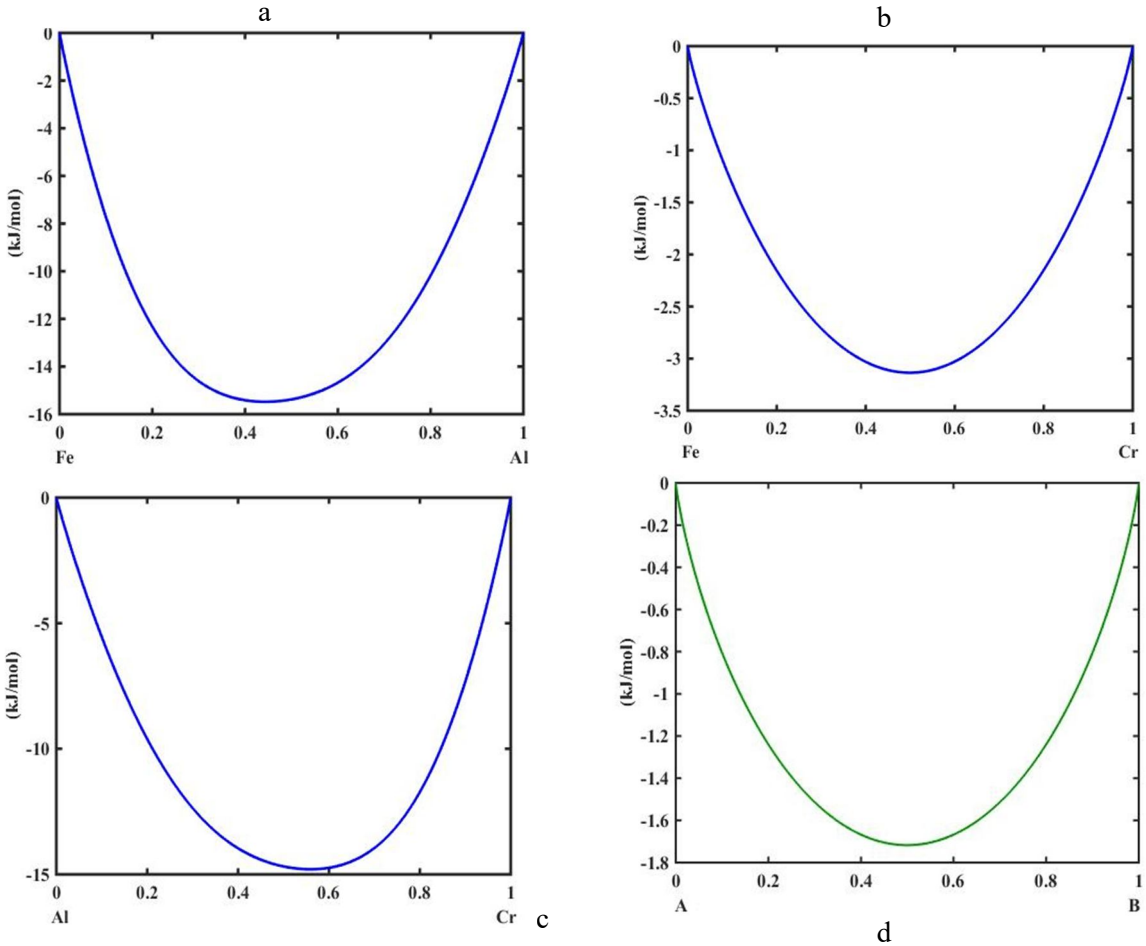

FIG. 1. Gibbs free energy of (a) Fe-Al, (b) Fe-Cr, and (c) Al-Cr alloys and (d) ideal Gibbs free energy.

The data presented in Fig. 2 provides valuable insights into the thermodynamic behavior of the Fe-Al-Cr alloy, specifically in terms of ΔG and ΔG^{ideal} values. The negative values of ΔG across the entire composition range indicate that there are driving forces promoting the formation of a solid solution from Fe, Al, and Cr. This implies that the thermodynamic conditions favor the mixing of these elements and the formation of a stable ternary alloy. The

negative ΔG values signify that the energy released during the formation of the solid solution exceeds the ideal energy required for a random mixture of the elements (ΔG^{ideal}). This suggests a favorable interaction between the Fe, Al, and Cr atoms within the ternary system.

It is worth noting that the largest ΔG values are observed in the vicinity of the Fe-Cr alloy. This indicates a relatively high energy release during the formation of Fe-Cr alloys, suggesting a stronger interaction between Fe and Cr atoms. Conversely, The Al-Cr alloy exhibits the lowest values of ΔG, indicating a lower energy release during the formation of Al-Cr alloy, suggesting a weaker interaction between Al and Cr atoms. These findings contribute to our understanding of the thermodynamics of the Fe-Al-Cr alloy and highlight the favorable conditions for the formation of solid solutions within this alloy system.

The addition of Cr to the Fe-Al composition leads to the most negative value of the formation enthalpy. This implies that converting the Fe-Al alloy to the Fe-Al-Cr alloy requires additional energy and heat, resulting in an increase in the process temperature. The more negative the value of ΔH, the stronger the bond and stability between Fe and Al atoms in the presence of Cr. This indicates that the connection between Fe, Al, and Cr atoms becomes more difficult to break, making the formation of the ternary Fe-Al-Cr alloy more challenging.

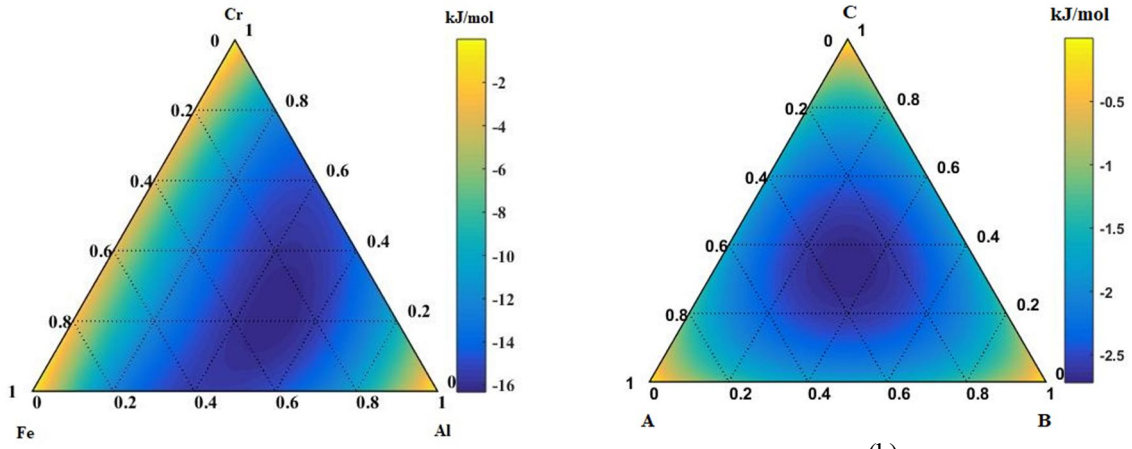

(a) (b)

FIG. 2. (a) Gibbs free energy of Fe-Al-Cr alloys. (b) Ideal Gibbs free energy.

3.2 Fe-Al-Cu Alloy

The information presented in Fig. 3 and Table 3 provides insights into the ΔG for the Fe-Cu and Al-Cu alloys. In the Fe-Cu system, the Gibbs free energy changes with mole fraction, with the highest values occurring near a mole fraction of 50%. This indicates limited solubility of Cu in α-iron under equilibrium conditions, as evidenced by the high positive values of Gibbs free energy. Such high positive values suggest that the formation of Fe-Cu alloys is thermodynamically unfavorable.

Conversely, in the Al-Cu alloy, the most negative value of the ΔG is observed. This indicates a thermodynamic driving force for the formation of the Al-Cu phase, with the system tending to release stored energy to achieve this phase. The negative Gibbs free energy implies that the formation of Al-Cu alloys is thermodynamically favorable.

However, it is worth noting that despite the small atomic radii mismatch between Cu and Fe, the positive ΔG value of Cu with Fe (11.23 kJ/mol) makes the formation of Fe-Cu alloy challenging and impractical within the context of Miedema's model used in the MAAT program. This suggests that there are additional factors beyond atomic radii considerations that impede the formation of Fe-Cu alloy according to this specific model.

It is important to emphasize that these conclusions are drawn from theoretical predictions based on thermodynamic calculations using Miedema's model. Experimental validation is necessary to confirm these findings and to assess the real-world feasibility of forming Fe-Cu alloys. Furthermore, factors such as kinetic barriers, processing parameters, and alloying effects must also be considered when evaluating the practical viability of alloy formation.

TABLE 3. Gibbs free energy in kJ/mol and atomic size mismatch for Fe-Cu and Al-Cu.

Binary alloy	(ΔG) [kJ/mol]	Atomic size mismatch %
Fe-Cu	11.23	**1.5**
Al-Cu	-6.92	10.4

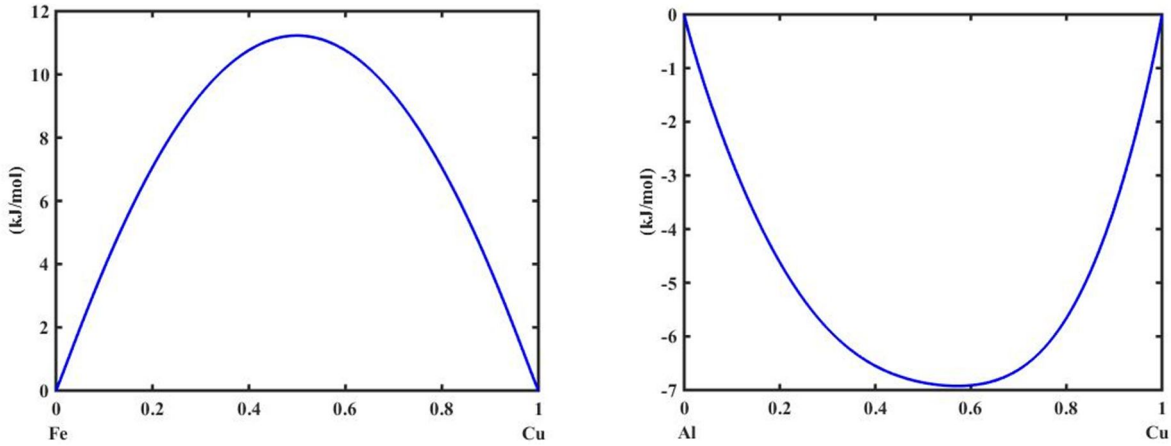

FIG. 3. Gibbs free energy of Fe-Cu and Al-Cu alloys.

The results presented in Fig. 4 indicate that the Fe-Al-Cu alloy exhibits the most negative Gibbs free energy at around a 50% mole fraction of Fe. This suggests that there is a thermodynamic driving force for the formation of the Fe-Al-Cu solid solution from elemental Fe, Al, and Cu. The fact that ΔG is smaller than ΔG^{ideal} further supports the feasibility of forming the ternary alloy through solid solution.

It is worth noting that the largest values of ΔG are observed near the Fe-Al system, indicating that the addition of Cu has a minimal effect on the thermodynamic stability of the Fe-Al-Cu alloy compared to the Fe-Al alloy. However, it is interesting to observe that the incorporation of Cu leads to a less negative value of ΔH for the Fe-Al-Cu alloy compared to the Fe-Al alloy. This suggests that the addition of Cu may influence other factors, such as improving the morphology of the phase boundary and slowing down grain growth, thereby enhancing the thermal stability of the Fe-Al alloy.

These findings have significant implications for the targeted application and desired performance properties of Fe-Al-Cu alloys. Understanding the role of Cu in modifying mechanical, thermal, and corrosion resistance properties is crucial for the alloy's effective use in engineering applications. Additionally, exploring the effects of microstructural features and phase distribution will further clarify the alloy's performance characteristics. It would also be beneficial to compare the thermodynamic results with experimental data, if available, to validate the accuracy and reliability of the theoretical predictions based on Miedema's model and the MAAT software.

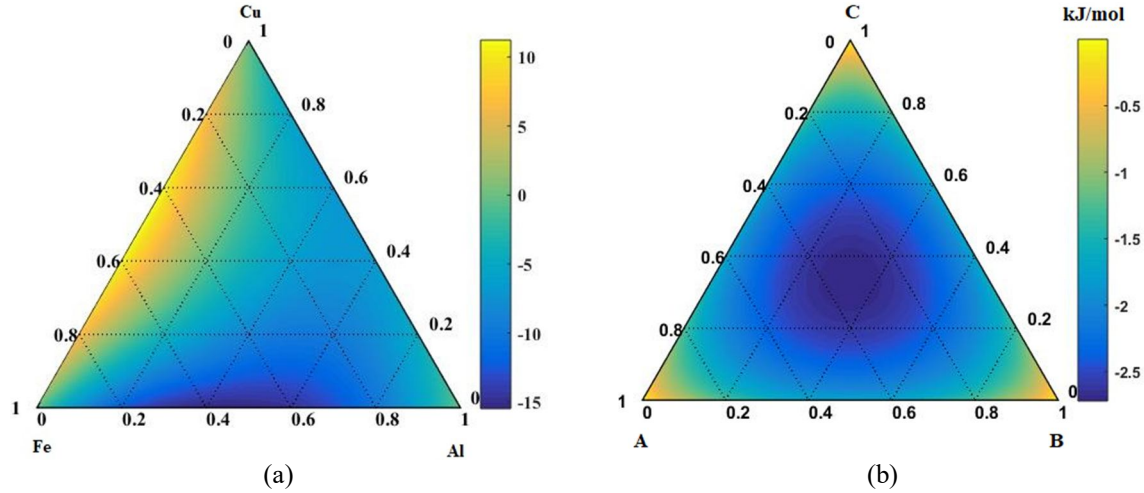

(a) (b)

FIG. 4. (a) Gibbs free energy of Fe-Al-Cu. (b) Ideal Gibbs free energy.

4. Conclusions

The calculations performed using Miedema's model and the MAAT program for the Fe-Al-Cr and Fe-Al-Cu alloys yield interesting results. The inclusion of Cr in the Fe-Al alloy leads to an improvement in the formation enthalpy, indicating a driving force for the formation of the Fe-Al-Cr solid solution. This suggests that the addition of Cr enhances the stability and thermodynamic favorability of the ternary alloy. Similarly, the addition of Cu in the Fe-Al alloy enhances the thermal stability of the alloy. This improvement in thermal stability can be attributed to the influence of Cu on the microstructure and phase distribution of the alloy. The presence of Cu may result in improved phase boundary morphology and hindered grain growth, contributing to increased thermal stability.

It is important to recognize that while these findings from theoretical models like Miedema's model provide valuable insights into the thermodynamic behavior of ternary alloys, experimental validation is necessary to confirm their accuracy and reliability. Further experimental studies could be undertaken to characterize the mechanical, thermal, and other relevant properties of the Fe-Al-Cr and Fe-Al-Cu alloys, thereby supporting and validating the findings obtained from theoretical calculations. Overall, the results suggest that the addition of specific alloying elements such as Cr and Cu can significantly influence the thermodynamic properties and thermal stability of Fe-Al-based ternary alloys. This knowledge can be applied in the design and optimization of these alloys for various engineering applications where stability, strength, and high-temperature performance are crucial factors to consider.

References

[1] Ouyang, Y., Zhong, X., Du, Y., Jin, Z., He, Y., and Yuan, Z., J. Alloys Compd., , 416 (1-2) (2006) 148.

[2] Zhang, R.F., Sheng, S.H., and Liu, B.X., Chem. Phys. Lett., 442 (4-6) (2007) 511.

[3] Niessen, A.K. et al., Calphad, 7 (1) (1983) 1.

[4] Al-Mathami, A., "Crystal Structure and Oxidation Behavior of Al-Containing Stainless-Steel Coatings Produced by Cryomilling and Spark Plasma Sintering", (2010).

[5] Jönsson, B., Berglund, R., Magnusson, J., Henning, P., and Hättestrand, M., Mater. Sci. Forum, 461 (2004) 455.

[6] Aghili, S.E., Enayati, M.H., and Karimzadeh, F., Mater. Manuf. Process., 27 (4) (2012) 467.

[7] Liu, H., Tang, W., Wang, Y., Liu, C., Xu, G., and Zheng, Z., J. Alloys Compd., 506 (2) (2010) 963.

[8] Göğebakan, M., Avar, B., and Zun, O., Mater. Sci., 27 (3) (2009) 0137.

[9] Bloom, P.D., Baikerikar, K.G., Otaigbe, J.U., and Sheares, V.V., Mater. Sci. Eng. A, 294 (2000) 156.

[10] Schwartz, C.J., Bahadur, S., and Mallapragada, S.K., Wear, 263 (7-12) (2007) 1072.

[11] Tcherdyntsev, V.V., Sviridova, T.A., Shevchukov, A.P., and Kaloshkin, S.D., Z. Kristallogr., 223 (11-12) (2008) 751.

[12] Mitka, M., Lityńska-Dobrzyńska, L., Góral, A., and Maziarz, W., Acta Phys. Pol. A, 126 (4) (2014).

[13] Travessa, D.N., Cardoso, K.R., Wolf, W., Jorge Junior, A.M., and Botta, W.J., Mater. Res., 15 (2012) 749.

[14] Tcherdyntsev, V.V., Kaloshkin, S.D., Salimon, A.I., Tomilin, I.A., and Korsunsky, A.M., J. Non-Cryst. Solids, 312 (2002) 522.

[15] Miedema, A.R., De Chatel, P.F., and De Boer, F.R., Physica B + C, 100 (1) (1980) 1.

[16] Aaronson, H.I., Enomoto, M., and Lee, J.K., "Mechanisms of Diffusional Phase Transformations in Metals and Alloys", (CRC Press, 2016).

[17] Callister Jr, W.D. and Rethwisch, D.G., "Fundamentals of Materials Science and Engineering: An Integrated Approach", (John Wiley & Sons, 2020).

[18] Wang, R.N., He, Y., and Feng, J.Y., Nucl. Instrum. Methods Phys. Res. B, 222 (3-4) (2004) 462.

[19] Chelikowsky, J.R., Phys. Rev. B, 25 (10) (1982) 6506.

[20] Zhang, R.F., Zhang, S.H., He, Z.J., Jing, J., and Sheng, S.H., Comput. Phys. Commun., 209 (2016) 58.

[21] Li, H., Sun, X., and Zhang, S., Mater. Trans., 55 (12) (2014) 1816.

[22] Alsaedi, A.K., Abbas, F.S., Alaboodi, A.S., and Abojassim, A.A., Malays. J. Sci., 41 (3) (2022) 22.

[23] Imani, M. and Enayati, M.H., J. Alloys Compd., 705 (2017) 462.

[24] Basu, J., Murty, B.S., Ranganathan, S., J. Alloys Compd., 465 (1-2) (2008) 163.

[25] Hillert, M., Calphad, 4 (1980) 1.

[26] Aguilar, C., Martinez, C., Tello, K., Palma, S., Delonca, A., San Martín, F., and Alfonso, I., Metals, 10 (4) (2020) 510.

[27] Eshelby, J.D., Appl. Phys., 25 (2) (1954) 255.

[28] Bakker, H., Modder, I.W., and Kuin, M.J., Intermetallics, 5 (7) (1997) 535.

Volume 18, Number 2, 2025. pp. 165-173

Jordan Journal of Physics

ARTICLE

Effects of Etching Solution Concentration on Silicon Surface Reflectivity as a Solar Cell Surface Modifier

Ammar Mahmoud Al-Husseini and **Bashar Lahlouh**

Department of Physics, The University of Jordan, Amman, 11942, Jordan.

Doi: **https://doi.org/10.47011/18.2.6**

Received on: 14/11/2023; *Accepted on: 07/03/2024*

Abstract: The surface structure of single-crystal silicon is known to be one of the best ways to reduce reflection, increase light trapping ability, and increase light absorption. The hierarchical surface structure plays an important role in reducing the reflectivity of single-crystalline silicon surfaces. Through this research, the size and density of the pyramids formed on the silicone surface, as well as their dependence on the concentration of the etching solution during silicone processing, were studied and evaluated. The pyramids etched on the silicon surface formed photo-traps that increased the efficiency of light absorption. The effects of hydroxylamine (NH_2OH) on a 20 wt.% KOH and 20 wt.% NaOH solutions were investigated. The concentration of NH_2OH varied from 6 to 18 wt.% while the etching temperature was kept at 70 °C and the etching time was 40 minutes. Optimal etching conditions were identified, with the 20 wt.% KOH + 18 wt.% NH_2OH solution yielding better results than the 20 wt.% KOH solution. The normal incidence percent reflectivity was 6.5%, at 640 nm wavelength for Si {100} surfaces etched in a 20 wt.% NaOH + 18 wt.% NH_2OH solution. This normal incidence percent reflectivity value was slightly higher than that achieved by the 20 wt.% pure NaOH solution, where a percent reflectivity of 6.0% was measured at the same wavelength. Moreover, the addition of NH_2OH significantly increased the size of the etched pyramid structures.

Keywords: Micro-Pyramid, Surface morphology, Percent reflectivity, Solar cell, NH_2OH.

1. Introduction

Silicone substrates with different surface structures of different sizes and shapes are very popular in industrial and research applications, since silicon is one of the most abundant elements in nature, and it is a relatively safe element for the environment. Silicon is also one of the leading materials in solar cell technologies, thanks to its relatively high efficiency and the well-established processing techniques. Surface texture plays a major role in improving solar cell efficiency, and it is beneficial for cost-effective crystalline silicon solar cells [1–3]. A textured surface can effectively reduce the light reflection of the surface of cells by enhancing appropriate light absorption via multiple intra-shape reflections when compared to a flat surface, thus increasing cells' efficiency [4–6]. Large-scale photovoltaic production uses potassium hydroxide (KOH) or sodium hydroxide (NaOH) as aqueous etching solutions. These alkaline solutions are anisotropic etchants for Si and produce randomly distributed pyramid structures on the Si surface [5–10].

In this study, the surface structure of silicon was studied based on free alkali profiling by mixing potassium hydroxide (KOH) with different concentrations of NH_2OH, and by mixing sodium hydroxide (NaOH) with different concentrations of NH_2OH. The resulting pyramid structures exhibited different sizes and shapes,

Corresponding Author: Ammar Mahmoud Al-Husseini **Email**: a.taha@ju.edu.jo

depending on the composition and concentration of the etching solutions. These variations in surface morphology have significant implications for reflectivity and are of great interest to the solar cell industry [11-17]. Therefore, to reduce the cost of solar cells, improve cell performance, and distribute the size of the pyramids more uniformly, the etching process must be carefully optimized and evaluated [18]. The goal of this study was to improve the surface structure of silicon to achieve lower reflectivity by controlling the properties of the pyramids pattern on the etched silicon surface. The shape, structure, and size of the pyramid are important factors that determine the interactions of the surface with incident light [7].

2. Experimental Procedure

In this work, 8 small pieces (1.5 cm^2 each) of p-type {100} single-crystalline silicon with a resistivity of 3–30 Ω.m and a thickness of 675 μm were used. Prior to mounting the samples on the etching stage, all samples were cleaned in an ethanol bath, and after that, they were rinsed in deionized water several times. The silicon wafers were then immersed in a 25 wt.% NaOH solution for 2 minutes to remove the oxide, and then rinsed in deionized water several times. After completing the cleaning process, the samples were placed in a drying oven (hot air) for 20 seconds at a temperature of 60°C to remove moisture, then these samples were etched with different concentrations of solutions of KOH, NaOH, and NH_2OH. In the first stage, 20 wt.% KOH was mixed with varying concentrations of NH_2OH (6, 12, and 18 wt.%). In the second stage, 20 wt.% NaOH was mixed with different concentrations of NH_2OH (6, 12, and 18 wt.%). During the experiment, the reaction temperature and the reaction time were kept constant at 70.0 ± 0.1°C and 40 minutes, respectively. At the end of the reaction, all treated wafers were washed again in ethanol and deionized water baths for 5 minutes, and then they were dried in a drying oven (hot air) for 20 seconds at a temperature of 60°C and prepared for testing. The morphology of all textured samples was studied using an FEI Inspect F50 scanning electron microscope (SEM). The reflectance ratio spectra of the etched surfaces were measured using a FilmTek 3000 spectrophotometer (SCI, USA) within the wavelength range of 240-840 nm. All percent reflectivity measurements were performed at normal incidence. Through the SEM images, the pyramidal number density and average pyramidal volume were evaluated. SEM images were analyzed using ImageJ software [7].

3. Results and Discussion

In anisotropic wet etching, the microscopic surface roughness is controlled by many factors. Among these factors are: 1) The formation of hydrogen bubbles, which hinder surface interactions and act as a mask on the surface. 2) The redeposition of etching byproducts, such as SiO_2 deposits resulting from etching the Si crystal and other contaminants above the surface, on the surface during the etching process. Microscopic roughness appears during the etching process in the form of micro pyramids. The size and density of these pyramids depend on various parameters, including etching time, solution concentration, temperature, and the crystalline orientation of the Si wafers.

In this study, the etching characteristics of Si{100} surfaces were investigated using different concentrations of KOH, NaOH, and NH_2OH mixtures. These solutions were used to pattern the silicon substrates at a temperature of 70 °C for 40 minutes. The surface morphology, pyramid size, pyramid density, and optical reflectivity of all samples were examined. Optical measurements confirmed that the applied etching treatments led to a significant reduction in surface reflectivity.

Figure 1 presents SEM images illustrating the surface morphology of four samples etched with varying NH_2OH concentrations (6 to 18 wt.%), while maintaining a constant KOH concentration of 20 wt.%. As shown in Fig. 1(a), samples etched with KOH alone exhibit small pyramids. In contrast, Fig. 1(b) shows that the addition of 6 wt.% NH_2OH to the KOH solution results in noticeably larger pyramids. Figs. 1(c) and 1(d) reveal that further increasing the NH_2OH concentration to 16 wt.% and 18 wt.%, respectively, leads to the formation of even larger pyramids. However, these higher concentrations also cause a nonuniform pyramid size distribution and the emergence of irregularly shaped pyramids.

This irregularity is likely due to enhanced anisotropic etching effects, which may result from increased hydrogen bubble formation and the inherent crystalline orientation of the silicon surface, as discussed earlier.

A closer look at Fig. 1(d) shows that the higher NH_2OH concentration enhances the formation of larger distorted pyramids with truncated apexes and with smaller pyramid formations on these apexes. This can be useful for suppressing reflection and can increase the light-trapping efficiency of the textured surface [19-22]. It is also worth mentioning that a native silicon oxide thin film forms on the surface immediately after taking the samples out of the etching solution. However, this rather thin layer is not visible in the SEM images, as it is transparent to the SEM technique.

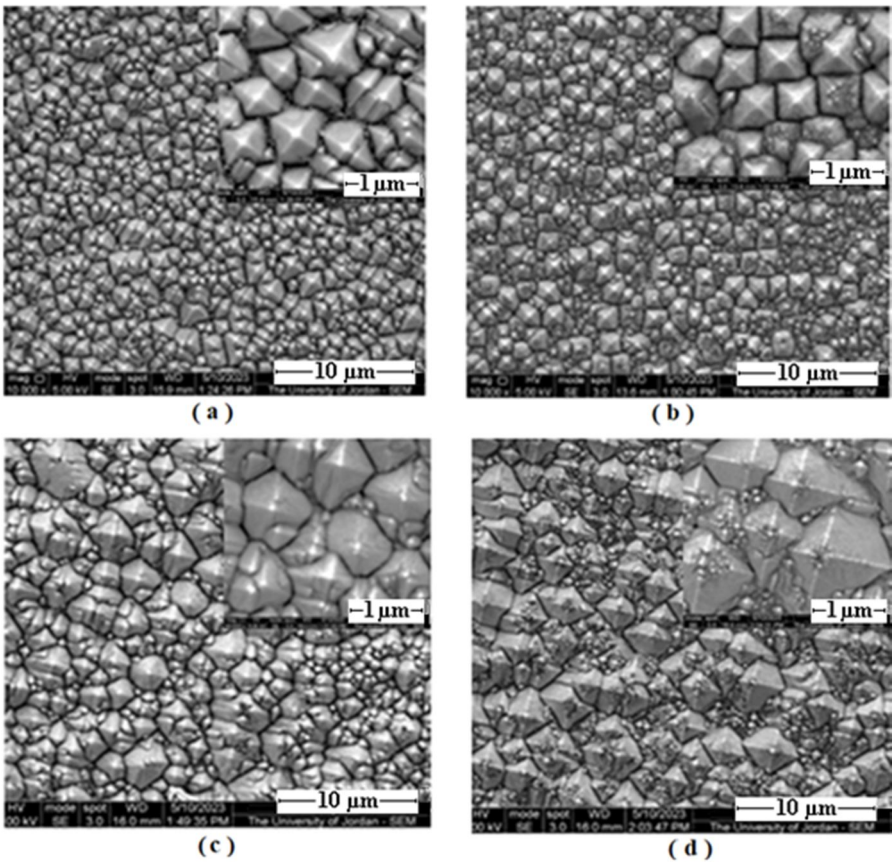

FIG. 1. SEM images of silicon surfaces etched using 20 wt.% KOH mixed with different NH_2OH concentrations at 70 °C for 40 minutes: (a) 0 wt.%, (b) 6 wt.%, (c) 12 wt.%, and (d) 18 wt.% NH_2OH.

The effect of NaOH mixed with different concentrations of NH_2OH on the etching process was also studied. NH_2OH at concentrations of 6, 12, and 18 wt.% was mixed with 20 wt.% NaOH at 70 °C for 40 minutes, and the solutions were used to etch the previously cleaned Si surfaces.

Figure 2 shows SEM images of the studied patterned substrates. The shape and density of the pyramids are directly related to the concentration of NH_2OH solution. At the NH_2OH solution concentration of 18 wt.%, the surface coverage of these pyramids covers the entire surface, and the size of the pyramids is large. As the concentration of NH_2OH increases and as it is added to the 20 wt.% NaOH solution, the dissolution kinetics is changed so that the removal of silicon atoms from the surface of the silicon crystal is very large. This change hinders the formation of orthosilicic acid, $Si(OH)_4$, which cannot keep up with the large Si dissolution rate. As the concentrations of these complexes also increase, a protective layer forms on the silicon surface, preventing etchants from reaching the surface of the silicon substrate [23].

Based on the results shown in Figs. 1 and 2, it can be said that modified etching is the best option for creating microstructures that require relatively low surface roughness. Surface roughness at the microscopic level is a direct result of irregular removal of atoms from the surface and their extension into the crystalline mass, and is the property of the formation of pyramids on the surface. In the case of wet etching, the surface roughness is strongly influenced by hydrogen bubble formation, which interferes with surface interactions and acts as a micro-mask, as well as by the redeposition of etching byproducts [24].

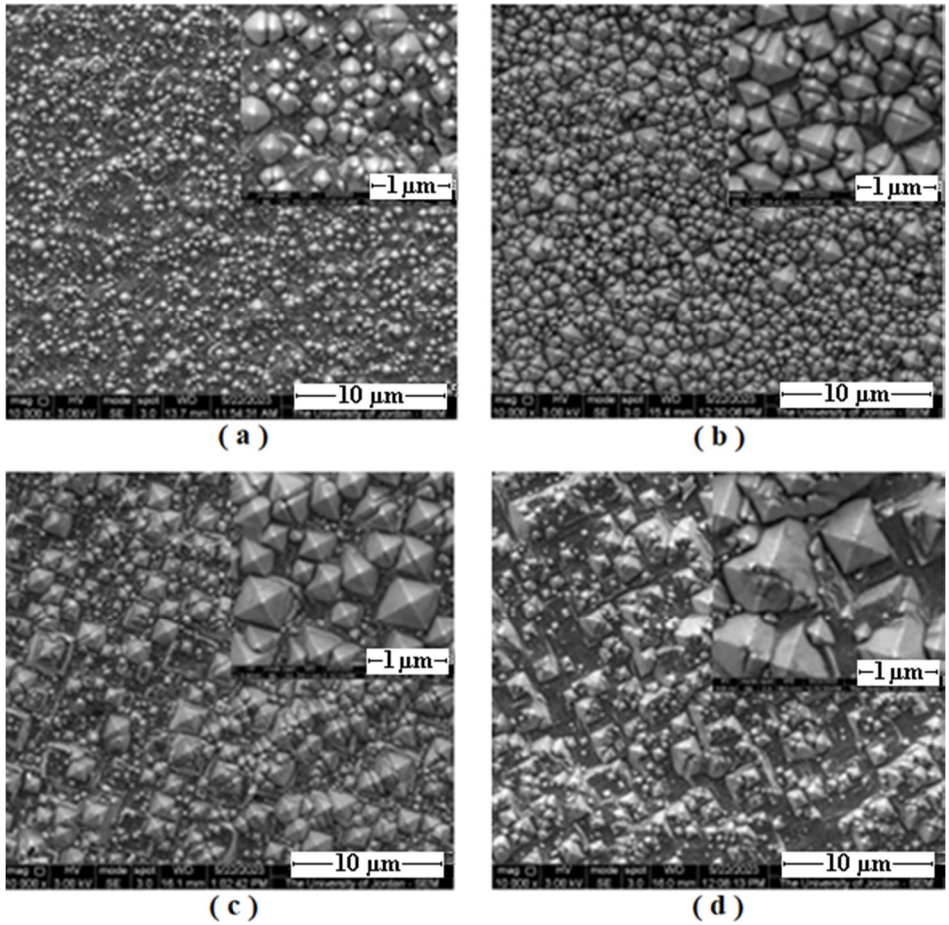

FIG. 2. SEM images of silicon surfaces etched using 20 wt.% NaOH mixed with different NH_2OH concentrations at 70 °C for 40 minutes: (a) 0 wt.%, (b) 6 wt.%, (c) 12 wt.%, and (d) 18 wt.% NH_2OH.

Figure 3 shows the number density distributions and sizes of the pyramids as a function of the concentration of KOH mixed with different NH_2OH concentrations. This figure clearly shows that increasing NH_2OH concentration leads to larger pyramid sizes and a lower average number density of pyramids compared to etching without NH_2OH. The average size of the pyramids increases with increasing concentration of NH_2OH. The average size of the pyramids is 0.940 ± 0.160 µm at 20 wt.% KOH mixed with 18 wt.% NH_2OH concentration, and it decreases to 0.530 ± 0.078 when no NH_2OH is added to the solution. The pyramids' number density decreases from 1.13 to 0.610 μm^{-2} with increasing NH_2OH concentration from 0 to 18 wt.%.

Figure 4 presents the size distribution of pyramids as a function of NaOH mixed with different NH_2OH concentrations. The largest pyramids were obtained using 20 wt.% NaOH mixed with 18 wt.% NH_2OH. Pyramid sizes increased from 0.280 ± 0.040 to 0.970 ± 0.110 µm (mean ± s.d.), and pyramid number density decreased from 2.60 to 0.600 μm^{-2} with the increase in NH_2OH concentration from 0 to 18 wt.%. The concentration of NH_2OH added to KOH or NaOH has an obvious effect on both the pyramid sizes and the average number density of pyramids. This is especially important for their application in solar cells.

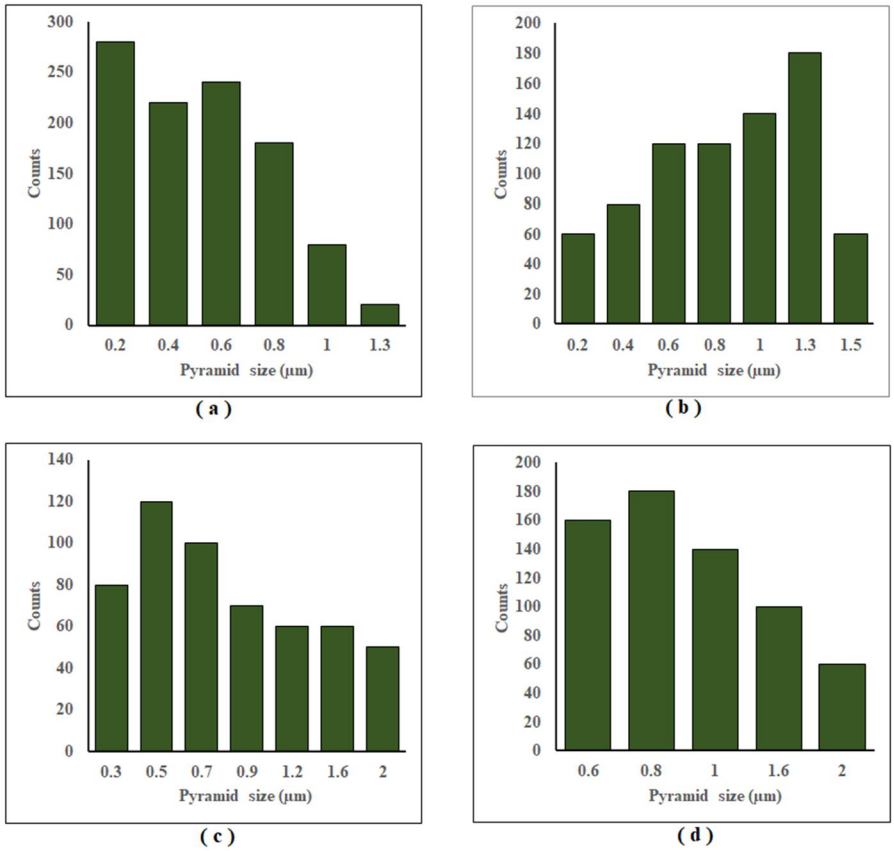

FIG. 3. Pyramid size distribution obtained using ImageJ software for 20 wt.% KOH mixed with different NH_2OH concentrations. (a) 0 wt.%, (b) 6 wt.%, (c) 12 wt.%, and (d) 18 wt.% NH_2OH.

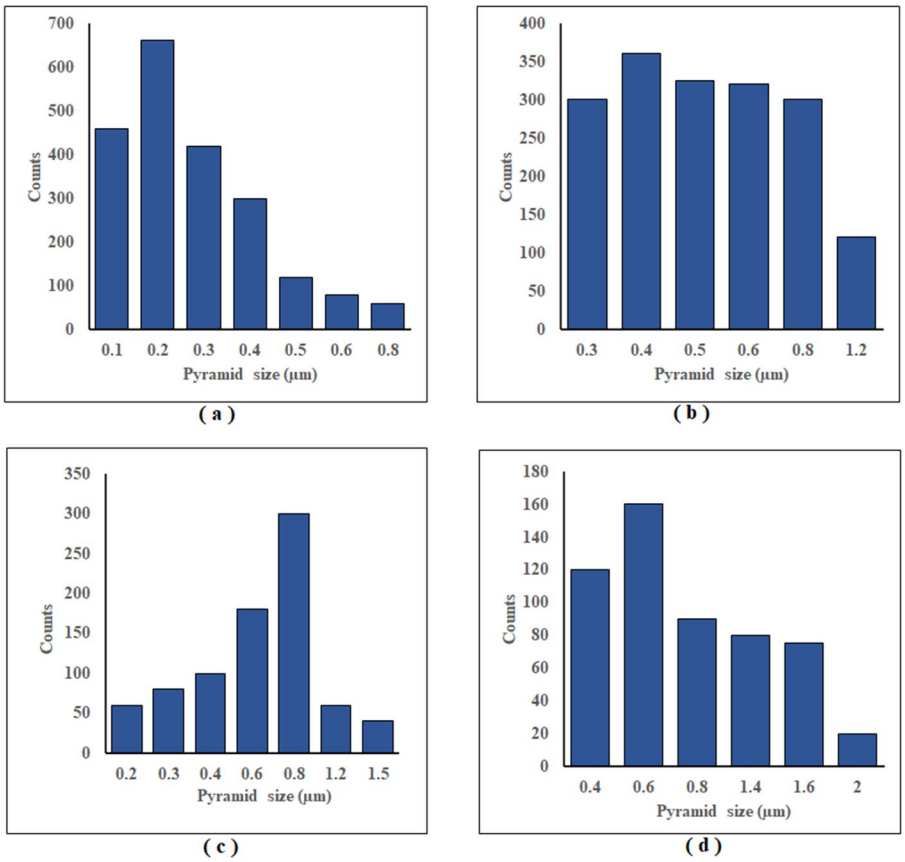

FIG. 4. Pyramid size distribution obtained using ImageJ software for 20 wt.% NaOH mixed with different NH_2OH concentrations. (a) 0 wt.%, (b) 6 wt.%, (c) 12 wt.%, and (d) 18 wt.% NH_2OH.

Figure 5(a) shows the optical reflectivity spectra of etched silicon wafers for different concentrations of NH_2OH mixed with 20 wt.% KOH. These spectra, as recorded in the wavelength range of 240-840 nm, show lower percent reflectivity values in the visible spectrum as well as in the near infrared region [21]. A lower reflectivity in the near infrared region ensures photon absorption, resulting in improved performance of solar cell devices. The percent reflectivity values of all samples remain almost constant in the visible wavelength range (440-600 nm) and begin to decrease with an increasing NH_2OH ratio until a minimum value of 6.5%, at 650 nm wavelength is reached at a concentration of 18 wt.% NH_2OH mixed with 20 wt.% KOH. A similar trend is observed for mixing different concentrations of NH_2OH with 20 wt.% NaOH, as can be seen in Fig. 6(a), where the percent reflectivity value reached 6.0% at a concentration of 18 wt.% NH_2OH mixed with 20 wt.% NaOH. Fig. 5(b) zooms in on the two peaks observed in the percent reflectivity spectra of the samples studied. These peaks are attributed to the crystalline silicon direct band gap [25]. The peak at around 272 nm does not show any appreciable shift, while the peak at around 364 nm for the polished silicon shifts toward 370 nm for the etched samples. This small shift may be related to changes in the stress in the etched samples. In Fig. 6(b), a similar behavior is observed but with the 364 nm peak shifting to a lower wavelength of 361 nm. This shift can also be associated with the changes in stress.

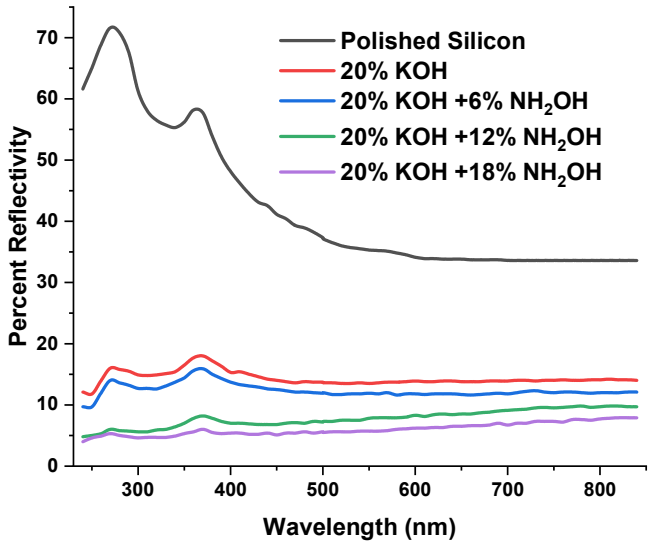

FIG. 5(a). Percent reflectivity of patterned silicon as a function of the wavelength for samples etched in 20 wt.% KOH mixed with different NH_2OH concentrations.

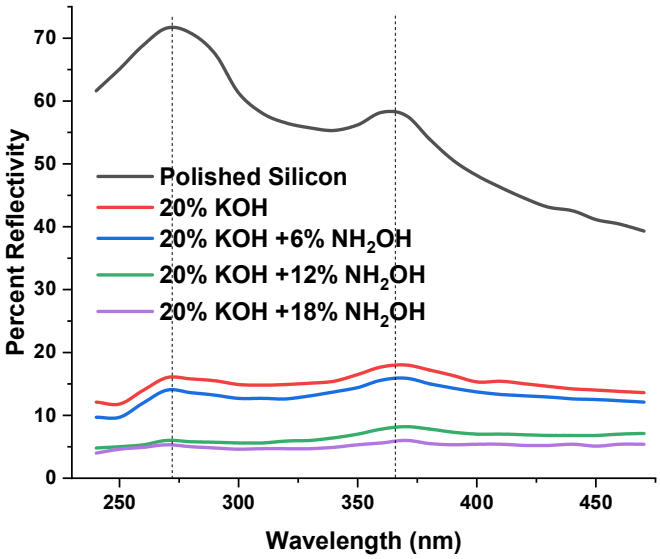

FIG. 5(b). A zoom in on the observed peaks in the percent reflectivity as a function of wavelength for samples etched in 20 wt.% KOH mixed with different NH_2OH concentrations.

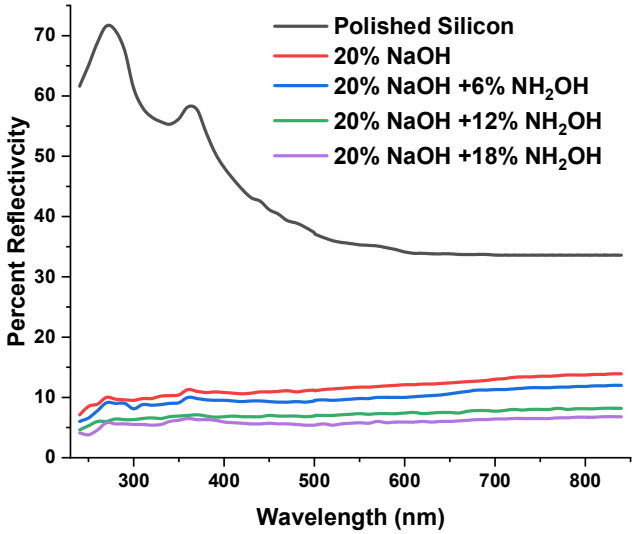

FIG. 6(a). Percent reflectivity of patterned silicon as a function of wavelength for samples etched in 20 wt.% NaOH mixed with different NH_2OH concentrations.

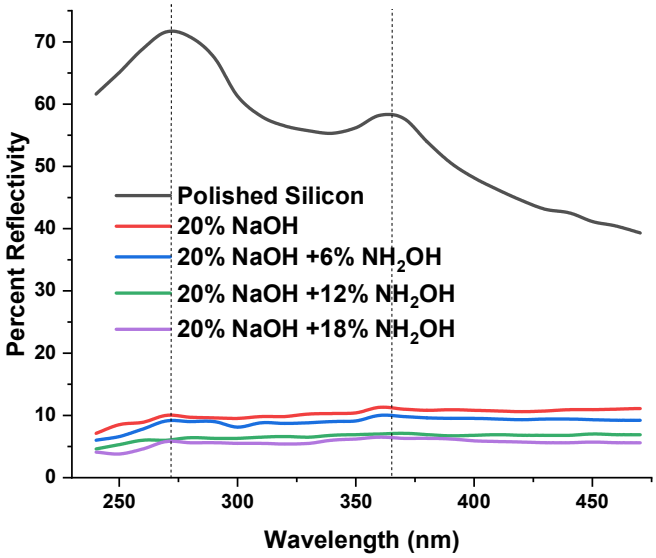

FIG. 6(b). A zoom in on the peaks observed in the percent reflectivity of silicon as a function of wavelength for samples etched in 20 wt.% NaOH mixed with different NH_2OH concentrations.

The percent reflectivity decreases from 13.8% to about 6.5% as the concentration of NH_2OH changes from 0 to 18 wt.% mixed with 20 wt.% KOH for samples measured at a wavelength of 640 nm, as shown in Fig. 7. A decrease in reflectivity from 12.4% to 6.0% is also observed as the concentration of NH_2OH increases from 0 to 18 wt.% mixed with 20 wt.% NaOH for the samples measured at a wavelength of 640 nm, as shown in Fig. 8. These differences in percentage reflectivity are due to changes in surface roughness resulting from the changes in the size and number density of the pyramids formed on the surface of the patterned silicon sample. The drop in the percent reflectivity indicates better light trapping properties, and it can lead to improvements in light harvesting properties of the modified surfaces and solar cells.

Table 1 summarizes the results for all the samples studied. This table shows the extent to which the percent reflectivity of light depends on the number density and the size of the pyramids resulting from changing the concentration of the NH_2OH solution mixed with 20 wt.% KOH or 20 wt.% NaOH solutions. Increasing the NH_2OH concentration leads to larger pyramid structures and a corresponding decrease in their number density [26].

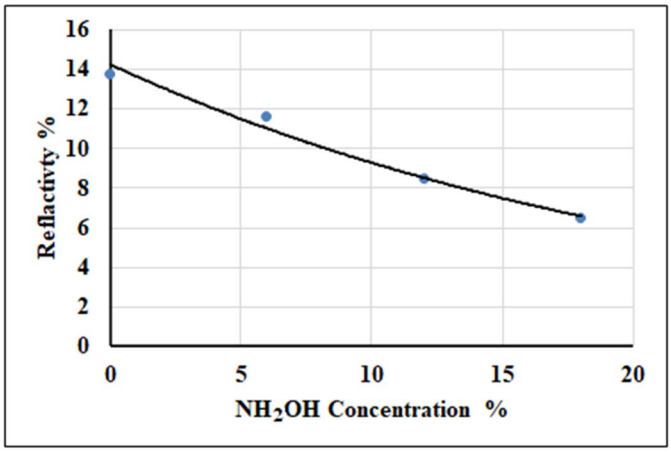

FIG. 7. Percent reflectivity of silicon surfaces etched with 20 wt.% KOH mixed with different NH_2OH concentrations at a wavelength of 640 nm.

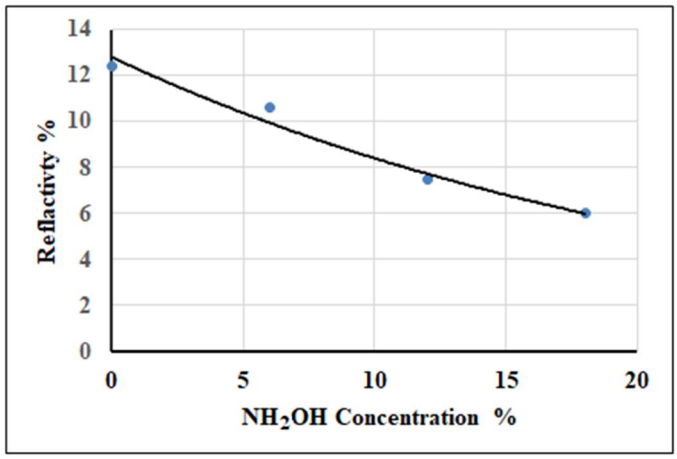

FIG. 8. Percent reflectivity of silicon surfaces etched with 20 wt.% NaOH mixed with different NH_2OH concentrations at a wavelength of 640 nm.

TABLE 1. Number of pyramids per mm^2, pyramids density, pyramid size (average ± s.d.), and average reflectivity (at λ = 640 nm) for eight samples prepared at 70 °C with an etching time of 40 minutes under different concentration texturing conditions.

Texturing conditions	Number of pyramids for each 1 mm^2	Density (μm^{-2})	Average pyramid size (μm)	Average reflectivity (λ = 640 nm) (%)
20 wt.% KOH	1020	1.130	0.530 ± 0.078	13.8
20 wt.% KOH + 6 wt.% NH_2OH	760	0.840	0.800 ± 0.111	11.7
20 wt.% KOH + 12 wt. % NH_2OH	640	0.650	0.930 ± 0.172	8.5
20 wt.% KOH + 18 wt.% NH_2OH	545	0.610	0.940 ± 0.160	6.5
20 wt.% NaOH	2100	2.600	0.280 ± 0.040	12.4
20 wt.% NaOH+ 6 wt.% NH_2OH	1725	2.010	0.570 ± 0.044	10.6
20 wt.% NaOH+ 12 wt.% NH_2OH	820	0.920	0.680 ± 0.108	7.5
20 wt.% NaOH+ 18 wt.% NH_2OH	540	0.600	0.970 ± 0.110	6.0

4. Conclusions

The effect of changing the concentration of hydroxylamine (NH_2OH) in solutions of 20 wt.% KOH and 20 wt.% NaOH on producing a homogeneous pyramidal pattern on the surface of single-crystal silicon was studied to obtain lower percent reflectivity values that enable the production of solar cells with higher efficiency. A percent reflectivity of 6.5% was obtained when mixing 20 wt.% KOH with 18 wt.% NH_2OH, while a percent reflectivity of 6.0% was obtained when mixing 20 wt.% NaOH with 18 wt.% NH_2OH. These low reflectivity values can be very useful for solar cells and photovoltaic applications.

References

[1] Zubel, I. and Kramkowska, M., J. Micromech. Microeng., 15 (2005) 485.

[2] Pal, P. and Sato, K., "Silicon Wet Bulk Micromachining for MEMS", (Jenny Stanford Publishing, New York, 2017).

[3] Yang, S., Zhang, L., and Ge, P., Int J. Adv. Manuf. Technol., 92 (2017) 3187.

[4] Alshahrie, A., Joudakzis, S., Al-Ghamdi, A.A., and Elsayed, W.E.M., Opt. Int. J. Light Electron Opt., 156 (2018) 778.

[5] Basher, M.K., Khalid Hossain, M., Jalal Uddin, M., Ak, M.A.R., and Shorowordi, K.M., Int. J. Light Electron Opt., 172 (2018) 801.

[6] Park, J.E., Han, C.-S., Choi, W.S., and Lim, D., Energies, 14 (2021) 4106.

[7] Al-Husseini, A.M. and Lahlouh, B., Bull. Mater. Sci., 42 (2019) 152.

[8] Silva, A.R., Miyoshi, J., Diniz, J.A., Doi, I., and Godoy, J., Energy Procedia, 44 (2014) 132.

[9] Baker-Finch, S. and McIntosh, K., Prog. Photovolt. Res. Appl., 19 (2011) 406.

[10] Hongjie, L., Honglie, S., Ye, J., Chao, G., Han, Z., and Jiren, Y., Appl. Surf. Sci., 258 (2012) 5451.

[11] Swarnalatha, V., Narasimha Rao, A.V., and Pal, P., Int. Sch. Sci. Res. Innov., 11(2017) 12.

[12] Narasimha Rao, A.V., Swarnalatha, V., and Pal, P., Micro Nano Syst. Lett., 5 (2017) 23.

[13] Singh, P.K., Kumar, R., Lal, M., Singh, S.N., and Das, B.K., Energy Mater. Sol. Cells, 70 (2001) 103.

[14] Ximello, N., Haverkamp, H., and Hahn, G., "New KOH-ETCH Solution to Produce Random Pyramid Structure on Monocrystalline Silicon at Elevated Processing Temperatures and Shortened Processing Times", Erschienen in: Proc. 24th Eur. PVSEC, Hamburg, Munchen (2009).

[15] Menon, P.K., Narasimha Rao, A.V., Murthy, A.L., Pandey, A.K., and Pal, P., Micro Nano Letters, 15 (2020) 365.

[16] Swarnalatha, V., Purohit, S., Pal, P., and Sharma, R.K., Micro Nano Syst. Lett., 10 (2022) 10.

[17] Iqbal, S., Zhang, L.-J., Fu, X.-C., Su, D., Zhou, H.-L., Wu, W., and Zhang, T., AIP Adv., 8 (2018) 025223.

[18] Kyu, M.H. and Jin, S., J. Korean Phys. Soc., 64 (2014) 1132.

[19] Wu, J., Liu, Y., Chen, W., Zhao, Y., Chen, Q., Tang, H., Wang, Y., and Du, X. Appl. Surf. Sci., 506 (2020) 144778.

[20] Qarony, W., Hossain, M.I., Hossain, M.K., Uddin, M.J., Haque, A., Saad, A.R., and Sang, Y.H.T., Results Phys., 7 (2017) 4287.

[21] Lahlouh, B., Al-Husseini, A.M., and Eniyazi, A., Appl. Nanosci., 10 (2020) 117.

[22] Svetoslav, K., Martin, S.B., and Martin, S., Appl. Phys. Lett., 88 (2006) 203107.

[23] Vazsonyi, E., De Clercq, K., Einhaus, R., Van Kerschaver, E., Said, K., Poortmans, J., et al., Energy Mater. Sol. Cells, 57(1999) 179.

[24] Al-Husseini, A.M. and Lahlouh, B., J. Appl. Sci., 17(2017) 374.

[25] Gonchar, K.A., Kitaeva, V.Y., Zharik, G.A., Eliseev, A. A., and Osminkina, L.A., Front. Chem., 6 (2019) 653.

[26] Chen, J., Zhang, N., Man, S., He, P., and Ye, Q., "Investigation of Texturization for Monocrystalline Silicon Wafers with NaOH and Na2B4O7·10H2O Solutions", 6th Int. Conf. Mach. Mater. Environ. Biotechnol. Comput. (2016).

Volume 18, Number 2, 2025. pp. 175-182

Jordan Journal of Physics

ARTICLE

Investigation of the ΔI = 2 Staggering in the Superdeformed Bands of ^{194}Hg Nuclei

K. A. Gado[a,b]

[a] *Department of Physics, Faculty of Science , Al-Baha University, Saudi Arabia.*

[b] *Basic Sciences Department, Bilbeis Higher Institute for Engineering (BHIE), Bilbeis 44713, Sharqia, Egypt.*

Doi: **https://doi.org/10.47011/18.2.7**

Received on: 15/11/2023; *Accepted on: 13/03/2024*

Abstract: The bandhead spin I_0 was determined by solving a quadratic equation based on the Harris parameters, α, β, γ, and δ, which were obtained by fitting the experimental dynamical moment of inertia ϑ_2 to the experimental rotational frequency ω. Due to its high compatibility with the gamma transition energies, the four-parameter collective rotational model of Bohr-Mottelson was employed to predict the transition energies and spins of the levels in the superdeformed (SD) bands of ^{194}Hg (b_1, b_2, b_3). The results show that the energy spectra obtained from the four-parameter collective rotational model are more accurate than those obtained previously. For the $A \sim 190$ mass region, ϑ_2 increases with increasing ω. It is suggested that a discrete approximation of the fourth derivative of the energy difference as a function of angular momentum can appropriately define the staggering in the bands for ^{194}Hg (b_1, b_2, b_3) superdeformed (SD) nuclei. In ^{194}Hg (b_1, b_2, b_3) with long bands ($I \geq 9$), this quantity displays a well-developed staggering pattern (zigzagging behaviour with alternating signs). The interaction between two sequences is shown to account for the staggering in a reasonable way. The model energy expression reproduces successfully the staggering pattern in all considered SD bands for ^{194}Hg (b_1, b_2, b_3) up to $I \sim 50$.

Keywords: Superdeformed band, Spin assignment, Bohr-Mottelson model.

Introduction

In the mass ranges $A \sim 190, 150, 130, 80,$ and 60, many SD bands have been found since the discovery of an SD rotational band in the rapidly spinning nucleus ^{152}Dy [1]. Sadly, gamma energies are the sole publicly available spectroscopic data for the SD bands, as discrete linking transitions between the low-lying normal deformation (ND) states and the SD states have not been observed [2]. The sole method to determine the spin value is theoretical, as there is little experimental data available for the spin of the rotational bands. There are several methods that have been suggested for giving spins to SD states [3]. These methods include both direct and indirect ways to give the states in the SD bands a spin. The direct method expresses the energy of the states of a rotating band as a function of spin, as demonstrated in our earlier studies [4, 5]. Conversely, the indirect methods primarily depend on the use of the Harris formula to match the experimental dynamical moment of inertia data [6]. The spin is then computed using the parameters derived from the fit. The spin can be described as an expansion in the rotational frequency in such a parameterization. Since SD states were seen down to relatively low spin and most bands have very similar, gradually rising dynamical moment of inertia values as increasing rotational frequency, the SD bands in the $A \sim 190$ region are of great interest. The gradual alignment of high-j intruder protons and neutrons in pairs, together with pair correlations,

Corresponding Author: K. A. Gado **Emails**: qjado76@gmail.com, kassem_gado@bhie.edu.eg

is the common source of this smooth rise in the dynamical moment of inertia. The $i_{\frac{13}{2}}$ protons and $j_{\frac{15}{2}}$ neutrons are the intruder orbitals that cause band crossing. Throughout the $A\sim 190$ region, there is virtually no variation in the high-N intruder orbital structure [7]. As a function of spin or rotational frequency, some SD nuclear bands exhibit a zigzag behavior in gamma transition energies. This is referred to as bifurcation or $\Delta I = 2$ staggering. Two $\Delta I = 4$ sequences with spin values $I + 4n$ and $I + 4n + 2$ $(n = 0,1,2,3,\ldots)$ are formed when the bands were perturbed. There are several interpretations for the $\Delta I = 2$ energy staggering. In contrast to a 180^0 rotation, which yields a typical $\Delta I = 2$ sequence, Hamamoto and Mottelson [8] proposed that there may be evidence for a novel symmetry in the nuclear Hamiltonian, specifically, invariance under a 90° rotation about a rotational axis. According to Pavlichenkov and Flibotte [9], the alignment of total nuclear angular momentum along the axis perpendicular to the long deformation axis of a prolate nucleus is thought to be connected to the staggering. According to Macchiavelli *et al.* [10], the $\Delta I = 2$ staggering results from the mixing of many rotating bands with $\Delta I = 4$ differences. The purpose of this study is to discuss the genesis of $\Delta I = 2$ staggering in the $A \sim 190$ mass region and to highlight several theoretical characteristics that are utilized to characterize the properties of SD nuclei. Specifically, we provide a way to assign bandhead spin. More than 85 SD bands have been detected in the $A = 190$ mass range alone in Au, Hg, Tl, Pb, Bi, and Po nuclei, making it a region of particular interest.

2. Bohr-Mottelson Model: Mathematical Review

In Ref. [11], the rotational energy is described as a function of $I(I + 1)$. An extension in powers of $I(I + 1)$ can be used for small enough values of I.

$$E_{rot}[I(I+1)] = AI(I+1) + B[I(I+1)]^2 + C[I(I+1)]^3 + D[I(I+1)]^4 + \cdots. \quad (1)$$

Here, $B, C, D, \ldots$ are corresponding higher-order inertial parameters, and A is the intrinsic matrix element. The ratio of angular momentum, $\hat{I} = \sqrt{I(I+1)}$, to angular frequency, ω, is known as the kinematic moment of inertia, ϑ_1.

$$\vartheta_1 = \frac{\hbar \hat{I}}{\omega}. \quad (2)$$

But

$$\omega = \frac{1}{\hbar}\frac{dE}{d\,\hat{I}}. \quad (3)$$

Substituting Eq. (3) into Eq. (2), we get:

$$\vartheta_1 = \frac{\hbar^2}{2}\left[\frac{dE}{d\hat{I}^2}\right]^{-1}. \quad (4)$$

One can easily demonstrate from the set of Eqs. (2)-(4):

$$\frac{dE}{d\omega^2} = \frac{dE}{d\hat{I}^2}\frac{d\hat{I}^2}{d\omega^2} = \frac{\hbar^2}{2\vartheta_1}\frac{d(\omega^2\vartheta_1^2)}{\hbar^2 d\omega^2} = \frac{1}{2\vartheta_1}\left[\vartheta_1^2 + 2\vartheta_1\omega^2\frac{d\vartheta_1}{d\omega^2}\right] = \frac{1}{2}\vartheta_1 + \omega^2\frac{d\vartheta_1}{d\omega^2}. \quad (5)$$

Differentiating Eq. (1) with respect to $\hat{I}^2$ and using the expansion $(1+x)^{-1}$ with $x = 2\frac{B}{A}\hat{I}^2 + 3\frac{C}{A}\hat{I}^4$, and neglecting higher-order terms due to their negligible influence at high spins, we find:

$$\vartheta_1 = \frac{\hbar^2}{2}\frac{1}{A} - \hbar^2\frac{B}{A^2}\hat{I}^2 + \frac{\hbar^2}{2}\left(\frac{4B^2}{A^3} - \frac{3C}{A^2}\right)\hat{I}^4 + 6\hbar^2\frac{BC}{A^3}\hat{I}^6 \quad (6)$$

An alternative approach substitutes the square of the angular velocity ω^2 as the expansion parameter in lieu of the variable $\hat{I}^2$.

$$\vartheta_1 = \frac{\hbar^2}{2}\frac{1}{A} - \hbar^2\frac{B}{A^2}\omega^2 + \frac{\hbar^2}{2}\left(\frac{4B^2}{A^3} - \frac{3C}{A^2}\right)\omega^4 + 6\hbar^2\frac{BC}{A^3}\omega^6 \quad (7)$$

Introducing Harris parameters, α, β, γ, and δ, the above equation reads [12]:

$$\vartheta_1 = \alpha - \beta\omega^2 + \gamma\omega^4 + \delta\omega^6 \quad (8)$$

Substitute the following for Eq. (5):

$$E(\omega) = \frac{1}{2}\alpha\omega^2 + \frac{3}{4}\beta\omega^4 + \frac{5}{6}\gamma\omega^6 + \frac{7}{8}\delta\omega^8. \quad (9)$$

From Eq. (3), one may find the dynamical moment of inertia by:

$$\omega\hbar d\hat{I} = dE$$

$$\omega\hbar\frac{d\hat{I}}{d\omega} = \frac{dE}{d\omega}$$

$$\vartheta_2 = \frac{1}{\omega}\frac{dE}{d\omega}. \quad (10)$$

Substitute the following for Eq. (9). After some simplification, we get:

$$\vartheta_2(\omega) = \alpha + 3\beta\omega^2 + 5\gamma\omega^4 + 7\delta\omega^6. \quad (11)$$

By fitting the experimental dynamical moment of inertia, defined as: $\vartheta_2 = \frac{4\hbar^2}{\Delta E_\gamma(I)}$

where $\Delta E_\gamma(I) = E_\gamma(I+2) - E_\gamma(I)$, and the experimental rotational frequency $\hbar\omega(I) = \frac{E_\gamma(I+2)+E_\gamma(I)}{4}$ one can extract the parameters α, β, γ and δ. As mentioned in the introduction, the relationship $\vartheta_2 = \hbar\frac{d\hat{I}}{d\omega}$ may be used to indirectly determine the band head spin by integrating Eq. (11) with respect to ω, leading to an expression for intermediate spin:

$$\hbar\hat{I} = \alpha\omega + \beta\omega^3 + \gamma\omega^5 + \delta\omega^7 + c, \quad (12)$$

where c is the constant of integration. Leave this to C. L. Wu [13]. For SD band cascade:

$$I_0 + 2n \rightarrow I_0 + 2n - 2 \rightarrow \ldots\ldots I_0 + 2 \rightarrow I_0. \quad (13)$$

The transition energies that were noticed are: $E_\gamma(I_0 + 2n), E_\gamma(I_0 + 2n - 2), E_\gamma(I_0 + 2n - 4), \ldots, E_\gamma(I_0 + 4), E_\gamma(I_0 + 2)$, where I_0 is the bandhead spin. As long as the discriminant is greater than or equal to zero, the bandhead spin may be determined using Eq. (12), as follows:

$$I_0^2 + 5I_0 + 6 - (\alpha\omega + \beta\omega^3 + \gamma\omega^5 + \delta\omega^7)^2 = 0. \quad (14)$$

The bandhead spin, I_0, is rounded to the nearest integer and is regarded as a free parameter. One way to confirm the effectiveness of the four-parameter collective rotational model for the Bohr-Mottelson is to observe the fluctuation in the experimental transition energies $E_\gamma(I)$ for ^{194}Hg (b_1, b_2, b_3) in a SD band ($\Delta I = 2$ staggering effect). In order to examine the $\Delta I = 2$ staggering in further detail, one computes the fourth derivative of the transition energies $\Delta^4 E_\gamma(I)$ at a given spin I by [14]:

$$\Delta^4 E_\gamma(I) = 2^{-4}\big[E_\gamma(I+4) - 4E_\gamma(I+2) + 6E_\gamma(I) - 4E_\gamma(I-2) + E_\gamma(I-4)\big]. \quad (15)$$

To be able to track higher-order changes in the SD bands' transition energies, we decided to employ the equation above.

3. Results and Discussion

We calculated I_0 of the SD bands of ^{194}Hg (b_1, b_2, b_3) using the Harris expansion for the current situation where we only know the experimental transition energies. The experimental dynamical moment of inertia was firstly fitted with rotational frequency using Eq. (11), and the band-head spin of the SD bands of ^{194}Hg (b_1, b_2, b_3) was then obtained by solving the quadratic Eq. (14), using the Harris parameters [15]. These parameter values, obtained from the fitting procedure, are presented in Table 1.

TABLE 1. The optimal Harris parameters were computed and adopted for the chosen SD nuclei in order to examine the bandhead spins.

SD band	Optimal Harris Parameters			
	$\alpha[\hbar^8 MeV^{-7}] \times 10^1$	$\beta[\hbar^6 MeV^{-5}] \times 10^1$	$\gamma[\hbar^4 MeV^{-3}] \times 10^2$	$\delta[\hbar^2 MeV^{-1}] \times 10^3$
^{194}Hg(b_1)	1.32	2.02	4.53	-2.09
^{194}Hg(b_2)	1.37	1.56	3.29	-1.34
^{194}Hg(b_3)	1.37	2.25	2.07	-0.92

Unfortunately, as indicated by Eq. (12)—specifically the integration constant—such a process involves some uncertainty. In order to resolve this stalemate, as imposed by C. L. Wu [13], the constant c is considered to be the initial alignment i_0, which can be assumed to be zero, since no alignment occurs at $\omega = 0$.

TABLE 2. Values of bandhead spin I_0 for studied SD bands, where b_1, b_2, and b_3 refer to band number 1, band number 2, and band number 3, respectively.

SD band	Bandhead spin, $I_0[\hbar]$			
	Present Work (PW)	Ref. [11]	Ref. [16]	Exp. [17]
^{194}Hg(b_1)	8	8	8	8
^{194}Hg(b_2)	7	8	8	8
^{194}Hg(b_3)	7	9	11	9

Table 2 clearly shows that the bandhead spin of the SD band of the ^{194}Hg (b1) is in good agreement with both the experimental analysis [17] and the theoretical analyses [11, 16]. In the second SD band, ^{194}Hg (b_2), the shift of spin levels from even to odd is attributed to a one-unit decrease in the band-head spin. Finally, for the third SD band, ^{194}Hg(b_3), the deviation in band-

head spin compared to Ref. [17] is the same as that reported in Ref. [16].

Under the adiabatic approximation, the transition energy Eγ(I)E_\gamma(I)

$E_\gamma(I)$ —where I is the spin of the state—can be expressed as:

$$E_\gamma(I) = Dg_4 + Cg_3 + Bg_2 + Ag_1, \quad (16)$$

where the four parameters $A, B, C,$ and D are determined by the Bohr-Mottelson model for an axially symmetric nucleus. Here, $g_i = (I^2 + 5I + 6)^i - (I^2 + I)^i$, $i = 1, 2, 3, 4$. Equation (16) was utilized to fit the angular spins of the experimental transition energies for the SD bands of ^{194}Hg (b_1, b_2, b_3) to get the parameters of our model, as shown in Table 3.

TABLE 3. The optimal parameters of the four-parameter collective rotational model for the Bohr-Mottelson were computed and adopted for the chosen SD nuclei.

SD band	Optimal parameters of the four-parameter collective rotational model			
	$D[MeV] \times 10^{-14}$	$C[MeV] \times 10^{-10}$	$B[MeV] \times 10^{-7}$	$A[MeV] \times 10^{-3}$
^{194}Hg(b_1)	2.70	-1.60	2.03	4.71
^{194}Hg(b_2)	1.80	-1.01	0.75	7.87
^{194}Hg(b_3)	-0.20	0.33	-2.54	5.33

In the SD band ^{194}Hg (b_1, b_2, b_3), the value of B/A is on the order of 10^{-4}, indicating that B/A decreases as one approaches the configurations for which the deformed shape is more stable.

TABLE 4. The calculated transition energies, E_γ, for our three SD bands in ^{194}Hg, compared to experimental data and other theoretical models.

SD band	Transition Energy, $E_\gamma[MeV]$							
	Present Work (PW)		Ref. [11]		Ref. [16]		Exp. [17]	
	I	E_γ	I	E_γ	I	E_γ	I	E_γ
	10	0.219	10	0.204	10	0.208	10	0.212
	12	0.258	12	0.246	12	0.250	12	0.254
	14	0.297	14	0.288	14	0.293	14	0.296
	16	0.336	16	0.330	16	0.335	16	0.337
	18	0.375	18	0.370	18	0.376	18	0.377
	20	0.413	20	0.411	20	0.416	20	0.417
	22	0.452	22	0.450	22	0.456	22	0.455
	24	0.49	24	0.489	24	0.494	24	0.492
	26	0.527	26	0.527	26	0.532	26	0.528
	28	0.563	28	0.563	28	0.569	28	0.563
^{194}Hg(b_1)	30	0.598	30	0.599	30	0.604	30	0.597
	32	0.632	32	0.634	32	0.639	32	0.630
	34	0.664	34	0.668	34	0.672	34	0.662
	36	0.695	36	0.701	36	0.703	36	0.693
	38	0.725	38	0.732	38	0.733	38	0.724
	40	0.754	40	0.762	40	0.762	40	0.754
	42	0.782	42	0.790	42	0.789	42	0.784
	44	0.811	44	0.817	44	0.814	44	0.813
	46	0.841	46	0.843	46	0.837	46	0.843
	48	0.874	48	0.867	48	0.858	48	0.872
	50	0.913	50	0.889	50	0.889	50	0.903
rms	9.05×10^{-3}		1.57×10^{-2}		1.11×10^{-2}			
	9	0.205	10	0.198	10	0.200	10	0.201
	11	0.244	12	0.239	12	0.241	12	0.242
	13	0.283	14	0.280	14	0.282	14	0.283
	15	0.322	16	0.320	16	0.322	16	0.323
^{194}Hg(b_2)	17	0.361	18	0.360	18	0.362	18	0.363
	19	0.400	20	0.400	20	0.402	20	0.402
	21	0.439	22	0.438	22	0.441	22	0.440
	23	0.476	24	0.476	24	0.479	24	0.478

SD band	Transition Energy, $E_\gamma[MeV]$							
	Present Work (PW)		Ref. [11]		Ref. [16]		Exp. [17]	
	25	0.514	26	0.514	26	0.516	26	0.514
	27	0.550	28	0.550	28	0.552	28	0.550
	29	0.586	30	0.586	30	0.588	30	0.585
	31	0.620	32	0.621	32	0.623	32	0.619
	33	0.653	34	0.655	34	0.656	34	0.652
	35	0.686	36	0.688	36	0.689	36	0.685
	37	0.717	38	0.720	38	0.720	38	0.716
	39	0.747	40	0.751	40	0.750	40	0.747
	41	0.777	42	0.780	42	0.779	42	0.778
	43	0.806	44	0.808	44	0.806	44	0.808
	45	0.837	46	0.835	46	0.832	46	0.837
	47	0.868	48	0.861	48	0.856	48	0.867
rms	5.35×10^{-3}		6.63×10^{-3}		5.00×10^{-3}			
	9	0.221	11	0.218	13	0.222	11	0.222
	11	0.262	13	0.258	15	0.260	13	0.262
	13	0.303	15	0.299	17	0.301	15	0.303
	15	0.343	17	0.339	19	0.341	17	0.343
	17	0.382	19	0.378	21	0.381	19	0.382
	19	0.420	21	0.418	23	0.420	21	0.420
	21	0.458	23	0.456	25	0.458	23	0.458
	23	0.495	25	0.494	27	0.496	25	0.495
	25	0.531	27	0.531	29	0.533	27	0.531
	27	0.566	29	0.567	31	0.569	29	0.566
^{194}Hg(b_3)	29	0.601	31	0.603	33	0.604	31	0.601
	31	0.635	33	0.637	35	0.639	33	0.635
	33	0.668	35	0.671	37	0.672	35	0.668
	35	0.700	37	0.704	39	0.704	37	0.700
	37	0.732	39	0.736	41	0.736	39	0.732
	39	0.763	41	0.766	43	0.766	41	0.763
	41	0.794	43	0.796	45	0.794	43	0.794
	43	0.824	45	0.824	47	0.822	45	0.824
	45	0.854	47	0.851	49	0.848	47	0.854
	47	0.884	49	0.877	51	0.873	49	0.884
rms	1.01×10^{-3}		7.83×10^{-3}		5.73×10^{-3}			

As shown in Table 4 and based on the root mean square (rms) deviation test results [18], the transition energies E_γ computed with our model correspond better with the experimental values than with other models, particularly for ^{194}Hg(b_1). We conclude that this deviation is due to the difference in the way the issue is addressed between our model and other models. The rotational frequency $\hbar\omega$, kinematic ϑ_1, and dynamic ϑ_2 moments of inertia are now related in the following way:

$$\hbar\omega(I) = 8D\hat{I}^7 + 6C\hat{I}^5 + 4B\hat{I}^3 + 2A\hat{I}. \quad (17)$$

$$\vartheta_1(I) = \frac{\hbar^2}{8D\hat{I}^6+6C\hat{I}^4+4B\hat{I}^2+2A}. \quad (18)$$

$$\vartheta_2(I) = \frac{\hbar^2}{56D\hat{I}^6+30C\hat{I}^4+12B\hat{I}^2+2A}. \quad (19)$$

Figure 1 shows that the behavior of the kinematic and dynamic inertia moments calculated from our model of ^{194}Hg (b_1, b_2, b_3) is in good agreement with the experimental data, with the dynamic moment showing the closest match. It demonstrates how well our model can describe the moment of inertia's behavior in the rotating region A~190. We suggest that the fourth derivative of the transition energy differences [Eq. (15)], as a function of angular momentum I, provides a more accurate representation of the observed staggering in the SD bands of ^{194}Hg (b_1, b_2, b_3) than a plot of the moment of inertia parameter versus the angular momentum. The transition energies between levels differing by two units of angular

momentum are experimentally well-determined quantities:

$$\Delta E_\gamma(I_j) = E_\gamma(I_j + 2) - E_\gamma(I_j). \quad (20)$$

We applied Eq. (15) and Eq. (20) to ^{194}Hg (b_1, b_2, b_3). Here, I_j is the angular momentum that our model assigns, $I_j = I_0 + 2j$, $j = 0, 1, 2, 3, \ldots$ to the region A~190, for which the experimentally reported transition energies are long enough ($I \geq 9$).

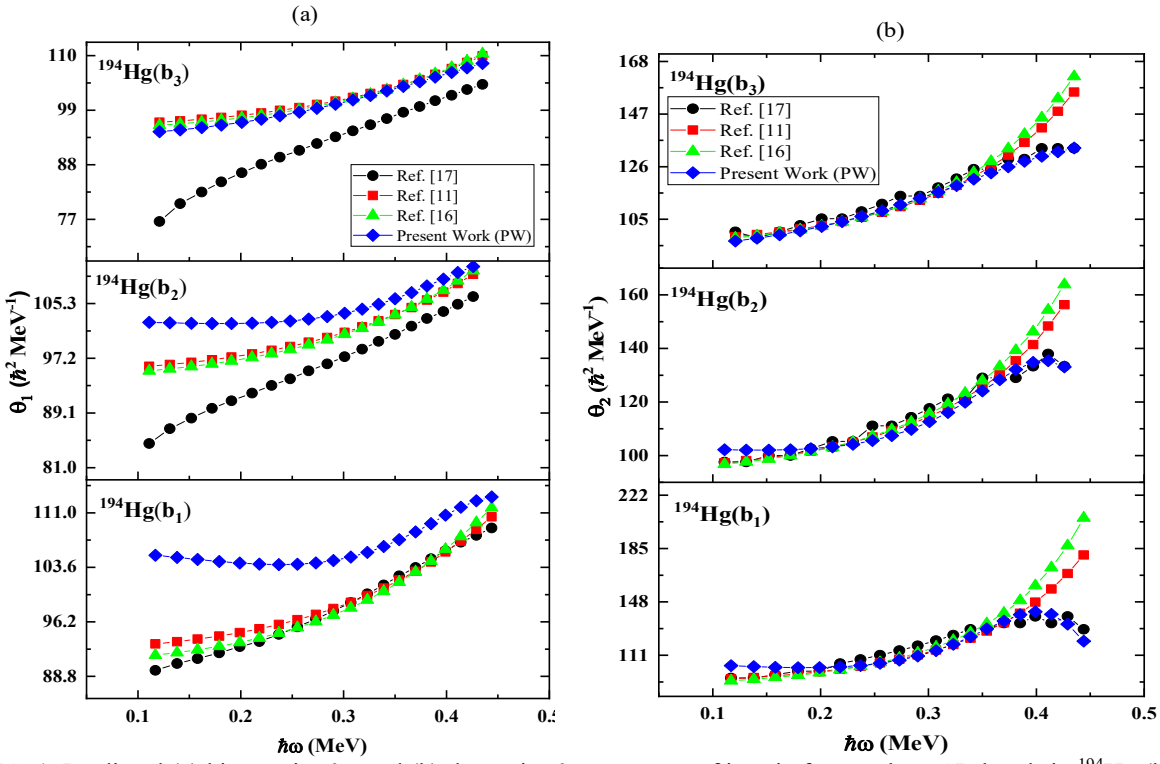

FIG. 1. Predicted (a) kinematic, ϑ_1, and (b) dynamic, ϑ_2, moments of inertia for our three SD bands in ^{194}Hg (b_1, b_2, b_3) against rotational frequency, $\hbar\omega$, along with a comparison with experimental data and alternative formulae (line with black circles representing, Δ^4 E_γ^Cal resulting from calculated transition energies, line with red squares representing experimental transition energies, and line with blue triangles representing the difference between them).

Figure 2 displays a discernible staggering pattern in all cases, ^{194}Hg (b_1, b_2, b_3). . Generally, one observes an identical behavior in the staggering between the $\Delta^4 E_\gamma^{Exp}$ and $\Delta^4 E_\gamma^{DeV}$ with fluctuations in the amplitude as the angular momentum I increases. This oscillation may be associated with the rotational structure of superdeformed bands of ^{194}Hg (b_1, b_2, b_3), which is somewhat perturbed. However, it is reasonable to interpret this behavior of the staggering effect in terms of the interaction between the two sequence bands. The amplitude of the staggering varies only slightly among the different bands. Therefore, any nonzero values of the parameter $\Delta^4 E_\gamma$ suggest that the order of rotational motion of the nuclear system exceeds $\hat{I}^4$. This supports and validates the applicability of our model. The results demonstrate that the four-parameter collective rotational model of Bohr and Mottelson provides a meaningful description of the $\Delta I = 2$ staggering effect in the superdeformed bands of ^{194}Hg (b_1, b_2, b_3). Furthermore, the behavior of this effect can potentially be estimated analytically based on collective properties of the nucleus.

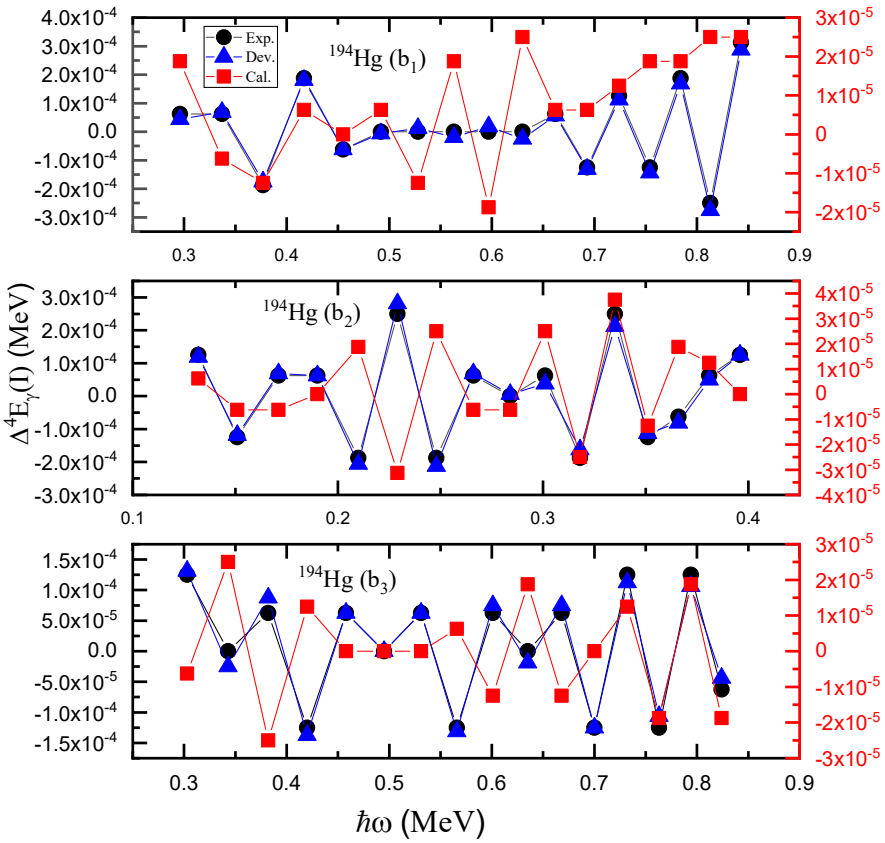

FIG. 2. $\Delta I = 2$ staggering, $\Delta^4 E_\gamma(I)$, calculated using the five-point formula versus nuclear rotational frequency for the SD bands in ^{194}Hg (b_1, b_2, b_3), experimental values, and the differences between them.

4. Conclusion

A theoretical version of the Harris four-parameter formula in even powers of angular frequency was used to fit the smoothed experimental dynamical moment of inertia data. A fitting approach was used to modify the expansion parameters. By integrating the computed ϑ_2, the spins of the SD rotational bands in ^{194}Hg (b_1, b_2, b_3) were assigned using the best expansion parameters from the fit by solving the quadratic equation. The closest integer of the fitted I_0 was used to determine the bandhead spin. The values of the bandhead spins of our selected SD band in ^{194}Hg (b_1, b_2, b_3) are fairly consistent with all the spin assignments of other approaches. In the $A \sim 190$ mass region, the dynamical moment of inertia increases with increasing rotational frequency. Within the scope of the four-parameter model, the SD band structure of ^{194}Hg (b_1, b_2, b_3) is accurately recreated. The finite difference approximation to the fourth derivative of the gamma transition energies is represented by a smooth reference, which also explains the $\Delta I = 2$ energy staggering found in three of our chosen SD bands. As spin or rotational frequency increases, the parameter $\Delta^4 E_\gamma(I)$ alternates in sign, a behavior characteristic of $\Delta I = 2$ staggering.

References:

[1] Shalaby, A.S., Commun. Theor. Phys., 41 (3), (2004) 454.

[2] Shalaby, A.S., Acta Phys. Hung. A, 25 (1) (2006) 117.

[3] Khalaf, A.M. et al., UPB Sci. Bull., Ser. A, 82 (3) (2020) 231.

[4] Gado, K.A., Nucl. Phys. At. Energy, 24 (2023) 336.

[5] Gado, K.A., Nucl. Phys. At. Energy, 25 (1) (2024) 19.

[6] Khalaf, A.M., Zaki, A.A., and Ismail, A.M., Int. J. Adv. Res. Phys. Sci., 3 (9) (2016) 21.

[7] Abdalaty, A.A., Kotb, M., Okasha, M.D., and Khalaf, A.M., Phys. At. Nucl., 83 (6) (2020) 849.

[8] Hamamoto, I. and Mottelson, B., Phys. Lett. B, 333 (1994) 294.

[9] Pavlichenkov, I.M. and Flibotte, S., Phys. Rev. C, 51 (1995) R460.

[10] Macchiavelli, A.O. et al., Phys. Rev. C, 51 (1) (1995) R1.

[11] Okasha, M.D., Glob. J. Sci. Front. Res. A Phys. Space Sci., 14 (3) (2014) 26.

[12] Khalaf, A.M. et al., Int. J. Theor. Appl. Sci., 7 (2) (2015) 33.

[13] Wu, C.L., Feng, D.H., and Guidry, M.W., Phys. Rev. Lett., 66 (10) (1991) 1377.

[14] Semple, A.T. et al., Phys. Rev. Lett., 76 (20) (1996) 3671.

[15] Saethre, O. et al., Nucl. Phys. A, 207 (1973) 486.

[16] Khalaf, A.M., Okasha, M.D., and Ragheb, E., Aust. J. Basic Appl. Sci.,10 (16) (2016) 192.

[17] Singh, B., Zywina, R., and Firestone, R.B., Nucl. Data Sheets, 97 (2002) 241.

[18] Khalaf, A.M. et al., Int. J. Theor. Appl. Sci., 6 (2) (2014) 47.

Volume 18, Number 2, 2025. pp. 183-196

Jordan Journal of Physics

ARTICLE

Growth and Properties of Pure Phase Kesterite CZTS Nanostructure for Electrochemical, Photocatalytic, and Antibacterial Applications

S. Manjula[a], **A. Sarathkumar**[a], **S. Nithishkumar**[a], **G. Sivakumar**[b] and **K. Mohanraj**[c]

[a] *Department of Science and Humanities-Physics, Krishnasamy College of Engineering and Technology, Tamil Nadu 607 109, India.*

[b] *CISL, Annamalai University, Tamil Nadu, 608 002 India.*

[c] *Department of Physics, School of Basic and Applied Sciences, Centra University of Tamil Nadu, Thiruvarur - 610 101, India.*

Doi: **https://doi.org/10.47011/18.2.8**

Received on: 23/11/2023; *Accepted on: 17/04/2024*

Abstract: Surfactant-free, high-grade, self-assembled quaternary copper zinc tin sulfide (CZTS) nanoparticles were synthesized successfully via a simple hydrothermal method. Different thiourea concentrations were used as chalcogen precursors, and their influences were investigated. The concentration of sulfur precursor gradually increased to obtain a pure kesterite phase, which was identified by X-ray diffractometer (XRD) and Fourier-transform Raman spectrometer (FT-Raman). Field emission scanning electron microscopy (FESEM) revealed diverse nanostructures, such as spheres, plates, and rose-like formations. The specific capacitance values of pure-phase kieserite CZTS nanoparticles were analyzed using a three-electrode system. The photocatalytic activity of CZTS nanoparticles against methylene blue (MB) and crystal violet (CV) degradation under visible light irradiation reached 93% and 89% within 70 min, respectively. Also, CZTS TU-10 nanostructures exhibited stronger antibacterial performance against both gram-positive (*Streptococcus pneumoniae, Streptococcus pyogenes*) and gram-negative (*Klebsiella pneumoniae, Vibrio parahaemolyticus*) pathogens. The maximum inhibition zone (26 mm) was obtained against *Vibrio parahaemolyticus* bacteria using the agar well diffusion method. These results imply that kesterite CZTS could be considered an efficient candidate for multiple applications.

Keywords: CZTS, Hydrothermal, Morphology, Electrochemical, Specific capacitance.

1. Introduction

Cu_2ZnSnS_4 (CZTS) is a p-type semiconducting material with promising potential for thermoelectric, photocatalytic, and energy harvesting applications [1]. Although CZTS nanoparticle synthesis has been reported already, some significant problems remain. The formation of these compounds is complicated by the multiple components that go into their production [2]. Due to the intrinsically small composition zone for a single-phase CZTS, the simplicity of component vaporization, and the high chemical potential for secondary phase formation, the formation of a pure single-phase structure of this product is challenging [3, 4]. Surfactant-free synthesis methods employing different sulfur sources and concentrations have received limited attention [5]. CZTS nanoparticles have been synthesized by hydrothermal, sol-gel [6], solvothermal [7], SILAR [8], hot injection [9], and pulsed laser deposition methods. Among these techniques, hydrothermal treatment is the most important due to its simple process, low cost, environmental friendliness, and control over the

Corresponding Author: G. Sivakumar **Email**: gskdopcisl@gmail.com

structure and morphology of the material [10]. Electrochemical supercapacitors are gaining much attention among the various energy storage technologies because of their exceptional durability [11], elevated energy and power density, expedited redox processes for charging and discharging, environmentally sustainable attributes, and cost-effectiveness [12]. However, limited research has focused on the electrochemical behavior and energy storage applications of CZTS nanostructures [13].

Hence, in the present work, we propose a facile one-step hydrothermal method for the preparation of kesterite CZTS nanostructures. The novelty of the present work lies in the surfactant-free synthesis of single-phase CZTS nanoparticles. A key objective is to investigate the effect of varying sulfur precursor concentrations on the phase formation of CZTS. Also, this study explores the specific capacitance of CZTS nanostructures through cyclic voltammetry (CV) and GCD charge-discharge techniques. The photocatalytic degradation of CZTS is tested using two different dyes. The antibacterial activity of CZTS nanostructure is examined against gram-positive and gram-negative bacteria.

2. Materials and Methods

Copper chloride dihydrate, zinc nitrate hexahydrate, and stannous chloride dihydrate were used as metal precursors for Cu, Zn, and Sn, respectively. For the sulfur source, thiourea was used. All the compounds were acquired from Lakshmi Scientific Company, Chidambaram, India, AR grade, and used without purification. Polyvinylidene fluoride (PVDF), carbon black, N-methyl 2-pyrrolidone solution (NMP), and nickel plate were purchased from Sabari Scientific Company, Tamil Nadu, India, for electrochemical processing.

2.1 Hydrothermal Synthesis of CZTS Nanostructures

To synthesize CZTS nanostructures by a hydrothermal method, thiourea (TU) was used as a sulfur source. In a typical synthesis of CZTS nanostructures (TU-4), the molar ratio (Cu:2, Zn:1, Sn:1, Tu:4) was taken as follows: 0.08 M copper chloride dihydrate (0.136 g/10 ml), 0.04 M zinc nitrate hexahydrate (0.059 g/5 ml), 0.04 M stannous chloride dihydrate (0.045 g/5 ml), and 0.16 M thiourea (TU - 0.243 g/20 ml). A solution was prepared using distilled water and stirred for 30 min. The resulting solution was transferred into a Teflon-lined stainless-steel autoclave and heated in a muffle furnace at 210 °C for 24 hours, as described in our earlier work [14]. After the reaction, the autoclave was allowed to cool naturally to room temperature. The obtained precipitate was cleaned using distilled water and ethanol and dried for 3 hours in a hot air oven at 70°C. The synthesis was performed without the addition of any surfactants or stabilizing/binding agents. Because of the high temperature used during the synthesis of CZTS nanoparticles, more thiourea was added to compensate for the amount that evaporated. To examine the growth and properties of pure phase kesterite Cu_2ZnSnS_4 nanostructure by using different sulfur/copper concentrations (S/Cu = 2, 3, 4, and 5) on the structural, phase formation, and morphological features of CZTS nanostructures, the above procedure was followed to synthesize TU-6 (2:1:1:6), TU-8 (2:1:1:8), and TU-10 (2:1:1:10) samples.

2.2 Characterization

The crystal structure and phase composition of the synthesized CZTS nanostructures were characterized by X-ray diffraction (XRD) using a PANalytical X'Pert PRO – Analytic, Germany, operated at 30 mA and 40 kV with Cu Kα radiation (λ = 1.54060Å). Phase confirmation was further carried out using a micro-laser Raman spectrometer (Seiki, Japan) at Alagappa University, Karaikudi.

Surface morphology and elemental composition were analyzed by field emission scanning electron microscopy (FESEM, Carl Zeiss Sigma 300) equipped with energy-dispersive X-ray spectroscopy (EDAX) at CISL, Annamalai University, Chidambaram. Transmission electron microscopy (TEM) was performed using a Tecnai G2 20 S-Twin (200 kV, Japan) at Madurai Kamaraj University, Madurai, to further study the structural properties.

2.2.1. Preparation of the CZTS electrode

To prepare the electrode, a slurry paste was obtained by mixing 80 wt.% CZTS powder, 10 wt.% PVDF, and 10 wt.% carbon black, with N-methyl-2-pyrrolidone (NMP) added dropwise until a uniform paste was formed. This slurry was coated onto a nickel plate (1 cm × 1 cm active area) and dried overnight at 80 °C. The

mass of active material on the electrode was approximately 5 mg. The electrochemical performance was evaluated using a three-electrode system consisting of the prepared CZTS electrode as the working electrode, a platinum wire as the counter electrode, and an Ag/AgCl electrode as the reference electrode. A 2 M KOH aqueous solution was used as the electrolyte.

2.2.2 Electrochemical Performance of the Supercapacitor

The electrochemical characteristics of CZTS nanoparticles were investigated by the cyclic voltammetry technique using a Metrohm Autolab M204 system and a three-electrode cell system with NOVA 2.1.4 software at Annamalai University. Cyclic voltammetry measurements calculated the specific capacitance of the CZTS electrode in the range of a potential window of 0 to 0.6 mV/s with varying scan rates. GCD analysis was performed at different current densities. To determine the specific capacitance (C_{sp}) of the CZTS electrode,[the following equations were used [15].

For cyclic voltammetry:

$$C_{sp} = \frac{\int I \Delta v}{Sm\Delta v} \text{F/g} \quad (1)$$

For GCD:

$$C_{sp} = \frac{Idt}{mdV} \text{F/g} \quad (2)$$

where C_{sp} (Fg^{-1}) is the specific capacitance, $\int I \Delta t$ is the area of the CV curve, s is the scan rate (mV/s), ΔV is the potential window (V), m is the mass of the loaded material (g), I is the current density (A), dt is the discharge time (s), g is the mass of the loaded material, and 'dV' is the potential (V).

2.2.3. Photocatalytic Measurements

The degradation of methylene blue (MB) and crystal violet (CV) dyes in an aqueous solution was used under sunlight as a radiation source. The photocatalytic reaction of the CZTS was measured by using a UV-Vis spectrophotometer. The optimal concentration for the dye is 10^{-4} mol. Blank solutions were prepared by dissolving the dye in 1 liter of distilled water. Initially, 0.05 g of prepared CZTS nanoparticles was added to 100 ml of blank dye solutions. To achieve adsorption-desorption equilibrium between the catalyst (CZTS) and dye, a beaker containing the dye solution and the catalyst was left in dark conditions for 30 minutes. The pH of the MB and CV dye solutions was recorded during photocatalytic activity. For the degradation of dyes, both solutions were stirred separately under sunlight. Every 10 minutes, 5 mL of the solution was collected from the beaker for UV-visible analysis.

2.3 Antibacterial Activity

The CZTS nanoparticles offer the advantages of low toxicity and significant antibacterial activity at low concentrations, all of which are needed for these nanomaterials to act as potent antimicrobial agents inside most living systems [16]. The CZTS was tested for its antibacterial properties by using the agar well diffusion method.

3. Results and Discussion

3.1 Structural Analysis

Structural characteristics of CZTS nanoparticles were analyzed by XRD for different concentrations of thiourea, and the results are presented in Figs. 1(a)-1(d). As seen in Fig. 1(a), the diffraction peaks of TU-4 at 29.07°, 31.53°, and 32.56° are attributed to (102), (103), and (006) hkl planes of CuS binary phase with the hexagonal system (JCPDS: 78-2121). The presence of other peaks at 2θ = 47.53° and 59.12° corresponds to (220) and (224) planes, confirming the presence of the CZTS phase with the tetragonal system (JCPDS: 26-0575) [17]. By increasing the TU concentration to TU-6 and TU-8, the intensity of characterization peaks of CZTS at 2θ = 28.49°, 47.27°, 56.66°, and 59.31° corresponding to the (112), (220), (312), and (224) planes increased. Additionally, the plane corresponding to (102), (103), (006), and (108) of CuS decreased gradually, while peaks related to the CuS phase (e.g., (102), (103), (006), and (108)) gradually diminished. At the highest thiourea concentration (TU-10), the CuS peaks disappeared entirely, and only prominent CZTS peaks were observed at 2θ = 28.42°, 47.58°, 56.14°, and 59.26°, confirming the successful formation of a pure kesterite phase. This indicates that an increased sulfur precursor is essential to suppress secondary phase formation due to sulfur evaporation at elevated temperatures during hydrothermal synthesis [18]. The crystallite size (D) was calculated using Eq.(3), [19]:

$$D = \frac{k\lambda}{\beta cos\theta} \quad (3)$$

The calculated crystallite sizes were 52 nm (TU-4), 45 nm (TU-6), 36 nm (TU-8), and 28 nm (TU-10), indicating the nanocrystalline nature of all samples. The small crystallite sizes indicated that the synthesized CZTS samples were nano-crystalline. Lattice parameters a = b and c ranged from 5.432 to 5.426 Å and 10.853 to 10.842 Å, respectively, in agreement with standard JCPDS values. These results demonstrate that the sulfur concentration significantly influences the structural parameters and phase purity of CZTS nanostructures.

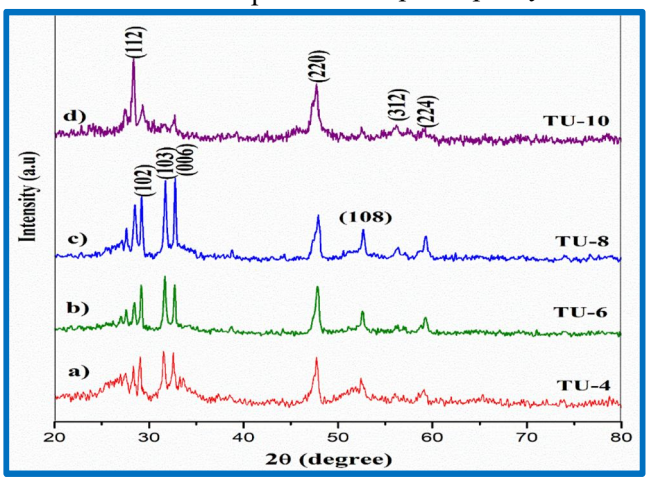

FIG. 1. XRD patterns of CZTS nanoparticles at different concentrations of thiourea (TU).

3.2. Raman Analysis

Raman analysis was carried out to confirm the appearance of minor phases and the phase purity of CZTS nanostructures. The Raman spectra of CZTS nanostructures with different concentrations of TU are shown in Figs. 2(a)-2(d). For the TU-4 sample, a strong Raman peak was observed in the range of 440–465 cm^{-1}, indicating the presence of a CuS secondary phase [4]. When thiourea concentrations were increased to TU-6, the Raman spectra exhibited one additional peak located at 323 cm^{-1}, which was attributed to the CZTS phase. Harinipriya *et al*. and Shalabayev *et al*. reported similar types of results and stated that kesterite CZTS showed Raman peaks at 338 cm^{-1} [5]. The characteristic peak (CZTS) intensity increased with the increasing sulfur concentration of sample TU-8 because the crystal structure of the synthesized CZTS was strongly affected by the initial formation of copper sulfide, which acts as a catalyst for CZTS growth [3]. With further increase in sulfur concentration (TU-10), the peak corresponding to the mixed phase, namely, CuS (467 cm^{-1}), vanished, and the intensity of the peak corresponding to CZTS (338 cm^{-1}) increased gradually. The exclusive presence of kesterite CZTS peaks in the TU-10 sample confirms the successful suppression of secondary phases. This high phase purity is particularly advantageous for photocatalytic and electrochemical applications.

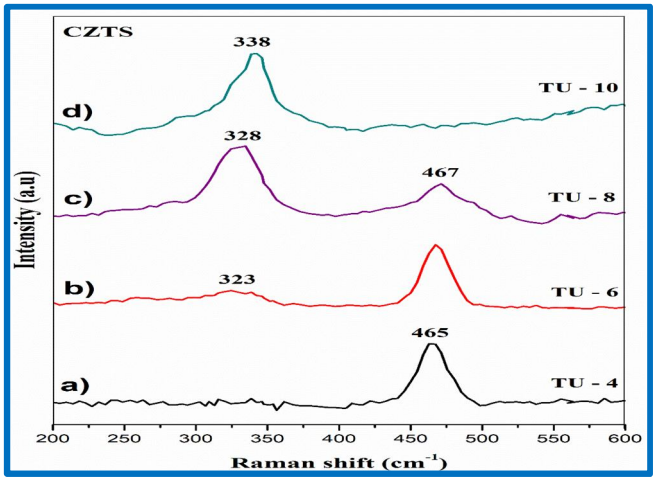

FIG. 2. Raman spectra of CZTS with different TU concentrations.

In addition, intermediate phases such as Cu_3SnS_4 (318 and 295 cm^{-1}), ZnS_2 (315 cm^{-1}), and SnS_2 (351 and 274 cm^{-1}) were not detected in the Raman spectra, indicating that the pure phase of CZTS nanostructures was observed at higher concentration. These results confirmed that the synthesized CZTS TU-10 nanostructure exhibited a pure Raman peak compared to other samples. A similar type of result was obtained from the XRD study.

3.3. Morphological Analysis

The lower (a) and higher (b) magnified FESEM images and EDS spectra (c) with atomic ratio (pie chart) of CZTS samples for different TU concentrations are shown in Figs. 3i-3iv. These analyses were performed to reveal the morphology and microstructural characteristics of the CZTS nanoparticles.

The lower concentration (Fig. 3i) of the TU-4 sample is heterogeneous (plate-like, cubical, and rod-like) in nature. In TU-6 (Fig. 3ii), many hierarchical spherical-like structures, typically measuring 1-2µm in size, are noticed. Upon further increasing the concentration (TU-8), the sphere-like structure changed to hexagonal nanosheets with an approximate thickness of 30-40 nm, attached as a bundle-like formation. At higher TU concentration (TU-10, Fig. 3iv), a well-defined rose-flower-like morphology was observed, composed of interlinked hexagonal nanosheets with an overall particle size in the range of 1–3 µm. The nanosheets result in numerous hierarchical pores on the nanoscale. Fig. 3iv(c) shows the EDS spectrum of the TU-10 sample with the inset depicting the average atomic ratio of the four elements. The atomic ratio of Cu:Zn:Sn:S was found to be 20.70:9.79:15.15:54.36, which is close to the stoichiometric ratio of Cu_2ZnSnS_4 and well matched with the XRD analysis. Table 1 reveals the different elemental composition atomic ratios of different TU concentrations.

The formation of the self-assembled flower-like CZTS nanostructure at high TU concentrations is proposed to occur via the following stages: initially, 1D CZTS nanoparticles form through homogeneous nucleation. These subsequently grow into 2D nanosheets through oriented aggregation, and eventually self-assemble into 3D rose-flower-like architectures via the Ostwald ripening mechanism [21]. This hierarchical structure, with nanosheets as the primary building block, is advantageous due to its large surface area and high aspect ratio, which are beneficial for enhancing electrochemical performance, as reported in previous studies [22].

The gradual release of S^{2-} ions from thiourea and the interaction between the $–NH_2$ groups of thiourea and CZTS nanoparticles are believed to facilitate these stepwise growth processes [21]. Furthermore, the absence of extraneous elements in the EDS spectra confirmed the successful formation of pure-phase CZTS nanostructures.

FE-SEM analysis of the TU-10 sample clearly highlights the influence of sulfur source and sulfur concentration on the size, nucleation extent, morphological changes, and structure of the synthesized CZTS nanostructures. The presence of flower-like morphology with hierarchical pore structure of CZTS nanoparticles confirms the synthesis of phase-pure CZTS, supported by the XRD and Raman studies as well. Hence, further characterization and application studies were carried out using CZTS TU–10 alone.

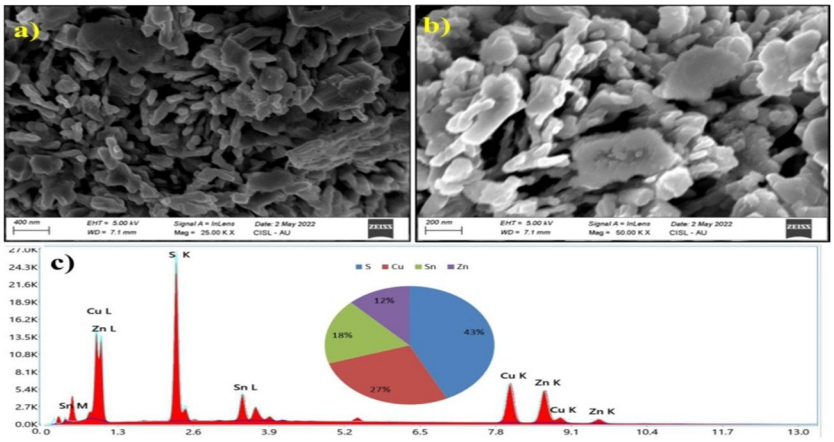

FIG. 3i. FESEM images of TU-4 at (a) lower and (b) higher magnification. (c) EDS spectrum with atomic ratio (inset pie chart).

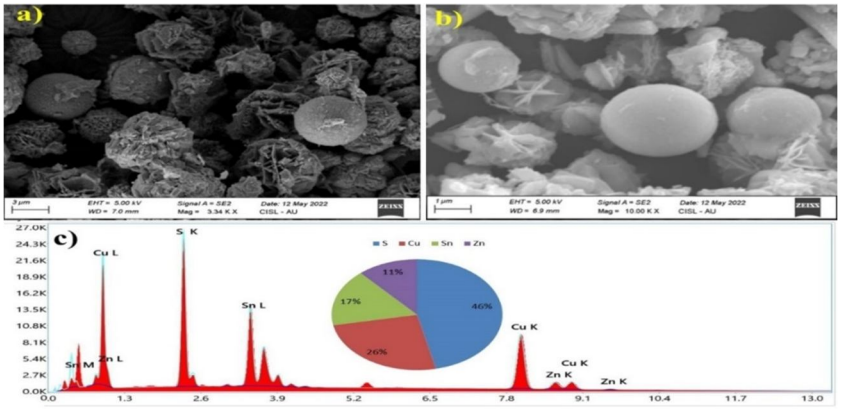

FIG. 3ii. FESEM images of TU-6.

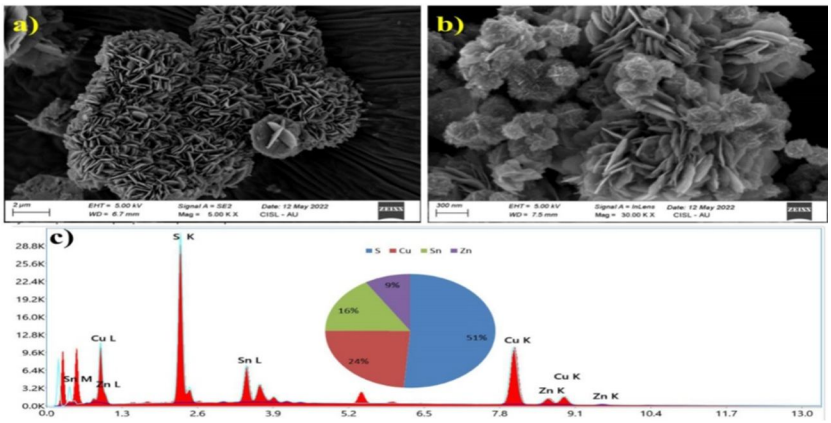

FIG. 3iii. FESEM images of TU-8.

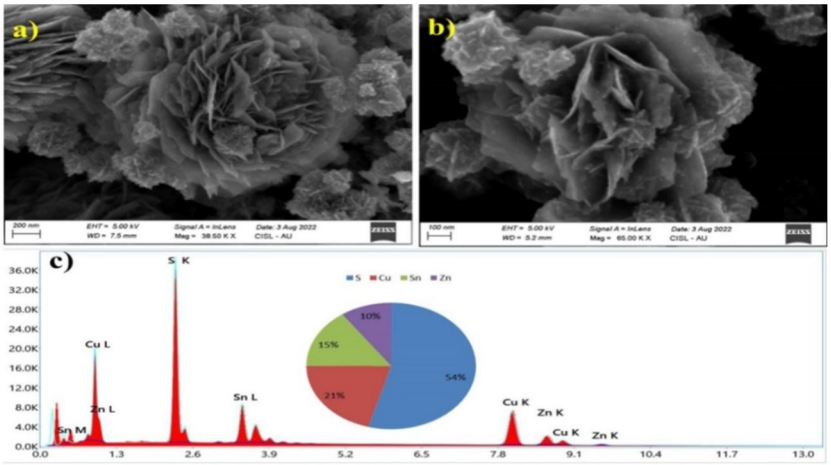

FIG. 3iv. FESEM images of TU-10.

TABLE 1. EDS analysis of CZTS recorded at different TU concentrations.

Composition Ratio (at %)	Sample			
	TU-4	TU-6	TU-8	TU-10
Cu	27.30	25.50	23.80	20.70
Zn	12.14	11.49	8.75	9.79
Sn	17.82	16.56	16.20	15.15
S	42.74	46.45	23.80	54.36
Cu/Zn+Sn	0.91	0.90	0.95	0.82
Zn/Sn	0.68	0.69	0.54	0.64
S/(Cu+Zn+Sn)	0.74	0.86	1.05	1.19
S/Cu	1.56	1.82	2.15	2.62

3.4. Transmission Electron Microscopy (TEM)

The structural and morphological characteristics of the CZTS TU-10 sample were further examined using high-resolution transmission electron microscopy (HRTEM). The different magnifications of the TEM images of the CZTS TU-10 nanostructures are depicted in Figs. 4(a)-4(d) and reveal that the nanoparticles are well dispersed with a rose flower-like structure. The average size of the flower-like structures is approximately 1-2 µm. As seen in Fig. 4(a), the flower-like morphology consists of interconnected nanosheets, consistent with the FESEM results. The number of hexagonal sheets that are less than 50 nm arranged together to form the flower-like structure, which is visually evident from Figs. 4(c)-4(d). Fig. 4(e) shows a single crystalline of the nanosheet that exhibits a lattice fringe value of 0.32 nm corresponding to the (112) plane of CZTS, which seems to be close to the earlier report by [23]. The bright spots in the SAED pattern in Fig. 4(f) corresponding to the (112), (220), and (224) planes were found to be consistent with the planes observed by XRD. The presence of four diffraction rings indicates that the nanoparticles are well crystallized, and the results witness the presence single crystal of pure-phase CZTS nanoparticles.

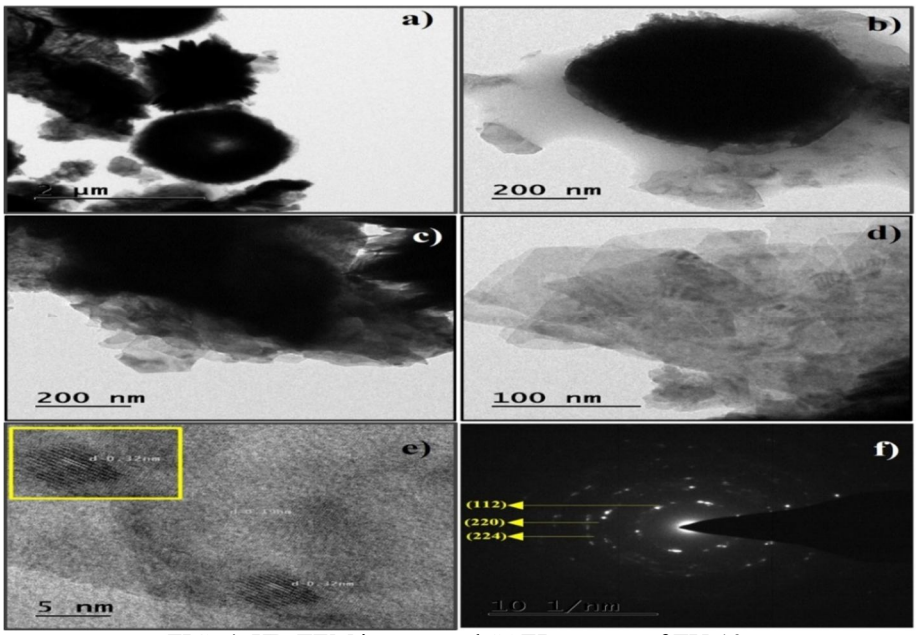

FIG. 4. HR-TEM images and SAED pattern of TU-10.

3.5. XPS Analysis

The CZTS TU-10 sample was examined using X-ray photoelectron spectroscopy to confirm the important information on the surface level, its chemical composition, and valence states. Fig. 5(a) depicts the survey scan spectrum of the CZTS sample, which includes Cu, Zn, Sn, and S. The peak at 284.6 eV C1s is used as a reference, and the peak at 532.9 eV is O1s corresponding to the water molecule at the surface of the sample [24].

High-resolution XPS spectrum of Cu 2p peaks, seen in Fig. 5(b), was found in the binding energies of Cu $2p_{3/2}$ and Cu $2p_{1/2}$ peaks at 933.8 and 953.7 eV, respectively, with a peak separation of 20.1 eV [19]. The observed results confirmed that the oxidation state of Cu is +1. For Zn, peaks split into two energy states, Zn $2p_{3/2}$ and Zn $2p_{1/2,}$ and detected at 1021.9 and 1044.9 eV, respectively, with the distance between the two peaks at 23 eV, as seen in Fig. 5(c). The obtained result proved that Zn is present in an oxidation state of +2 [25]. The Sn peaks observed in Fig. 3.5(d) are found at binding energies of 486.2 and 494.4 eV and could be attributed to the Sn $3d_{5/2}$ and Sn $3d_{3/2}$ peaks, which match the conventional splitting of 8.2 eV [26]. As shown in Fig. 5(e), the S 2p peaks were successfully deconvoluted into two distinct peaks. The primary peaks located at 164.8 eV and the secondary peaks detected at 165.9 eV were assigned for $2p_{3/2}$ and $2p_{1/2}$, and the difference is 1.1 eV, corresponding to S^{2-} [27]. The obtained valence states of Cu^{1+}, Zn^{2+}, Sn^{4+}, and S^{2-} provide evidence that the prepared CZTS TU-10 sample was in good agreement with the pure phase kesterite Cu_2ZnSnS_4.

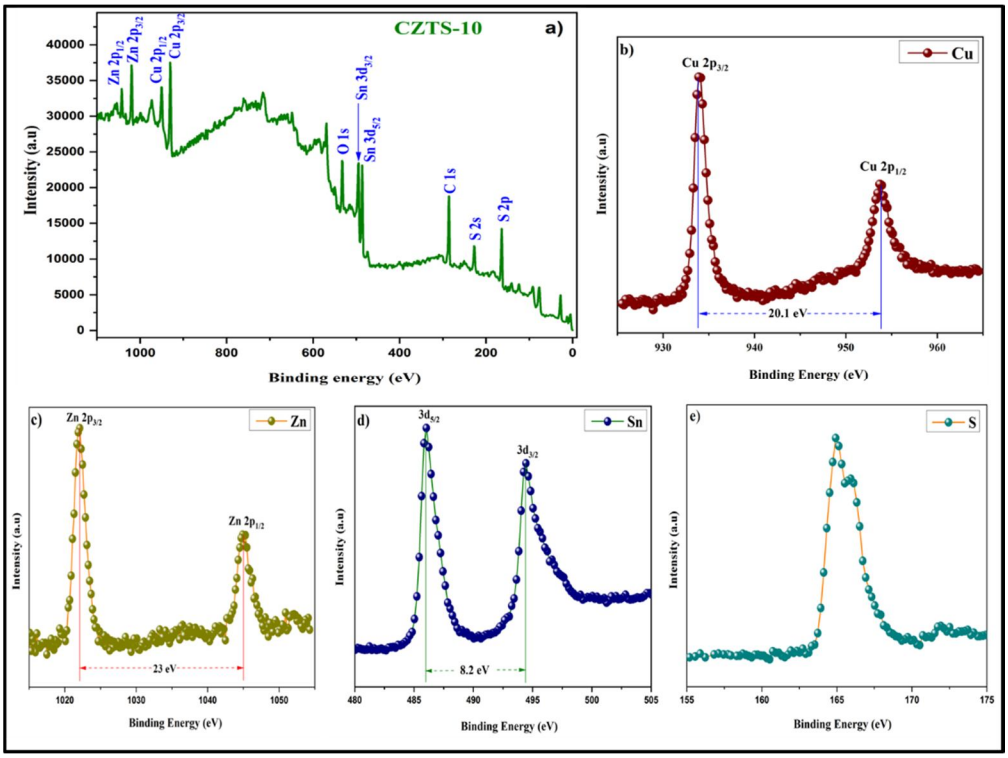

FIG. 5. XPS spectra of CZTS TU-10 nanostructures. (a) Survey scan spectrum, (b) Cu, (c) Zn, (d) Sn, and (e) S.

3.6. Optical Properties

To estimate the value of the direct bandgap, the optical absorption characteristics of CZTS TU-10 were investigated by using UV-Vis spectroscopy in the 200-800 nm wavelength range. Fig. 6(a) shows the presence of a strong absorption spectrum, suggesting that the CZTS TU-10 sample exhibited significant potential application in photocatalytic measurements [28]. By using Tauc's plot [29], the optical bandgap of CZTS TU-10 nanostructure was determined for direct bandgap energy:

$$\alpha h\nu = A(h\nu - E_g)^n \quad (4)$$

where hν is the photon energy, Eg is the optical bandgap of the products, A is a constant, and n is 1/2 for the direct bandgap semiconductor. The optical bandgap energy (Eg) of the CZTS sample was calculated by extrapolating the linear portion of $(\alpha h\nu)^2$ on the y-axis versus hν on the x-axis, as shown in the inset of Fig. 5(b) The calculated band gap value of CZTS TU-10 nanostructures was found to be 1.52 eV, which could be attributed to the enhanced ordering within nanocrystals with a better crystalline nature. This value is close to the optimum value for better electrochemical and photocatalytic applications. Furthermore, the obtained band gap value coincides well with the previously reported value [30].

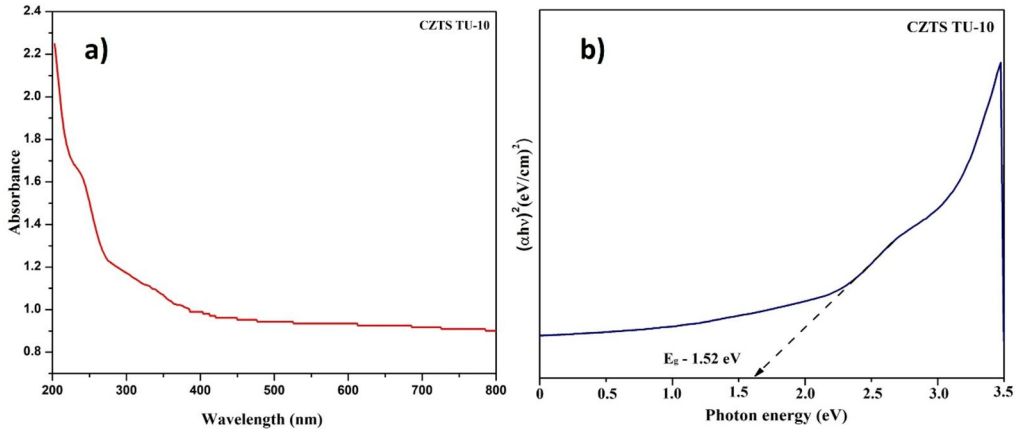

FIG. 6. Optical properties of CZTS TU-10 nanostructures. (a) UV-Vis absorbance, (b) band gap.

3.7. Electrochemical Applications

a) Cyclic Voltammetry

The cyclic voltammetry (CV) curves were obtained for the CZTS TU-10 electrode at 0 to 0.6 V while employing scanning rates ranging from 10 to 100 mV/s. As illustrated in Fig. 7(a), the redox activity of the CZTS TU-10 electrode was confirmed by two redox peaks and shifted in higher positive (oxidation) and lower negative (reduction) potentials as the scan rate increased, which might be related to electric polarization and irreversible reactions [31]. Due to faster kinetics, the CV profiles demonstrated a steady voltammogram shape at increased scan rates, confirming that the electrode material has pseudo-capacitance behavior and better rate performance. The specific capacitance (C_{sp}) of the CZTS TU-10 electrode was calculated using Eq. (1). The calculated C_{sp} values are 389, 290, 232, 179, and 155 F/g for different scan rates of 10, 20, 55, 70, and 100 mV/s, respectively, as shown in Fig. 7(b). Among the scan rates, the lower scan rate has a higher specific capacitance of 389 F/g, which could be attributed to both the inner and outer surfaces involved in tuning the specific capacitance, which results in higher capacitance values [32]. The decrease in specific capacitance with increased scan rates was caused by the rapid redox reaction. While increasing the scan rates, the interplay of various ions at the interface between the electrode and electrolyte was observed at higher scan rates, hence leading to decreased values of Csp.

b) Galvanostatic Charge-Discharge

The specific capacitance of the fabricated electrode was determined by utilizing GCD charge-discharge measurements within the potential range of 0-0.6 V with various current densities (1-5 A/g), as shown in Fig. 7(c). The nonlinear shape of the GCD profile with humbs revealed faradic effects of the constructed electrode for different current density values. The calculated Csp values, calculated using Eq. (2), are found to be 368, 252, 216, 134, and 113 Fg^{-1} for different current densities 1, 2, 3, 4, and 5 Ag^{-1}, respectively. The obtained results indicate that the decreased Csp values were inversely proportional to increasing current densities. This phenomenon could be ascribed to two key factors:
(i) At higher current densities, ion diffusion is limited, preventing full access to the active material;
(ii) Redox reactions are confined mainly to the electrode surface, leading to reduced utilization of active sites [33].

The CZTS TU-10 electrode had a high specific capacitance value of 368 Fg^{-1} for a current density of 1 Ag^{-1} due to the better electrochemical performance with a large surface area. The GCD curve corresponding to 1 Ag^{-1} shows a wide potential plateau. The results discussed above clearly indicate that the sulfur-rich, surfactant-free CZTS TU-10 electrode material will exhibit high performance when utilized in energy storage applications.

c) EIS Spectroscopy

The CZTS TU-10 electrode was subjected to electrochemical impedance spectroscopy (EIS) to examine the fundamental characteristics of the electrode and electrolyte interfaces where charge reactions and ion transfer occur in the system. EIS spectrum was plotted using the real compound (Z') vs imaginary part (Z''), as shown in Fig. 7(d).

The imaginary part (Z'') of the impedance defines the interphase resistance between the working electrode and the electrolyte. The phenomenon of a semicircle transition into a straight line was noticed at higher frequencies. The charge transfer resistance occurs at the interface of the active material as revealed by the small semicircle [34]. The plot shows a large slope in the straight-line part that confirms the CZTS TU-10 electrode has high capacitance and low ion diffusion resistance.

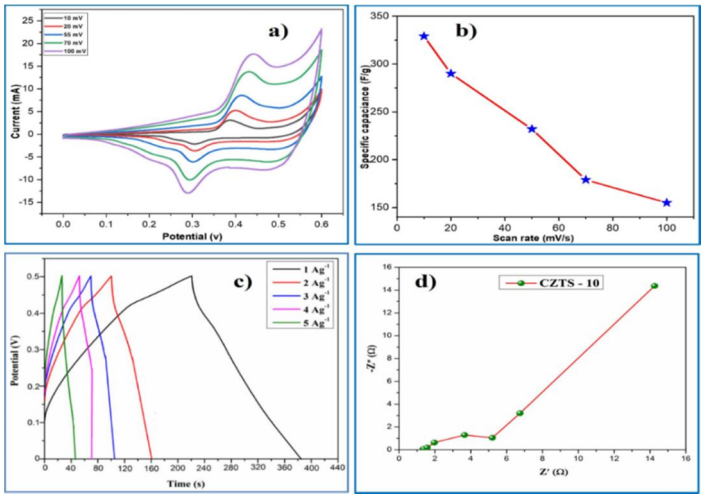

FIG. 7. Electrochemical analysis of CZTS TU-10 nanoparticles. (a) CV, (b) scan rate vs specific capacitance, (c) GCD, and (d) EIS spectrum.

3.8. Photocatalytic Measurements

Figure 8(a) shows the absorption spectra of the CZTS catalyst recorded against the degradation of CV and MB dye solutions under sunlight. The spectra revealed that the maximum absorbance wavelengths of CV and MB dyes were centered at 590 nm and 664 nm, respectively. The absorbance of the solution decreases with increasing time intervals, indicating that the dye concentration decreases as the exposure time increases [35]. The photocatalytic degradation efficiency was evaluated by Eq. (5):

$$\text{Efficiency } (\eta\%) = \left(1 - \frac{C}{C_o}\right) \times 100 \qquad (5)$$

where C and C_o are the initial and final irradiation of the dye solution, respectively. Figs. 8(b) and 9(b) show the absorbance vs time for CV and MB dyes, respectively. The CZTS nanostructures using CV dye had the highest degradation efficiency at 93% [Fig. 8(c)] compared to MB dye at 89% [Fig. 9(c)] within 70 minutes. Fig.s 8(d) and 9(d) show the C/C_0 vs reaction time curves of CV and MB in the presence and absence of a CZTS catalyst. It is well known that a material's large surface area, morphology, crystallinity, and size are crucial to its photocatalytic activity. Consequently, morphology may play a significant role in calculating the final degradation efficiency. In the present work, a flower-like CZTS TU-10 sample exhibited high removal efficiency due to the higher surface area with an optimal particle size of the CZTS catalyst and suitable preparation conditions.

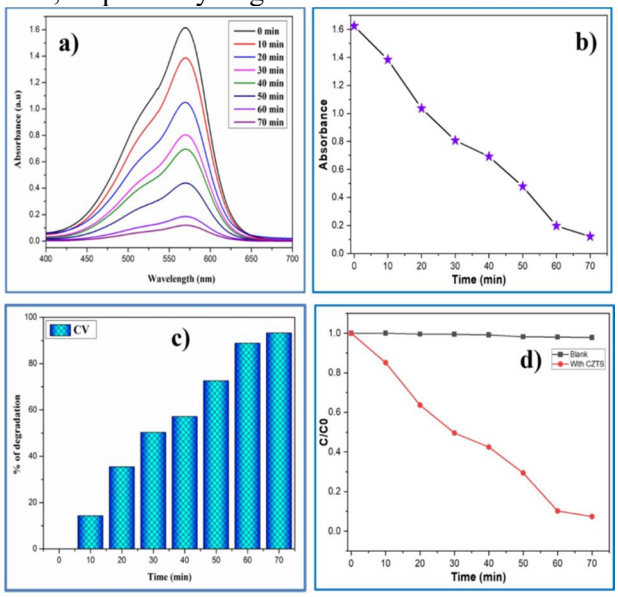

FIG. 8. (a) Absorbance vs wavelength spectra of CZTS TU-10 catalyst for CV dye, (b) absorbance vs irradiation time, (c) degradation efficiency, and (d) C/C_0 vs reaction time.

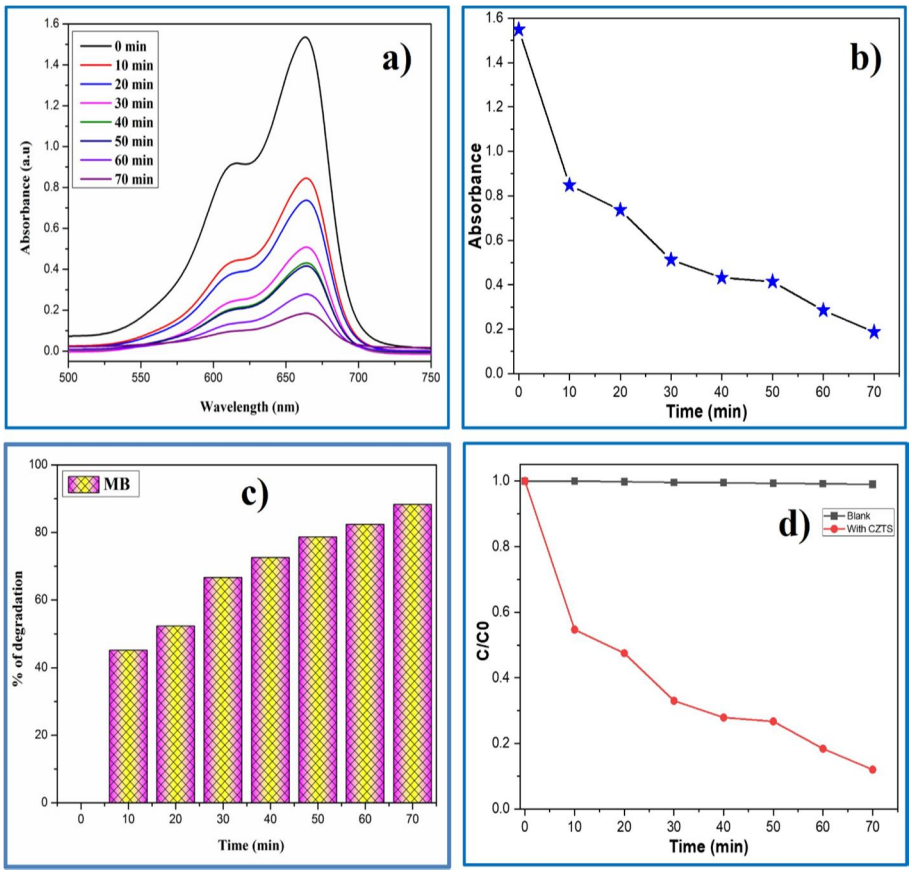

FIG. 9. (a) Absorbance vs wavelength spectra of CZTS TU-10 catalyst for MB dye, (b) absorbance vs irradiation time, (c) degradation efficiency, and (d) C/C_0 vs reaction time.

Moreover, the surfactant-free CZTS nanoparticles produced by the hydrothermal process serve as an efficient photocatalyst for degrading toxic dyes. In a photocatalytic system, a photo-induced molecular transformation occurs on the surface of the photocatalyst. Electrons jump from the valence band to the conduction band when the surface of a photocatalytic material is exposed to energy equal to or greater than the band gap. This causes a negatively charged electron to appear in the conduction band and a positively charged hole to appear in the valence band. The conduction band electron reduces the adsorbed oxygen onto the photocatalytic surface, and the positively charged hole oxidizes the organic contaminants into hydroxyl free radicals.

Table 2 summarizes the photodegradation efficiency of CZTS with previously reported data, prepared by various synthesis processes, as well as their morphology, efficiencies, type of dyes, and degradation rates of dyes. By overall photocatalytic performance, the prepared CZTS TU-10 nanostructures led to a higher degradation rate of MB and CV dyes due to the rose flower-like nanosheet morphology.

TABLE 2. Degradation efficiency of CZTS catalyst with previous studies.

Method	Morphology	Dye	Degradation efficiency / Time (% / min)	Ref
Hydrothermal	Agglomerated	MB	50 / 45	[28]
Hydrothermal	Spherical	RhB	55 / 240	[36]
Hydrothermal	Flower-like	MB	60 / 90	[37]
Hot-injection	Nano-Spheres	pollutants	73 / 150	[38]
Hot-injection	Nano-rods	pollutants	90.3 / 160	[38]
Hydrothermal	Rose-flower like	MB	89 / 70	Present work
Hydrothermal	Rose-flower like	CV	93 / 70	Present work

3.9 Antibacterial Activity

The antibacterial activity of the synthesized CZTS TU-10 nanostructure was carried out against both gram-positive (*Streptococcus pneumoniae, Streptococcus pyogenes*) and gram-negative (*Klebsiella pneumoniae, Vibrio parahaemolyticus*) pathogens. The CZTS TU-10 was tested for its antibacterial properties by using the agar well diffusion method. Figs. 10 (a)-10(d) show the results of the investigation on the antibacterial properties of CZTS nanostructure evaluated by the zone of inhibition (ZOI). Remarkably, following 24 hours of incubation, the synthesized CZTS nanostructures exhibited an inhibition zone around them for all the bacterial strains that were subjected to testing. After incubating the plates for 24 hours at 35℃, the diameter of the inhibitory zones was measured in mm and recorded. The zone of inhibition diameter was calculated corresponding to pathogens, and the values are listed in Table 3. The results revealed that the inhibition of growth increased with increasing concentrations of CZTS. The maximum inhibition zone was obtained against *Vibrio parahaemolyticus* bacteria at 18, 20, 22, and 26 mm, corresponding to 25, 50, 75, and 100 µg/ml.

This observation serves as an indication of the bacteriostatic capability of the CZTS nanostructures. Additionally, the size of the inhibition zone varied depending on the specific type of bacteria [39]. The observed suppression of bacterial growth could be related to the detrimental effects on the bacterial cell membrane and the expulsion of cytoplasmic contents, ultimately leading to the death of the bacterium. The change in the inhibition zone depended on the type of bacteria, the morphology of the nanoparticle, and the behavior of their development.

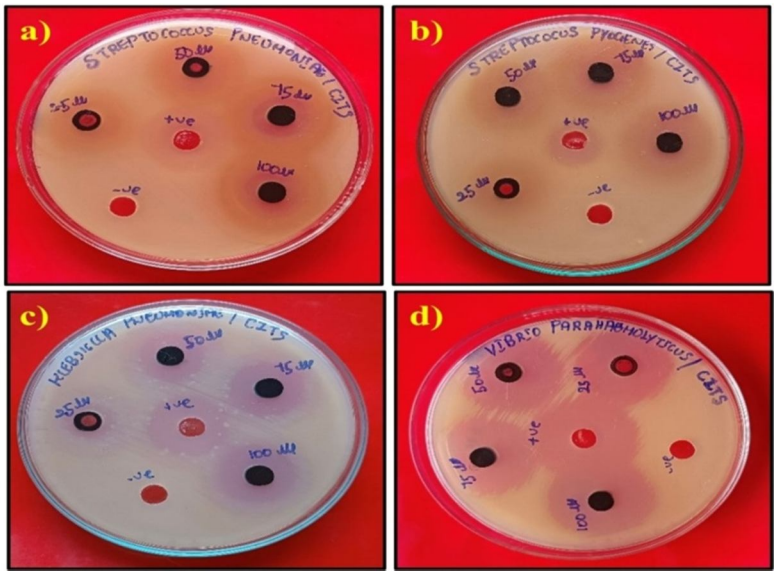

FIG. 10. Antibacterial activity of the CZTS TU-10 nanostructures against (a) *Streptococcus pneumoniae*, (b) *Streptococcus pyogenes*, (c) *Klebsiella pneumoniae*, and (d) *Vibrio parahaemolyticus*.

TABLE 3. Antibacterial activity of CZTS TU-10 nanostructures

S. No	Test Organisms	Zone of inhibition (mm)				
		25 µg/ml	50 µg/ml	75 µg/ml	100 µg/ml	Positive control
1.	*Streptococcus Pneumoniae*	12	14	16	20	26
2.	*Streptococcus Pyogenes*	14	16	18	21	26
3.	*Klebsiella Pneumoniae*	12	14	16	18	26
4.	*Vibrio parahaemolyticus*	18	20	22	26	29

To date, some mechanisms have been suggested for the antibacterial properties exhibited by inorganic nanoparticles. (i) The release of metal cations from nanoparticles leads to interactions with proteins, nucleic acids, and microbial membranes, resulting in structural modifications and inhibition of microbial replication. (ii) The internalization of nanoparticles through ion channels or proteins at the cell wall results in the mechanical breakdown of the cell membrane. (iii) The nanoparticle surface generates reactive oxygen species

(ROS), including hydroxyl radicals (OH), hydrogen peroxide (H_2O_2), and superoxide ($\dot{O_2^-}$). These ROS have the potential to cause significant damage to lipids, DNA, and proteins within the cell membrane, resulting in leakage and degradation of the bacterial cell membrane [40]. Based on this investigation, hydrothermally prepared CZTS TU-10 nanostructures have stronger antibacterial performance against *Vibrio parahaemolyticus* bacteria due to their particle size and better morphology.

4. Conclusion

The pure kesterite phase of CZTS nanostructures was successfully synthesized through a low-cost hydrothermal method without the assistance of surfactants or capping agents by using different concentrations of thiourea. XRD and FT-Raman studies confirmed the growth of pure-phase CZTS nanostructures at higher sulfur concentrations. FESEM studies indicated that different Cu/S ratios had a strong influence on the morphological changes of CZTS. The interplanar distance value was calculated from the HRTEM image and found to be 0.32 nm, which strongly supported the XRD result. The valence states of Cu^{1+}, Zn^{2+}, Sn^{4+}, and S^{2-} were confirmed by XPS. Surfactant-free pure kesterite CZTS TU-10 was found to be a good photocatalyst for CV and MB dyes with degradation efficiencies of 93% and 89% within 70 minutes. The prepared CZTS electrode offered an excellent specific capacity of 389F/g at 10 mV/s by CV measurements. Finally, the surfactant-free CZTS TU-10 sample possessed a flower-like morphology and showed excellent degradation efficiency, better antibacterial activity, and high specific capacitance, all of which revealed that the prepared CZTS nanostructures could be potential candidates for future applications**.**

Acknowledgment

The corresponding author wishes to thank the Head of the Department of Physics and the Centralized Instrumentation and Service Laboratory (CISL), Annamalai University, Annamalai Nagar, Tamil Nādu, India, for providing the CV and analytical instrument facilities.

Funding Information

No funding was received for conducting this study.

Conflict of Interest

The authors declare no conflict of interest.

References

[1] Patil, S.S., Nadaf, S.N., Mali, S.S., Hong, C.K., and Bhosale, P.N., Ind. Eng. Chem. Res., 60 (21) (2021) 7816.

[2] Harinipriya, S., Cassian, H., and Sudha, V., J. Mater. Res. Technol., 15 (2021) 3558.

[3] Patil, U., Dhanasekar, M., Kadrekar, R., Arya, A., Bhat, S.V., and Late, D.J., Ceram. Int., 48 (19) (2022) 28898.

[4] Paraye, A., Ramachandran, M., and Selvam, N.V., Period. Polytech. Chem. Eng., 65(1) (2021) 42.

[5] Saha, S., Int. J. Photoenergy, 2020 (2020) 1.

[6] Qiu, L., Xu, J., Cai, W., Xie, Z., and Yang, Y., Superlattices Microstruct., 126 (2019) 83.

[7] Ahmad, R., Saddiqi, N., and Wu, M., Inorg. Chem., 59 (3) (2020) 1973.

[8] Banerjee, G., Das, S., and Ghosh, S., Mater. Today Proc., 18 (2019) 494.

[9] Engberg, S., Symonowicz, J., Schou, J., Canulescu, S., and Jensen, K.M.Ø., ACS Omega, 5 (18) (2020) 10501.

[10] Vavale, S.D., Pawar, S.G., and Deepti, H., Int. J. Innov. Knowl. Concepts, 6 (11) (2018) 126.

[11] Pathak, M., Bhatt, D., Bhatt, R.C., and Bohra, B.S., Chem. Rec., 24 (1) (2023) e202300236.

[12] Abdel Maksoud, M.I.A., Fahim, R.A., Shalan, A.E., and Abd Elkodous, M.S., Environ. Chem. Lett., 19 (2021) 375.

[13] Tang, Q., Shen, H., Yao, H., Wang, W., Jiang, Y., and Zheng, C., Ceram. Int., 42 (8) (2016) 10452.

[14] Manjula, S., Sarathkumar, A., and Sivakumar, G., J. Nano Res., 79 (2023) 25.

[15] Robati, S.M., Imani, M., and Tadjarodi, Mater. Lett., 225 (2018) 9.

[16] Hirpara, A.B., Chaki, S.H., Kannaujiya, R.M., Khimani, A.J., and Parekh, Appl. Surf. Sci. Adv., 12 (2022) 100338.

[17] Long, B., Cheng, S., Ye, D., Yue, C., and Liao, J., Mater. Res. Bull., 115 (2019) 182.

[18] Mkawi, E.M., Al-Hadeethi, Y., Shalaan, E., and Bekyarova, E., Ceram. Int., 46 (16) (2020) 24916.

[19] Patil, S.S., Mane, R.M., Mali, S.S., Hong, C.K., and Bhosale, P.N., Sol. Energy, 201 (2020) 102.

[20] Shalabayev, Z., Baláz, M., Daneu, N., Kanuchová, M., ... and Burkitbayev, M., ACS Sustain. Chem. Eng., 7 (15) (2019) 12897.

[21] Singh, O.P., Parmar, R., Gour, K.S., Dalai, M.K., Tawale, J., Singh, S.P., and Singh, V.N., Superlatticesand Microstruct., 88 (2015) 281.

[22] Ghosh, A., Biswas, A., Thangavel, R., and Udayabhanu, G., RSC Adv., 6 (98) (2016) 96025.

[23] Rajesh, G., Muthukumarasamy, N., Velauthapillai, D., and Batabyal, S.K., Langmuir, 33 (24) (2017) 6151.

[24] Henríquez, R., Nogales, P.S., Moreno, P.G., Cartagena, E.M., Bongiorno, P.L., Navarrete-Astorga, E., and Dalchiele, E.A., Nanomaterials, 13 (11) (2023) 1731.

[25] Zaman, M.B., Mir, R.A., and Poolla, R., Int. J. Hydrogen Energy, 44 (41) (2019) 23023.

[26] Valdés, M., Pascual-Winter, M.F., and Vázquez, M., Phys. Status Solidi A, 215 (24) (2018) 1800639.

[27] Das, S., Sa, K., Alam, I., and Mahanandia, P., Mater. Lett., 232 (2018) 232.

[28] Phaltane, S.A., Vanalakar, S.A., Bhat, T.S., Patil, P.S., Sartale, S.D., and Kadam, L.D., J. Mater. Sci. Mater. Electron., 28 (2017) 8186.

[29] Baid, M., Hashmi, A., Jain, B., Singh, A.K., Susan, M.A.B.H., and Aleksandrova, M., Opt. Quantum Electron., 53 (2021) 1.

[30] Padhy, S., Mannu, R., and Singh, U.P., Sol. Energy, 216 (2021) 601.

[31] Zhao, Y., Yan, J., Huang, Y., Lian, J., Qiu, J., Bao, J., Cheng, M., Xu, H., Li, H., and Chen, K., J. Mater. Sci. Mater. Electron., 29 (2018) 11498.

[32] Premkumar, V.K., Sivakumar, G., Dinesh, S., and Barathan, S., J. Mater. Sci. Mater. Electron., 28 (2017) 4780.

[33] Farzi, M., Moradi, M., Hajati, S., Toth, J., and Kazemzadeh, A., Synth. Met., 278 (2021) 116815.

[34] Sarkar, S., Howli, P., Das, B., Das, N.S., Samanta, M., Das, G.C., and Chattopadhyay, K.K., ACS Appl. Mater. Interfaces, 9 (27) (2017) 22652.

[35] Selvam, M., Sivakumar, G., and Ayyar, M., Z. Phys. Chem., 0 (2024).

[36] Sawant, J.P., Rajput, R., Patil, S., Ryu, J., Patil, D.R., and Kale, R.B., J. Mater. Sci. Mater. Electron., 32 (2021) 22803.

[37] Sheebha, I., Venugopal, V., James, J., Maheskumar, V., Sakunthala, A., and Vidhya, B., Int. J. Hydrogen Energy, 45 (15) (2020) 8139.

[38] Semalti, P., Sharma, V., and Sharma, S.N., J. Materiomics, 7 (5) (2021) 904.

[39] Hirpara, A.B., Chaki, S.H., Kannaujiya, R.M., Khimani, A.J., Appl. Surf. Sci. Adv., 12 (2022) 100338.

[40] Ocakoglu, K., Dizge, N., and Colak, S.G., Colloids Surf. A Physicochem. Eng. Asp., 616 (2021) 126230.

Volume 18, Number 2, 2025. pp. 197-206

Jordan Journal of Physics

ARTICLE

Sensing Efficacy of ZnO Film Towards Ethanol and Acetone

Dinesh K. CHAUDHARY[a], **Surya K. JOSHI**[b] and **Agni DHAKAL**[c]

[a] *Physics Department, Amrit Campus, Tribhuvan University, Kathmandu, 44600 Nepal.*

[b] *Central Department of Chemistry, Tribhuvan University, Kirtipur, Kathmandu, 44618 Nepal.*

[c] *Research Division, Nepal Academy of Science and Technology, Khumaltar, Lalitpur, 44700, Nepal.*

Doi: **https://doi.org/10.47011/18.2.9**

Received on: 18/12/2023; *Accepted on: 28/03/2024*

Abstract: In this work, zinc oxide nanoparticles (ZnO NPs) were synthesized via the co-precipitation method and analyzed by X-ray diffraction (XRD), scanning electron microscopy (SEM), and energy dispersive X-ray diffraction (EDX). The ethanol and acetone vapor detection abilities of the ZnO film were comprehensively examined at temperatures ranging from 100°C to 330°C. The XRD results revealed a polycrystalline nature with a mean crystallite size of 27.3898 ± 0.5472 nm. The SEM and EDX analyses demonstrated the formation of nano-leaf structures of ZnO. Gas sensing measurements showed a higher response of 52.08 ± 1.23 and 25.62 ± 1.21 at 285 °C at 800 ppm ethanol and acetone vapor exposure, respectively, i.e., selectivity towards ethanol. The film exhibited rapid response times of 5 s for ethanol and 11 s for acetone. Repeatability and stability tests over multiple cycles demonstrated consistent performance, surpassing that of similar reported sensors. These results support the development of a cost-effective and efficient gas sensor capable of detecting ethanol and acetone vapors at concentrations as low as 40 ppm, which is below the permissible exposure limits set by the Occupational Safety and Health Administration (OSHA).

Keywords: Zinc Oxide, Gas response, Response time, Selectivity.
PACs Code: 07.07 Df.

1. Introduction

Over the past couple of decades, metal oxide semiconductor (MOS) nanomaterials have garnered significant attention due to their wide range of industrial uses, including biomedical, chemical, and food industries, as well as in optoelectronic devices, resonators, solar cells, agriculture, etc. [1–4]. Among various MOS, ZnO is emerging as a potential material because of its tunable electrical, optical, and surface characteristics, which are useful for a variety of applications, such as photocatalytic activity, solar cells, gas sensors, and so on [5–7]. One of the most notable uses of ZnO is as a gas-sensing material, because its sensing capability is well known and controlled mostly by its surface properties and working temperature [8–10]. ZnO responds to gas exposure. However, the lower response, high operating temperature, and selectivity are the major problems. Currently, significant efforts are underway to enhance the gas-sensing capabilities and selectivity of MOS-based sensors through surface modification, metal doping, conducting polymer doping, nano-composing, etc. [8, 11–14]. Among these strategies, surface modification has been shown to be effective in improving gas sensing capabilities [8, 9]. The morphology of ZnO depends strongly on the preparation method [15–18]. In this regard, the co-precipitation method has proven to be one of the most essential, low-

Corresponding Author: Dinesh Kumar CHAUDHARY **Email**: dinesh.chaudhary@ac.tu.edu.np

cost, and time-consuming approaches for producing ZnO nanoparticles. This method does not require a vacuum system and can yield substantial quantities in a single batch.

Acetone is a clear, colorless, volatile organic liquid that evaporates quickly. It is used as the laboratory solvent for materials like paints, grease, plastics, synthetic fibers, etc., and for rinsing glassware and equipment. Excessive exposure to acetone fumes can cause irritation of the eyes, nose, throat, and lungs in a couple of minutes. It can cause headaches, dizziness, damage to the nervous system, confusion, or unconsciousness [19–21]. Likewise, ethanol is a widely used toxic chemical in various industries, such as the production of food additives, medicines, antibacterial products, alcoholic drinks, and cosmetic products [22–24]. Its excessive exposure might have negative consequences for living beings. Exposure to ethanol vapor induces a ventricular and septal wall stiffening during growth [22, 25].

As a consequence of the above-mentioned things, there is a pressing demand for acetone and ethanol sensors capable of detecting low concentrations of vapor with fast and high response. ZnO film was found to be sensitive to both ethanol and acetone at the working temperature >300 ºC [24, 26-30]. However, reports focusing on the selectivity of ZnO among ethanol and acetone are scarce.

In this work, ZnO NPs were synthesized by the economical co-precipitation method and characterized to study their sensing capability towards ethanol and acetone vapors. The results of extensive investigations on the structural, morphological, and gas-sensing characteristics are presented and compared to the results of the published reports. This work reports a higher response of the 0.5 M ZnO film towards ethanol than towards acetone. Also, the gas response of 0.5 M ZnO film towards the investigated vapors (ethanol and acetone) was found to be higher at relatively lower operating temperatures than the available published reports [15, 17, 18, 20-22, 27, 28, 30]. In addition, the gas sensing mechanism of ZnO film is discussed.

2. Experimental

2.1 Materials

Analytical-grade chemicals [zinc acetate di-hydrate ($Zn(CH_3CO_2)_2{:}2H_2O$), ethanol (CH_3CH_2OH), sodium hydroxide (NaOH), stannous chloride di-hydrate ($SnCl_2{:}2H_2O$), conc. hydrochloric acid (HCl), deionized water, and vinegar] were used without further modifications throughout the experiment to synthesize ZnO NPs.

2.2 Preparation and Characterization

Clean glass substrates were initially coated with fluorine-doped tin oxide (FTO) layers via the spray pyrolysis technique. To make the FTO solution, 21.051 g of $SnCl_2{:}\ 2H_2O$ was dissolved in 10 ml concentrated hydrochloric acid using a magnetic stirrer at 90 ± 10 °C. After that, 40 ml of deionized water was added, and the mixture was stirred for 15 minutes at 60 ± 10 °C. Meanwhile, NH_4F was dissolved in 50 ml of deionized water in another vessel. Following that, both of these solutions were put together, stirred for 1 hour, and then aged for 24 hours [31].

For ZnO NPs synthesis, zinc acetate dihydrate was dissolved in ethanol and shaken using a magnetic stirrer for 2 hours at 60 ± 10°C. 2M NaOH solution was added dropwise to the solution under continual stirring conditions to form the precipitate (ppt), maintaining the PH 12 of the solution. The precipitated material was centrifuged at 2000 rpm, carefully scrubbed, and rinsed 5 times with deionized water. The obtained material was subsequently dried for 16 hours at 100°C in a furnace. The ZnO paste was made with ethanol and 3 drops of vinegar. The vinegar serves as a binder. The ZnO film was created on the FTO-coated glass substrate by spreading the paste using a sharp blade. The film was then annealed for 1 hour at 550 ± 2 °C and aged for an additional 21 days to adhere to the substrate [32]. Finally, the ZnO nanoparticles were analyzed using XRD, SEM, and EDX.

Gas-sensing performance was evaluated at 100–350 °C using a custom-built gas-detection system consisting of an airtight glass chamber with inlet and outlet ports. The chamber was placed on a digital temperature-controlled hot plate (TALBOYS 7X7 CER HP 230 V ADV, Henry Troemner, LLC, USA). The ZnO film was positioned inside the chamber facing downward. A Ni-Cr micro-heater allowed heating up to 370 °C, with temperature regulated via a variable-voltage power supply. To prevent condensation, the chamber temperature was maintained just above the boiling point of the test vapors.

The gas response or sensitivity of the device fabricated with the ZnO film was estimated by measuring the resistance of the ZnO film in two distinct environments: in air and in gaseous environments. The gas response (R) is defined as

$$R = \frac{R_a}{R_g} \quad (1)$$

Here, R_a and R_g are the ZnO film resistances in air and gaseous environments [28]. To measure the resistance, two electrodes were fabricated on the ZnO film using silver paste and copper wire. The electrodes were separated by 1 cm. The electrodes were connected to the ohm meter (multi-meter, Fluke 101) to measure the resistance of the ZnO film.

3. Results and Discussion

3.1 Structural analysis

The structural characteristics were examined using the X-ray diffraction (XRD) technique. Fig. 1 depicts the X-ray diffraction pattern of ZnO NPs, which was performed using an X-ray diffractometer (Bruker AXS D2 PHASER A26-X1-A2BOB2A-, Serial No: 207047) employing Cu-K radiation of wavelength 1.54056 Å. The existence of several prominent steep peaks in the XRD spectrum demonstrates the polycrystalline structure of ZnO. The prominent steep peaks observed at 2θ = 31.9763°, 34.6344°, 36.4623°, 47.7476°, 56.8084°, 63.0683°, 66.5568°, 68.1557°, 69.2983°, and 77.1542 ° corresponding to (100), (002), (101), (102), (110), (103), (200), (112), (201), and (202) planes, respectively, which have been found to be matching the normal range values of JCPDS card number 36-1451 [33]. There was no further impurity peaks observed, indicating that pure ZnO had been synthesized. The size of crystallites (D) was calculated using the Debye–Scherrer equation:

$$D = \frac{0.9\lambda}{\beta cos\theta} \quad (2)$$

Here, λ is the wavelength of X-radiation and β is the full width at half maximum of the diffraction peak.

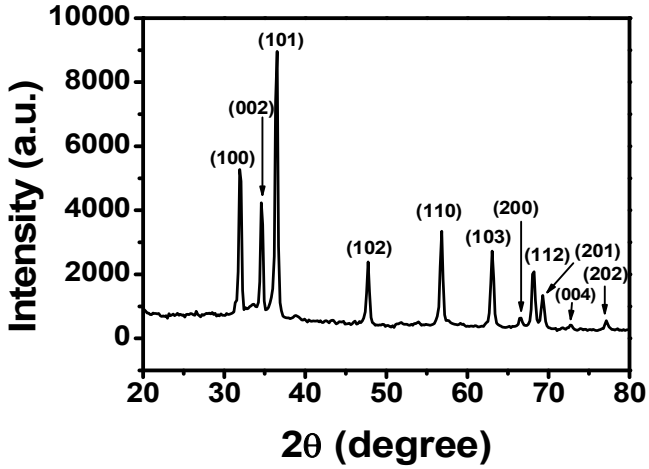

FIG. 1. XRD pattern of ZnO.

The crystallite size D and d-spacing corresponding to the most intense peak (101) were 28.4172 ± 0.9012 nm and 2.46123 ± 0.12011 Å, respectively. The mean crystallite was estimated to be 27.39 ± 0.5472 nm. The two lattice parameters, a and c, were estimated using formulas:

$$a = \frac{\lambda}{\sqrt{3}\, sin\theta} \quad (3)$$

and

$$c = \frac{\lambda}{sin\theta} \quad (4)$$

respectively [34, 35]. The values of a and c were 3.2280 ± 0.1199 Å and 5.1736 ± 0.0008 Å, respectively, with c/a = 1.5999 ± 0.0595, suggesting a hexagonal wurtzite phase.

3.2 Surface Morphology and Elemental Analysis

The gas-sensing characteristics of ZnO films depend critically on their surface morphology [8, 9]. The surface morphology was examined using a scanning electron microscope (SEM) and is depicted in Fig. 2(a). It clearly shows the nanoflake-like structure. The elemental composition was examined using the EDX technique, and the result is presented in Fig. 2(b). The EDX spectrum showed the atomic percentages of Zn and O as 48.03 and 51.97%, respectively, indicating the purity of the product.

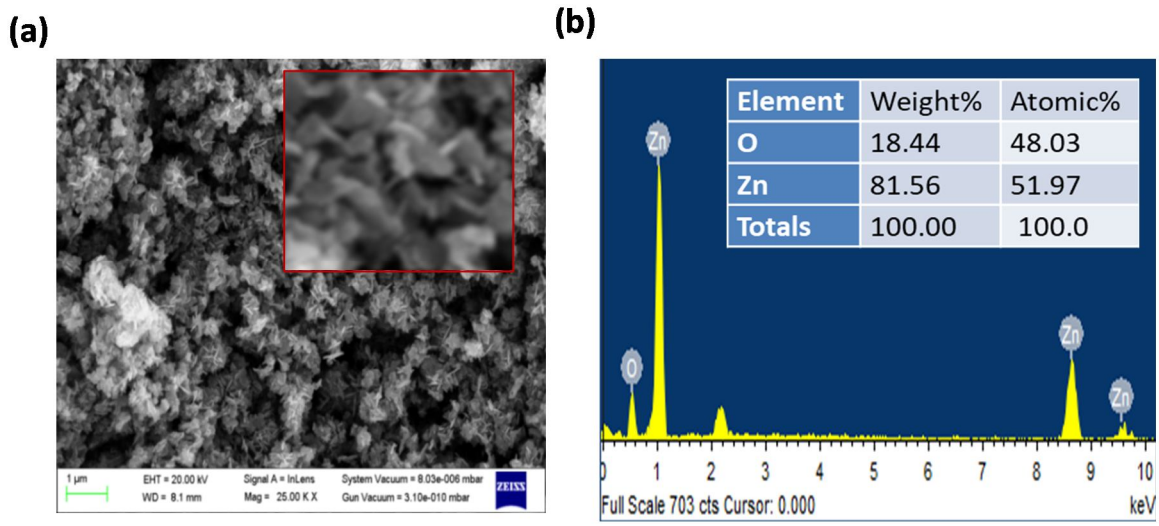

FIG. 2. (a) SEM image and (b) EDX spectra of ZnO.

3.3 Gas Sensing Behavior

The gas-sensing capability of ZnO-based gas sensors depends greatly on the temperature [36]. Initially, the gas-sensing capability was investigated over a temperature range of 100°C - 330°C at 800 ppm of ethanol and acetone exposure, separately. It was done by measuring the résistances R_a and R_g of the ZnO film in air and gaseous environments, respectively, and then calculating the gas response (R) using the formula in Eq. (1).

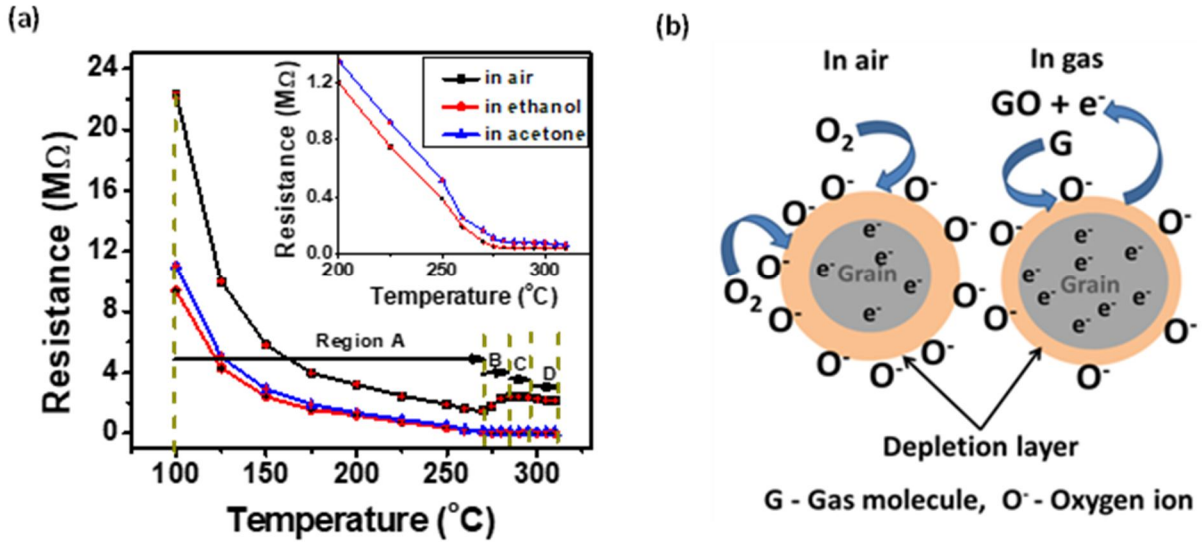

FIG. 3. (a) Resistance variation of the ZnO film with temperature in air, 800 ppm of ethanol and acetone vapors, (b) Illustration of gas-sensing mechanism of the ZnO film.

Figure 3(a) depicts the plot of resistance with temperature of the ZnO film in air, ethanol, and acetone vapor. The resistance of the ZnO film decreased with increasing température, exhibiting semiconducting behavior. To explain the variation of resistance of ZnO in air with temperature, the curve may be divided into four regions: A, B, C, and D. In région A, the resistance decreased with increasing temperature up to 270°C due to the thermal activation of conduction band électrons, which is the dominant factor. The resistance then increased with temperature rising to 285°C in region B, indicating the semiconducting characteristics. This increase is likely due to the formation of oxygen vacancies, which promotes the adsorption of oxygen molecules onto the ZnO surface [37]. The adsorbed oxygen captures free electrons from the conduction band, forming negatively charged oxygen species, thereby increasing the resistance of the film.

In region C (285–295 °C), the resistance remains nearly constant. This plateau suggests a dynamic equilibrium between the thermal

excitation of charge carriers and the oxygen adsorption process [38].

The resistance of the ZnO film decreased beyond 295 °C in region D, likely due to the dominant thermal activation of the electrons and desorption of oxygen species. The temperature around 285-295 °C is thought to be suitable for sensor functioning due to the small temperature dependence. [38].

The resistance of the sample was lower in a gaseous environment than in the air, as shown in Fig. 3(a). Also, the resistance of the sample was lower in ethanol than in acetone vapor [inset of Fig. 3(a)]. The classical model of gas-sensing can be used to explain it [Fig. 3(b)]. In the ambient atmosphere, the oxygen was adsorbed onto the ZnO surface, which extracted the electrons from the conduction band, and oxygen ions (O^-, O_2^-, or O^{2-}) were formed. It increased the depletion layer and the ZnO film resistance, as shown in Fig. 3(b) [39]. The form of adsorbed oxygen ions depends on the ZnO surface temperature. The oxygen adsorption and oxygen ion formation processes on the ZnO surface are expressed by Eqs. (5)-(8). At a temperature of 25–150 °C, O_2^- is the predominant species among the adsorbed oxygen ions, which indicates that oxygen ions are primarily adsorbed in the form of O_2^- ions at lower temperatures. As the temperature increases between 150 and 350 °C, the O_2^- ions decompose, and the adsorbed species consist of O^- and O^{2-} ions. Among these two species, the O^- ions become dominant. Finally, when the temperature surpasses 350 °C, O^{2-} ions become more prevalent on the ZnO surface [40].

$$O_{2(g)} \leftrightarrow O_{2(ads)} \quad (5)$$

$$O_{2(ads)} + e^- \leftrightarrow O_{2(ads)}^- \text{ (Room temperature to 150 °C)} \quad (6)$$

$$O_{2(ads)}^- + e^- \leftrightarrow 2O_{(ads)}^- \ (150 - 350\ ^\circ\text{C}) \quad (7)$$

$$O_{(ads)}^- + e^- \leftrightarrow O_{(ads)}^{2-} \text{ (above 350 °C)} \quad (8)$$

In the gaseous environment, the gas molecules interacted with oxygen ions and released the electrons back to the ZnO surface, which decreased the depletion layer and the resistance of ZnO [Fig. 4(b)]. The possible interaction of gas molecules with the oxygen ions and the release of electrons back to the ZnO surface are illustrated in Eqs. (9) and (10), respectively [27, 39].

$$CH_3CH_2OH(ethanol) + 6O_{ads}^- \rightarrow 2CO_2 + H_2O + 6e^- \quad (9)$$

$$CH_3COCH_3(Acetone) + 8O_{ads}^- \rightarrow 3CO_2 + H_2O + 8e^- \quad (10)$$

The resistance of the film decreased more in the case of ethanol exposure than in the case of acetone exposure [Inset of Fig. 4(a)]. It is attributed to the lower ignition point (365 °C) and smaller kinetic diameter (0.45 Å) of the ethanol molecule compared to that of acetone. The ignition point and kinetic diameter of acetone are 465 °C and 0.46 Å, respectively. The lower ignition point and smaller kinetic diameter of ethanol facilitate greater thermal activation and deeper penetration of ethanol vapor molecules into the porous structure of the ZnO film compared to acetone vapor molecules. This enables the ethanol molecules to interact more readily with a larger number of oxygen ions. Consequently, more electrons are released back to the ZnO surface, resulting in a greater reduction in resistance under ethanol exposure than under acetone exposure [40].

Figure 4 illustrates the relationship between gas response and temperature, measured separately at 800 ppm ethanol and acetone exposure. The gas response initially increased with rising temperature, reaching maximum values of 53.5284 ± 1.2311 for ethanol and 25.6119 ± 1.2311 for acetone, respectively, at 285 °C, and then decreased beyond this temperature. This behavior is due to the proportional relationship between gas response and the reaction rate coefficient K_{Eth} [40]. The reaction rate coefficient varies with temperature in Kelvin as:

$$K_{Eth}(T) = A\, e^{-E_a/k_B T} \quad (11)$$

where k_B is the Boltzmann constant, and E_a is the activation energy barrier of reaction [39].

As the temperature increases, thermal energy also increases. When the thermal energy approaches to E_a, the concentration of charge carriers increases significantly, enhancing oxygen adsorption onto the ZnO surface and resulting in a high sensor response. Beyond this temperature, oxygen desorption dominates, leading to a decrease in gas response [42].

The gas response of the ZnO film was higher under ethanol exposure than under acetone exposure. At 285 °C, the film exhibited gas responses of 53.5284 ± 1.2311 and 25.6119 ±

1.2311 to 800 ppm ethanol and acetone, respectively. This is attributed to the greater reduction in resistance upon ethanol exposure compared to acetone exposure [inset of Fig. 3(a)].

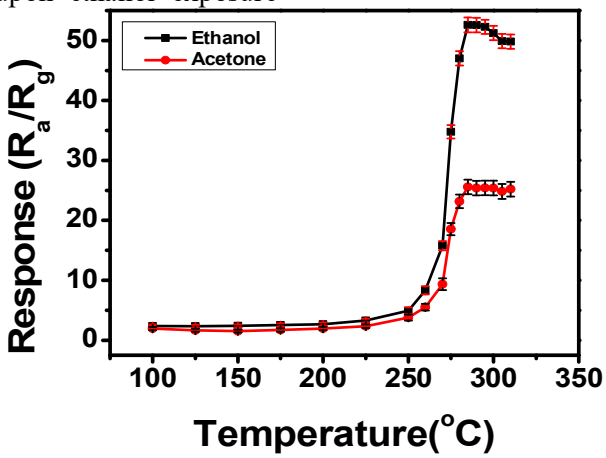

FIG. 4. Gas response variation with temperature at 800 ppm of ethanol and acetone exposure.

Further, the experiment was performed to study the repeatability and the capability of detecting low ppm of the targeted vapors. Figs. 5(a) and 5(b) illustrate the transient resistance responses at 800 ppm exposure of ethanol and acetone vapors, respectively, over four cycles at 285 °C. The resistance dropped to nearly the same stable value. The resistance dropped from an average value of 2.4612 ± 0.0039 MΩ to 0.0460 ± 0.0004 MΩ with an average gas response of 53.3222 ± 1.2311 under ethanol exposure and 2.2218 ± 0.0022 MΩ to 0.086 ± 0.0008 MΩ with an average gas response of 25.6235 ± 0.9735 under acetone exposure, respectively, indicating good repeatability.

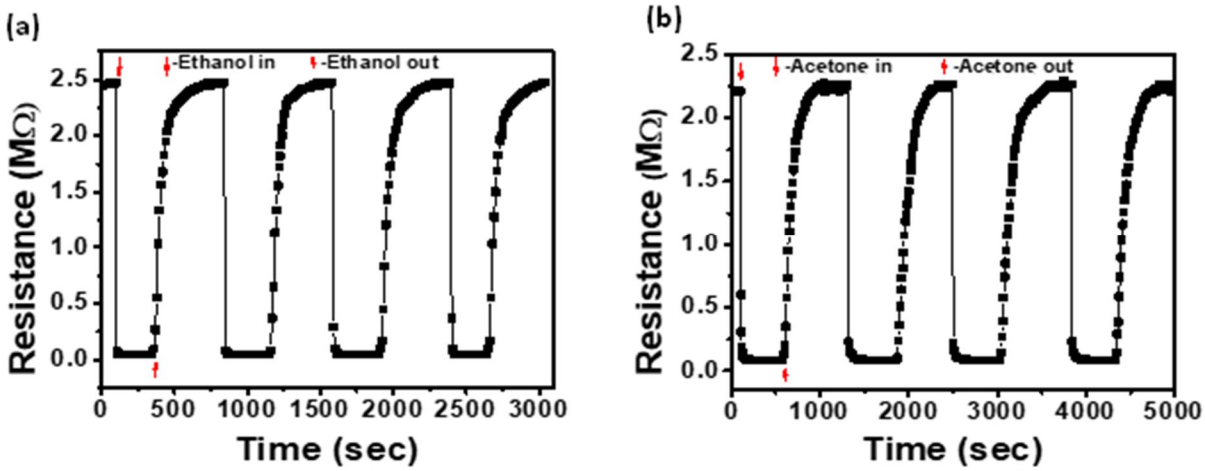

FIG. 5. Transient resistance response of the ZnO film at an exposure of 800 ppm of (a) ethanol, and (b) acetone vapors for four cycles.

Figures 6(a) and 6(b) show the plots of the transient resistance responses measured at 40–800 ppm ethanol and acetone exposure, respectively, at 285 °C. The resistance decreased abruptly at first and then acquired a stable value in both ethanol and acetone vapor environments. The resistance change was more significant at an exposure to higher amount of vapor. The average resistance of the ZnO NPs film changed from 2.4612 ± 0.0039 MΩ to 0.6333 ± 0.0057 MΩ at 40 ppm of ethanol exposure and 2.2218 ±0.0022 MΩ to 0.7351 ± 0.0066 MΩ at the same amount of acetone exposure.

Figure 7 shows the gas response of the ZnO film at various concentrations (40–800 ppm) of ethanol and acetone exposures. The film detected as low as 40 ppm of both vapors, with responses of 4.0618 ± 0.4923 for ethanol and 3.4912 ± 0.5813 for acetone. The gas response value was large at higher concentrations of vapor. This behavior is attributed to the greater surface coverage of the ZnO film by the test gas molecules at higher concentrations, which

enhanced their interaction with the adsorbed oxygen ions. The two essential gas sensing parameters are the response time and the recovery time. These refer to the times required for the resistance to change by 90% from the stable value following the exposure to, and removal of, the test gas from the sensing chamber, respectively.

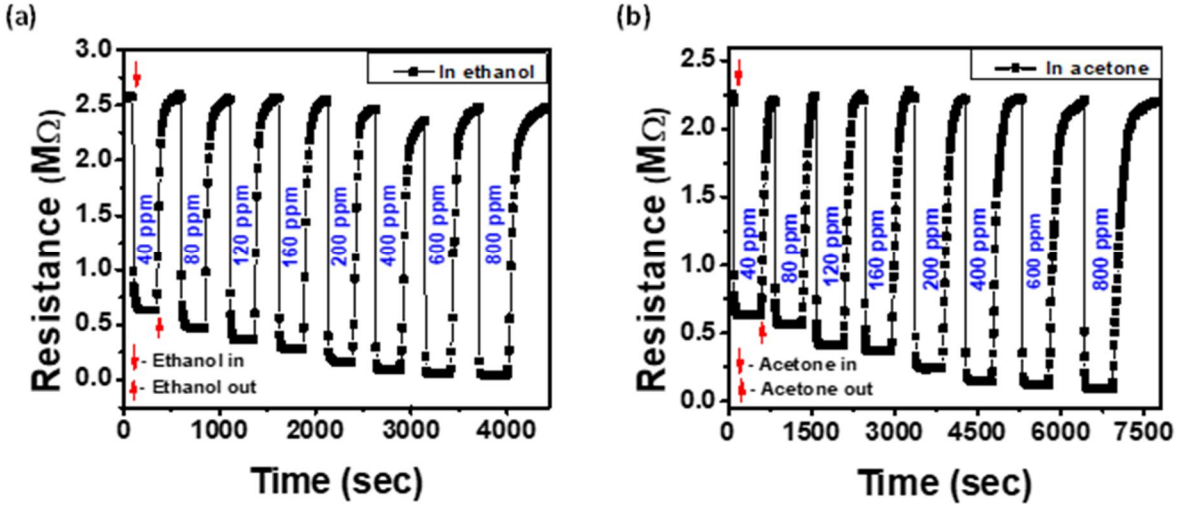

FIG. 6. Transient resistance responses of the ZnO nps film at an exposure of various concentrations (40-800 ppm) of (a) ethanol and (b) acetone vapors at 285 °C.

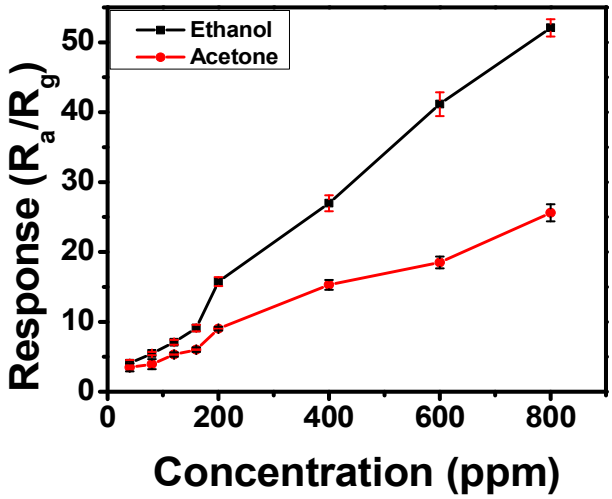

FIG. 7. Gas response at exposure various concentrations of ethanol and acetone

Figures 8(a) and 8(b) illustrate the graphical method of calculation of these two parameters at 800 ppm ethanol and acetone exposure at 285 °C. The plots of the response and recovery times with various concentrations (40-800 ppm) of tested vapors are depicted in Figs. 9(a)-9(b). The ZnO film exhibited a fast response and recovery in the case of ethanol exposure, with response times of 4.7 ± 0.3 to 6.1 ± 0.2 s and recovery times of 80.0 ± 0.7 to 148 ± 3.4 s for various concentrations. In contrast, for acetone exposure, the response and recovery times ranged from 9.4 ± 0.3 to 11.0 ± 0.3 s and 141.0 ± 0.7 to 290.7 ± 3.9 s, respectively. It may be due to the lower ignition point of ethanol than that of acetone, which facilitates the higher thermal activation and rapid ejection of ethanol vapor from the test chamber. As a result, the adsorption of oxygen started quickly.

The gas sensing results indicate that the gas sensing capability of the ZnO film was better for ethanol detection in comparison to acetone detection. The results of this study were compared with those of previously published studies (Tables 1 and 2). Compared to ZnO films made using other techniques, such as electrospinning [17], solvothermal [18], thermal evaporation [28], and RF magnetron sputtering [38], the 0.5 M ZnO film produced in our work showed improved gas sensing capability towards ethanol (Table 1). In addition, it demonstrated superior acetone sensing capability compared to other sensors made using other methods,

including the solvothermal and vapor-solid approaches [15, 18]. Furthermore, the relative analysis indicates that the ZnO film sensor operating temperature in this study was slightly lower than that of the published reports for detecting acetone (Table 2). Based on these findings, we conclude that the 0.5 M ZnO film can be effectively utilized as a sensing element for detecting both acetone and ethanol, with a notable selectivity towards ethanol.

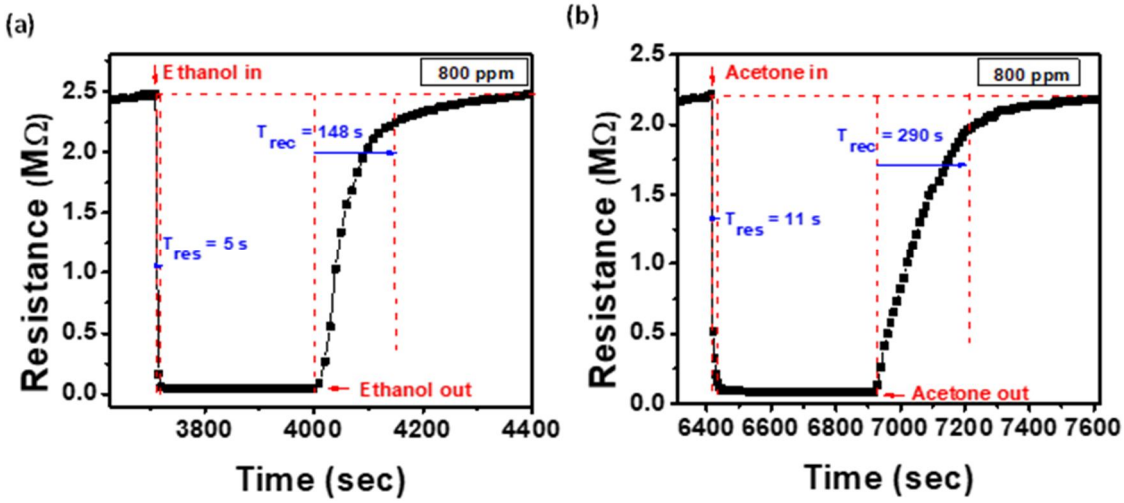

FIG. 8. Graphical calculation of response time and recovery time at 800 ppm (a) ethanol and (b) acetone vapors exposure.

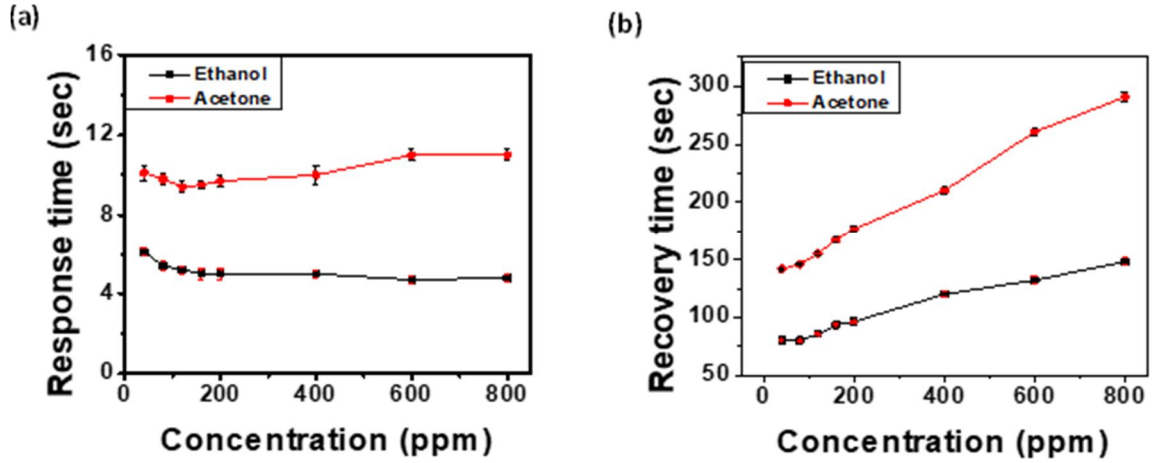

FIG. 9. (a) Response time and (b) recovery time at 40-800 ppm of ethanol and acetone vapor exposure at 285 °C.

TABLE 1. Comparison of the ethanol-sensing result of this work with the published reports

Materials	Method	Operating Temperature (°C)	Ethanol (ppm)	Response or Sensitivity (%)	Res/Rec time (sec)	References
ZnO nanofibers	Electrospining	300	1000	46.4	3/8	[17]
NiO/ZnO	Solvothermal	400	800	40	2.1/4.1	[18]
Al-ZnO	Thermal evaporation	290	3000	200	8/10	[22]
ZnO	Thermal evaporation	250	450 50	22 4.2	NR	[28]
Fe-ZnO	RF Magnetron sputtering	300	300	2.91	20/38	[39]
Fe-ZnO	Hydrothermal	270	500	19		[42]
ZnO	Co-precipitation	285	800 40	52.08 ± 1.23 4.06 ± 0.49	4.8/148 5.4 /180	This work

$\text{Response} = \frac{R_a}{R_g}$ and $\text{sensitivity} = \frac{R_a - R_g}{R_a} \times 100\%$

TABLE 2. Comparison of the acetone-sensing result of this work with the published reports

Materials	Method	Operating Temperature (°C)	Acetone (ppm)	Response or Sensitivity (%)	Res/Rec time (sec)	References
ZnO Sn-ZnO	Vapor-Solid Technique	370	200	65% 90%	NR	[15]
NiO/ZnO	Solvothermal	400	500	Nearly 5	NR	[18]
Sb-In_2O_3	Spray Pyrolysis	300	80	Nearly 95%	NR	[20]
ZnO	Fecile Solution	300	3000	170	1.5/3	[21]
La-ZnO	Solvothermal	425	1000	1826	16/3	[27]
ZnO	Sol-gel	340	500	63		[30]
ZnOnps Pd-ZnOnps	Chemical Solution	370 340	100 100	36 76	12/14 8/10	[32]
ZnOnps	Co-precipitation	285	800 40	25.61±1.21 3.49 ± 0.58	11/291 10.1 /141	This work

4. Conclusions

To sum up, the 0.5M ZnO NPs powder prepared by the co-precipitation method exhibited a polycrystalline nature with a mean crystallite size of 27.39 ± 0.55 nm. The morphological and elemental analyses revealed a flake-like structure with a high degree of purity. The ZnO film showed a better response to ethanol than to acetone. The gas response value at 800 ppm ethanol exposure at 285 °C was nearly twice that of acetone at the same concentration, with values of 53.5284 ± 1.2311 and 25.6119 ± 1.2111 for 800 ppm ethanol and acetone exposure, respectively. Also, the film exhibited faster response and recovery times when tested with ethanol compared to acetone. The response time and recovery time were 5 ± 1 s and 148 ± 3 s, respectively, at 800 ppm ethanol exposure and 11 ± 1 s and 290 ± 4 s for the same concentration of acetone exposure at 285 °C. Upon comparison with the published reports, the outcomes of this work were determined to be efficacious. The gas response towards ethanol was found to be greater than that reported in earlier literature. Remarkably, this work concludes that the 0.5M ZnO film can be useful to fabricate a stable, inexpensive gas sensor that can effectively detect extremely low concentrations (40 ppm) of ethanol and acetone vapors, which is somewhat below the OSHA-recommended lower limit of health hazards.

Data Availability

Data will be provided upon request.

Conflict of Interest

The authors declare that there are no known financial or personal conflicts that could have influenced the conclusions of this work.

Funding statement

This work was partially supported by the Institute of Science and Technology at Tribhuvan University, Nepal, which provided funding for the fabrication of the gas sensor setup and the procurement of necessary chemicals.

Acknowledgements

The authors are thankful to the Indian Institute of Technology (IIT) in Roorkee, Uttarakhand, India, for carrying out the SEM and EDX experiments.

References

[1] Xavier, J.R., Dhanalakshmi, C., Chandraraj, S.S., and Vinodhini, S.P., Trans. Nonferrous Met. Soc. China, 33 (2023) 2136.

[2] Kidowaki, H., Oku, T., Akiyama, T., Suzuki, A., Jeyadevan, B., and Cuya, J., J. Mater. Sci. Res., 1 (2011) 138.

[3] Liu, Q., Wang, B., Wang, Z., Wang, B., Xie, F., and Chang, J., Mater. Today: ProcA2333, 2S (2015) S348.

[4] Sabir, S., Arshad, M., and Chaudhari, S.K., Sci. World. J., 2014 (2014) 1.

[5] Roy, S. and Basu, S., Bull. Mater. Sci., 25 (2002) 513.

[6] Zahoor, R., Jalil, A., Ilyas, S.Z., Ahmed, S., and Hassan, A., Result Surf. Interfaces, 2 (2021) 100003.

[7] Mohd Adnan, M.A., Julkapli, N.M., and Abd Hamid, S.B., Rev. Inorg. Chem., 36 (2016) 77.

[8] Cui, J., Shi, L., Xie, T., Wang, D., and Lin, Y., Sens. Actuators B Chem., 227 (2016) 220.

[9] Zhu, L. and Zeng, W., Sens. Actuators A Phys., 267 (2017) 242.

[10] Wei, A., Pan, L., and Huang, W., J. Mater. Sci. Eng. B, 176 (2011) 1409.

[11] Luo, Y., Ly, A., Lahem, D., Zhang, C., and Debliquy, M., J. Mater. Sci., 56 (2021) 3230.

[12] Poloju, M., Jayababu, N., Ramana Reddy, M.V., J. Mater. Sci. Eng. B., 227 (2018) 61.

[13] Do, J.-S. and Wang, S.-H., Sens. Actuators B Chem., 185 (2013) 39.

[14] Cai, Y., Fan, H., Xu, M., Li, Q., and Long, C., Cryst. Eng. Comm., 15 (36) (2013) 7339.

[15] Sinha, S.K. and Ghosh, S., Adv. Powder Technol., 28 (2017) 2766.

[16] Liu, B. and Zeng, H.C., J. Am. Chem. Soc., 125 (2003) 4430.

[17] Wang, W., Huang, H., Li, Z., Zhang, H., Wang, Y., Zheng, W., and Wang, C., J. Am. Ceram. Soc., 91 (2008) 3817.

[18] Deng, X., Zhang, L., Guo, J., Chen, Q., Ma, J., Mater. Res. Bull., 90 (2017) 170.

[19] Bamsaoud, S.F., Rane, S.B., Karekar, R.N., and Aiyer, R.C., Sens. Actuators B Chem., 153(2) (2011) 382.

[20] Pramod, N.G. and Pandey, S.N., Ceram. Int., 40 (2014) 3461.

[21] Qi, Q., Zhang, T., Liu, L., Zheng, X., Yu, Q., Zeng, Y., and Yang, H., Sens. Actuators B Chem., 134 (1) (2008) 166.

[22] Yang, Z., Huang, Y., Chen, G., Guo, Z., Cheng, S., and Huang, S., Sens. Actuators B Chem., 140 (2) (2009) 549.

[23] Arshak, K. and Gaidan, I., Mater. Sci. Eng. B, 118 (2005) 44.

[24] Lei, M., Gao, M., Yang, X., Zou, Y., Alghamdi, A., Ren, Y., Deng, Y., and ACS, Y., Appl. Mater. Interfaces, 13 (44) (2021), 51933.

[25] Harper, C. and Matsumoto, I., Curr. Opin. Pharmacol., 5 (2005) 73.

[26] Tang, H., Li, Y., Zheng, C., Ye, J., Hou, X., and Lv, Y., Talanta 72 (2007) 1593.

[27] Chu, X., Zhu, X., Dong, Y., Ge, X., Zhang, S., and Sun, W., J. Mater. Sci. Technol., 28 (2012) 200.

[28] Bhatia, S., Verma, N., and Bedi, R.K., Results Phys., 7 (2017) 801.

[29] Yoo, R., Güntner, A.T., Park, Y., Rim, H.J., Lee, H.-S., and Lee, W., Sens. Actuators B Chem., 283 (2019) 107.

[30] Deshwal, M. and Arora, A., J. Mater. Sci. Mater. Electron., 29 (2018) 15315.

[31] Shanthi, S., Subramanian, C., and Ramasamy, P., Mater. Sci. Eng. B, 57 (1999) 127.

[32] Zhang, Y.-H., Liu, C.-Y., Jiu, B.-B., Liu, Y., and Gong, F.-L., Res. Chem. Intermed., 44 (2018) 1569.

[33] Chaudhary, D.K., Kshetri, M.B., Thapa, S., and Joshi, S.K., Mater. Sci. Forum, 1074 (2022) 107.

[34] Srinivasulu, T., Saritha, K., and Reddy, K.T.R., Mod. Electron. Mater., 3 (2017) 76.

[35] Ilican, S., Caglar, Y., and Caglar, M., J. Optoelectron. Adv. Mater., 10 (2008) 2578.

[36] Seiyama, T. and Kagawa, S., Anal. Chem., 38 (1966) 1069.

[37] Roy, T.K., Sanyal, D., Bhowmick, D., and Chakrabarti, A., Mater. Sci. Semicond. Process, 16 (2013) 332.

[38] Kwon, C.H., Hong, H.-K., Yun, D.H., Lee, K., Kim, S.-T., Roh, Y.-H., and Lee, B.-H., Sens. Actuators B Chem., 25 (1995) 610.

[39] Hassan, M.M., Khan, W., Naqvi, A.H., Mishra, P., and Islam, S.S., J. Mater. Sci., 49 (2014) 6248.

[40] Hongsith, N., Wongrat, E., Kerdcharoen, T., and Choopun, S., Sens. Actuators B Chem., 144 (2010) 67.

[41] Kulandaisamy, A.J., Reddy, J.R., Srinivasan, P., Babu, K.J., Mani, G.K., Shankar, P., and Rayappan, J.B.B., J. Alloys Compd., 688 (2016) 422.

[42] Khayatian, A., Kashi, M.A., Azimirad, R., and Safa, S., J. Phys. D Appl. Phys., 47 (2014) 075003.

Volume 18, Number 2, 2025. pp. 207-224

Jordan Journal of Physics

ARTICLE

Dimensionality Impact on Two Rydberg-Dressed Atoms Confined in a Harmonic Trap

Leila Chia[a,b] and **Nabila Grar**[b]

[a] *Laboratory of Materials Physics, Radiation and Nanostructures, University Mohamed El Bachir El Ibrahimi of Bordj Bou Arreridj 34000, Algeria.*

[b] *Department of Material Sciences, University Mohamed El Bachir El Ibrahimi, Bordj Bou Arreridj 34000, Algeria.*

Doi: **https://doi.org/10.47011/18.2.10**

Received on: 18/12/2023; *Accepted on: 20/02/2024*

Abstract: An analytical solution is possible for the Schrödinger equation for two particles interacting via a step-like potential and confined in a harmonic trap. This model is assumed to be very close to the real case of two confined Rydberg-dressed atoms. In this contribution, we thoroughly examine the validity of this approximation to describe the realistic situation. We analyze in detail the impact of the dimensionality on the spatial correlation of the system. The impact of the dimensionality on the dynamics of the system under a quench scenario is also investigated.

Keywords: Two atoms in a harmonic trap, Cold Rydberg atoms, Analytical solution of the Schrödinger equation, Spatial correlations, Quenching.

PACS: 31.15.ac; 03.65.-w; 32.50.+d.

1. Introduction

Matter is a huge and intricate assembly of some “fundamental” constituents, within which the individuality of these elements often appears to be lost. Understanding how finite micro elements lead to the macroscopic structure is of paramount importance in both nuclear and condensed matter physics. It aims not only to the comprehension of the constituents’ structure but also to the elucidation of the correlations and the interplay among constituents. On the other hand, experiments involving confined cold few particles are nowadays very accessible and are becoming a matter of routine. In fact, a number of system parameters, such as the confinement potential and the particle-particle interaction features, can be controlled on demand [1, 2]. This way, it is possible to verify experimentally the validity of a number of quantum simplified models studied in the past and explore fundamental physics concepts. It is also true that more efforts are necessary in order to devise new “toy” models targeting a detailed comprehension of the features of the interaction at different levels of approximation as well as different dimensionalities (1D, 2D, and 3D). An exact solution for the Schrödinger equation established in the case of different and sometimes complicated potentials, can be found in the literature (see, for example, Refs. [3-7]). Most of these solutions are given for the case of a single particle system. The situation becomes quite complicated when considering the case of two particles as a first step on the path towards the description of cold, confined few-body systems [8-10]. The difficulty resides in the consideration of both confinement potential characteristics and a realistic interaction potential. The hard-core interaction is the most simplified interaction scheme, and in this case, it is possible to achieve a quasi-exact solution for the two-particle

Corresponding Author: Nabila Grar **Email**: nabila.grar@univ-bba.dz

system. A theoretical study encompassing the three dimensionalities and a delta-like interaction for a system of two particles was developed in the seminal work of Busch *et al*. [11, 12]. In that work, a quasi-exact solution is derived under the assumption of a contact interaction (an s-wave for bosons and a p-wave for fermions). In order to take into account a certain interaction range, a Gaussian-like potential can be considered, which also allows for a quasi-analytical solution [13, 14]. These interaction models, however, ignore the long-range nature of the interaction for dipolar atoms or the Rydberg-dressed interaction behaving like $1/r^6$ and which can be very important either fundamentally or experimentally [15, 16]. An analytical solution for this interaction is still to be found. Nevertheless, a simplification of this interaction as a step function was proposed by Kościk *et al*. [17]. This approach enables a quasi-exact solution in one and two dimensions and allows for a detailed investigation of the system's various features. These quasi-solvable models are of extreme importance for advances in cold confined few-particle systems. It can be considered as a set of models to be validated experimentally as well as an exact basis to construct the solution for few-body systems exploiting different strategies, such as variational, *ab initio*, or interacting configurations [8-10]. The aim of the present study is to conduct a comparative analysis of the quasi-exact solvable model of Kościk *et al*. in the three dimensionalities and highlight the most important players for the considered interaction. We are unavoidably concerned by the analysis of the spatial correlations, which provide essential insight into the system's internal structure. We focus on the effects of the dimensionality on the spatial distribution of the system. The study is first established in a static regime and then enlarged to a dynamical one. In the dynamical regime, we are interested in the influence of the dimensionality on the evolution of the correlation under different quench scenarios. However, before proceeding with the details of the study, we establish the validity of using a step-function potential as a substitute for the more realistic Rydberg interaction is appropriate. To this end, we apply perturbation theory to identify potential discrepancies between results obtained using the approximate step function and those derived from the original long-range potential. The paper is organized as follows: In the second section, we review the key theoretical framework and provide the essential formulas and energy spectra relevant to the subsequent analysis. The third section presents a perturbative treatment of the system under the step-function potential and illustrates the convergence of its results toward those of the realistic interaction model. The fourth section is devoted to analyzing the energy spectra associated with the relative motion in the two-particle system for various interaction ranges, emphasizing the role of dimensionality. In this section, we also examine the relative radial spatial correlation and investigate the interplay between the centrifugal barrier, interaction range, and interaction strength in one, two, and three dimensions. In the fifth section, we present a time-dependent analysis of the system, focusing on the effects of dimensionality and sudden parameter changes (quench scenarios) on the evolution of spatial correlations. The main findings are summarized in the concluding section.

2. Theoretical Background

The different models aim to establish an analytical solution for the following Schrödinger equation for a system of two identical spinless quantum particles, having a mass m and trapped in an external potential:

$$\left(\sum_{i=1}^{2} \frac{-\hbar^2}{2m} \nabla_i^2 + v_{ext} + v\right) \psi(\vec{r_1}, \vec{r_2}) = E\psi(\vec{r_1}, \vec{r_2}), \quad (1)$$

where v_{ext} is the confining potential, v is the interaction potential depending on the particles' separation, and $\vec{r_i}$ is the vector position for each particle. To simplify the calculation, the particles are assumed to be point-like (structureless), and the confining potential is taken to be harmonic. The constraints imposed on the harmonic potential in different spatial directions determine the motion of the particles and thus define the dimensionality of the problem [18-20]. The same confining potential is imposed on both particles, and the equation becomes:

$$\left(\left(\sum_{i=1}^{2} \frac{-\hbar^2}{2m} \nabla_i^2 + \frac{1}{2} m\omega^2 r_i^2\right) + v(|\vec{r_1} - \vec{r_2}|)\right) \psi(\vec{r_1}, \vec{r_2}) = E\psi(\vec{r_1}, \vec{r_2}). \quad (2)$$

For this quadratic potential, it is possible to single out the center-of-mass contribution to the motion from the relative one. The equation then

becomes:

$$\left(\frac{-\hbar^2}{2M}\nabla_{\vec{R}}^2+\frac{1}{2}M\omega^2R^2+\frac{-\hbar^2}{2\mu}\nabla_{\vec{r}}^2+\frac{1}{2}\mu\omega^2r^2+v(r)\right)\psi(\vec{R},\vec{r})=E\psi(\vec{R},\vec{r}), \quad (3)$$

where $M=2m$, $\mu=m/2$ (the reduced mass), $R=|\overrightarrow{r_1}+\overrightarrow{r_2}|/2$, and $r=|\overrightarrow{r_1}-\overrightarrow{r_2}|$. The wave function can be written in a separable form as:

$$\psi(\vec{R},\vec{r})=\chi(\vec{R})\varphi(\vec{r}). \quad (4)$$

Consequently, we can separate the center-of-mass motion from the relative one as:

$$\left(\frac{-\hbar^2}{2M}\nabla_{\vec{R}}^2+\frac{1}{2}M\omega^2R^2-E_c\right)\chi(\vec{R})=0, \quad (5)$$

$$\left(\frac{-\hbar^2}{2\mu}\nabla_{\vec{r}}^2+\frac{1}{2}\mu\omega^2r^2+v(r)-E_r\right)\varphi(\vec{r})=0, \quad (6)$$

with $E=E_c+E_r$. The first equation is just an equation for a harmonic oscillator with known solutions. The difficulty resides in finding a solution for the second equation, where handling a realistic interaction can be quite challenging. It is important to note that the symmetry of the total wave function depends only on the relative part of the wave function since the center-of-mass part is symmetric by construction. Operating the adequate changes in the appropriate coordinate system [21], we can express Eq. (6) for three dimensions (1D, 2D, and 3D), respectively, as:

$$\left(\frac{-d^2}{dr^2}+\frac{1}{4}r^2+v(r)-E_r\right)f(r)=0, \quad (7)$$

$$\left(\frac{-d^2}{dr^2}+\frac{l^2-1/4}{r^2}+\frac{1}{4}r^2+v(r)-E_r\right)f(r)=0, \quad (8)$$

$$\left(\frac{-d^2}{dr^2}+\frac{l(l+1)}{r^2}+\frac{1}{4}r^2+v(r)-E_r\right)f(r)=0. \quad (9)$$

Here, the energy, the position, and the angular momentum quantum number l are expressed in $\hbar\omega$, $\sqrt{\frac{\hbar}{m\omega}}$, and $\sqrt{\hbar m\omega}$ units, respectively. The second term in Eqs. (8) and (9) represents the centrifugal potential. The last two equations are just the relative-radial part of the Schrödinger equation. Notice that we can shift from Eq. (8) to Eq. (9) by operating the following change:

$$l_{2D}\rightarrow l_{3D}+1/2. \quad (10)$$

This means that it is possible to find the solution for the 3D case by solving the equation for the 2D case, provided that the appropriate relation between the angular momentum quantum numbers is respected [17]. It is clear from the equations that the centrifugal effect is completely absent in 1D (Eq. 7) and is increasing when passing from 2D to 3D [Eqs. (8) and (9)]. It is also important to recall that the total wave function is defined by the quantum number n in 1D, by n and l in 2D, and by $n, l,$ and m in 3D. This wave function is symmetric for even n in 1D and even l for 2D and 3D; it is antisymmetric for odd n in 1D and odd l for 2D and 3D. A symmetric total wave function defines a bosonic state, whereas an antisymmetric total wave function defines a fermionic one.

Solving Eqs. (7), (8), and (9) relies on the form considered for the interaction potential. For our study, we are interested in the long-range nature of the interaction. This is the case for the interaction between two non-symmetric neutral charged distributions. Such interactions involve multipolar excitations, particularly when atoms are excited to high principal quantum numbers, known as Rydberg states [22]. The potential for this interaction can be approximated to the first order as composed of a short-ranged part, to which we add a van der Waals long-ranged interaction. This last one is the main contribution to the multipolar excitations. In this case, the interaction potential can be given as [17, 23]:

$$v(r)=\frac{g}{1+\left(\frac{r}{R_C}\right)^6}, \quad (11)$$

where g is the strength and R_c is the range of the potential (see Fig. 1). We will call this potential the Rydberg interaction in the following sections. It is not yet possible to find an exact solution to the Eqs. (7), (8), and (9) with this realistic interaction along with the harmonic confinement. Nevertheless, a quasi-exact solution is achieved for an interaction potential defined as a step function [17]. This approximation mimics the previous expression quite fairly for the short-range part and then falls abruptly to zero. It is given as:

$$v(x)=\begin{cases}v_0 \ pour\ x\leq a\\ 0\ x>a,\end{cases} \quad (12)$$

where we can relate v_0 and a to the strength and the range (g and R_C), respectively (Fig. 1) [17].

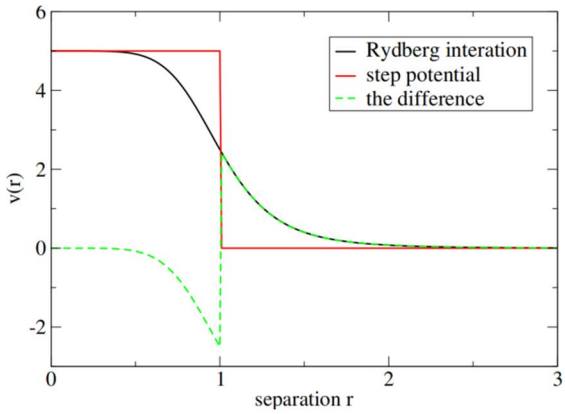

FIG. 1. Comparison between the realistic Rydberg interaction, the step function, and the difference between these two potentials. v_0 is set to 5, and the range is equal to one. The difference is considered as a perturbation (see Sec. 3).

This simplification is justified by the fact that the main contribution to the realistic potential comes from the flat part. In the case of this approximation, it is possible to establish a quasi-exact solution by reducing the 1D equation [Eq. (7)] to a Weber form, while the 2D and 3D relative-radial equations [Eqs. (8) and (9)] are transformed into Kummer-type differential equations. The solution is expressed as a function of the confluent hypergeometric function of the first kind in the region $[0, a]$, and as a function of the Tricomi function elsewhere [17, 24-26]. In order to guarantee a physical behavior of the whole solution, a condition for the continuity of the two functions and their derivatives is imposed at $r = a$, leading to transcendental equations. Solving these equations quantizes the energy, which allows for the retrieval of the energy spectrum with different combinations of strength v_0 and range a. Figs. 2 and 3 display representative energy spectra obtained from this model. Fig. 2 shows the energy versus the interaction strength for different values of the range in the case of 1D, whereas Fig. 3 is the same illustration for the 2D and 3D cases. These figures are mostly the same as the ones illustrated in [17, 27] and are reproduced here just to clarify and justify some of the results developed in subsequent sections. It is worth signaling the fermionization limits in 1D calculations where the bosons' energy levels are converging to the fermions' ones. This is known as the bosons-fermions mapping or the Tonks-Girardeau limit [28]. The results for the 3D case are similar to the 2D case but are shifted to higher energy levels. This result derives straightforwardly from the relation given by Eq. (10). This remark will be used to expect or justify some of the following results.

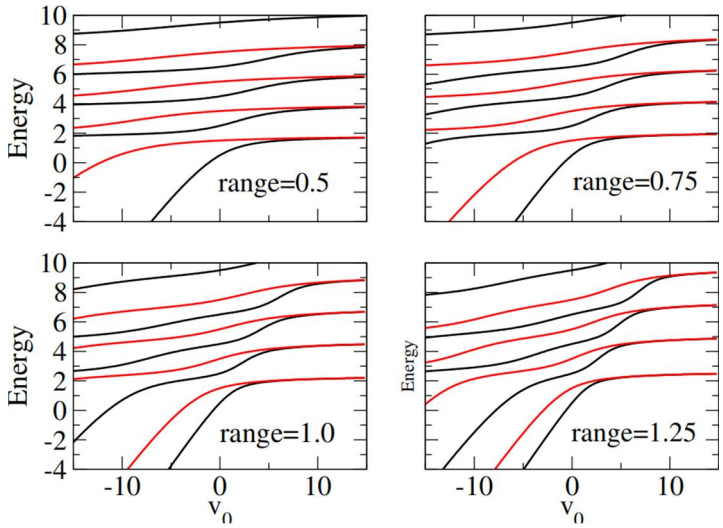

FIG. 2. (a) Energy spectrum in one dimension versus v_0 with increasing values of n (n = 0, 1 ... 8, bottom to top). Even values of n correspond to bosons (black), while odd values represent fermions (red). The value of the range a is indicated in each panel.

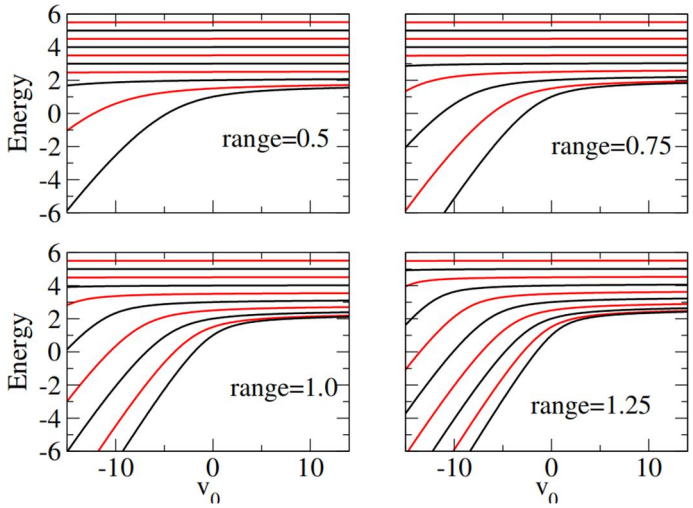

FIG. 3. Energy spectrum for the fundamental state (n = 0) versus v_0 with increasing values of the angular momentum quantum number $l = 0, 1, 2, 3, 4$ (from bottom to top) in three (red) and two (black) dimensions. The value of the range a is indicated in each panel.

These results are only possible for a harmonic trap and a step-like potential interaction, where an analytical solution is possible. Plenty of other complicated trap shapes, along with different interactions, are possible. However, only numerical approaches in these cases are used to investigate the system of two trapped particles [29].

3. Perturbation Treatment

Before proceeding to the main topic of this contribution, namely, the study of the impact of the dimensionality on some properties of the studied system, we first aim to assess the accuracy of approximating the Rydberg interaction with a step-function potential. We are interested in discrepancies between these two results by employing adequate tools in order to ameliorate the initial model. To this end, we employ perturbation theory to compare the following:

1. The analytical results for a step-like potential;
2. The numerical results for the exact formulation of the potential [Eq.(11)];
3. The results of the perturbation treatment of a step-like potential.

We have to clarify here that in the reference [17], both the numerical (Rydberg interaction) and analytical (step potential) results for the energy spectra are plotted on the same graphs, showing a discrepancy between these two results, a discrepancy that becomes more apparent for important ranges and in two dimensions. Similarly, in Ref. [30], an approximate value of the threshold interaction strength is calculated analytically for the step potential and compared to the numerical results for the Rydberg interaction. This is done in one dimension, and a tiny discrepancy is found between the two results. In our calculation, we are not only concerned with reporting the existing discrepancy but also try to bridge the gap between the two situations (numerical solution for the exact potential and the analytical solution for the step-like potential) for the cases of 3D, 2D, and 1D, using the perturbation tool. This calculation is important from two perspectives. First, reaching an agreement between the two results would confirm the adequacy of the step function as a replacement of the realistic Rydberg potential, as it confirms that the missing part is just a perturbation. Second, it would enable the construction of a more accurate wave function basis if a description of few-particle systems is targeted.

To start with, the exact potential is written as:

$$v(r) = \frac{g}{1+\left(\frac{r}{R_c}\right)^6} = v_s(r) - v_s(r) + \frac{g}{1+\left(\frac{r}{R_c}\right)^6} = v_s(r) + v_{pert}, \quad (13)$$

where $v_{pert}(r) = \frac{g}{1+\left(\frac{r}{R_c}\right)^6} - v_s(r)$ and $v_s(r)$ is the step function defined in Eq. (12). This way, it is possible to write the exact potential as a step function for which we already know the solutions and an extra quantity v_{pert} that we assume to be a perturbation. A plot for this potential for the case where the step is equal to 5 and the range of the potential is equal to 1, is illustrated in Fig. 1. The Numerov approach [31] is used to obtain the numerical results for the

exact potential (the Rydberg potential). In our case, the goal is to demonstrate that the perturbative approach applied to the step potential can reproduce the numerical results with high fidelity, thereby validating the approximation and enhancing our model's predictive power. Let us mention that we use a forward and inward integration method, and we impose the continuity of the wave function and its derivative at the turning points [31] to ensure the stability of the Numerov calculation. The perturbation correction is assumed to be of the first order for the eigenvalues and the eigenvectors.

3.1 Eigenvalues

The comparison of the eigenvalues (energies) versus v_0 for one dimension and different ranges is presented in Fig. 4. It is clear from this figure that the correction to the first order is sufficient to reach a fair agreement with the numerical results. Higher energy levels are less affected by the interaction according to their range, and are thus already too close to the numerical results. Conversely, the low levels are more affected by the interaction, making the correction for these levels quite important. This correction demonstrates an energy level for fermionization, which is higher than the one without the correction. In the same manner as previously, we extend the perturbation calculation to the radial part of the Schrödinger equation for 2D [Eq. (8)]. The perturbation potential is the same as before. The only difference is the centrifugal term making a logarithmic mapping and a transformation of the radial solution necessary for the densification of the points around zero for the wave function and for recovering the Numerov shape of the equation, respectively [31]. The comparison of the spectra versus v_0 and for different ranges a is illustrated in Fig. 5. The correction to the first order for both intermediate and large ranges is making the agreement with the numerical solution more satisfactory, especially for the repulsive regime (v_0 positive), where the curves are indistinguishable. In the attractive regime (v_0 negative), the corrected results for the lower levels are more satisfactory. The results for the 3D are quite similar to those of 2D (not shown here for brevity), as the only difference between the two cases is an addition in orbital momentum quantum number, which shifts the entire energy spectrum to higher values.

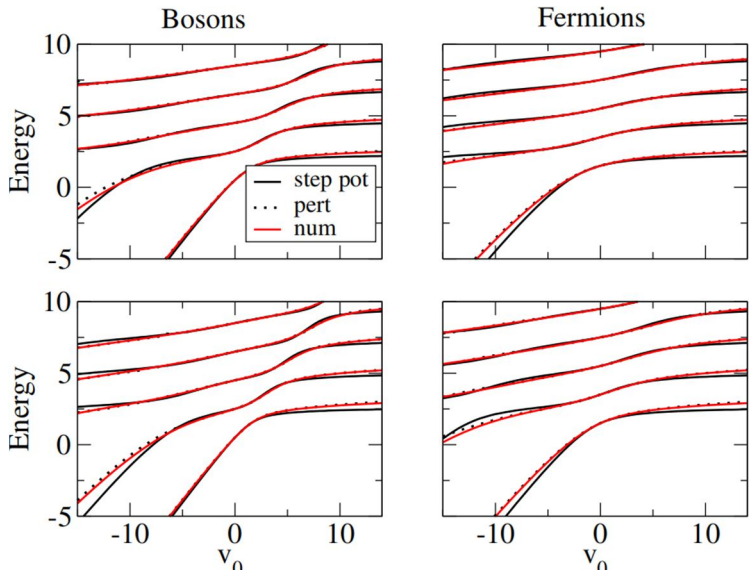

FIG. 4. Comparison of the energy versus v_0 for bosons and fermions (columns) at two ranges: a=1 and a=1.25 (rows from the top to the bottom, respectively) in one dimension. In each panel, the calculation for the step function (step pot), perturbation correction (pert), and the numerical results (num) are compared.

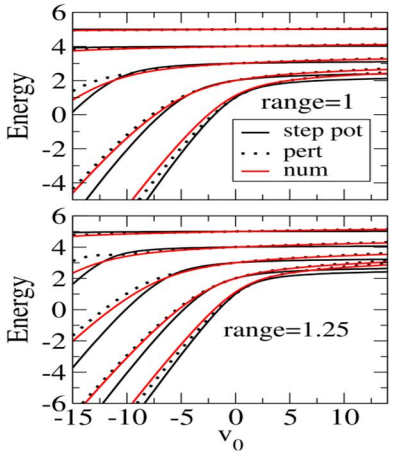

FIG. 5. Comparison of the energy versus v_0 in two dimensions for l = 0, 1, 2, 3, and 4 (from bottom to top) for two ranges: a = 1 and a = 1.25. Even and odd values of l are for bosons and fermions, respectively. Each panel shows results for the step-function (step pot), perturbation correction (pert), and the numerical results (num).

3.2 Eigenvectors

After showing the perturbation treatment results for the eigenvalues, we move now to the illustration of the eigenvectors using the same strategy. In Fig. 6, we compare the ground-state wave functions obtained via three methods (numerical, perturbation, and the step potential). The comparison is illustrated for different values of the strength v_0 and the range a. The three calculations (numerical, perturbation, and the step potential) coincide in the attractive regime (v_0 negative) and for a = 1. In the case of the repulsive regime (v_0 positive) and for the same value of a, the perturbation treatment deteriorates, whereas the results for the step potential are closer to the numerical ones. This is because the neighbouring states are degenerated (fermionization limit), and, consequently, the energy singularity affects the perturbation treatment. We can notice that the situation is worse in 1D. When doing the same calculation for a = 1.5, the perturbation treatment starts to deteriorate even in the attractive regime, while the step-function potential provides a better approximation to the numerically obtained wave functions. The same calculations for the first excited state (Fig. 6) are quite similar, although the perturbation treatment describes the numerical results for the attractive regime and for a = 1 better.

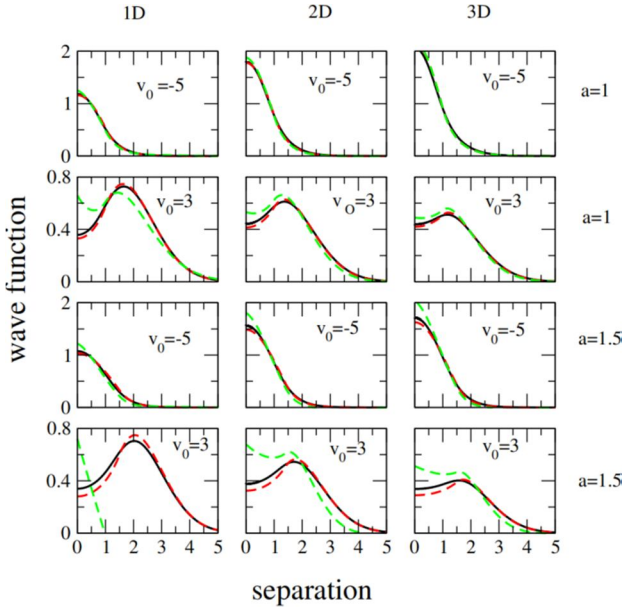

FIG. 6. Ground-state wave function in 1D, 2D, and 3D for the indicated value of the strength v_0 and the range a. Each panel compares the results obtained using the step-function potential (dashed red), the first-order perturbation correction (dashed green), and the full numerical solution (solid black). The three curves are indistinguishable for v_0 = -5 and a = 1 in 3D, though the top of the curves does not appear in order not to change the scale.

To sum up, we can say that the perturbation treatment allowed us to establish a better convergence of the analytical results toward the numerical ones for the energy spectra, whether for the intermediate or important values of the interaction range. However, the perturbation treatment does not yield a noticeable improvement for the eigenvectors of our problem. The results are sensitive to the range of the interaction as well as to the degeneracy of the energy levels occurring in the repulsive regime, especially in 1D. Consequently, the perturbation treatment is failing to establish a more accurate wave function basis to describe few-body problems. We have to notice, however, that, for small ranges, the three calculations are almost indistinguishable across all dimensionalities in the attractive regime, whether for the eigenvectors or the eigenvalues. The perturbation treatment result is even better for the first excited state in the attractive regime. This is setting some considerations for which it is possible to assert that the step potential results and/or ("or" for the case of the first excited level) the corrected ones are giving mainly the exact energies as well as the exact wave functions. Consequently, in the region where these considerations are fulfilled, it is possible to ascertain that we can establish an almost exact analytical wave function basis for describing few-body problems, with higher levels being almost insensitive to the interaction.

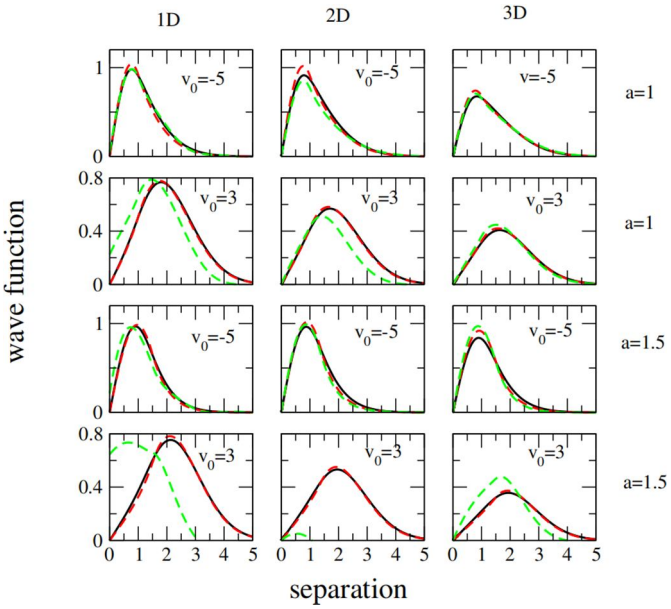

FIG. 7. First excited state wave function in 1D, 2D, and 3D for the indicated value of the strength v_0 and range a. In each panel, the results from the step-function (dashed red), perturbation correction (dashed green), and the numerical results (solid black) are compared.

4. Spatial Correlations

The representation of the energy versus v_0 for different values of the range is frequently used to show the effect of the interaction on the energy spectrum. In order to grasp the dimensionality effect on the spatial correlation, it would be preferable to use an alternative representation: energy spectrum versus the range for different values of v_0. This alternative is presented in Fig. 8 for the case of two dimensions. The advantage of representing energy versus the range over the usually used representation is that it can show the critical range at which we can observe the onset of any change in the different curves. In Fig. 8 and for the attractive regime, one observes that the point of inflection in the energy curves shifts gradually with increasing values of l. It becomes evident that the primary parameter dictating the critical range, where the inflection begins, is the angular quantum number in connection with the strength and the range of the interaction. This is the case even for the first level ($l = 0$), where the onset of the inflection of the curve is not zero but a certain finite value (see discussion in the following section). For the repulsive regime, however, the centrifugal potential and the interaction potential act in the same direction, producing a monotonic increase in energy. The same qualitative behavior is observed in three dimensions, although the energy levels are shifted to higher values due to the increased dimensionality (not shown here for clarity).

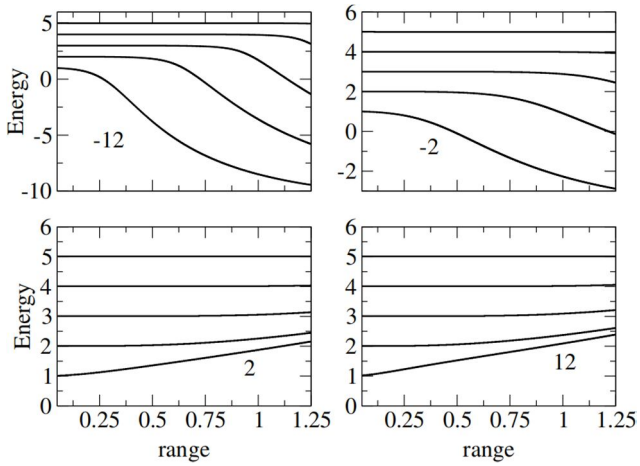

FIG. 8. Energy spectrum for the fundamental relative-radial state (n = 0) versus the range with increasing values of the angular momentum quantum number (l = 0, 1, 2, 3, 4 from bottom to top) in two dimensions. Even values of l are for bosons, and odd ones are for fermions. The numbers on each panel indicate the value of v_0.

The previous results are to be contrasted with the case of 1D in Fig. 9, where the energy is represented versus the range for different values of v_0. One can find that the onset of the inflection is not as gradual for all the levels as previously, when comparing bosonic and fermionic states. Indeed, for the first bosonic state, the inflection starts from zero, whereas for the first fermionic state, a certain critical range has to be reached in order for the inflection to occur. For the higher bosonic and fermionic levels, we can observe an evolution that is not as straight as in the case for the first levels but proceeds via several inflection points and is tightly related to the change of the interaction strength and range. The understanding of the behavior of the first bosonic and fermionic levels is quite straightforward and is due to the additional repulsion resulting from the fermionic statistics. For the repulsive regime, we can observe the same tendency to fermionization, except that in this case, the limits are not flat but continue to increase monotonically with increasing value of the range.

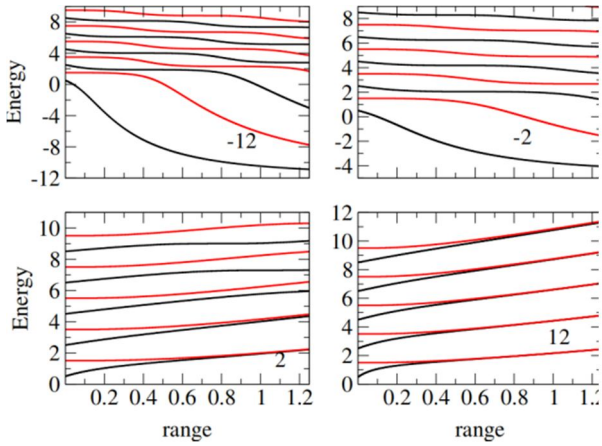

FIG. 9. Energy spectrum in one dimension versus the range with increasing value of n (n = 0, 1,..., 8, from bottom to top) with even values of n for bosons (black) and odd ones for fermions (red). The numbers on each panel indicate the value of v_0 .

We intend to show in this part, by using the results of the previous model (analytical solution for the step-like potential), the impact of the dimensionality on the space correlation of the two particles forming our system. By plotting the energy of the ground state of the relative part of the solution versus the range and for the attractive regime (Fig. 10 (a), v_0 = -5, solid lines), we observe a threshold behavior indicating the onset of binding: the energy becomes increasingly negative, signifying the formation of a bound state. Notably, this critical range, defined as the minimum range at which the attraction begins to significantly lower the energy, depends on the system's dimensionality. Specifically, the critical range is largest in the 3D case, followed by the 2D case, while in 1D, the critical range is effectively zero. The increase

in the case of a repulsive regime (Fig. 10 (a), v_0 = 5, dashed lines) is more straight with no critical range. Interestingly, the energy curves in this case converge to a common limiting value across all three dimensionalities. The different thresholds in the attractive regime are the result of the interplay between the centrifugal repulsion and the attractive interaction. In the case of 1D, the centrifugal potential is absent [Eq. (7)] and, consequently, the critical range is null. For the 3D case, even if we set $l = 0$ for the ground state, we still are left with $l = 1/2$ in 2D, as explained before. Consequently, though the centrifugal potential is equal to zero in this case, still $l_{2D} = 1/2$ appears within the arguments of the confluent hypergeometric solution of the 3D equation [17] and, consequently, this is affecting the solution. Similarly, setting $l = 0$ in 2D will not annihilate the centrifugal potential since in this case we are left with the residual term $\frac{-1/4}{r^2}$ [Eq. (8)]. It is clear from Fig. 10 (a) that the amount of the centrifugal effect is increasing gradually from the 1D case to the 3D case, passing by the 2D case.

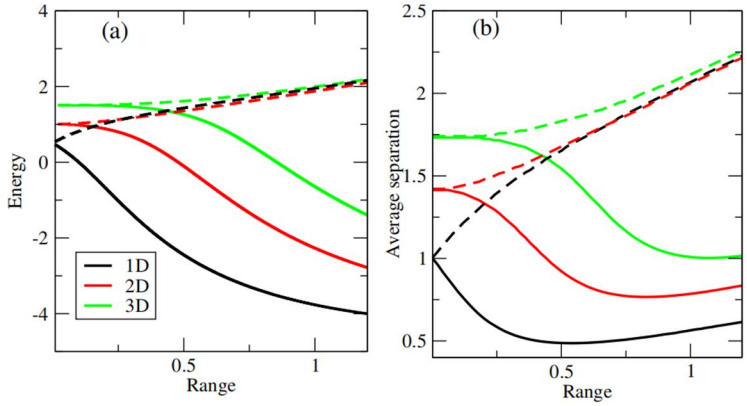

FIG. 10. (a) Comparison of the ground state energy (n = 0 for 1D, and n = 0, l = 0 for 2D and 3D) versus the range of the interaction for the three dimensionalities. (b) Comparison of the average separation between the two particles in the ground state versus the range for the three dimensionalities. Solid curves are for the attractive case (v_0 = -5) and the dashed curves are for the repulsive case (v_0 = 5).

How do these effects impact the spatial or pair correlation? To investigate this point, we plot the average separation between the two particles versus the range of the interaction for the three dimensionalities [Fig. 10 (b)]. The average separation is defined as $\sqrt{\langle x^2 \rangle}$, and the average value is calculated using the normalized total relative function (the radial part of the wave function for 2D and 3D). We plot the average separation versus the range for two different values of v_0 (v_0 = -5 for the attractive regime and v_0 = 5 for the repulsive one). The average separation is evaluated across the full spatial domain, while the interaction range is defined as half the total spatial extent, consistent with earlier sections where the range refers to the distance from the origin to the edge of the step potential (as shown in Fig. 1). This induces a factor of 2 between the two quantities. Let us first notice the similarity between the curves in Figs. 10(a) and 10(b). For the attractive regime in 1D, represented by the black solid curve in Fig. 10 (b), the average separation for a range that is nearly null is 1, consistent with the result for the non-interacting harmonic oscillator ground state. As the range increases, the average separation initially decreases, reaching a minimum, before gradually increasing and saturating. We have to notice here that the decrease occurs smoothly without a critical range. The 2D and 3D cases (Fig. 10(b), red and green solid curves) exhibit a similar trend, but with a noticeable critical range after which the average separation starts to decrease. The critical range and the curve minimum are more important for the 3D case than for the 2D one. These results show that for the 1D case, the average separation starts from a value where interaction has no effect, and when increasing the range, the system immediately feels attraction, and hence it is driven to a closer separation. Afterwards, the saturation of the average separation occurs because of the saturation of the energy for the bonded state [Fig. 10(a)]. This means that no energy is available to drive the system any closer. The same explanation holds for the 2D and 3D cases, except that in these cases, the centrifugal effect enters into play. This results in a starting average separation which is higher and, consequently, a

larger range is needed in order for the system to overcome the centrifugal repulsion and to feel the effect of the attraction. The saturation of the average separation in 2D and 3D is also due to the saturation of the bonding energy. Once the minimum is overcome, the difference in the average separation between the three dimensionalities stays nearly constant. In Fig. 10(b), the repulsive regime ($v_0 = 5$, dashed curves) for the three dimensionalities is also plotted. In this case, the average separation increases gradually for the whole extent of the range. The results for 1D, 2D, and 3D converge to the same limit. This behavior is replicating the behavior of the available energy in the repulsive regime. We also find in this case that the average separation for the three dimensionalities is almost equal to the range of the interaction (bear in mind the factor of 2 between the range and the average separation, as mentioned before). The spatial correlation for the same system is also studied for 1D in Ref. [27] using the two-particle density profile. The results are shown only for the repulsive regime where the inter-particle distance increases gradually with the increase of the range, as confirmed by our calculation. While our method does not resolve the exact localization of particles within the trap, we are able to quantify the average separation on the whole extent of the range for the different dimensionalities and for different regimes in a very simple manner. This approach clearly illustrates the interplay between the interaction strength and the centrifugal potential (which depends on dimensionality) and their combined effect on spatial correlations.

In Fig. 11, we present the same illustration as in Fig. 10 but for the first excited state for the three dimensionalities (n = 0 for 1D, and n = 0, l = 1 for 2D and 3D). The results are quite similar, though it is clear that the critical range at which we have the onset of the inflection in this case is more important, whether for the energy or the average separation. This is expected, as these excited states are fermionic and thus subject to Pauli repulsion. Furthermore, the value of the angular momentum quantum number in 2D and 3D increases the centrifugal potential. As expected, the value of energy for a range that is null as well as the average separation are more important in this case compared to the results for the ground state (Fig. 10). Unfortunately, it is not possible to extend the plot beyond the range of 1.25 (the calculation breaks down because of the singular behavior of the confluent hypergeometric functions beyond the plotted region). However, based on the observed trends, we can expect the same saturation result in the attractive regime.

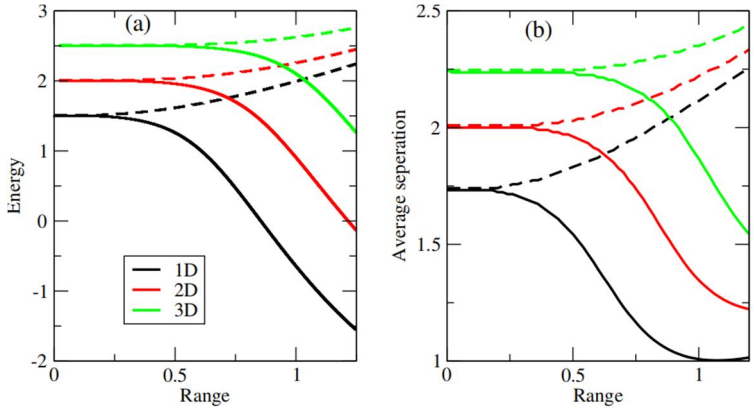

FIG. 11 (a) Comparison of the first excited state energy (n = 1 for 1D; n = 0, l = 1 for 2D and 3D) energy versus the range of the interaction for the three dimensionalities. (b) Comparison of the average separation between the two particles in the first excited state versus the range for the three dimensionalities. Solid curves are for the attractive case (v_0 = -5), and the dashed curves are for the repulsive case (v_0 = 5).

5. **Dynamical Aspects**

There is a growing interest in the study of the non-equilibrium evolution of cold, confined few-particle systems. Recent research in this area has led to intriguing findings that deepen our understanding of the fundamental dynamics governing such systems [30, 32]. In particular, the availability of analytical solutions for certain prototype models has proven to be highly beneficial in exploring key dynamical features. Many of these analytical approaches are based on the assumption of contact interactions, which serve as a reliable approximation in dilute systems [33].

In what follows, we present some preliminary results that can be obtained by using our step-like potential model to describe a system of two confined bosons. The analysis is carried out in a simplified framework, aiming to offer qualitative insight into the potential dynamical behavior of such systems beyond the static properties discussed earlier.

This interaction choice could be a good candidate in the case of Rydberg atom systems. To our best knowledge, no such investigation was carried out before. Only delta-like or Gaussian interactions were studied [33, 34]. The evolution of the system properties with time requires the solution of the time-dependent Schrödinger equation. Our goal is to investigate the evolution of the system under the initial interaction features compared with the change of the behavior of the system under a sudden change of these same features. This is what is known as a quenched interaction. We are elaborating these calculations for the three dimensionalities. To solve the time-dependent Schrödinger equation, we employ the Crank-Nicolson method together with the tridiagonal matrix algorithm, exploiting the built-in programs provided by the LAPACK library [35]. We consider grid sizes of Δt =0.0002 and Δx = 0.04. We take a space of $-30 \leq x \leq 30$. While the time step is fine enough to avoid any distortions during time, the step and the extent of the space are constrained by computational resources. Nevertheless, these are quite satisfactory for the present calculations to reach convergence. The initial wave function from which the evolution of the system starts is considered to be the exact analytical ground state solution already found by resolving the time-independent Schrödinger equation for a step potential interaction. We focus solely on the relative part of the wave function, since the center of motion is not affected by the interaction [Eq. (4)]. This implies that the initial exact ground-state solution we have established by resolving the time-independent Schrödinger equation, is evolves in time, either in the same initial potential or under a suddenly modified potential features at t = 0. In the first situation, we have just a stationary state, and in the second situation, the systems are no longer stationary but start to evolve under the new potential.

5.1 1D Case

In Figs. 12, 13, and 14, we present different quench scenarios, each starting from a different initial point. In Fig. 12, the starting point is v_0 = -5, and the first panel shows the stationary case. This 2D plot illustrates the probability density as a function of both average separation and time. At each time *t*, the probability density is calculated as $f(r)f^*(r)$, where *f(r,t)* is the normalized temporal (either stationnary or quenched) evolution of the wave function *f(r,0),* the properly normalized wave function *f(r,0)* being determined by Eq. (8). This stationary evolution reproduces a well-localized probability distribution with a nearly constant interparticle separation, demonstrating the reliability and internal consistency of our computational implementation. Only very tiny numerical kinks start to develop with time. This is due to the known Crank-Nicolson spurious oscillations that contaminate the wave function at each time iteration without compromising the physical results [36]. From this initial state, we perform different sudden changes on the strength of the potential. We can see that changing v_0 from -5 to -12 confines the probability density to a slightly narrower separation and hence a better localization of the system is reached throughout the whole time interval. Switching the interaction strength from -5 to 0 leads to a breathing mode, characterized by regular oscillations of the average separation between two extreme values. In the case where v_0 is switched from -5 to 12, we can witness a high fragmentation of the density probability with a very poor localization of the system. When we change the starting point (Fig. 13) and set v_0 = 5, the stationary case gives, as expected, two well-localized pics of the probability density. Switching v_0 from 5 to 0 results in a regular pattern with an oscillatory behavior of the separation over time. A sudden change of v_0 from 5 to -12 leads to significant fragmentation of the probability density. Although the resulting pattern remains somewhat regular, there is a clear tendency for the density to shift toward the center, driven by the attractive post-quench interaction. Interestingly, when v_0 is changed from 5 to 12, the system remains nearly in a stationary regime: the separation between the particles is largely preserved, indicating that the increase in repulsion does not significantly push the particles further apart. Let us now investigate the particular case where the starting point is v_0 = 0 (Fig. 14). Here, we have a well-localized pic in the stationary regime. However, setting the

change of v_0 from 0 to -12 gives a variation of the separation between two extreme positions. Changing v_0 from 0 to 12 yields the same result as when starting with v_0 = -5. To summarize these results at the level of the average separation, we present the results for the average separation for the different quench scenarios in Fig. 15. This figure also includes the average separation for the stationary cases (v_0 = -5, 0, and 5, plotted in gray). Additionally, we include the intermediate quenches towards v_0 = 5 or -5. Fig. 15 clearly shows that the already stated oscillatory and fragmented behaviors of the probability density for different scenarios are replicated in the average separation. We can also see that we have only a small perturbation of the average separation around its initial value when we have a transition from attractive to attractive or zero to attractive potential [Figs. 15 (a) and 15(b)] for the transition to the attractive potential. We have this same result when the system is initiated with a repulsive potential, regardless of the nature of the transition operated [Fig. 15 (c)]. However, initiating the system from an attractive potential and operating a transition towards a repulsive potential creates an important average separation as well as an irregular oscillation of its value. It seems that the greater the transition towards an important value of the potential, the longer the system takes to settle into a nearly constant value (note the damping of the oscillations in Fig. 15 (a) for the transition to the repulsive potential).

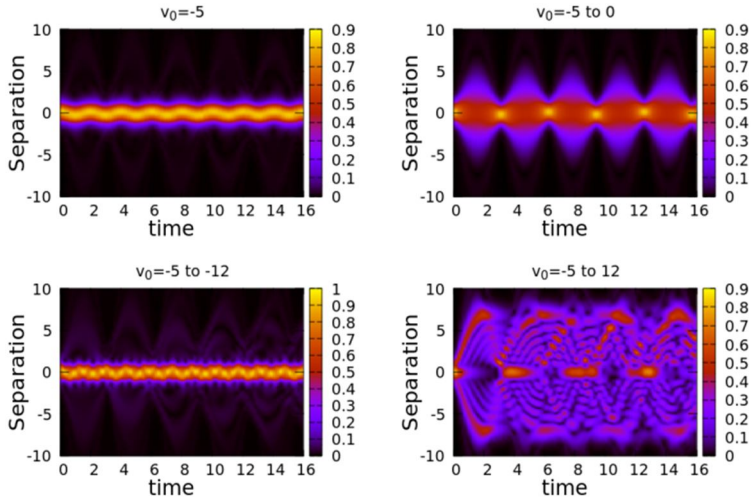

FIG. 12. Time evolution of the probability density for different indicated quench scenarios and one-dimensional fundamental state. The initial state is for v_0 = -5, and the range is fixed to 1.

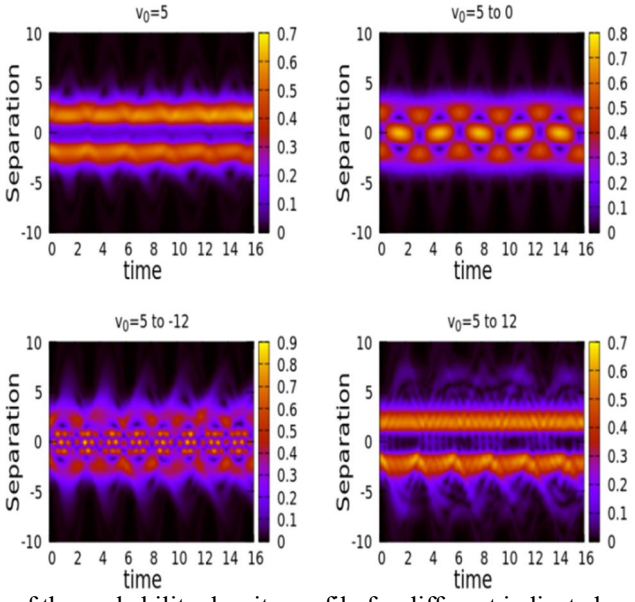

FIG. 13. Time evolution of the probability density profile for different indicated quench scenarios and one-dimensional fundamental state. The initial state is for v_0 = 5, and the range is fixed to 1.

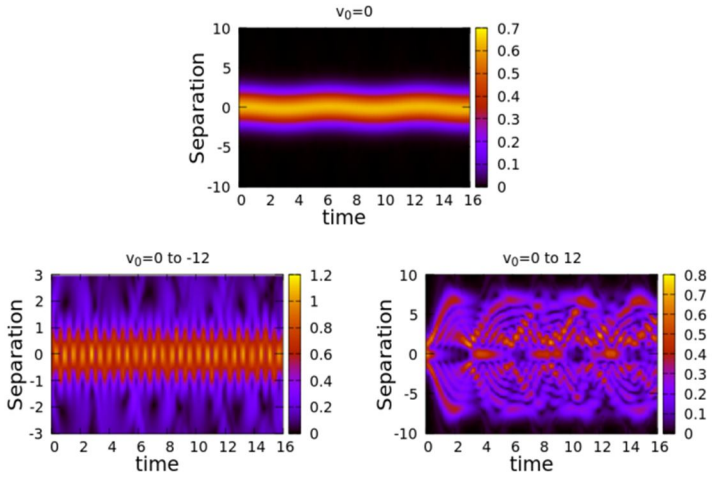

FIG. 14. Time evolution of the probability density profile for different indicated quench scenarios in the one-dimensional fundamental state. The initial state for v_0 is set to 0, and the range is fixed to 1.

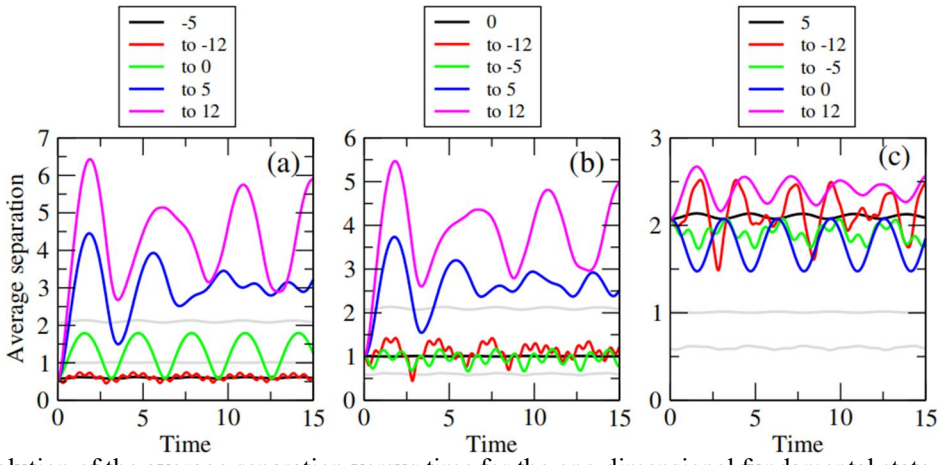

FIG. 15. Evolution of the average separation versus time for the one-dimensional fundamental state. The average separation for the stationary states for each fixed potential is shown in black for the corresponding potential and in gray for the other two potentials in each panel. Different scenarios of sudden changes in the potential strength from the initial value are given in the legend. The range of the interaction is fixed at 1. (a) The initial state is the one for v_0 = -5, (b) the initial state is the one for v_0 = 0, and (c) the initial state is one for v_0 = 5.

5.2. 2D Case

For the 2D case, the probability density at each time t is calculated as $f(r)f^*(r)$, where *f(r,t)* is the normalized temporal (either stationnary or quenched) evolution of the wave function *f(r,0),* the properly normalized wave function *f(r,0)* being determined by Eq. (8). To elaborate the calculation for this part, we are facing the problem of the singularity of the centrifugal potential at r = 0 when we set $l = 0$ in the Eq. (8). In fact, in this case when setting l = 0, we are left with $\frac{-1/4}{r^2}$ for the centrifugal potential. It is not possible to avoid the region where r = 0, as the correlation must be studied in the whole space of the trap. To remedy this situation, the usual numerical solution is to soften the singularity by introducing a small constant α in the denominator [37]. We propose the following transformation:

$$\frac{-1/4}{r^2} \rightarrow \frac{-1/4}{\sqrt{(r^4+\alpha)}} \tag{14}$$

To establish the best choice of the value of α, we must check that it is the smallest value that reproduces the stationary regime. We found that α=0.001 for $v_0 \geq 0$, and α = 0.0000001 for $v_0 < 0$. Using these values for the calculations, we reproduce the same quench scenarios for the 2D case as those shown for 1D in Figs. 16, 17, and 18. Comparing the 1D and 2D results, we notice that qualitatively the behavior is similar, except that the breathing mode seen for the v_0= -5 to 0 has disappeared (Fig. 16). We notice also that the fragmentation for v_0 = -5 to 12 and v_0= 0 to 12 is less pronounced (Figs. 16 and 18). The results for quench scenarios starting from v_0 = 5 are more affected by numerical errors caused by spurious oscillations inherent to the Crank-Nicolson method (Fig. 17). In this scenario, the

fraction of the density probability driven to the center when setting v_0 = 5 to -12 is also less important. We plot the average separation for these different scenarios in Fig. 19. As observed previously, only a quench from an attractive or null potential to a repulsive one is able to noticeably change the spatial correlation between the two particles. However, the transition from an attractive potential to a repulsive one leads obviously to a greater average separation compared to the 1D case. It is important to note here that some of the results could be just numerical artefacts (particularly the disappearance of the breathing mode), and the singularity of the centrifugal potential should be properly dealt with.

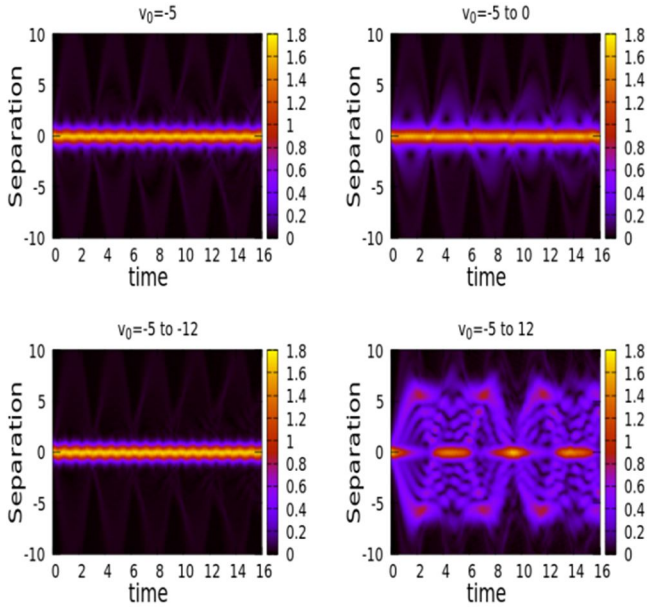

FIG. 16 Time evolution of the probability density for different indicated quench scenarios in the two-dimensional fundamental state. The initial state is v_0 = -5, and the range is fixed at 1.

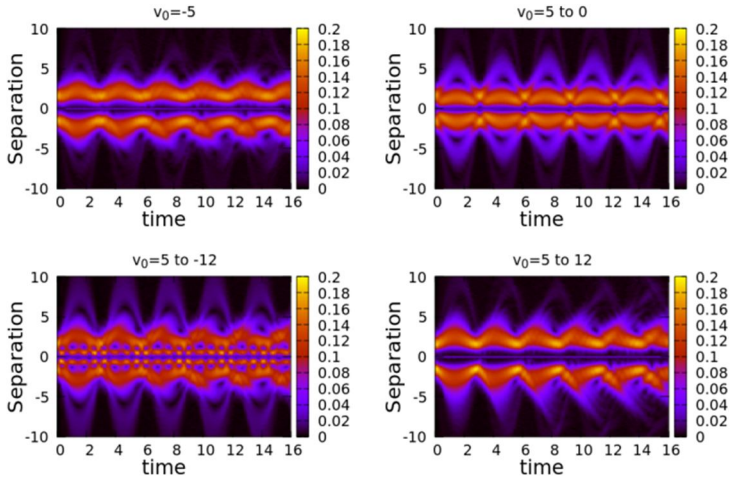

FIG. 17. Time evolution of the probability density profile for different indicated quench scenarios in the two-dimensional fundamental state. The initial state is v_0 = 5, and the range is fixed at 1.

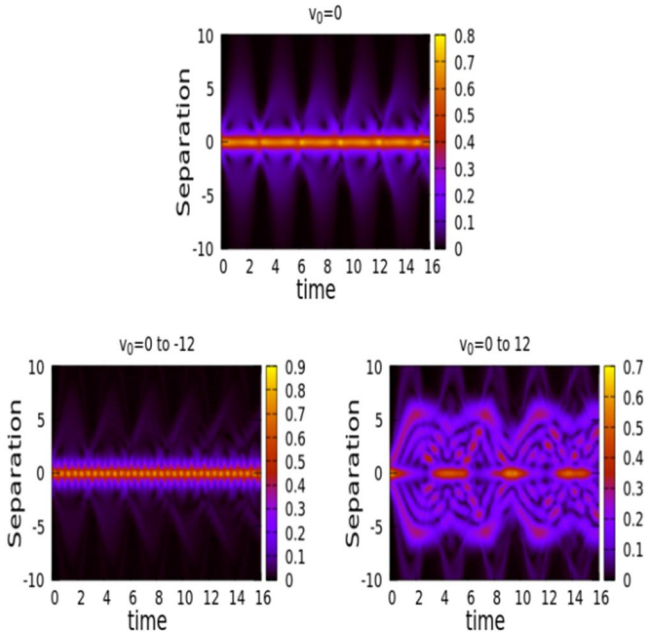

FIG.18. Time evolution of the probability density profile for different indicated quench scenarios in the two-dimensional fundamental state. The initial state is $v_0 = 0$, and the range is fixed at 1.

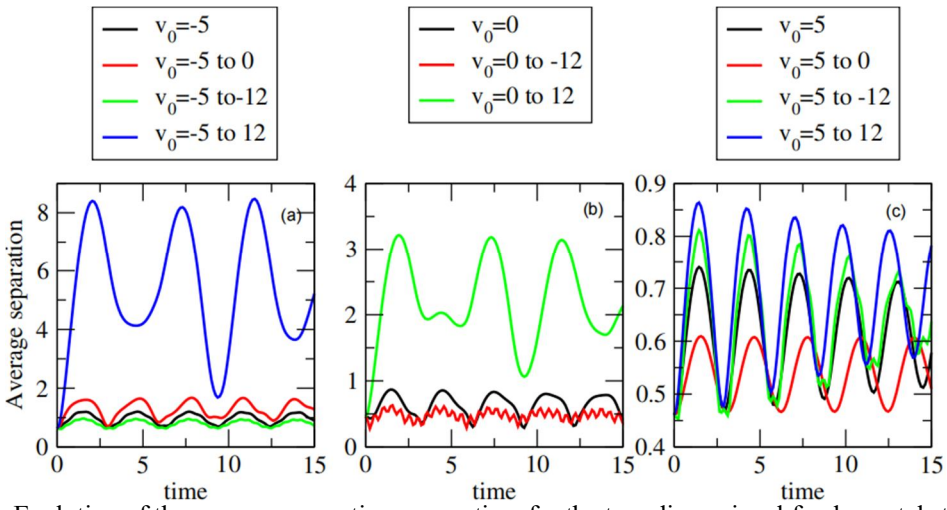

FIG. 19. Evolution of the average separation versus time for the two-dimensional fundamental state. The different scenarios of the sudden change in the potential strength from the initial value are given in the legend. The range of interaction is fixed at 1. (a) The initial state is $v_0 = -5$, (b) the initial state is $v_0 = 0$, and (c) the initial state is $v_0 = 5$.

5.3. 3D Case

For the 3D case, the probability density at each time t is calculated as $f(r)f^*(r)$, where *f(r,t)* is the normalized temporal (either stationary or quenched) evolution of the wave function *f(r,0)*. The properly normalized wave function *f(r,0)* is determined by Eq. (9). As we have explained before, in the 3D case setting $l_{3D} = 0$ for the fundamental state means $l_{2D} = 1/2$ [see Eq. (10)]. This value of the angular quantum number appears in the argument of the confluent hypergeometric function, influencing the results even if apparently the centrifugal potential is reduced to zero. For the sake of brevity, we present only the average separation for the different quench scenarios in the 3D case (Fig. 20). Qualitatively, the results are the same as before. However, the average separation is notably larger when the system undergoes a transition from an attractive to a repulsive potential [Fig. 20 (a)]. Moreover, transitions from a repulsive potential show less sensitivity to perturbations compared to the other dimensionalities [Fig. 20 (c)].

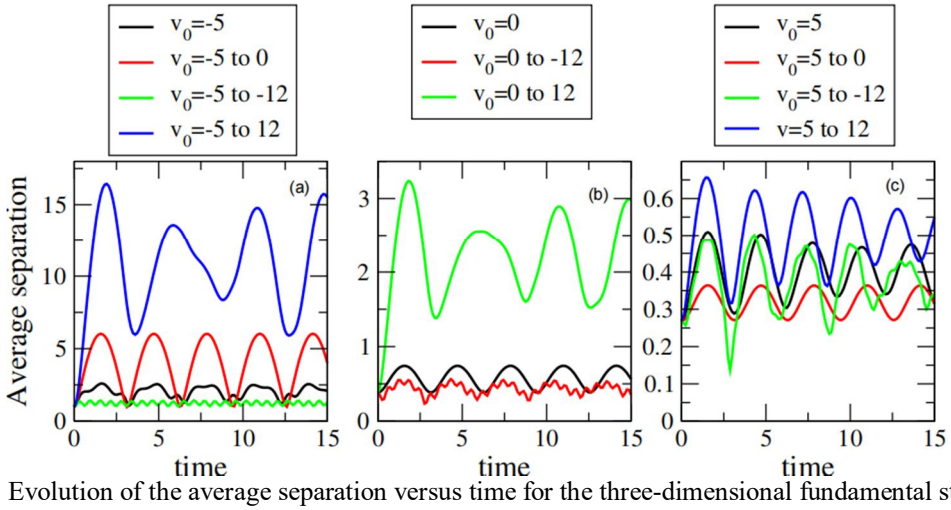

FIG. 20. Evolution of the average separation versus time for the three-dimensional fundamental state. The different scenarios of sudden changes in the potential strength from the initial value are given in the legend. The range of interaction is fixed at 1. (a) The initial state is v_0 = -5, (b) the initial state is v_0 = 0, and (c) the initial state is v_0 = 5.

6. Conclusion

The aim of this study is to highlight the features that arise in different aspects of a system of two Rydberg atoms confined in a harmonic trap under different dimensionalities. To conduct the study, we use the exact solution provided by the Schrödinger equation with a step-like potential. To prove the adequacy of this model for describing the targeted Rydberg interactions, we developed a perturbation treatment of the proposed model. The results offer a more accurate description of the energy spectra. The results for eigenvectors are less satisfactory, fundamentally because of the energy degeneracy between neighboring levels, which causes the mathematical formulation to become singular. Far from the region where this degeneracy occurs, it is possible to establish acceptable results that could be fairly used as a wave function basis for few-body systems. Being more confident about the used model, we move in the second part to the characterization of the spatial correlation of the studied system. The results shed light on the role played by the interrelation between the interaction features and the centrifugal potential arising from the considered dimensionality, and how this interplay affects spatial correlations. In the attractive regime, a complex behavior emerges because the interaction and centrifugal repulsion act antagonistically. In contrast, in the repulsive regime, where interaction and centrifugal repulsion act in the same direction, the spatial correlation is primarily dictated by the interaction features. For both regimes, the results also demonstrate the impact of the energy available to the state, which clearly influences the overall trend of spatial correlation. In the final part, we investigate the effect of dimensionality on the temporal evolution of the system under different quench scenarios. Here, we also employ the exact solution for the step-like interaction. This specific interaction must be contrasted with delta-like and Gaussian interactions, as the step-like interaction is spatially extended with a constant strength over the considered range, unlike the localized delta or Gaussian potentials. Our preliminary results illustrate how the density profile evolves and reveal how the quench scenario affects the probability density distribution and, consequently, the spatial correlation of the system.

In this study, the quench is applied solely to the interaction strength, but it can be easily extended to the interaction range as well. Gathering extensive data on these dynamical aspects while distinguishing numerical artifacts could provide important insights into both theoretical and technological aspects of cold few-particle systems. A deeper investigation along these lines could shed more light on fundamental aspects related to strongly correlated systems and may also offer experimental clues on how to monitor system correlations.

References

[1] Blume, D., Rep. Prog. Phys., 75 (2012) 046401.

[2] Abraham, J.W. and Bonitz, M., Contrib. Plasma Phys., 54 (2014) 27.

[3] Turbiner, A.V., Phys. Rep., 642 (2016) 1.

[4] Morales, J., Garcia-Martinez, J., Garcia-Ravelo, J., and Pena, J.J., J. Appl. Math. Phys., 3 (2015) 454.

[5] Gao, B., Phys. Rev. A, 58 (1998) 1728.

[6] Gao, B., Phys. Rev. A, 59 (1999) 2778.

[7] Ginocchio, J.N., Ann. Phys., 152 (1984) 203.

[8] Blaizot, J-P. and Ripka, G., "Quantum Theory of Finite Systems", 1st Ed., (MIT Press, Massachusetts, 1985).

[9] Pitaevskii, L. and Stringari, S., "Bose-Einstein condensation", 1st Ed., (Clarendon Press, Oxford, 2003).

[10] Kościk, P., Kuroś, A., Pieprzycki, A., and Sowiński, T., Sci. Rep., 11 (2021) 13168.

[11] Busch, T., Englert, B-G., Rzazewski, K., and Wilkens, M., Found. Phys., 28 (1998) 549.

[12] Wei, B-B., Int. J. Mod. Phys. B, 23 (2009) 3709.

[13] Doganov, R.A., Klaiman, S., Alon, O.E., Streltsov, A.I., and Cederbaum, L.S., Phys. Rev. A, 87 (2013) 033631.

[14] Mujal, P., Polls, A., and Julia-Diaz, B., Condens. Matter, 3 (2018) 9.

[15] Ołdziejewski, R., Górecki, W., and Rzaźewski, K., Europh. Lett., 114 (2016) 4.

[16] Lim, J., Lee, H-G., and Ahn, J., J. Korean Phys. Soc., 63 (2013) 867.

[17] Kościk, P. and Sowiński, T., Sci. Rep., 8 (2019) 12018.

[18] Zinner, P.N.T., EPJ Web Conf., 113 (2016) 01002.

[19] Islam, R. et al., Science, 340 (2013) 583.

[20] Görlitz, A. et al., Phys. Rev. Lett., 87 (2001) 130402.

[21] Grar, N. and Chia, L., J. Phys. Chem. Res., 1 (2022) 7.

[22] Gallagher, T.F., Rep. Prog. Phys., 51 (1988) 143.

[23] Dalibard, J., "Les Interactions Entre Atomes Dans Les Gaz Quantiques", (College de France, lecture notes, 2020) [in French].

[24] Mathews, Jr.W.N., Esrick, M.A., Teoh, Z., and Freerick, J.K., "A Physicist's Guide to the Solution of Kummer's Equation and Confluent Hypergeometric Functions", (arxiv, 2021).

[25] Abramowitz, M. and Stegan, I., "Handbook of Mathematical Functions with Formulas, Graphs, and Mathematical Tables", 10th Ed., (U.S. Government Printing Office, Washington, 1964).

[26] Digital Library of Mathematical Functions, (2021), http://dlmf.nist.gov.

[27] Kościk, P. and Sowiński, T., Sci. Rep., 8 (2018) 48.

[28] Girardeau, M., J. Math. Phys., 1 (1960) 516.

[29] Okopińska, A. and Kościk, P., Few-Body Syst., 45 (2009) 223.

[30] Dobrzyniecki, J. and Sowiński, T., Phys. Rev. A, 103 (2021) 013304.

[31] Giannozzi, P., Ercolessi, F., and Gironcoli, S.D., "Numerical Methods in Quantum Mechanic", (Lecture notes, 2021).

[32] Kehrberger, L.M.A., Bolsinger, V.J., and Schmelcher, P., Phys. Rev. A, 2018 (2018) 01360697.

[33] Budewig, L., Mistakidis, S.I., and Schmelcher, P., Mol. Phys., 117 (2019) 2043.

[34] Ishmukhamedov, I.S., Phys. E, 142 (2022) 115228.

[35] Koonin, S.E. and Meredith, D.C., "Computational Physics: Fortran Version", 1st Ed., (CRC Press, 1990).

[36] Neto, A.B., Mansur, W.J., and Ferreira, W.G., Sci. Rep., 12 (2022) 18887.

[37] Loudon, R., Am. J. Phys., 27 (1959) 649.

Volume 18, Number 2, 2025. pp. 225-240

Jordan Journal of Physics

ARTICLE

Geometrical Interpretation of Lorentz Transformation Equations in Two and Three Dimensions of Space

Chandra Bahadur Khadka

Department of Physics, Tri-Chandra Multiple Campus, Tribhuvan University, Kathmandu-44600, Nepal.

Doi: **https://doi.org/10.47011/18.2.11**

Received on: 15/01/2024; *Accepted on: 20/02/2024*

Abstract: This study introduces a new method to interpret the mathematical formulation of the Lorentz transformation by extending relative motion between inertial frames to two- and three-dimensional space. Here, the space-time coordinate transformations along X-, Y-, and Z-directions are formulated by developing the relation between Cartesian and polar coordinates. Based on this modified theory, the correct transformation equations along X-, Y-, and Z-directions are formulated as: $x' = x\left(1 - vt/\sqrt{x^2+y^2+z^2}\right)/\sqrt{1-v^2/c^2}$, $y' = y\left(1 - vt/\sqrt{x^2+y^2+z^2}\right)/\sqrt{1-v^2/c^2}$ and $z' = z\left(1 - vt/\sqrt{x^2+y^2+z^2}\right)/\sqrt{1-v^2/c^2}$, where (x, y, z, t) and (x', y', z', t') denote the space-time coordinates measured in the stationary and moving frames of reference, respectively. Using these modified transformation equations, the invariance of space-time interval and relativity of simultaneity have been studied extensively. In this charming topic of relativistic mechanics, our specific purpose is not to enter into the merits of the existing one-dimensional Lorentz transformation, but rather to propose a brief and carefully reasoned mathematical derivation demonstrating how the Lorentz transformation can be extended to two- or three-dimensional space.

Keywords: Frame of reference, Lorentz transformation, Relativistic mechanics, Special relativity.

1. Introduction

Based on the relativistic concept of space-time, Lorentz [1] introduced the transformation equations under which the velocity of light in a vacuum remains constant and independent of the relative motion of the source and observer. A form of the Lorentz transformation, very close to its modern version, was recorded in 1905 by Poincaré [2]. Einstein derived the correct transformation formula of coordinates based on the postulate of constant speed of light [3, 4]. These are given as:

$$x' = \frac{x - vt}{\sqrt{1 - v^2/c^2}},\ y' = y,\ z' = z$$

$$t' = \frac{t - \frac{xv}{c^2}}{\sqrt{1 - v^2/c^2}} \quad (1)$$

Derivations of the Lorentz transformation, including the above version of coordinate transformation, namely Eq. (1), are presented in several excellent textbooks [5, 6], including the famous "The Feynman Lectures on Physics" [7]. For many years, researchers have focused on the theoretical studies of the Lorentz transformation to propagate the relativistic mechanics in several different directions. In Ref. [8], the authors derived the Lorentz transformation equations by changing the synchronization of clocks in an inertial coordinate system. Such space-time coordinate transformation equations were further extended to incorporate the one-way speed of light in free space by Selleri [9, 10]. Lee *et al.*

Corresponding Author: Chandra Bahadur Khadka **Email**: chandrabahadur9988@gmail.com

[11] presented a derivation of the Lorentz transformation by invoking the principle of relativity alone, without resorting to an *a priori* assumption of the existence of a universal limiting velocity. Levy [12] derived the Lorentz transformation from a simple thought experiment by using the vector formula from elementary geometry. In Ref. [13], a mathematical analysis describing the concepts of the time dilation phenomenon in the realm of relativistic mechanics was presented. In Ref. [14], the authors explained the Lorentz transformation in terms of changes in the wave characteristics of matter as it transitions between inertial frames. Moreover, Pagano *et al*. [15] discussed different roles of the Lorentz transformation in classical wave propagation theories and relativistic mechanics. Also, there are numerous papers showing the paradoxes of special relativity developed by some contemporary independent scholars [16]. In Ref. [17], new mathematical formalisms of the special theory of relativity were developed. Research was also conducted on the practical aspects of relativistic mechanics [18]. In articles [19, 20], it has been demonstrated that the length, breadth, and height of a cuboid appear to be shortened to the observer when there is simultaneous relative motion between the cuboid and the observer in the three dimensions of space. The author in the works [21, 22] introduces the concept of multidimensional temporal coordinates in the theory of relativity. Additionally, the author in work [23] demonstrates the variation of mass in a gravitational field using the equation $E = mc^2$. In work [24], the matrix representation of Lorentz transformation equations between inertial frames of reference moving in three-dimensional space has been developed. The article [25] provides a reformulation of the main equations of linear momentum, force, and kinetic energy in the context of special relativity. Reference [26] contributes significantly to special relativity by formulating a three-dimensional form of the Lorentz transformation. There are many publications on special relativity with important theoretical results, but all such publications are connected with Lorentz transformation equations derived from one-dimensional motion between inertial frames. Lorentz transformation equations extended to accommodate motion in all three spatial dimensions have yet to be thoroughly investigated.

This paper addresses that gap by exploring new space-time concepts in relativistic mechanics through the introduction of relative motion between inertial frames in two- and three-dimensional space. The modified Lorentz transformation equations along the

X-, Y-, and Z-directions, replacing those in Eq. (1), are given by:

$$x' = \frac{x\left(1-\frac{vt}{\sqrt{x^2+y^2+z^2}}\right)}{\sqrt{1-v^2/c^2}}, \qquad y' = \frac{y\left(1-\frac{vt}{\sqrt{x^2+y^2+z^2}}\right)}{\sqrt{1-v^2/c^2}},$$

$$z' = \frac{z\left(1-\frac{vt}{\sqrt{x^2+y^2+z^2}}\right)}{\sqrt{1-v^2/c^2}} \tag{2}$$

The time transformation equation is given by:

$$t' = \frac{t-\frac{v\sqrt{x^2+y^2+z^2}}{c^2}}{\sqrt{1-v^2/c^2}} \tag{3}$$

where x', y', z', t' denote space-time coordinates measured in the moving frame, and x, y, z, t denote space-time coordinates measured in the initial frame.

With the above motivation, the remainder of the paper is organized as follows. Section 2 outlines the complete mathematical derivation of space-time coordinate transformations between two inertial frames moving with uniform velocity in the two-dimensional XY-plane. Section 3.1 formulates the Lorentz transformation equations in terms of radius vectors d and d' in three − dimensinal space, while Section 3.2 presents the relationship between polar and Cartesian coordinates for both the stationary and moving frames. Section 3.3 derives the Lorentz transformation equations along the X-, Y-, and Z- axes in three-dimensional space. Section 3.4 verifies the invariance of the space-time interval, expressed by the equation $x^2 + y^2 + z^2 - c^2t^2 = x'^2 + y'^2 + z'^2 - c^2t'^2$. Section 3.5 presents the analysis of the relativity of simultaneity. Finally, Section 4 delineates the concluding remarks on the present study.

2. Two-Dimensional Transformation Equations

2.1 Geometrical Calculations

Let us consider two inertial reference frames, S and S′. The reference frame S′ moves with a

constant velocity v relative to S in the two-dimensional XY-plane, as shown in Fig. 1. At $t = t' = 0$, when the two frames are superimposed, a photon of light leaves the origin of both frames and travels with velocity c. When the photon reaches a point P, let its space-time coordinates as measured in frames S and S′ be $(x, y, z = 0, t)$ and $(x', y', z' = 0, t')$, respectively.

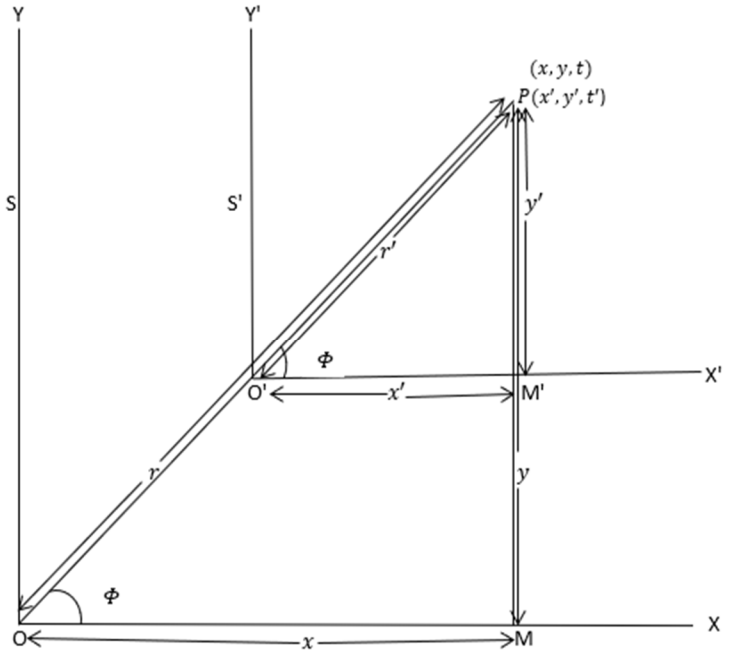

FIG. 1. Motion between two inertial frames in two-dimensional space.

The time taken by the photon to reach P from the observer O is:

$$t = \frac{OP}{c} = \frac{r}{c}$$

or

$$r = ct \tag{4}$$

Similarly, the time taken by the photon to reach P from the observer O′ is:

$$t' = \frac{O'P}{c} = \frac{r'}{c}$$

or

$$r' = c\,t' \tag{5}$$

Draw PM′ and PM perpendicular to the X′- and X-axis, respectively. From Fig. 1, in the triangles OPM and O′PM′:

(I) Angle OPM = Angle O′PM′ (Same angle)

(II) Angle OMP = Angle O′M′P (Right angle)

(III) Angle POM = Angle PO′M′ (Remaining angle)

Therefore, angle POM = angle PO′M′= ϕ.

In the right-angled triangle OPM:

$$\sin\phi = \frac{PM}{PO} = \frac{y}{r}$$

or

$$y = r\sin\phi \tag{6}$$

From Eqs. (4) and (6) we get:

$$y = ct\sin\phi \tag{7}$$

and $\cos\phi = \frac{MO}{PO} = \frac{x}{r}$

or

$$x = r\cos\phi \tag{8}$$

From Eqs. (4) and (8) we get:

$$x = ct\cos\phi \tag{9}$$

also, $OP^2 = OM^2 + MP^2$

or

$$r^2 = x^2 + y^2$$

or

$$r = \sqrt{x^2 + y^2} \tag{10}$$

which is the radius vector in the S frame of reference.

Similarly, in the right-angled triangle O′PM′,

$$\sin\phi = \frac{PM'}{PO'} = \frac{y'}{r'}$$

or

$$y' = \mathrm{r}'\sin\phi \quad (11)$$

From Eqs (5) and (11) we get:

$$\mathrm{y}' = c\mathrm{t}'\sin\phi \quad (12)$$

and $\cos\phi = \frac{\mathrm{M}'\mathrm{O}'}{P\mathrm{O}'} = \frac{x'}{r'}$

or

$$x' = \mathrm{r}'\cos\phi \quad (13)$$

From Eqs. (5) and (13) we get:

$$x' = c\mathrm{t}'\cos\phi \quad (14)$$

also, $\mathrm{O}'P^2 = \mathrm{O}'\mathrm{M}'^2 + \mathrm{M}'P^2$

or

$$\mathrm{r}'^2 = x'^2 + y'^2$$

Or

$$\mathrm{r}' = \sqrt{x'^2 + y'^2} \quad (15)$$

which is the radius vector in the S′ frame of reference.

2.2 Relativistic Transformation Equations

The following relation can be easily written based on Fig. 1:

$$\mathrm{O}'P = OP - O\mathrm{O}'$$

or

$$r' = r - vt$$

This is the Galilean transformation equation in terms of radius vector from frame S to S′, since there is no Lorentz factor (α). Therefore, the above transformation equation on relativistic mechanics is given by:

$$r' = \alpha(r - vt) \quad (16)$$

Multiplying both sides of Eq. (16) by sinϕ, we get:

$$r'\sin\phi = \alpha(r\sin\phi - vt\sin\phi)$$

Using Eq. (11), we get:

$$\mathrm{y}' = \alpha(r\sin\phi - vt\sin\phi) \quad (17)$$

From Eq. (6) we get:

$$y' = \alpha(y - vt\sin\phi) \quad (18)$$

Again, multiplying both sides of Eq. (16) by cosϕ, we get:

$$r'\cos\phi = \alpha(r\cos\phi - vt\cos\phi)$$

Using Eq. (13), we get:

$$x' = \alpha(r\cos\phi - vt\cos\phi) \quad (19)$$

From Eq. (8) we get:

$$x' = \alpha(x - vt\cos\phi) \quad (20)$$

Therefore, Eqs. (18) and (20) are the required Lorentz transformation equations along the Y- and X-axes when there is relative motion along both axes simultaneously.

Similarly, the following relation can be easily written based on Fig. 1:

$$OP = \mathrm{O}'P + O\mathrm{O}'$$

or

$$r = r' + v\mathrm{t}'$$

This is the inverse Galilean transformation equation in terms of radius vector from frame S′ to S, since there is no Lorentz factor (α). Therefore, the above inverse transformation equation on relativistic mechanics is given by:

$$r = \alpha(r' + vt') \quad (21)$$

Multiplying both sides of Eq. (21) by sinϕ, we get:

$$rsin\phi = \alpha(\, r'sin\phi + v\, t'sin\phi)$$

Using Eqs. (6) and (11), we get:

$$y = \alpha(y' + v\mathrm{t}'\sin\phi) \quad (22)$$

Again, multiplying both sides of Eq. (21) by cosϕ, we get:

$$rcos\phi = \alpha(r'cos\phi + vt'cos\phi)$$

Using Eqs. (8) and (13), we get:

$$x = \alpha(\, x' + v\, t'cos\phi) \quad (23)$$

Therefore, Eqs. (22) and (23) are the required inverse Lorentz transformation equations along the Y- and X-axes when there is relative motion along both axes simultaneously.

2.3 Determination of the Lorentz Factor

From Eq. (16) we have:

$$r' = \alpha(r - vt)$$

Substituting the value of t from Eq. (4), we get:

$$r' = \alpha\left(r - v\frac{r}{c}\right)$$

or

$$r' = \alpha r\left(1 - \frac{v}{c}\right) \quad (24)$$

From Eq. (21) we have:

$$r = \alpha(r' + vt')$$

Substituting the value of t' from Eq. (5), we get:

$$r = \alpha\left(r' + v\frac{r'}{c}\right)$$

or

$$r = \alpha r'\left(1 + \frac{v}{c}\right) \quad (25)$$

Putting the value of r' from Eq. (24), we get:

$$r = \alpha^2 r\left(1 - \frac{v}{c}\right)\left(1 + \frac{v}{c}\right)$$

or

$$1 = \alpha^2\left(1 - \frac{v^2}{c^2}\right)$$

or

$$\alpha^2 = \frac{1}{1-\frac{v^2}{c^2}}$$

or

$$\alpha = \frac{1}{\sqrt{1-\frac{v^2}{c^2}}} \quad (26)$$

This is the required value of the Lorentz factor.

2.4 The Relativistic Transformation Equations of Spatial Coordinates Along Radius Vector

From the transformation Eq. (16), we have:

$$r' = \alpha(r - vt)$$

Putting the value of α from Eq. (26), we have:

$$r' = \frac{r-vt}{\sqrt{1-\frac{v^2}{c^2}}} \quad (27)$$

Putting the value of r' and r from Eqs. (10) and (15), we get:

$$\sqrt{x'^2 + y'^2} = \frac{\sqrt{x^2+y^2}-vt}{\sqrt{1-\frac{v^2}{c^2}}} \quad (28)$$

This is the Lorentz transformation equation that converts the space measurement noted in frame S into those in frame S′ when the relative motion between inertial frames is in the two-dimensional XY-plane.

From Eq. (21) we get:

$$r = \alpha(r' + vt')$$

Putting the value of α from Eq. (26), we have:

$$r = \frac{r'+vt'}{\sqrt{1-\frac{v^2}{c^2}}} \quad (29)$$

Putting the value of r' and r from Eqs. (10) and (15), we get:

$$\sqrt{x^2 + y^2} = \frac{\sqrt{x'^2+y'^2}+vt'}{\sqrt{1-\frac{v^2}{c^2}}} \quad (30)$$

This is the inverse Lorentz transformation, converting the space measurement noted in frame S′ into those in frame S when the relative motion between inertial frames is in the two-dimensional XY-plane.

2.5 The Relativistic Transformation Equations of Spatial Coordinates Along the Y-Axis

From Eq. (18):

$$y' = \alpha(y - vt\sin\phi)$$

Putting the value of α from Eq. (26), we have:

$$y' = \frac{y-vt\sin\phi}{\sqrt{1-\frac{v^2}{c^2}}} \quad (31)$$

Substituting the value of $\sin\phi$ from Eq. (6), we get:

$$y' = \frac{y-\frac{vty}{r}}{\sqrt{1-\frac{v^2}{c^2}}}$$

or

$$y' = \frac{y\left(1-\frac{vt}{r}\right)}{\sqrt{1-\frac{v^2}{c^2}}}$$

or

$$y' = \frac{y\left(1-\frac{vt}{\sqrt{x^2+y^2}}\right)}{\sqrt{1-\frac{v^2}{c^2}}} \quad (32)$$

Equation (32) converts the space measurement of the Y-axis noted in frame S into those in frame S′ when the relative motion between inertial frames is in the two-dimensional XY-plane.

From Eq. (22) we get:

$$y = \alpha(y' + vt'\sin\phi)$$

Putting the value of α from Eq. (26), we have:

$$y = \frac{y'+vt'\sin\phi}{\sqrt{1-\frac{v^2}{c^2}}} \quad (33)$$

Substituting the value of $\sin\phi$ from Eq. (11), we get:

$$y = \frac{y' + \frac{vt'y'}{r'}}{\sqrt{1-\frac{v^2}{c^2}}}$$

or

$$y = \frac{y'\left(1+\frac{vt'}{r'}\right)}{\sqrt{1-\frac{v^2}{c^2}}}$$

or

$$y = y' \frac{\left(1+\frac{vt'}{\sqrt{x'^2+y'^2}}\right)}{\sqrt{1-\frac{v^2}{c^2}}} \quad (34)$$

This is the inverse Lorentz transformation for the Y-axis, which converts the space measurement of the Y-axis noted in frame S′ into those in frame S when the relative motion between inertial frames is in the two-dimensional XY-plane.

2.6 The Relativistic Transformation Equations of Spatial Coordinates Along the X-Axis

From Eq. (20), we have:

$$x' = \alpha(x - vt\cos\phi)$$

Putting the value of α from Eq. (26), we have:

$$x' = \frac{x - vt\cos\phi}{\sqrt{1-\frac{v^2}{c^2}}} \quad (35)$$

Substituting the value of $\cos\phi$ from Eq. (8), we get:

$$x' = \frac{x - \frac{vtx}{r}}{\sqrt{1-\frac{v^2}{c^2}}}$$

or

$$x' = \frac{x\left(1-\frac{vt}{r}\right)}{\sqrt{1-\frac{v^2}{c^2}}} \quad (36)$$

or

$$x' = \frac{x\left(1-\frac{vt}{\sqrt{x^2+y^2}}\right)}{\sqrt{1-\frac{v^2}{c^2}}} \quad (37)$$

Equation (37) converts the space measurement of the X-axis noted in frame S into those in frame S′ when the relative motion between the inertial frames is in the two-dimensional XY-plane.

From Eq. (23), the inverse transformation is:

$$x = \alpha(x' + v\,t'\cos\phi)$$

Putting the value of α from Eq. (26), we have:

$$x = \frac{x' + v\,t'\cos\phi}{\sqrt{1-\frac{v^2}{c^2}}} \quad (38)$$

Substituting the value of $\cos\phi$ from Eq. (13), we get:

$$x = \frac{x' + \frac{vt'x'}{r'}}{\sqrt{1-\frac{v^2}{c^2}}}$$

or

$$x = \frac{x'\left(1+\frac{vt'}{r'}\right)}{\sqrt{1-\frac{v^2}{c^2}}}$$

or

$$x = x' \frac{\left(1+\frac{vt'}{\sqrt{x'^2+y'^2}}\right)}{\sqrt{1-\frac{v^2}{c^2}}} \quad (39)$$

This is the inverse Lorentz transformation for the X-axis, which converts the space measurement of the X-axis noted in frame S′ into those in frame S when the relative motion between the inertial frames is in the two-dimensional XY-plane.

The radius vector in frame S can be written from Eq. (15) as follows:

$$r' = \sqrt{x'^2 + y'^2}$$

Substituting the values of x and y from Eqs. (32) and (37), we get:

$$r' = \sqrt{x^2\left[\frac{\left(1-\frac{vt}{\sqrt{x^2+y^2}}\right)}{\sqrt{1-\frac{v^2}{c^2}}}\right]^2 + y^2\left[\frac{\left(1-\frac{vt}{\sqrt{x^2+y^2}}\right)}{\sqrt{1-\frac{v^2}{c^2}}}\right]^2}$$

or

$$r' = \frac{\left(1-\frac{vt}{\sqrt{x^2+y^2}}\right)}{\sqrt{1-\frac{v^2}{c^2}}}\sqrt{x^2+y}$$

or

$$r' = \frac{r\left(1-\frac{vt}{r}\right)}{\sqrt{1-\frac{v^2}{c^2}}}$$

or

$$r' = \frac{r - vt}{\sqrt{1-\frac{v^2}{c^2}}} \quad (40)$$

This process of calculation clearly reveals that the derived transformation equations along the X- and Y-axes generate exactly the same transformation equations for the radius vector as given in Eq. (27). Hence, all proposed transformation equations are entirely accurate.

2.7 The Transformation Equations for Time Coordinate in Two-Dimensional Space

From Eq. (40), we have:

$$r' = \frac{r - vt}{\sqrt{1-\frac{v^2}{c^2}}}$$

Putting the value of t from Eq. (4), we get:

$$r' = \frac{r - \frac{vr}{c}}{\sqrt{1-\frac{v^2}{c^2}}}$$

Since $r = \sqrt{x^2 + y^2}$ from Eq. (10), then the above equation reduces to:

$$r' = \frac{r - \frac{v\sqrt{x^2+y^2}}{c}}{\sqrt{1-\frac{v^2}{c^2}}}$$

Putting the value of r and r' from Eqs. (4) and (5), we get:

$$ct' = \frac{ct - \frac{v\sqrt{x^2+y^2}}{c}}{\sqrt{1-\frac{v^2}{c^2}}}$$

or

$$t' = \frac{t - \frac{v\sqrt{x^2+y^2}}{c^2}}{\sqrt{1-\frac{v^2}{c^2}}} \quad (41)$$

This is the required expression of time coordinates transformation from frame S to S' when there is the relative motion along the X- and Y-axis simultaneously.

Case I: If the motion between the inertial frames is one-dimensional along the Y-axis, then $x = x' = 0$, and Eq. (41) reduces to:

$$t' = \frac{t - \frac{v\sqrt{0^2+y^2}}{c^2}}{\sqrt{1-\frac{v^2}{c^2}}}$$

or

$$t' = \frac{t - \frac{vy}{c^2}}{\sqrt{1-\frac{v^2}{c^2}}} \quad (42)$$

This is the ordinary transformation equation of time for the one-dimensional relative motion along the Y-axis.

Case II: If motion between inertial frames is one-dimensional along the X-axis, then $y = y' = 0$, and Eq. (41) reduces to:

$$t' = \frac{t - \frac{v\sqrt{x^2+0^2}}{c^2}}{\sqrt{1-\frac{v^2}{c^2}}}$$

or

$$t' = \frac{t - \frac{vx}{c^2}}{\sqrt{1-\frac{v^2}{c^2}}} \quad (43)$$

This is the ordinary transformation equation of time for the one-dimensional relative motion along the X-axis.

Rewriting Eq. (29) for the inverse Lorentz transformation equation of time:

$$\mathrm{r} = \frac{\mathrm{r}' + v\mathrm{t}'}{\sqrt{1-\frac{v^2}{c^2}}}$$

Putting the value of t' from Eq. (5), we get:

$$\mathrm{r} = \frac{\mathrm{r}' + \frac{v\mathrm{r}'}{c}}{\sqrt{1-\frac{v^2}{c^2}}}$$

Since $\mathrm{r}' = \sqrt{x'^2 + y'^2}$ from Eq. (15), then the above equation reduces to:

$$\mathrm{r} = \frac{r' + \frac{v\sqrt{x'^2+y'^2}}{c}}{\sqrt{1-\frac{v^2}{c^2}}}$$

Putting the value of r and r' from Eqs. (4) and (5), we get:

$$\mathrm{ct} = \frac{ct' + \frac{v\sqrt{x'^2+y'^2}}{c}}{\sqrt{1-\frac{v^2}{c^2}}}$$

or

$$t = \frac{t' + \frac{v\sqrt{x'^2+y'^2}}{c^2}}{\sqrt{1-\frac{v^2}{c^2}}} \quad (44)$$

This is the required expression of time coordinates transformation from frame S' to S, called the inverse Lorentz transformation, when

there is the relative motion along the X- and Y-axes simultaneously. All time transformation scenarios between two inertial frames moving relative to each other in two-dimensional space are outlined in Eqs. (41), (42), (43), and (44). In two-dimensional motion, space coordinate transformation equations along the X-axis are displayed in Eqs. (37) and (39), while transformation equations along the Y-axis are displayed in Eqs. (32) and (34). These transformation equations between inertial frames are thoroughly discussed in Table 1.

TABLE 1. Space coordinates transformation equations.

S.N.	Direction of motion	Value of Y and X coordinates	Space Coordinates	
			Along the Y-axis	Along the X-axis
1	Along both Y and X-directions	From Eqs. (6) and (8), $y = r\sin\phi$ $x = r\cos\phi$	From Eq. (17), $y' = \frac{r\sin\phi - vt\sin\phi}{\sqrt{1-\frac{v^2}{c^2}}}$	From Eq. (19), $x' = \frac{r\cos\phi - vt\cos\phi}{\sqrt{1-\frac{v^2}{c^2}}}$
2	Along the Y-axis only $\phi = \frac{\pi}{2}$	$y = r\sin\frac{\pi}{2} = r$ $x = r\cos\frac{\pi}{2} = 0$	$y' = \frac{r\sin\frac{\pi}{2} - vt\sin\frac{\pi}{2}}{\sqrt{1-\frac{v^2}{c^2}}}$ $y' = \frac{\sqrt{x^2+y^2} - vt}{\sqrt{1-\frac{v^2}{c^2}}}$ $y' = \frac{\sqrt{0^2+y^2} - vt}{\sqrt{1-\frac{v^2}{c^2}}}$ $y' = \frac{y - vt}{\sqrt{1-\frac{v^2}{c^2}}}$	$x' = \frac{r\cos 0 - vt\cos 0}{\sqrt{1-\frac{v^2}{c^2}}}$ $x' = 0$
3	Along the X-axis only $\phi = 0$	$y = r\sin 0 = 0$ $x = r\cos 0 = r$	$y' = \frac{\sin 0 - vt\sin 0}{\sqrt{1-\frac{v^2}{c^2}}}$ $y' = 0$	$x' = \frac{r\cos 0 - vt\cos 0}{\sqrt{1-\frac{v^2}{c^2}}}$ $x' = \frac{\sqrt{x^2+y^2} - vt}{\sqrt{1-\frac{v^2}{c^2}}}$ $x' = \frac{\sqrt{x^2+0^2} - vt}{\sqrt{1-\frac{v^2}{c^2}}}$ $x' = \frac{x - vt}{\sqrt{1-\frac{v^2}{c^2}}}$

From the first row of Table 1, it is obviously seen that space-time coordinates take place along both the X- and Y-axes when relative motion between inertial frames occurs in the two-dimensional XY-plane. In contrast, the second row reveals that space coordinate transformation occurs only along the Y-axis when the relative motion between frames is one-dimensional along the Y-axis. Similarly, the third row demonstrates that there is no space coordinate transformation along the Y-axis when the relative motion between two frames is restricted to the X-axis only.

3. Three-dimensional Transformation Equations

3.1 Relativistic Transformation Equations of Spatial Coordinates Along the Radius Vector

Consider an inertial frame S and another inertial frame S' which moves at a constant relative velocity v with respect to S in three dimensions of space, as shown in Fig. 2.

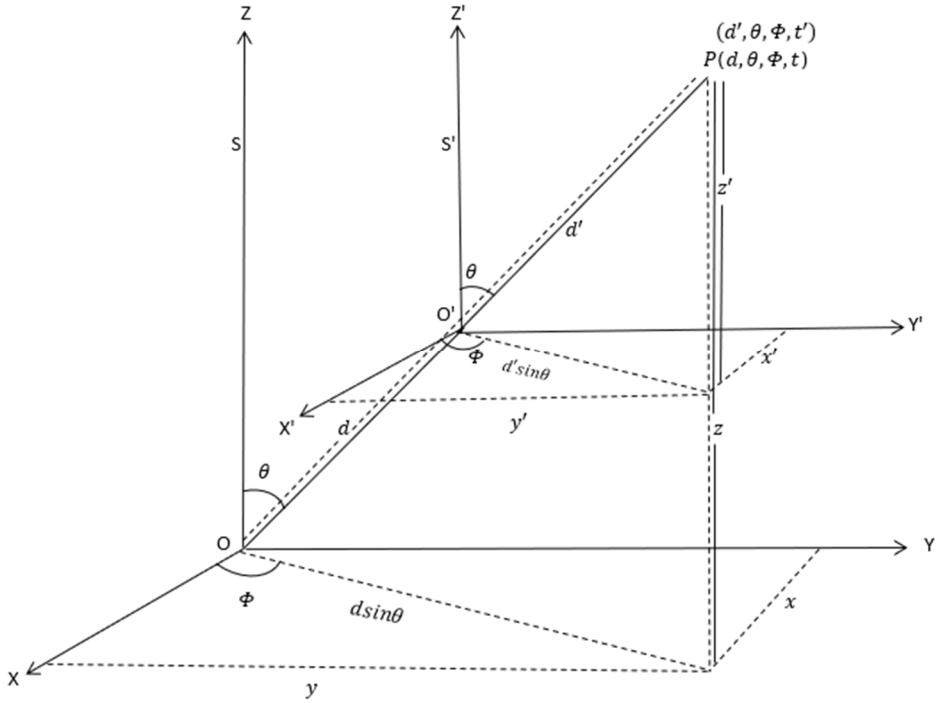

FIG. 2. Motion between inertial frames in three dimensions of space.

Let an event occur at point P, whose space and time coordinates are measured in each inertial frame. An observer attached to S records the location and time of occurrence of this event, ascribing a location coordinate d (radius vector in frame S) and time t. An observer attached to S' specifies the same event by location coordinates d' (radius vector in frame S') and time t'. Now, the transformation equations that relate one observer's space-time coordinates of an event with the other observer's coordinates of the same event must be linear, so the most general form they can take is

$$d' = ad + bt \tag{45}$$

or

$$t' = fd + gt \tag{46}$$

Here, the coefficients a, b, f, and g are constants that we must determine to obtain the exact transformation equations. Suppose the event occurs at the origin O' of S' frame at time t'. Obviously, at frame S', this event occurs at $d' = 0$. Now, from Fig. 2:

$$O'P = OP + OO'$$

or $d' = d - vt$

If an event occurs at origin O', then $d' = 0$. Hence, the above equation reduces to:

$$0 = d - vt$$

or

$$d = vt$$

It means that the same event, as seen from S, occurs at a distance $d = vt$ at time t. Now, putting this value in Eq. (45), we get:

$$0 = avt + bt$$

or

$$b = -av$$

Putting the value of b in Eq. (45), we get:

$$d' = ad - avt$$

or

$$d' = a(d - vt)$$

Therefore, Eqs. (45) and (46) are reduced to:

$$d' = a(d - vt) \tag{47}$$

or

$$t' = fd + gt \tag{48}$$

There remains the task of determining values of the coefficients a, f, and g. To do this, let us assume that at the time $t = 0$ a light pulse leaves the origin of S, which coincides with the origin of S' at that moment. The light pulse propagates with speed c in the direction of the moving frame and reaches point P at times t and t',

measured from S and S', as shown in Fig. 2. For an observer at O, the distance to point P is:

$$OP = ct$$

or

$$d = ct$$

Squaring both sides, we get:

$$d^2 = c^2t^2$$

or

$$d^2 - c^2t^2 = 0 \quad (49)$$

Similarly, for an observer at O', the distance to point P is:

$$O'P = ct'$$

or

$$d' = ct'$$

Squaring both sides, we get:

$$d'^2 = c^2t'^2$$

or

$$d'^2 - c^2t'^2 = 0 \quad (50)$$

Now, substituting Eqs. (47) and (48) into Eq. (50), we get:

$$a^2(d - vt)^2 - c^2(fd + gt)^2 = 0$$

or $a^2d^2 - 2a^2vtd + a^2v^2t^2 - c^2f^2d^2 - 2c^2fgtd - c^2g^2t^2 = 0$

or $d^2(a^2 - c^2f^2) - 2td(a^2v + c^2fg) + t^2(a^2v^2 - c^2g^2) = 0$

In order for this equation to agree with Eq. (49), we must have:

$$a^2 - c^2f^2 = 1 \quad (51)$$

$$a^2v + c^2fg = 0 \quad (52)$$

$$a^2v^2 - c^2g^2 = -c^2 \quad (53)$$

From Eq. (53):

$$c^2g^2 = a^2v^2 + c^2$$

or

$$g^2 = \frac{a^2v^2 + c^2}{c^2}$$

or

$$g = \sqrt{\frac{a^2v^2 + c^2}{c^2}} \quad (54)$$

From Eq. (51):

$$c^2f^2 = a^2 - 1$$

or

$$f^2 = \frac{a^2 - 1}{c^2}$$

or

$$f = \sqrt{\frac{a^2 - 1}{c^2}} \quad (55)$$

Using Eqs. (54) and (55) in Eq. (52) we get:

$$a^2v + c^2\sqrt{\frac{a^2 - 1}{c^2}}\sqrt{\frac{a^2v^2 + c^2}{c^2}} = 0$$

or, $a^2v + \sqrt{a^2 - 1}\sqrt{a^2v^2 + c^2} = 0$

or, $a^2v = -\sqrt{a^2 - 1}\sqrt{a^2v^2 + c^2}$

Squaring both sides of the above equation, we get:

$$a^4v^2 = (a^2 - 1)(a^2v^2 + c^2)$$

or, $a^4v^2 = a^4v^2 + a^2c^2 - a^2v^2 - c^2$

or, $a^2c^2 - a^2v^2 = c^2$

or, $a^2 = \frac{c^2}{c^2 - v^2}$

or, $a = \frac{1}{\sqrt{1 - \frac{v^2}{c^2}}}$ (56)

Putting this value in Eq. (51), we get:

$$\frac{1}{\left(\sqrt{1 - \frac{v^2}{c^2}}\right)^2} - c^2f^2 = 1$$

or, $\frac{c^2}{c^2 - v^2} - 1 = c^2f^2$

or, $\frac{v^2}{c^2 - v^2} = c^2f^2$

or, $f^2 = \frac{v^2}{c^2(c^2 - v^2)}$

or, $f^2 = \frac{v^2}{c^4\left(1 - \frac{v^2}{c^2}\right)}$

or, $f = -\frac{v}{c^2\sqrt{1 - \frac{v^2}{c^2}}}$ (57)

Using Eqs. (56) and (57) in Eq. (52) we get:

$$\frac{v}{\left(\sqrt{1 - \frac{v^2}{c^2}}\right)^2} - \frac{gvc^2}{c^2\sqrt{1 - \frac{v^2}{c^2}}} = 0$$

or, $\frac{1}{1 - \frac{v^2}{c^2}} = \frac{g}{\sqrt{1 - \frac{v^2}{c^2}}}$

or, $g = \frac{1}{\sqrt{1 - \frac{v^2}{c^2}}}$ (58)

From Eqs. (47) and (56) we get:

$$d' = \frac{d-vt}{\sqrt{1-\frac{v^2}{c^2}}} \quad (59)$$

Also, putting the values of f and g in Eq. (48), we get:

$$t' = fd + gt$$

or

$$t' = -\frac{vd}{c^2\sqrt{1-\frac{v^2}{c^2}}} + \frac{t}{\sqrt{1-\frac{v^2}{c^2}}}$$

or

$$t' = \frac{t-\frac{vd}{c^2}}{\sqrt{1-\frac{v^2}{c^2}}} \quad (60)$$

Equations (59) and (60) are the Lorentz transformation equations in terms of radius vectors d and d'.

Putting these values ($d = \sqrt{x^2+y^2+z^2}$ and $d' = \sqrt{x'^2+y'^2+z'^2}$) in Eqs. (59) and (60), we get:

$$\sqrt{x'^2+y'^2+z'^2} = \frac{\sqrt{x^2+y^2+z^2}-vt}{\sqrt{1-\frac{v^2}{c^2}}} \quad (61)$$

$$t' = \frac{t-\frac{v\sqrt{x^2+y^2+z^2}}{c^2}}{\sqrt{1-\frac{v^2}{c^2}}} \quad (62)$$

The inverse transformation equations can be obtained by changing the sign of relative velocity in the equations and interchanging the coordinates. Thus:

$$\sqrt{x^2+y^2+z^2} = \frac{\sqrt{x'^2+y'^2+z'^2}+vt'}{\sqrt{1-\frac{v^2}{c^2}}} \quad (63)$$

$$t = \frac{t'+\frac{v\sqrt{x'^2+y'^2+z'^2}}{c^2}}{\sqrt{1-\frac{v^2}{c^2}}} \quad (64)$$

Equations (63) and (64) convert the space-time measurements made in frame S' into those in frame S. When we substitute $x' = x = 0$ and $y' = y = 0$ in the above equations to achieve the one-dimensional inverse Lorentz transformations, we get:

$$\sqrt{x^2+0^2+0^2} = \frac{\sqrt{x'^2+0^2+o^2}+vt'}{\sqrt{1-\frac{v^2}{c^2}}}$$

or

$$x = \frac{x'+vt'}{\sqrt{1-\frac{v^2}{c^2}}}$$

and

$$t = \frac{t'+\frac{v\sqrt{x'^2+0^2+0^2}}{c^2}}{\sqrt{1-\frac{v^2}{c^2}}} = \frac{t'+\frac{vx'}{c^2}}{\sqrt{1-\frac{v^2}{c^2}}}$$

The expression obtained in the above equations is in complete agreement with the inverse Lorentz transformation equations when the relative motion between the inertial frames is reduced to a one-dimensional system. Hence, derived transformations, Eqs. (61), (62), (63), and (64), are completely true.

3.2 The Transformation between Cartesian and Polar Coordinates

In Fig. 1, let point P have Cartesian coordinates (x, y, z) in frame S, and (x', y', z') in frame S'. Then the spherical polar coordinates of point P are specified $(d, \theta, \Phi,)$ and $(d', \theta, \Phi,)$ in frame S and S', respectively, where $OP = d$ and $O'P = d'$ are radius vectors of point P measured from frames S and S', θ is the colatitude i.e., angle between OP and Z-axis, and Φ is the longitudinal or azimuthal angle i.e. the angle included between YZ plane the plane OPZ, as shown in Fig. 2. The transformation between Cartesian coordinates and polar coordinates in frame S are given by:

$$x = dsin\theta cos\Phi \quad (65)$$

$$y = dsin\theta sin\Phi \quad (66)$$

$$z = dcos\theta \quad (67)$$

Squaring and adding Eqs. (65), (66), and (67), we get:

$$x^2+y^2+z^2 = d^2sin^2\theta cos^2\Phi + d^2sin^2\theta sin^2\Phi + d^2cos^2\theta$$

or

$$x^2+y^2+z^2 = d^2sin^2\theta(cos^2\Phi + sin^2\Phi) + d^2cos^2\theta$$

or

$$x^2+y^2+z^2 = d^2sin^2\theta + d^2cos^2\theta$$

or

$$x^2+y^2+z^2 = d^2$$

or

$$d = \sqrt{x^2 + y^2 + z^2} \quad (68)$$

This value of d denotes the radius vector that joins the origin O and point P in frame S. Similarly, the transformation between Cartesian coordinates and polar coordinates in frame S' is given by:

$$x' = d' sin\theta cos\Phi \quad (69)$$

$$y' = d' sin\theta sin\Phi \quad (70)$$

$$z' = d' cos\theta \quad (71)$$

Squaring and adding Eqs. (69), (70), and (71), we get:

$$x'^2 + y'^2 + z'^2 = d'^2 sin^2\theta cos^2\Phi + d'^2 sin^2\theta sin^2\Phi + d'^2 cos^2\theta$$

or

$$x'^2 + y'^2 + z'^2 = d'^2 sin^2\theta(cos^2\Phi + sin^2\Phi) + d'^2 cos^2\theta$$

or

$$x'^2 + y'^2 + z'^2 = d'^2 sin^2\theta + d'^2 cos^2\theta$$

or

$$x'^2 + y'^2 + z'^2 = d'^2$$

or

$$d' = \sqrt{x'^2 + y'^2 + z'^2} \quad (72)$$

This value of d' denotes the radius vector that joins the origin O' and point P in frame S'.

3.3 Transformation Equations Along the X-, Y-, and Z-Directions

In the previous section, we derived transformation equations along the radius vectors d and d', as delineated in Eqs. (59) and (60). In this section, we further extend these equations to discover the new transformation equations along each axis.

Rewriting Eq. (59), we get:

$$d' = \frac{d - vt}{\sqrt{1 - \frac{v^2}{c^2}}}$$

Multiplying both sides by $sin\theta cos\Phi$

$$d' sin\theta cos\Phi = \frac{d sin\theta cos\Phi - vt sin\theta cos\Phi}{\sqrt{1 - \frac{v^2}{c^2}}}$$

Using Eqs. (65) and (69), we get:

$$x' = \frac{x - vt sin\theta cos\Phi}{\sqrt{1 - \frac{v^2}{c^2}}}$$

Putting the value of $sin\theta cos\Phi$ from Eq. (65), we get:

$$x' = \frac{x - \frac{vtx}{d}}{\sqrt{1 - \frac{v^2}{c^2}}}$$

Substituting the value of d from Eq. (68), we get:

$$x' = \frac{x - \frac{vtx}{\sqrt{x^2 + y^2 + z^2}}}{\sqrt{1 - \frac{v^2}{c^2}}} \quad (73)$$

The inverse Lorentz transformation equation along the X-axis can be obtained by interchanging the coordinates and replacing v with $-v$ in the above equation.

$$x = \frac{x' + \frac{vx't'}{\sqrt{x'^2 + y'^2 + z'^2}}}{\sqrt{1 - \frac{v^2}{c^2}}} \quad (74)$$

Again, rewriting Eq. (17), we get:

$$d' = \frac{d - vt}{\sqrt{1 - \frac{v^2}{c^2}}}$$

Multiplying both sides by $sin\theta\ sin\Phi$

$$d' sin\theta sin\Phi = \frac{d sin\theta sin\Phi - vt sin\theta sin\Phi}{\sqrt{1 - \frac{v^2}{c^2}}}$$

Using Eqs. (66) and (70), we get:

$$y' = \frac{y - vt sin\theta sin\Phi}{\sqrt{1 - \frac{v^2}{c^2}}}$$

Putting the value of $sin\theta\ sin\Phi$ from Eq. (66), we get:

$$y' = \frac{y - \frac{vty}{d}}{\sqrt{1 - \frac{v^2}{c^2}}}$$

Substituting the value of d from Eq. (68), we get:

$$y' = \frac{y - \frac{vty}{\sqrt{x^2 + y^2 + z^2}}}{\sqrt{1 - \frac{v^2}{c^2}}} \quad (75)$$

The inverse Lorentz transformation equation along the Y-axis can be obtained by interchanging the coordinates and replacing v with $-v$ in the above equation.

$$y = \frac{y' + \frac{vy't'}{\sqrt{x'^2+y'^2+z'^2}}}{\sqrt{1-\frac{v^2}{c^2}}} \quad (76)$$

Again, rewriting Eq. (59), we get:

$$d' = \frac{d-vt}{\sqrt{1-\frac{v^2}{c^2}}}$$

Multiplying both sides by $cos\theta$

$$d'cos\theta = \frac{dcos\theta - vtcos\theta}{\sqrt{1-\frac{v^2}{c^2}}}$$

Using Eqs. (67) and (71), we get:

$$z' = \frac{z - vtcos\theta}{\sqrt{1-\frac{v^2}{c^2}}}$$

Putting the value of $cos\theta$ from Eq. (67), we get:

$$z' = \frac{z - \frac{vtz}{d}}{\sqrt{1-\frac{v^2}{c^2}}}$$

Substituting the value of d from Eq. (68), we get:

$$z' = \frac{z - \frac{vtz}{\sqrt{x^2+y^2+z^2}}}{\sqrt{1-\frac{v^2}{c^2}}} \quad (77)$$

The inverse Lorentz transformation equation along the Z-axis can be obtained by interchanging the coordinates and replacing v with $-v$ in the above equation.

$$z = \frac{z' + \frac{vz't'}{\sqrt{x'^2+y'^2+z'^2}}}{\sqrt{1-\frac{v^2}{c^2}}} \quad (78)$$

Equations (73), (75), and (77) are the required Lorentz transformation equations along the X-, Y-, and Z-directions, while Eqs. (74), (76), and (78) are the required inverse Lorentz transformation equations along the X-, Y-, and Z-directions when the relative motion between inertial frames is in three-dimensional space.

3.4 Invariance of the Space-Time Interval Equation

In this section, we verify the invariance of the following space-time interval equation with the help of the modified Lorentz transformation equations obtained in the previous section.

$$x^2 + y^2 + z^2 - c^2t^2 = x'^2 + y'^2 + z'^2 - c^2t'^2 \quad (79)$$

where (x, y, z, t) and (x', y', z', t') are the coordinates of the same event as observed by two observers in frames S and S', while S' is moving with velocity v relative to S.

Let us consider the expression

$$x'^2 + y'^2 + z'^2 - c^2t'^2$$

Putting the values of $x', y', z', and\ t'$ from Eqs. (73), (75), (77), and (62), respectively, we get:

$$= \left(\frac{x - \frac{vtx}{\sqrt{x^2+y^2+z^2}}}{\sqrt{1-\frac{v^2}{c^2}}}\right)^2 + \left(\frac{y - \frac{vty}{\sqrt{x^2+y^2+z^2}}}{\sqrt{1-\frac{v^2}{c^2}}}\right)^2 + \left(\frac{y - \frac{vty}{\sqrt{x^2+y^2+z^2}}}{\sqrt{1-\frac{v^2}{c^2}}}\right)^2 - c^2\left(\frac{t - \frac{v\sqrt{x^2+y^2+z^2}}{c^2}}{\sqrt{1-\frac{v^2}{c^2}}}\right)^2$$

$$= x^2\left(\frac{1 - \frac{vt}{\sqrt{x^2+y^2+z^2}}}{\sqrt{1-\frac{v^2}{c^2}}}\right)^2 + y^2\left(\frac{1 - \frac{vt}{\sqrt{x^2+y^2+z^2}}}{\sqrt{1-\frac{v^2}{c^2}}}\right)^2 + z^2\left(\frac{1 - \frac{vt}{\sqrt{x^2+y^2+z^2}}}{\sqrt{1-\frac{v^2}{c^2}}}\right)^2 - c^2\left(\frac{t - \frac{v\sqrt{x^2+y^2+z^2}}{c^2}}{\sqrt{1-\frac{v^2}{c^2}}}\right)^2$$

$$= \frac{x^2\left(1 - \frac{vt}{\sqrt{x^2+y^2+z^2}}\right)^2 + y^2\left(1 - \frac{vt}{\sqrt{x^2+y^2+z^2}}\right)^2 + z^2\left(1 - \frac{vt}{\sqrt{x^2+y^2+z^2}}\right)^2 - c^2\left(t - \frac{v\sqrt{x^2+y^2+z^2}}{c^2}\right)^2}{1-\frac{v^2}{c^2}}$$

$$= \frac{c^2}{c^2-v^2}\left[(x^2+y^2+z^2)\left(1 - \frac{vt}{\sqrt{x^2+y^2+z^2}}\right)^2 - c^2\left(t - \frac{v\sqrt{x^2+y^2+z^2}}{c^2}\right)^2\right]$$

$$= \frac{c^2}{c^2-v^2}\left[(x^2+y^2+z^2)\left(1 - \frac{vt}{\sqrt{x^2+y^2+z^2}}\right)^2 - c^2\left(t - \frac{v\sqrt{x^2+y^2+z^2}}{c^2}\right)^2\right]$$

$$= \frac{c^2}{c^2-v^2}\left[(x^2+y^2+z^2)\left(1 - \frac{2vt}{\sqrt{x^2+y^2+z^2}} + \frac{v^2t^2}{x^2+y^2+z^2}\right) - c^2\left(t^2 - \frac{2tv\sqrt{x^2+y^2+z^2}}{c^2} + \frac{v^2(x^2+y^2+z^2)}{c^4}\right)\right]$$

$$= \frac{c^2}{c^2-v^2}\left[x^2+y^2+z^2-2vt\sqrt{x^2+y^2+z^2}+ v^2t^2-c^2t^2+2tv\sqrt{x^2+y^2+z^2}- \frac{v^2(x^2+y^2+z^2)}{c^2}\right]$$

$$= \frac{c^2}{c^2-v^2}\left[x^2+y^2+z^2+v^2t^2-c^2t^2- \frac{v^2(x^2+y^2+z^2)}{c^2}\right]$$

$$= \frac{1}{c^2-v^2}[c^2(x^2+y^2+z^2)+c^2v^2t^2-c^4t^2- v^2(x^2+y^2+z^2)]$$

$$= \frac{1}{c^2-v^2}[(x^2+y^2+z^2)(c^2-v^2)- c^2t^2(c^2-v^2)]$$

$$= \frac{1}{c^2-v^2}(x^2+y^2+z^2-c^2t^2)(c^2-v^2)$$

$$= x^2+y^2+z^2-c^2t^2 \quad (80)$$

Thus, we proved that $x^2+y^2+z^2-c^2t^2 = x'^2+y'^2+z'^2-c^2t'^2$. Hence, the space-time interval equation is invariant under the modified Lorentz transformation equations.

3.5 Relativity of Simultaneity

One of the important consequences of the Lorentz transformation is that simultaneity is relative. Consider two events occurring at the same time at two different position coordinates, (x_1, y_1, z_1) and (x_2, y_2, z_2), in the inertial frame S. Let t_1' and t_2' be the times at which the two events are observed in the frame S', which is moving with velocity v.

Using the Lorentz transformation Eq. (62), we get:

$$t_1' = \frac{t-\frac{v\sqrt{{x_1}^2+{y_1}^2+{z_1}^2}}{c^2}}{\sqrt{1-\frac{v^2}{c^2}}}$$

$$t_2' = \frac{t-\frac{v\sqrt{{x_2}^2+{y_2}^2+{z_2}^2}}{c^2}}{\sqrt{1-\frac{v^2}{c^2}}}$$

The apparent time interval, i.e., the time interval between two events as observed by the observer in S', is:

$$t_2'-t_1' = \frac{t-\frac{v\sqrt{{x_2}^2+{y_2}^2+{z_2}^2}}{c^2}}{\sqrt{1-\frac{v^2}{c^2}}} - \frac{t-\frac{v\sqrt{{x_1}^2+{y_1}^2+{z_1}^2}}{c^2}}{\sqrt{1-\frac{v^2}{c^2}}}$$

$$t_2'-t_1' = \frac{v}{c^2\sqrt{1-\frac{v^2}{c^2}}}\left(\sqrt{{x_2}^2+{y_2}^2+{z_2}^2}- \sqrt{{x_1}^2+{y_1}^2+{z_1}^2}\right) \quad (81)$$

This indicates that two events which are simultaneous in the reference frame S are not simultaneous in another frame of reference S' moving relative to the first.

3.6 Time Dilation

Consider two frames of reference, S and S', where the S' frame of reference is moving with velocity v in three-dimensional space, as shown in Fig. 3.

Assume two clocks are initially synchronized at the origin of two frames of reference. Then their origins just cross each other. If two events occur at any point $d' = \sqrt{x'^2+y'^2+z'^2}$ in frame S', at times t_1' and t_2', as noted by an observer in S' frame, and at times t_1 and t_2, as noted by an observer in frame S, we clearly have time interval between two events in both frames. The time interval as measured by an observer in S' frame of reference for two successive events at point d' is given by $t_0 = t_2'-t_1'$. This time interval is known as the proper time interval. For the relativistic time, consider the inverse Lorentz transformation of time from Eq. (64):

$$t_1 = \frac{t_1'+\frac{v\sqrt{x'^2+y'^2+z'^2}}{c^2}}{\sqrt{1-\frac{v^2}{c^2}}} \text{ and } t_2 = \frac{t_2'+\frac{v\sqrt{x'^2+y'^2+z'^2}}{c^2}}{\sqrt{1-\frac{v^2}{c^2}}}$$

$$t_2-t_1 = \frac{t_2'+\frac{v\sqrt{x'^2+y'^2+z'^2}}{c^2}}{\sqrt{1-\frac{v^2}{c^2}}} - \frac{t_1'+\frac{v\sqrt{x'^2+y'^2+z'^2}}{c^2}}{\sqrt{1-\frac{v^2}{c^2}}}$$

$$t_2-t_1 = \frac{t_2'-t_1'}{\sqrt{1-\frac{v^2}{c^2}}}$$

$$t = \frac{t_0}{\sqrt{1-\frac{v^2}{c^2}}}$$

where $t = t_2-t_1$is the time interval between the events as measured by an observer in inertial frame S, which is moving relative to the clock. This is called the improper or relativistic time.

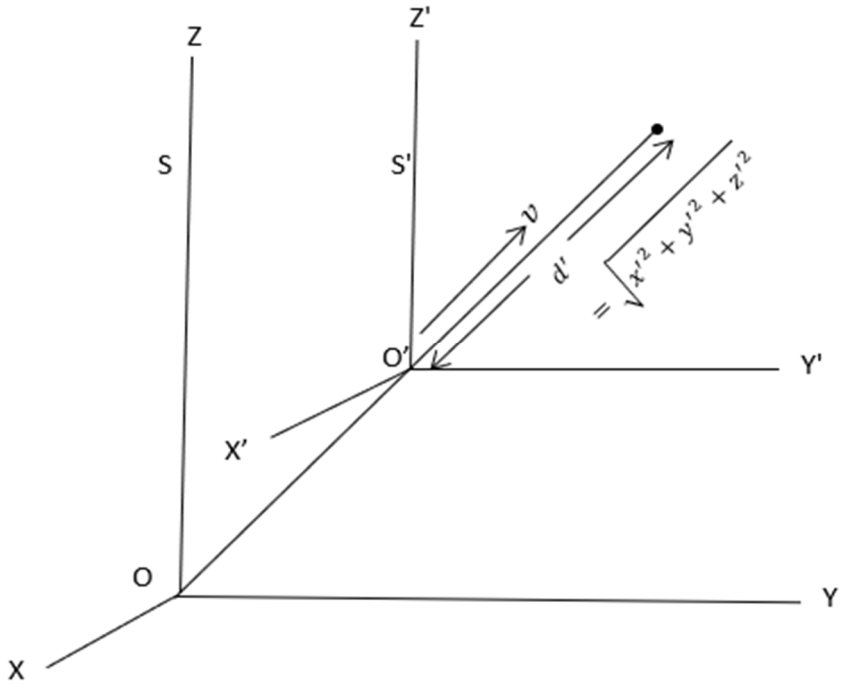

FIG. 3. Frame S' moves with velocity v relative to frame S to show time dilation.

4. Conclusions

In this study, we obtained the extended version of the Lorentz transformation equations in two- and three-dimensional space and further demonstrated the advantage of using these extended transformations to investigate the phenomena of time dilation and the invariance of the space-time interval. The modified transformation equations involving all X, Y, and Z coordinates in three-dimensional space can be written from Eqs. (61) and (62) as follows:

$$\sqrt{x'^2 + y'^2 + z'^2} = \frac{\sqrt{x^2+y^2+z^2} - vt}{\sqrt{1-\frac{v^2}{c^2}}},$$

$$t' = \frac{t - \frac{v\sqrt{x^2+y^2+z^2}}{c^2}}{\sqrt{1-\frac{v^2}{c^2}}}$$

The transformation equations developed for two- and three-dimensional motion between inertial frames are better than those of a one-dimensional system, and our results relating to the mathematical applications of the proposed equations are better than those of the existing transformation equations. Furthermore, our modified transformation formulas can be used to analyze the relativity of simultaneity in a more efficient and accurate way, as discussed in Section 3.5. Finally, the future scope of this work includes presenting a mathematical interpretation of four-vectors, exploring the transformation of momentum, and providing an explanation of Minkowski space using the two- and three-dimensional Lorentz transformation equations.

References

[1] Lorentz, H.A., Proc. R. Netherlands Acad. Arts Sci., 6 (1904) 809.

[2] Poincare, H., Proc. Academic Sci., 140 (1905) 1504.

[3] Einstein, A., Ann. Phys., 17 (1905) 891.

[4] Einstein, A., Am. J. Phys., 45 (1977) 512.

[5] Goldstein, H., Poole, C., and Safko, J., "Classical Mechanics", 3rd Ed., (Addison-Wesley, New York, 2001).

[6] Marion, J.B. and Thornton, S.T., "Classical Dynamics of Particle and System", 5th Ed., (Brooks/ Cole-Thomson Learning, Belmont, 2003).

[7] Feynman, R., Leighton, R.B., and Sands, M., "The Feynman Lectures on Physics", (Basic books, New York, 2011).

[8] Mansouri, R. and Sexl, R.U., Gen. Relativ. Gravit., 8 (1877) 497.

[9] Selleri, F., Found. Phys., 26 (1996) 641.

[10] Selleri, F., Found. Phys. Lett., 10 (1997) 73.

[11] Lee, A.R. and Kalotas, T.M., Am. J. Phys., 43 (1975) 434.

[12] Levy, J.M., Am. J. Phys., 75 (2007) 615.

[13] Nawrot, W., Phys. Essays, 27 (2014) 598.

[14] Shanahan, D., Found. Phys., 44 (2014) 349.

[15] Pagano, A. and Pagano, E.V., Eur. Phys. J. H, 44 (2019) 321.

[16] Szostek, K. and Szostek R., Jordan J. Phys., 15 (2022) 457.

[17] Marcin, K.G., Results in Physics, 24 (2021) 104121.

[18] Fedosin, S.G., Jordan J. Phys., 14 (2021) 379.

[19] Khadka, C.B., SPbPU J. Phys. Math., 17 (2024) 160.

[20] Khadka, C.B., BIBECHANA, 21 (2024) 103.

[21] Khadka, C.B., Mod. Phys. Lett. A, 40 (2025) 2550011.

[22] Khadka, C.B. and Karki B., The scientific World Journal, 2025 (2025) 7149569.

[23] Khadka, C.B., JNPS, 9 (2023) 129.

[24] Khadka, C.B., Jordan J. Phys., 18 (2025), accepted for publication.

[25] Khadka, C.B., BIBECHANA, 20 (2023) 257.

[26] Khadka, C.B., SPbPU J. Phys. Math., 16 (2023) 115.

Volume 18, Number 2, 2025. pp. 241-248

Jordan Journal of Physics

ARTICLE

Coupling Concept for Cross-Bar H-Type Cavities

Ali M. Almomani[a] and **Ulrich Ratzinger**[b]

[a] *Physics Department, Faculty of Science, Yarmouk University, 211-63 Irbid, Jordan.*
[b] *Institute for Applied Physics, J. W. Goethe University, Max-von-Laue Str. 1, 60438 Frankfurt am Main, Germany.*

Doi: **https://doi.org/10.47011/18.2.12**
Received on: 16/01/2024; *Accepted on: 06/03/2024*

Abstract: Crossbar H-type cavities (CH-cavities) have been investigated in the last two decades in different laboratories. They have promising features when compared with conventional drift tube linac (DTL) structures in terms of field gradient, shunt impedance, and costs. The KONUS beam dynamics concept allows for short drift tube sections without focusing lenses, resulting in a limited number of gaps per CH-cavity. With the available 3 MW klystron, the short cavity structure does not use the full amplifier power. Therefore, the RF- coupling of two single cavities seems to be an applicable solution to have more gaps per structure without harming the beam dynamics. This concept is realized by coupling three resonators and operating them as a single structure in the zero mode. In this paper, two identical CH tanks—each with 13 gaps—are coupled using a coupling cell containing a quadrupole triplet. The results are compared with theory. This type of cavity is called a coupled CH-cavity (CCH). The design frequency and field distribution result from an optimization of the three coupled resonators and are described in this paper. The fine-tuning is done by fixed and movable tuners along the structure.

Keywords: Drift tube linac, Coupled CH cavity, KONUS beam dynamics.

1. Introduction

H-type structures [1] are an alternative to the conventional drift tube linac (DTL) at energies up to around 100 MeV per nucleon (A MeV). “H-mode” and “TE-mode” are equivalent designations for modes with an H-field component along the direction of wave propagation. In these structures, a combination of slim, lens-free drift tubes with the Kombinierte Null Grad Struktur (Combined Zero-Degree Structure, KONUS) beam dynamics [2] allows for reaching a high effective field gradient and a high shunt impedance at modest structural costs [3, 4, 5].

In contrast to the Alvarez DTL (E010-mode), the electric field lines in H-type cavities without a drift tube structure are oriented transversally to the beam axis [1]. Fig. 1 shows the electric and magnetic fields of a pillbox cavity excited in H_{211} mode, based on CST-MW calculations [6]. All simulations in this paper were performed using this commercial software.

Since the axial electric field required for particle acceleration is zero in empty H-type cavities, one has to introduce a sequence of drift tubes along the cavity axis. These drift tubes are connected to the cavity tank wall by stems. This array generates the longitudinal electric field for beam acceleration. H-type structures have excellent properties in terms of RF efficiency, beam quality, operation reliability, and cost efficiency, making them attractive for low and medium β-acceleration. Two kinds of structures are realized and operated as H-modes: IH- and CH-DTLs (Fig. 2).

Corresponding Author: Ali M. Almomani **Email**: ali.almomani@yu.edu.jo

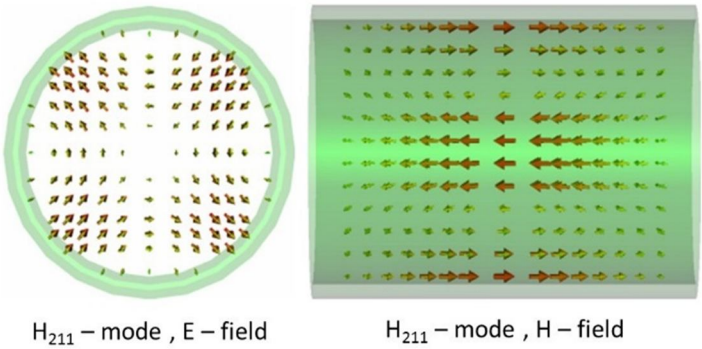

FIG. 1. Electric and magnetic field distributions for the H_{211}-mode in a pillbox cavity.

FIG. 2. Views into IH-DTL (left) and CH-DTL (right) cavities.

In the low beta range, the interdigital (IH) DTL can be used to accelerate particles up to a normalized velocity of $\beta = v/c \approx 0.25$ [1]. The operational frequency for such cavities was below 300 MHz so far. Beyond this point, the dimensions of the IH-DTL are too small, and the mechanical design becomes very difficult to realize. Thus, at higher β, one can use the crossbar H-type (CH) DTL in the H_{211} or H_{210} mode. The cavity dimensions are convenient for frequencies between 150 and 600 MHz [7, 8]. CH-cavities have been investigated by IAP-Frankfurt, GSI-Darmstadt, and LANL in Los Alamos [9]. Moreover, the new FAIR proton injector, currently under construction, is based on CH structures [10].

The available 3 MW klystrons encourage increasing the number of gaps per CH-cavity in order to take advantage of using this power. But, due to the KONUS beam dynamics, which couples short, lens-free accelerating sections by quadrupole triplets, the gap numbers in each section are limited. Consequently, RF-coupling of two CH sections by a coupling cell that contains a quadrupole lens presents an attractive solution. It allows to have similar power requests in each cavity, which fits well with the power level of an industrial amplifier (in our case, a 3 MW klystron). This concept is used in the first three cavities of the FAIR proton linac [3, 10, 11]. In this paper, the applied coupling concept based on theory and simulations is discussed.

2. Coupling Structures Concept

To understand the physical concept of coupled CH sections, coupled by a lens-containing drift tube, consider a system of three magnetically coupled oscillators, as shown in Fig. 3 [12]. Each oscillator has the same frequency ω_0, which is defined as

$$\omega_0 = 1/\sqrt{L_0 C_0} \quad (1)$$

where L_0 is the resonator inductance and C_0 is the resonator capacitance.

This is a very simplified model of our situation.

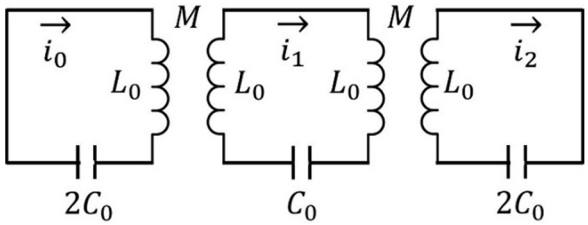

FIG. 3. A system of three magnetically coupled resonators [12], where M is the mutual inductance, L_0 is the resonator inductance, and i_0, i_1, and i_2 are the currents in each resonator.

The first and third oscillators represent the two CH accelerating sections, while the central oscillator represents the coupling section, which contains the magnetic quadrupole triplet.

The central oscillator is coupled with the other two oscillators by a mutual inductance M with a coupling strength that is defined as the ratio between the mutual inductance and the resonator inductance L_0. This is the coupling constant:

$$k = M/L_0 \tag{2}$$

Applying Kirchhoff's laws to this system leads to a system of coupled equations [12]. By solving these equations, one can find three eigenmodes:

- Zero mode, where all oscillators oscillate in phase at a frequency of

$$\Omega_0 = \frac{\omega_0}{\sqrt{1+k}} \tag{3}$$

- $\pi/2$ −mode, where the two accelerating sections at each end oscillate in opposite phase compared to the zero mode. The frequency is

$$\Omega_{\pi/2} = \omega_0 \tag{4}$$

The coupling cell in between shows zero amplitude in this case.

- The π −mode, where all sections are shifted against each other by π. The mode frequency is

$$\Omega_\pi = \frac{\omega_0}{\sqrt{1-k}} \tag{5}$$

The frequency difference between π −mode and 0 −mode is defined as the bandwidth and is given in a good approximation at small k by

$$\delta\omega = \Omega_\pi - \Omega_0 \approx k\omega_0 \tag{6}$$

In the following sections, the coupled CH-DTL is simulated with the commercial package CST-MW [6], and the results are compared to this model. CST-MW is a versatile 3D simulation tool for fast and accurate 3D electromagnetic simulation of high-frequency problems.

3. Concept of Coupled CH (CCH) – Cavity

To show the coupling concept without the disturbance by a real drift tube structure with its beta-profile, we simplified the geometry with respect to that point. The simulated CCH cavity has 26 gaps in total, and the energy profile is constant. For this investigation, the cavity structure consists of two identical accelerating sections, each has 13 accelerating gaps, and the coupling cell in between is 2βλ long in this example. The layout of the cavity is shown in Fig. 4, and Table 1 shows the main cavity parameters.

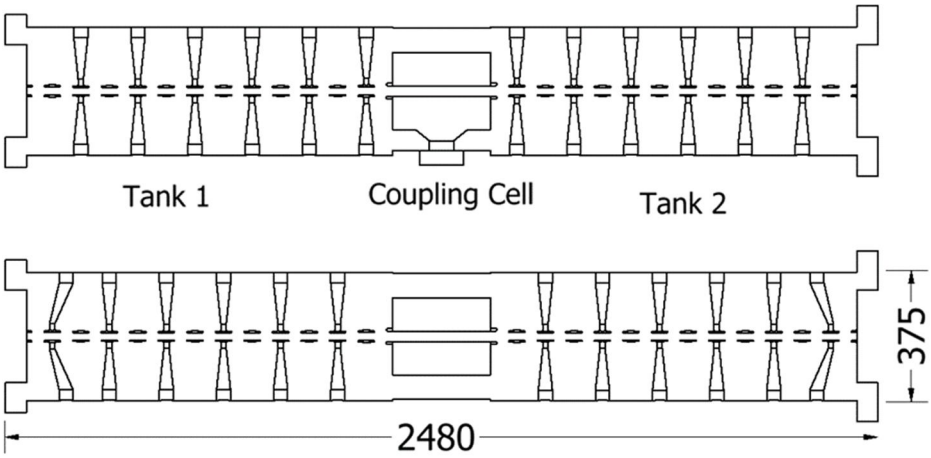

FIG. 4. Layout of the constant beta CCH cavity showing the main dimensions.

TABLE 1. Main parameters of the coupled CH cavity.

Number of Gaps	26
Design Frequency (MHz)	325.224
Eff. Accel. Length (mm)	2480
Shunt Impedance Z_0 (MΩ/m)	84.4
Q_0 – value	14400
Drift tube Aperture (mm)	20
Lens Aperture (mm)	20
$\Delta f_{\pi/2} = f_{\pi/2} - f_0$ (kHz)	700
$\Delta f_{\pi} = f_{\pi} - f_0$ (kHz)	4700

RF simulations show that the two CH tanks are coupled efficiently after optimizing the cavity and coupling cell dimensions. The coupling in such a CCH cavity is achieved after tuning each of the three cavity parts separately to the operating frequency.

When the three coupled oscillators model from section 2 is applied to this cavity, one can derive the coupling factor from the resonance frequencies of the three lowest modes as described in Eq. (5). This results in k = 0.011. On the other hand, one can compare the frequency shift between π – mode and 0 – mode, and π/2 – and 0 – mode, which is asymmetric as can be seen in Table 1. This is a hint that the three coupled oscillators model does not apply very well. The explanation is given below through the analysis of the gap voltage distribution for the three lowest cavity modes.

Another tuning subject was the field tuning at the end cells of the cavity, to reach a zero-like mode $H_{21(0)}$.

To solve this issue, the end shapes in the cavity were modified as shown in Fig. 4. By increasing the cavity diameter locally, the inductance is increased to get the end cells in resonance. As a result, the electric fields in the end gaps increased by a factor of two. By that method, the matched cavity ends become short, allowing for an improved mechanical integration of the inter-tank quadrupole triplets. Short drift lengths between cavities improve the longitudinal beam dynamics, as the bunch length can be kept short. Fig. 5 shows the on-axis electric field for the final cavity design in the operating mode (quasi-zero mode). It was calculated by CST-MW. The same curve can be measured by bead-pull measurements along the beam axis of a cavity. The peaks show the field distribution $|E_z(z)|$ along all gaps. The effective shunt impedance increases as well with the new end shapes by 15%, as the total cavity length is reduced.

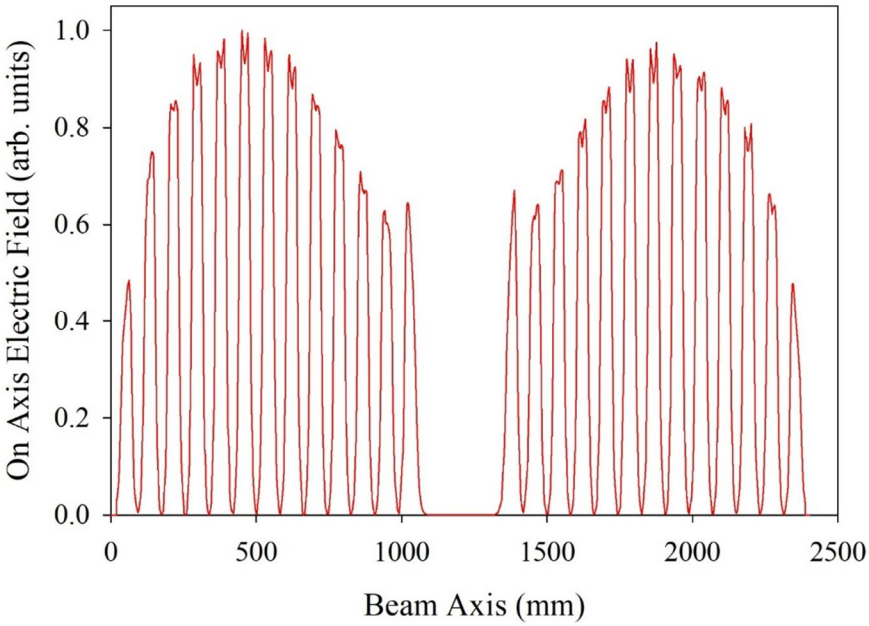

FIG. 5. The absolute on-axis electric field $|E_z(z)|$ distribution along the CCH cavity in quasi-zero-mode.

The effective gap voltage distribution is calculated from the longitudinal electric field distribution by applying the transit time factors for each gap. The results are shown in Fig. 6. The transit time factors can be either obtained from the LORASR beam dynamics code [13] or calculated from the CST field distribution. This controlled process is repeated until the gap voltage deviation between the two distributions falls below approximately 2%. Final optimization of the cavity's field distribution and simulated gap voltages in the beam dynamics code is achieved by inductive tuners (see next section). The 3D electric field distribution of the CCH cavity for the zero mode is shown in Fig. 7.

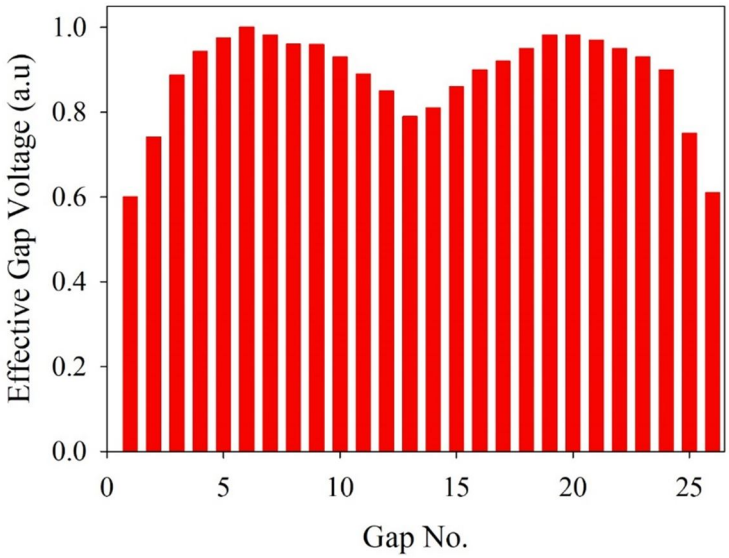

FIG. 6. Effective gap voltage distribution from field simulations by CST-MW.

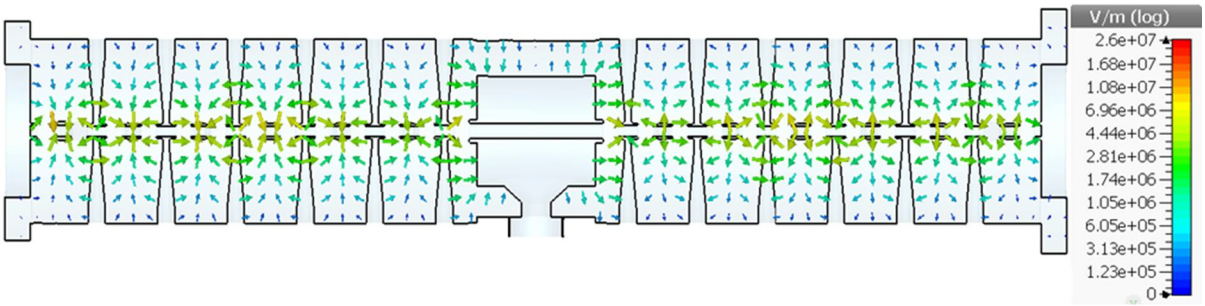

FIG. 7. The 3D electric field distribution along the yz symmetry-plane for the CCH cavity.

As mentioned before, the two CH-drift tube sections are coupled by the coupling cell containing a quadrupole triplet which oscillates in Alvarez mode (E_{010} – mode), as shown in Figs. 8 and 9.

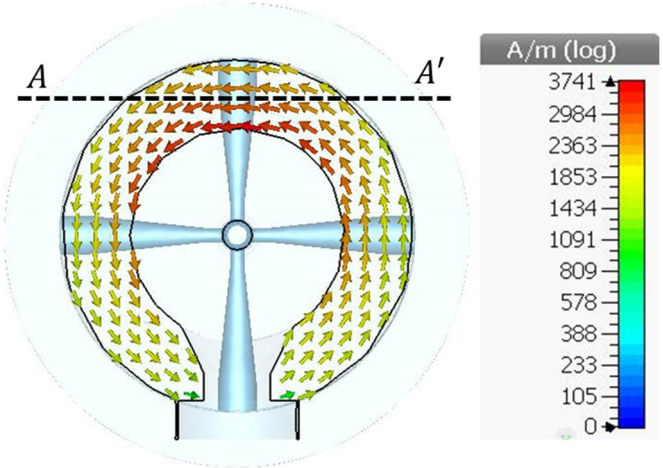

FIG. 8. The magnetic field distribution in the middle plane of the coupling cell.

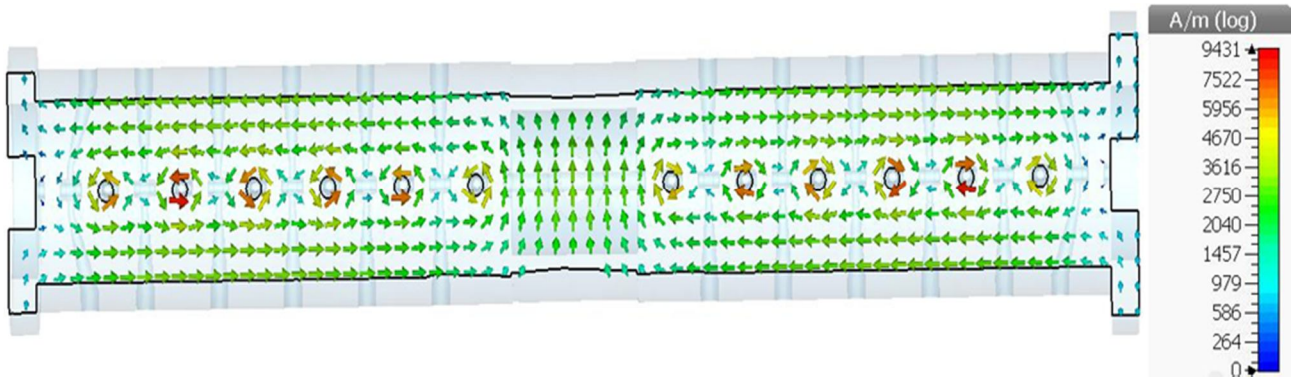

FIG. 9. Magnetic field distribution in shifted xz −plane (AA' in Figure 8) for the CCH cavity.

The magnetic field lines within each quadrant of the drift tube sections are parallel and antiparallel to the beam axis (Fig. 9). Around the coupling lens, however, the angular field direction is dominating. Additionally, the local field lines around the stems are clearly visible in Fig. 9.

The on-axis electric field distributions for the $\pi/2$ – and π – modes are shown in Figs. 10 and 11. Fig. 10 shows that each of the three coupled resonators oscillates with phase relations in the central parts fitting to this simplified model at a first glance. However, the phase relations along the cells of each drift tube section are changed significantly. Although the beta lambda half cells of an H-type structure are coupled very strongly to each other, with coupling constants k typically about 0.3 [14], the phase modulation within each drift tube section plays an important role for the CCH cavity. This should explain why the three coupled oscillators model does not apply too well. Alternative descriptions of the CCH cavity are under development.

The design operating frequency of the investigated coupled CH cavity in this study is 325.224 MHz. For field and gap voltage final tuning, one may apply inductive tuning by cylindrically shaped plungers mainly, as this technique does not influence locally the high electric field regions near the aperture. Moreover, the simple cylindrical tuner body and its short length make cooling easy, and there is no risk of harming the mechanical tuner's vibrations. Also, multipacting is not critical.

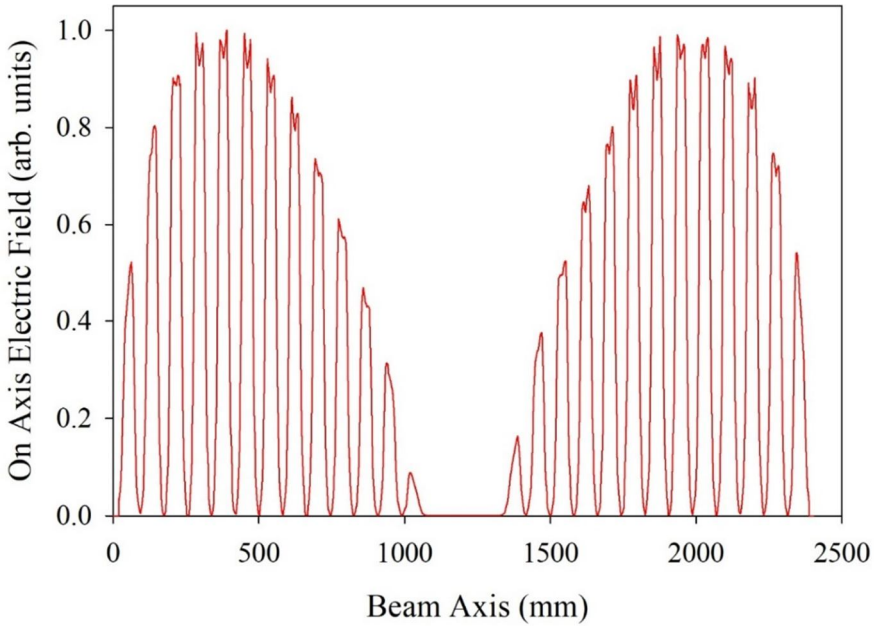

FIG. 10. The absolute on-axis electric field $|E_z(z)|$ distribution along the CCH cavity in $\pi/2$ – mode.

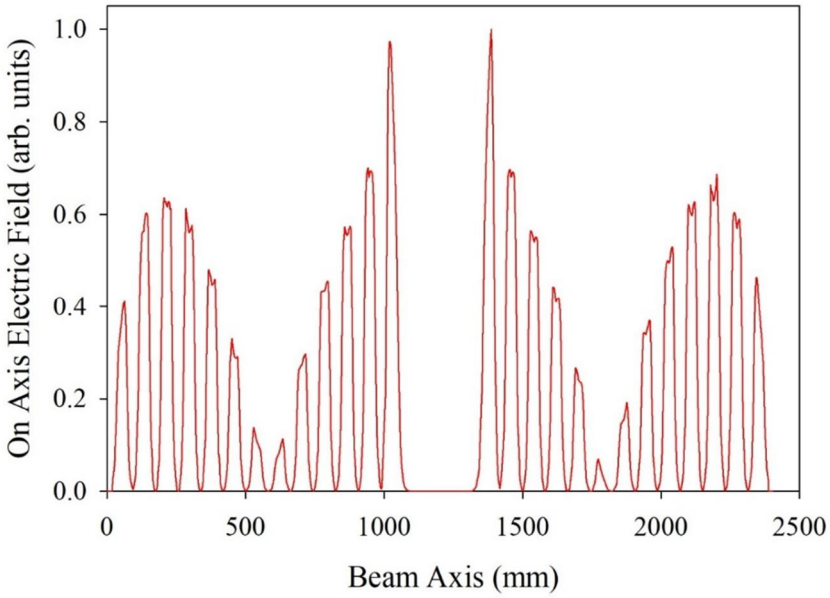

FIG. 11. The absolute on-axis electric field $|E_z(z)|$ distribution along the CCH cavity in π – mode.

In a first rough consideration, it is assumed that the relative frequency shift $\Delta\omega_0/\omega_0$ is proportional to the relative volume change of the cavity $\Delta V_{tuner}/V_{cavity}$, which is valid in the case of a constant absolute magnetic field value in the whole cavity volume:

$$\frac{\Delta\omega_0}{\omega_0} = \frac{\Delta U_m}{U_c} \cong \frac{\Delta V_{tuner}}{V_{cavity}} \tag{7}$$

where ΔU_m is the magnetic field energy in the displaced plunger volume, while U_c denotes the stored cavity field energy. For the cavity volume estimation, the cylindrical cavity volume between the two outer gap centers was taken.

A comparison with the simulations for the coupled CH cavity shows that, for the linear part of the curves in Fig. 12, the following approximation is valid:

$$\frac{\Delta\omega_0}{\omega_0}(simulations) \cong 0.7\frac{\Delta V_{tuner}}{V_{cavity}}\ ; \tag{8}$$

Figure 12 shows the frequency shift against the tuner depth in the case of the CCH cavity. In this simulation, a total of five cylindrical tuners, with a diameter of 60 mm, were moved in parallel. Two of them acted on each drift tube section, while the fifth one acted against the internal lens. The slope up to a tuner length of 40 mm agrees well with Eq. (8). At increased tuner length, the tuner head enters a region with increasing electric field density, resulting in a reduced frequency increase and finally in a decrease when the electric field density is dominating. It is intended to use the most efficient tuning range, up to around 80 mm.

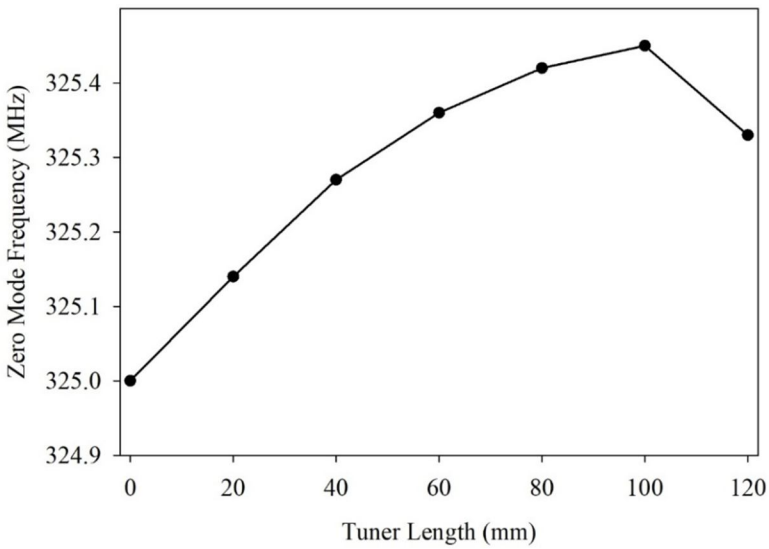

FIG. 12. Simulated frequency shifts by parallel action of five tuners along the coupled CH cavity.

While the field and frequency are fine-tuned by fixed tuners, frequency control during operation is handled by a single mobile tuner which acts within a small tuning range, as the CH cavity temperature is controlled by intensive water-cooling.

4. Conclusion

The coupling of two CH cavities is an important issue for the low-energy part of a CH-DTL. Developments in H-type cavities (IH-DTL and CH-DTL) over the past decades have led to a robust and efficient class of cavities, which can serve as an attractive alternative to the Alvarez DTL in many cases.

To have short drifts between accelerating sections for placing quadrupole lenses and to allow a match of RF power requirements and attractive RF amplifier solutions, the coupling of short CH structures is helpful in the low-energy part of DTL. The coupling method was tested by a simplified three coupled resonators model. The details of the RF coupling of two CH tanks by a coupling cell $2\beta\lambda$ in length containing a triplet lens were described by simulation results.

It has been shown that the fine tuning of a CCH cavity can be accomplished by fixed cylindrical volume tuners.

The concept described in this paper enables the realization of a CH-DTL with KONUS beam dynamics. At the same time, the largest available RF amplifiers of the 3 MW class can be efficiently coupled one by one to the cavities by using CCH cavities at lower beam energies.

References

[1] Ratzinger, U., "H-type Linac Structures", In: Proc. CAS CERN Accelerator School, Radio Frequency Engineering, Seeheim, Germany, 8-16 May 2000, ISBN 92-9083-249-5, p. 351 – 379.

[2] Ratzinger, U., Hähnel, H., Tiede, R., Kaiser, J., and Almomani, A., Phys. Rev. Accel. Beams, 22 (2019) 114801.

[3] Ratzinger, U., A Low Beta RF Linac-Structure of the IH-type with Improved Radial Acceptance, in Proc. 1988 Linear Accelerator Conference (LINAC'88) Newport News, VA (JACoW, Geneva, 2003), p. 185.

[4] Clemente, G. et al., Phys. Rev. Accel. Beams, 14, (2011) 110101.

[5] Broere, J., Kugler, H., Vertenar, M., Rarzinger, U., and Krietenstein, B., High Power Conditioning of the 202 MHz IH Tank 2 at the CERN LINAC3, Proc. LINAC98, Chicago, USA, p. 771 (1998).

[6] CST MICROWAVE. http://www.cst.com/.

[7] Ratzinger, U., The New High Current Ion Accelerator at GSI and Perspectives for Linac Design Based on H-mode Cavities, in Proc. European Particle Accelerator Conf., Vienna, 2000 (EPS, Geneva, 2000), pp. 98–102.

[8] Almomani, A. and Ratzinger, U., Status of a 325 MHz High Gradient CH - Cavity, in Proceedings of 28th Linear Accelerator Conf. (LINAC'16), East Lansing, MI, USA, THPLR059, pp. 982-984 (2016).

[9] Carneiro, J.-P., Mustapha, B., and Ostroumov, P.N., Nucl. Instrum. Methods Phys. Res., Sect. A, 606, (2009) 271.

[10] Almomani, A., Busch, M., Dziuba, F.D., Kleffner, C.M., Ratzinger, U., and Tiede, R., Journal of Physics: Conference Series, 874 (2017) 012046.

[11] Brodhage, R., Vinzenz, W., Clemente, G., and Ratzinger, U., First Coupled CH Power Cavity for the FAIR Proton Injector, in Proceedings of the 5th International Particle Accelerator Conference IPAC14, Dresden, Germany, pp. 3232–3234 (2014).

[12] Wangler, T., "RF Linear Accelerators", 2nd Ed., (Wiley-VCH Verlag GmbH & Co. KGaA, Weinheim, 2008).

[13] Tiede, R., Clemente, G., Podlech, H., Ratzinger, U., Sauer, A., and Minaev, S., LORASR Code Development, in Proceedings of the European Particle Accelerator Conference EPAC06, Edinburgh, Scotland, WEPCH118, pp. 2194-2196 (2006).

[14] Lapostolle, P.M. and Septier, A.L., "Linear Accelerators", North Holland Publishing Company, 1970; ISBN, 0720401569, 9780720401561.

الجداول: تعطى الجداول أرقاما متسلسلة يشار إليها في النص. ويجب طباعة كل جدول على صفحة منفصلة مع عنوان فوق الجدول. أما الحواشي التفسيرية، التي يشار إليها بحرف فوقي، فتكتب أسفل الجدول.

الرسوم التوضيحية: يتم ترقيم الأشكال والرسومات والرسومات البيانية (المخططات) والصور، بصورة متسلسلة كما وردت في النص.

تقبل الرسوم التوضيحية المستخرجة من الحاسوب والصور الرقمية ذات النوعية الجيدة بالأبيض والأسود، على ان تكون أصيلة وليست نسخة عنها، وكل منها على ورقة منفصلة ومعرفة برقمها بالمقابل. ويجب تزويد المجلة بالرسومات بحجمها الأصلي بحيث لا تحتاج إلى معالجة لاحقة، وألا تقل الحروف عن الحجم 8 من نوع Times New Roman، وألا تقل سماكة الخطوط عن 0.5 وبكثافة متجانسة. ويجب إزالة جميع الألوان من الرسومات ما عدا تلك التي ستنشر ملونة. وفي حالة إرسال الرسومات بصورة رقمية، يجب أن تتوافق مع متطلبات الحد الأدنى من التمايز (1200 dpi Resolution) لرسومات الأبيض والأسود الخطية، و 600 dpi للرسومات باللون الرمادي، و300 dpi للرسومات الملونة. ويجب تخزين جميع ملفات الرسومات على شكل (jpg)، وأن ترسل الرسوم التوضيحية بالحجم الفعلي الذي سيظهر في المجلة. وسواء أرسل المخطوط بالبريد أو عن طريق الشبكة (Online)، يجب أرسال نسخة ورقية أصلية ذات نوعية جيدة للرسومات التوضيحية.

مواد إضافية: تشجع المجلة الباحثين على إرفاق جميع المواد الإضافية التي يمكن أن تسهل عملية التحكيم. وتشمل المواد الإضافية أي اشتقاقات رياضية مفصلة لا تظهر في المخطوط.

المخطوط المنقح (المعدّل) والأقراص المدمجة: بعد قبول البحث للنشر وإجراء جميع التعديلات المطلوبة، فعلى الباحثين تقديم نسخة أصلية ونسخة أخرى مطابقة للأصلية مطبوعة بأسطر مزدوجة، وكذلك تقديم نسخة إلكترونية تحتوي على المخطوط كاملا مكتوبا على Microsoft Word for Windows 2000 أو ما هو استجد منه. ويجب إرفاق الأشكال الأصلية مع المخطوط النهائي المعدل حتى لو تم تقديم الأشكال إلكترونيا. وتخزن جميع ملفات الرسومات على شكل (jpg)، وتقدم جميع الرسومات التوضيحية بالحجم الحقيقي الذي ستظهر به في المجلة. ويجب إرفاق قائمة ببرامج الحاسوب التي استعملت في كتابة النص، وأسماء الملفات على قرص مدمج، حيث يعلَم القرص بالاسم الأخير للباحث، وبالرقم المرجعي للمخطوط للمراسلة، وعنوان المقالة، والتاريخ. ويحفظ في مغلف واقٍ.

حقوق الطبع

يُشَكِّل تقديم مخطوط البحث للمجلة اعترافاً صريحاً من الباحثين بأنّ مخطوط البحث لم يُنْشَر ولم يُقَدَّم للنشر لدى أي جِهَة أخرى كانت وبأي صيغة ورقية أو إلكترونية أو غيرها. ويُشترط على الباحثين ملء أنموذج يَنُصُّ على نقْل حقوق الطبع لتُصبح ملكاً لجامعة اليرموك قبل الموافقة على نشر المخطوط. ويقوم رئيس التحرير بتزويد الباحثين بإنموذج نقل حقوق الطبع مع النسخة المُرْسَلَة للتنقيح. كما ويُمنع إعادة إنتاج أيِّ جزء من الأعمال المنشورة في المجلّة من دون إذن خَطِّيٍّ مُسْبَق من رئيس التحرير.

إخلاء المسؤولية

إن ما ورد في هذه المجلة يعبر عن آراء المؤلفين، ولا يعكس بالضرورة آراء هيئة التحرير أو الجامعة أو سياسة اللجنة العليا للبحث العلمي أو وزارة التعليم العالي والبحث العلمي. ولا يتحمل ناشر المجلة أي تبعات مادية أو معنوية أو مسؤوليات عن استعمال المعلومات المنشورة في المجلة أو سوء استعمالها.

الفهرسة: المجلة مفهرسة في:

Scopus	**Emerging Sources Citation Index (ESCI)** Journal Impact Factor 2022 0.7
ULRICHSWEB GLOBAL SERIALS DIRECTORY	

معلومات عامة

المجلة الأردنية للفيزياء هي مجلة بحوث علميّة عالمية متخصصة مُحكمة تصدر بدعم من صندوق دعم البحث العلمي والابتكار، وزارة التعليم العالي والبحث العلمي، عمان، الأردن. وتقوم بنشر المجلة عمادة البحث العلمي والدراسات العليا في جامعة اليرموك، إربد، الأردن. وتنشر البحوث العلمية الأصيلة، إضافة إلى المراسلات القصيرة Short Communications، والملاحظات الفنية Technical Notes، والمقالات الخاصّة Feature Articles، ومقالات المراجعة Review Articles، في مجالات الفيزياء النظرية والتجريبية، باللغتين العربية والإنجليزية.

تقديم مخطوط البحث

تقدم المخطوطات إلكترونيًا عن طريق موقع المجلة: https://jjp.yu.edu.jo

ويجري تحكيمُ البحوثِ الأصيلة والمراسلات القصيرة والملاحظات الفنية من جانب مُحكِّمين اثنين في الأقل من ذوي الاختصاص والخبرة. وتُشَجِّع المجلة الباحثين على اقتراح أسماء المحكمين. أما نشر المقالات الخاصّة في المجالات الفيزيائية النَشِطَة، فيتم بدعوة من هيئة التحرير، ويُشار إليها كذلك عند النشر. ويُطْلَب من كاتب المقال الخاص تقديم تقرير واضح يتّسم بالدقة والإيجاز عن مجال البحث تمهيداً للمقال. وتنشر المجلةُ أيضاً مقالات المراجعة في الحقول الفيزيائية النشطة سريعة التغيُّر، وتُشَجّع كاتبي مقالات المراجعة أو مُستَكتبيها على إرسال مقترحٍ من صفحتين إلى رئيس التحرير. ويُرْفَق مع البحث المكتوب باللغة العربية ملخص (Abstract) وكلمات دالة (Keywords) باللغة الإنجليزية.

ترتيب مخطوط البحث

يجب أن تتم طباعة مخطوط البحث ببنط 12 نوعه Times New Roman، وبسطر مزدوج، على وجه واحد من ورق A4 (21.6 × 27.9 سم) مع حواشي 3.71 سم ، باستخدام معالج كلمات ميكروسوفت وورد 2000 أو ما استُجِدَ منه. ويجري تنظيم أجزاء المخطوط وفق الترتيب التالي: صفحة العنوان، الملخص، رموز التصنيف (PACS)، المقدّمة، طرق البحث، النتائج، المناقشة، الخلاصة، الشكر والعرفان، المراجع، الجداول، قائمة بدليل الأشكال والصور والإيضاحات، ثَمَّ الأشكال والصور والإيضاحات. وتُكْتَب العناوين الرئيسة بخطٍ **غامق**، بينما تُكْتَب العناوين الفرعية بخطٍ *مائل*.

صفحة العنوان: وتشمل عنوان المقالة، أسماء الباحثين الكاملة وعناوين العمل كاملة. ويكتب الباحث المسؤول عن المراسلات اسمه مشارا إليه بنجمة، والبريد الإلكتروني الخاص به. ويجب أن يكون عنوان المقالة موجزا وواضحا ومعبرا عن فحوى (محتوى) المخطوط، وذلك لأهمية هذا العنوان لأغراض استرجاع المعلومات.

الملخص: المطلوب كتابة فقرة واحدة لا تزيد على مائتي كلمة، موضحة هدف البحث، والمنهج المتبع فيه والنتائج وأهم ما توصل إليه الباحثون.

الكلمات الدالة: يجب أن يلي الملخص قائمة من 4-6 كلمات دالة تعبر عن المحتوى الدقيق للمخطوط لأغراض الفهرسة.

PACS: يجب إرفاق الرموز التصنيفية، وهي متوافرة في الموقع http://www.aip.org/pacs/pacs06/pacs06-toc.html.

المقدمة: يجب أن توضّح الهدف من الدراسة وعلاقتها بالأعمال السابقة في المجال، لا أن تكون مراجعة مكثفة لما نشر (لا تزيد المقدمة عن صفحة ونصف الصفحة مطبوعة).

طرائق البحث (التجريبية / النظرية): يجب أن تكون هذه الطرائق موضحة بتفصيل كاف لإتاحة إعادة إجرائها بكفاءة، ولكن باختصار مناسب، حتى لا تكون تكرارا للطرائق المنشورة سابقا.

النتائج: يستحسن عرض النتائج على صورة جداول وأشكال حيثما أمكن، مع شرح قليل في النص ومن دون مناقشة تفصيلية.

المناقشة: يجب أن تكون موجزة وتركز على تفسير النتائج.

الاستنتاج: يجب أن يكون وصفا موجزا لأهم ما توصلت إليه الدراسة ولا يزيد عن صفحة مطبوعة واحدة.

الشكر والعرفان: الشكر والإشارة إلى مصدر المنح والدعم المالي يكتبان في فقرة واحدة تسبق المراجع مباشرة.

المراجع: يجب طباعة المراجع بأسطر مزدوجة ومرقمة حسب تسلسلها في النص. وتكتب المراجع في النص بين قوسين مربعين. ويتم اعتماد اختصارات الدوريات حسب نظام Wordlist of Scientific Reviewers.

Subscription Form

Jordan Journal of PHYSICS

An International Peer-Reviewed Research Journal issued by the Support of the Scientific Research and Innovation Support Fund

Published by the Deanship of Research & Graduate Studies, Yarmouk University, Irbid, Jordan

Name: ..... الأسم:

Specialty:..... التخصص:

Address: ..... العنوان:

P.O. Box:..... صندوق البريد:

City & Postal Code: ..... المدينة/الرمز البريدي:

Country: ..... الدولة:

Phone: ..... رقم الهاتف:

Fax No:..... رقم الفاكس:

E-mail:..... البريد الإلكتروني:

No. of Subscription: ..... عدد الإشتراكات:

Method of Payment:..... طريقة الدفع:

Amount Enclosed:..... المبلغ المرفق:

Signature: ..... التوقيع:

Cheques should be paid to Deanship of Research and Graduate Studies - Yarmouk University.

I would like to subscribe to the Journal
For

- One Year
- Two Years
- Three Years

One Year Subscription Rates

	Inside Jordan	Outside Jordan
Individuals	JD 8	€ 40
Students	JD 4	€ 20
Institutions	JD 12	€ 60

Correspondence

Subscriptions and Sales:

Prof. Muhammad S. Bawa'aneh
Deanship of Research and Graduate Studies
Yarmouk University
Irbid – Jordan
Telephone: 00 962 2 711111 Ext. 2074
Fax No.: 00 962 2 7211121

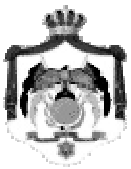

المملكة الأردنية الهاشمية

جامعة اليرموك

المجلة الأردنية
للفيزياء

مجلة بحوث علمية عالمية متخصصة محكّمة

تصدر بدعم من صندوق دعم البحث العلمي والابتكار

المجلد (18)، العدد (2)، حزيران 2025م / محرم 1447هـ

المجلة الأردنية

للفيزياء

مجلة بحوث علمية عالمية محكّمة

المجلد (18)، العدد (2)، حزيران 2025م / محرم 1447هـ

المجلة الأردنية للفيزياء: مجلة علمية عالمية متخصصة محكّمة تصدر بدعم من صندوق دعم البحث العلمي والإبتكار، عمان، الأردن، وتصدر عن عمادة البحث العلمي والدراسات العليا، جامعة اليرموك، إربد، الأردن.

ترسل البحوث إلى العنوان التالي:

الأستاذ الدكتور محمد سالم بواعنة

رئيس تحرير المجلة الأردنية للفيزياء

عمادة البحث العلمي والدراسات العليا، جامعة اليرموك

إربد ، الأردن

هاتف 7211111 2 962 00 **فرعي** 2074

E-mail: *jjp@yu.edu.jo* **Website**: *http:// jjp.yu.edu.jo*